



Commande Robuste Structurée : Application Co-Design Mécanique / Contrôle d'Attitude d'un Satellite Flexible

José Alvaro Perez Gonzalez

► To cite this version:

José Alvaro Perez Gonzalez. Commande Robuste Structurée : Application Co-Design Mécanique / Contrôle d'Attitude d'un Satellite Flexible. Physique de l'espace [physics.space-ph]. INSTITUT SUPERIEUR DE L'AERONAUTIQUE ET DE L'ESPACE (ISAE), 2016. Français. NNT : . tel-01434160

HAL Id: tel-01434160

<https://hal.science/tel-01434160>

Submitted on 13 Jan 2017

HAL is a multi-disciplinary open access archive for the deposit and dissemination of scientific research documents, whether they are published or not. The documents may come from teaching and research institutions in France or abroad, or from public or private research centers.

L'archive ouverte pluridisciplinaire **HAL**, est destinée au dépôt et à la diffusion de documents scientifiques de niveau recherche, publiés ou non, émanant des établissements d'enseignement et de recherche français ou étrangers, des laboratoires publics ou privés.



THÈSE

En vue de l'obtention du

DOCTORAT DE L'UNIVERSITÉ DE TOULOUSE

Délivré par : *l'Institut Supérieur de l'Aéronautique et de l'Espace (ISAE)*

Présentée et soutenue le 14/11/2016 par :

JOSE ALVARO PEREZ GONZALEZ

**Commande Robuste Structurée : Application Co-Design Mécanique /
Contrôle d'Attitude d'un Satellite Flexible**

JURY

DANIEL ALAZARD
THOMAS LOQUEN
CHRISTELLE PITTET
YANN LE GORREC
PAOLO GASBARRI
FRANCK CAZAURANG

Université de Toulouse/ISAE
ONERA
CNES
Institut FEMTO-ST
Università Roma La Sapienza
Université de Bordeaux

Directeur de thèse
Co-directeur de thèse
Encadrante de thèse
Examineur
Rapporteur
Rapporteur

École doctorale et spécialité :

EDSYS : Automatique 4200046

Unité de Recherche :

ONERA (DCSD)

Directeur(s) de Thèse :

Daniel ALAZARD, Thomas LOQUEN et Christelle PITTET

Rapporteurs :

Paolo GASBARRI et Frank CAZAURANG

Integrated Control/Structure Design of a Flexible Satellite Using Structured Robust Control Synthesis

A PHD DISSERTATION
SUBMITTED IN PARTIAL FULFILLMENT OF THE REQUIREMENTS FOR THE DEGREE OF
DOCTOR OF PHILOSOPHY
(AUTOMATIC CONTROL IN AEROSPACE ENGINEERING)

AUTHORED BY

JOSE ALVARO PEREZ GONZALEZ

SUPERVISED BY

DANIEL ALAZARD
THOMAS LOQUEN
CHRISTELLE PITTET

SEPTEMBER 2016
INSTITUT SUPERIEUR DE L'AERONAUTIQUE ET DE L'ESPACE

ECOLE DOCTORALE SYSTEMES



*In dedication to my parents, Maria
and Jose, for making me be who I am,
and my girlfriend Silvia, for supporting
me all the way...*

Acknowledgments

First, I would like to express my sincere gratitude to my advisor Prof. Daniel Alazard for the continuous support of my Ph.D study and related research, for his patience, motivation, and immense knowledge. I would like to thank as well my co-advisors Thomas Loquen and Christelle Pittet for encouraging my research and for allowing me to grow as a research engineer. Your advice on both research as well as on my career have been priceless. Besides my advisors, I would like to thank the rest of my thesis committee: Prof. Paolo Gasbarri, Prof. Franck Cazaurang, and Dr. Le Gorrec, for accepting being members of my evaluation committee, for reviewing and evaluating the manuscript and for their insightful comments. I would like to thank as well Christelle Cumer, who has been very helpful at the beginning of the study and who has encouraged me during the whole thesis. I would like to thank the rest of the DCSD department of ONERA for making me feel at home, especially Mathieu Rognant, Charles Poussot and Cedric Seren for their help and support during these years.

Second, it is my pleasure to thank all my fellow labmates in ONERA for the stimulating coffee breaks and all the funny discussions we have had during lunch time and other non-official meetings. It is hardly difficult to make you understand how important you have been to me during all these years, and even more difficult to transmit this to the people who have already left ONERA or who do not have time to read this paragraph. Anyway, since this thesis will remain in the archives for ages, I hope one day you will do. Thanks to Emmanuel C., Jeremy L., Adrien M., Elodie D., Guillaume C., Patrick B. and Henry S. for integrating me in the group of PhD students during my first year, even though it was really difficult to understand my hard Spanish accent. Your attitude and understanding showed me the way for staying on my feet during this hard test. My second year has been marked by the meeting of Hélène E., with whom I have shared many unforgettable moments discussing about space, control/mechanics theory and ordinary-life problems, and by getting to know Mathieu B., Guillaume A. and Jorrit T., with whom I have shared many pleasant discussions. The third year has been even brighter than the previous ones thanks to the illuminating and generous smiles of Adèle B., Marine H. and Lylia S., who have transmitted me their happiness and optimism. I cannot forget my office colleague Martin S., with whom I have shared many great moments and interesting discussions about life and the career. And thanks as well to the new arrivals, Pauline K., Matteo G., Mehdi, Lucie and Vincent B., who have taught me

the knowledge of the street and with whom I wish I have spent more time... Thank you all, the past, the present and the future *doctorants*, you make the DCSD a really nice place to work.

Finally, I would not like to finish this part of the acknowledgements without thanking the rest of the research and education community at ONERA, CNES and ISAE-Supaero. Elyse R., thank you for helping me with my English and, the most important, for the many pleasant times I have had in your class discussing about space, philosophy and life in general. Your support and comprehension have been very valuable all these years. I would like to thank my other teacher, Sylvie S., who has helped me improve my French and with whom I have shared many interesting conversations about literature and history. Thanks a lot to Sofia U. as well, our far away coffee breaks have helped to decrease the stress of the thesis. To conclude, I want to thank all the invisible effort that many different Spanish and French professors have put on my education. None of this would have been possible without their altruistic help.

En esta segunda parte de los agradecimientos, quiero aprovechar mi mayor destreza con la lengua de Cervantes para agradecer, de corazón, a la gente que puede entenderme ya sea porque hablan español o porque lo entienden.

Durante estos tres largos años he tenido el privilegio de compartir casa y vivencias con varias personas que, inevitablemente, quedaran grabadas en mi memoria. Muchas gracias a Adrián C., que me ofreció mudarme a su casa y jugar con su consola a pesar de lo malo que era. Además, me enseñaste que si algo se quiere intensamente, con sacrificio y con un plan se puede conseguir. Mi querido Igor, aunque desaparecieras todos los días para ir a trabajar con tu tesis, que sepas que guardo muy buenos recuerdos de nuestras bromas y nuestros cantos con tu guitarra, lástima que tuvieras que ir a EEUU y dejar el apartamento. Y como no olvidarme de mi doblemente compañero de piso, Andrea S., con quien nunca he parado de aprender cosas, de reírme, de debatir amablemente y de cocinar. Has sido un ejemplo para mí en todo, desde la actitud hacia el trabajo hasta la forma de tratarse a uno mismo, y es por eso que todo lo que pueda escribir aquí para agradecértelo, es poco.

En ONERA tuve la suerte de compartir mis inquietudes en largos paseos al sol alrededor del edificio E con mi garant, vecino, co-worker, *spotter*, *doer* y amigo, el ahora Doctor Gustavo A., Dr Gus. Siendo los dos ingenieros con la misma visión de las cosas, con la misma escuela, con el mismo parcours, con el mismo humor e incluso con las mismas raíces, era obvio que acabaríamos entablando una gran amistad. Gracias a él hoy puedo (podemos) decir que he (hemos) acabado la tesis con un mínimo de dignidad y de cordura. Por no hablar de su crucial ayuda hacia el final, cuando tuve que compaginar Cannes con Toulouse. Raquel B. también tiene un gran mérito en este logro, puesto que incluso cogió un día de sus vacaciones para ayudarme el día de mi soutenance. Y además hace unas croquetas buenísimas. No me voy a cansar de agradecerles a Gus y Raquel lo mucho que me han ayudado y servido como apoyo a lo largo de la tesis, sobre todo los últimos meses en los que ya estaba solo contra el peligro.

También en ONERA conocí a otra persona increíble, Lucia S., que desde el primer día me ilumino con su alegría y generosidad. Probablemente el primer año hubiera tirado la toalla si no fuera porque durante los seis meses que ella estuvo allí siempre me animó y alegró las

mañanas, y también los fines de semana con planes superguays y videos de youtube aún más *incréíbles*. Gracias de corazón. También gracias a su chico, Sergi L., que siempre ha estado ahí para lo que hiciera falta y que no dudó en ningún momento en dejarme su casa para que pudiera estar tranquilo el día de mi soutenance. También gracias a Oleguer B., que aunque se fue al principio y me dejó solo ante el peligro, siempre nos ha seguido uniendo la amistad que forjamos aquí en Toulouse cuando todo era más difícil para los dos.

El tiempo no perdona a nadie, y estos tres años han estado marcados por la gente que ha tenido que irse de Toulouse y por la gente que he tenido la oportunidad de conocer. Gracias a los dobles diplomas, Maxi L., Joaquin G., Javier S., Jordi M. y Fernando G., que aunque os fuisteis yendo uno a uno y parecía como si poco a poco arrancasen nuestra foto de Toulouse, siempre hemos estado en contacto y viéndonos de vez en cuando sin que el paso del tiempo afectara nuestra amistad. También gracias al grupo thirsty monk, Iñigo T., Guiomar D., Juan I., Antonio F., Xavier G., Marine W. y Rubenes, con los que me lo he pasado muy bien y que han supuesto mi reavituallamiento de esta larga maratón. También un agradecimiento especial a Jesus J., mi mexicano favorito y que ha tenido siempre la virtud de saber aguantarnos a Andrea y a mí.

Y cuando hecho la vista atrás, no puedo olvidarme de mi gran amigo Pablo S. con el que he compartido de todo: profesores cizalladores de cerebros (martensita revenida), cursos infumables (mmm mathematica, docaer), cervezas, sentimientos (es guy love), películas (la pesca del salmon en yemen la mejor), piso (la maison de merabti), agua y gas (cortes en la maison de merabti), y, sobre todo, amistad. Tantas veces me has ayudado o iluminado que ya he perdido la cuenta... y lo mínimo era ponértelo por escrito aquí y ahora. Y ya que estoy en Madrid, quisiera agradecer la pequeña contribución de mis amigos de toda la vida, Alberto P., Ruben M., Alejandro P., Maria, Laura A. y Sara, que siempre que volvía a Madrid estaban deseando verme sin yo merecerlo mucho.

Y ya no tengo palabras ni vocabulario ni expresiones suficientes para agradecerle a Silvia P. lo que ha hecho por mí, no ya solo por esta tesis, sino en mi vida. Cuando nadie miraba, cuando todo estaba oscuro y no parecía haber ni un atisbo de luz, ella siempre estaba ahí, cálida, comprensiva y sonriente, para guiarme hacia la salida. Aun habiendo visto y vivido mi lado más oscuro, siempre ha decidido estar a mi lado ayudándome en mis proyectos. Por todo esto y mucho más, no puedo más que consolarme a solamente poder amarla hasta el último aliento esperando que algún día mi deuda se salde, algo que probablemente ocurrirá cuando los átomos que alguna vez formaron mi cuerpo se desintegren en el núcleo de una nueva estrella dentro de eones y eones.

Por último, quisiera agradecer a mi familia los esfuerzos que han hecho durante toda mi vida para ayudarme a estar hoy aquí. Mis padres, mi hermana, mis abuelos, mi tía y mi prima en la distancia siempre han estado apoyándome para que esto saliera adelante, haciendo de mi entorno un lugar estable para que pudiera crecer como profesional y como persona. Su sacrificio siempre ha sido y será un ejemplo para mí y para mi futuro.

Contents

Acronyms and Abbreviations	xix
Nomenclature	xxi
I Background	1
1 Introduction	3
1.1 Control of Flexible Space Structures: A Brief History	3
1.2 Thesis Context	8
1.3 Thesis Overview	9
2 Literature Review	11
2.1 Studies on the Modeling of Large Flexible Structures	12
2.2 Studies on Control of Large Flexible Structures	18
2.3 Studies on Integrated Control/Structure Design	21
3 Materials and Methods	25
3.1 Introduction to Mechanics	26
3.2 Introduction to Robust Control Theory	31

II	Study	35
4	Setting the Modeling Framework of Flexible Multi-Body Structures in Automatic Control	37
4.1	Selection of the Motion's Kinematic Description	39
4.2	The Double-Port Approach as an Overlapping Mechanism	41
4.3	Substructure's EOM Manipulation	48
5	Modeling of Flexible Multibody Structures for Integrated Control/Structure Design	57
5.1	One Connection Point	58
5.2	Two Connection Points	61
5.3	Extension to Revolute joint	64
5.4	Extension to Piezoelectric Actuators	66
5.5	Implementation of Parametric Variations	71
5.6	TITOP Modeling of Flexible Multibody Systems	74
6	Application and Validation of the TITOP Technique for the Modeling of Flexible Multibody Systems	77
6.1	Beam-like Substructures	78
6.2	Planar Rotatory Flexible Spacecraft	90
6.3	Two-Link Flexible Manipulator	98
7	Control Strategies Evaluation for Control of Flexible Multibody Structures	105
7.1	Control of Rigid Body Motion	106
7.2	Control of Flexible Modes	113
8	Implementation of Integrated Control/Structure Design in Structured \mathcal{H}_∞ Form	123
8.1	General Procedure and Scheme for Integrated Design	124

8.2	Implementation of Specifications and Constraints	126
8.3	Co-Design of a Rotatory Spacecraft	134
9	Integrated Control/Structure Design of a Flexible Satellite	143
9.1	System Description	144
9.2	System Modeling	146
9.3	System Specifications	148
9.4	Integrated Design Study	151
III	Conclusions	163
10	Discussion	165
10.1	Results in Flexible Multibody Systems Modeling	165
10.2	Results in Integrated Design	166
11	Conclusion	169
	Résumé de Thèse en Français	173
12	Résumé en Français de la Thèse	173
12.1	Introduction, état de l'art et méthodes	173
12.2	Cadre pour la Modélisation de Structures Flexibles Multi-Corps	174
12.3	Modélisation de Systèmes Multi-Corps Flexibles pour le Co-Design . .	177
12.4	Application et Validation de la Technique TITOP aux FMS	182
12.5	Evaluation des Stratégies de Contrôle pour les FMS	183
12.6	Mise en œuvre du Co-Design sous Forme \mathcal{H}_∞ structuré	185
12.7	Co-Design Contrôle/Structure d'un Satellite Flexible	188
12.8	Conclusion	191

APPENDIX	195
A Superelements	195
B Beam Finite Elements	199
C Thermal Induced Vibrations	203
D Code Matlab Functions	207
D.1 Conversion of Δ block	207
D.2 Derivation of the TITOP Model	208
E Other Figures	217
E.1 Complementary Figures from Chapter 6	217
E.2 Complementary Figures from Chapter 7	220
BIBLIOGRAPHY	221

List of Figures

1.1	First flexible spacecraft	4
1.2	OGO III	5
1.3	NuSTAR Illustration	6
1.4	NuSTAR Thermal Distortion	6
1.5	ASTRO-H Illustration	7
1.6	ASTRO-H debris	7
3.1	Direct dynamics block diagram	29
3.2	Standard form representation	32
3.3	Small-gain theorem diagram	33
3.4	Multi-channel synthesis	34
4.1	Substructure representation with two connection points	39
4.2	Representation of the floating frame approach	40
4.3	TITOP block diagram	42
4.4	Flexible pointing system illustration	43
4.5	Flexible pointing system decomposition	44
4.6	Block diagram of Appendage 1 DP model	46
4.7	DP assembly of the flexible pointing system	47
4.8	Displacement decomposition in CMS	49

5.1	Substructure representation with one connection point	59
5.2	Substructure block diagram with one connection point	60
5.3	Substructure representation with two connection points	61
5.4	TITOP block diagram	63
5.5	Substructure representation with revolute joint	65
5.6	Substructure block Diagram with revolute joint	66
5.7	Substructure representation with bonded piezoelectric material	68
5.8	Actuated TITOP block diagram	71
5.9	TITOP LFR Model	73
5.10	Illustration of a FMS	75
5.11	TITOP Modeling and assembly of a FMS	76
6.1	Chain of flexible beams	79
6.2	Concatenation of flexible beams	79
6.3	Z-Dynamics of chainlike flexible beams illustration	80
6.4	Bode response beam chain Z	80
6.5	Y-dynamics of chain-like flexible beams illustration	81
6.6	Bode response beam chain Y	81
6.7	Piezoelectric beam element	82
6.8	Beam with piezoelectric material frequency response, single voltage case . . .	84
6.9	Beam with piezoelectric material frequency response, multi voltage case . . .	85
6.10	Charge-Voltage transfer functions	85
6.11	Transfer function for small variations	86
6.12	Transfer function for large variations	87
6.13	Transfer function small variations chain of beams	88
6.14	Transfer function large variations chain of beams	89
6.15	Illustration of the Maneuverable Flexible Spacecraft	91

6.16 Rotatory spacecraft's TITOP modeling	92
6.17 Bode TITOP vs AMM for nominal case	95
6.18 Bode TITOP vs AMM for no tip mass case	96
6.19 Bode TITOP vs AMM for heavy tip mass case	97
6.20 Uncertain rotatory spacecraft representation	97
6.21 Error comparison TITOP/AMM	97
6.22 Bode plot of symmetric variations	98
6.23 Bode plot of asymmetric variations	99
6.24 Illustration of the planar two-link flexible arm	100
6.25 Assembly of a two-link flexible arm	101
6.26 Time response TITOP VS Nonlinear model of the two-link flexible arm . . .	102
7.1 Rigid synthesis of a PD controller	107
7.2 Root locus of the flexible pointing system	108
7.3 Nichols Diagram for the controlled system with real actuator dynamics (10 ms delay)	109
7.4 Robust synthesis of the PD controller	109
7.5 Nichols plots comparing robust synthesis with standard rigid approach	110
7.6 Nichols plots comparing standard rigid approach alone and with closed-loop active damping	111
7.7 Nichols Plot comparing decentralized optimization to centralized optimization	112
7.8 Acceleration feedback applied to the flexible pointing system and to a flexible beam	114
7.9 SOF applied to the flexible pointing system and to a flexible beam	115
7.10 Integral Force Feedback applied to the flexible pointing system and to a flexible beam	116
7.11 Other active damping strategies	118
7.12 Root locus of the flexible pointing system with heavier appendage($m_2 = 1.2$ kg)	119
7.13 Pole zero flipping of a flexible system	120

7.14 Recovering alternate pole zero of a flexible system	120
7.15 Root locus considering real actuator dynamics	121
8.1 Integrated design scheme	126
8.2 ASF Template	128
8.3 SOTAS synthesis scheme	129
8.4 SOTAS synthesis scheme with integral effect	129
8.5 SOTAS synthesis in a FMS TITOP assembly scheme	130
8.6 SOTAS synthesis scheme with flexible motion specifications	131
8.7 Slope comparison	133
8.8 Bode ID vs Control Optimization Alone	135
8.9 Dynamic specifications template and system response before optimization . .	137
8.10 Dynamic specifications template and system response after optimization . . .	139
8.11 Nichols Plot comparing the response of the ICSD and COA solutions	140
8.12 Time-domain Plot comparing the response of the ICSD and COA solutions .	140
9.1 Illustration of the Extra Long Mast Observatory (ELMO)	145
9.2 Sketch of ELMO	146
9.3 Mast prototype	147
9.4 TITOP modeling of ELMO	148
9.5 Template requirements and ELMO frequency response	151
9.6 ASF Template and the obtained controlled system transfers	153
9.7 Nichols Comparison with/without active damping strategies	154
9.8 Nichols Comparison among active damping strategies	155
9.9 Nichols plot comparison with/without rolloff	156
9.10 Responses to disturbance impulse at the hub with VM and perfect dynamics	156
9.11 Responses to disturbance impulse at the tip with VM and perfect dynamics .	157

9.12	Instability of the PD alone strategy in the VM	157
9.13	Hub position and thermal torque disturbance	158
9.14	Nichols comparison for different actuator placement	159
9.15	Performance comparison of different actuator placement	160
9.16	System mode shapes for different configurations	160
9.17	Optimized PEA configuration VS nominal PEA configuration	161
A.1	Superelement Representation	196
C.1	Thermal disturbance	204
E.1	Transfer Functions at point P for small variations on the beam's length . . .	217
E.2	Transfer Functions at point P for large variations on the beam's length . . .	218
E.3	Transfer Functions at point C for small variations on the beam's length inside the chain of beams	218
E.4	Transfer Functions at point C for large variations on the beam's length inside the chain of beams	219
E.5	SOF controller applied to the flexible pointing system with heavy flexible ap- pendage ($m_2 = 1.2$ kg)	220
E.6	SOF controller with complex zero applied to the flexible pointing system with heavy flexible appendage ($m_2 = 1.2$ kg)	220

List of Tables

6.1	Table of beam and piezoelectric parameters	82
6.2	Error analysis single beam parameterization for 100 samples	87
6.3	Spacecraft configuration parameters	91
6.4	Frequency comparison rotatory spacecraft	95
6.5	Arm configuration parameters	100
6.6	Frequency comparison TITOP vs Nonlinear for the two-Link flexible arm . . .	101
8.1	Rotatory spacecraft ICSD results	138
9.1	ELMO configuration parameters	146
9.2	Summary of the results of the ICSD of ELMO	152
9.3	Fail/success summary of PEAs location $x_1 = 2m$	159
9.4	Fail/success summary of PEAs location $x_1 = 3m$	159

Acronyms and Abbreviations

ACS	<i>Attitude Control System</i>
AF	<i>Acceleration Feedback</i>
AMM	<i>Assumed Modes Method</i>
AOCS	<i>Attitude and Orbit Control System</i>
ASF	<i>Acceleration Sensitivity Function</i>
CMS	<i>Component Modes Synthesis</i>
COA	<i>Control Optimization Alone</i>
CSI	<i>Control-Structure Interaction</i>
DP	<i>Double-Port</i>
DOF	<i>Degrees Of Freedom</i>
ELMO	<i>Extra Long Mast Observatory</i>
EOM	<i>Equation of Motion</i>
FE	<i>Finite Element</i>
FEM	<i>Finite Element Model</i>
FM	<i>Flexible Mode</i>
FMD	<i>Flexible Multibody Dynamics</i>
FMS	<i>Flexible Multibody System</i>
FE-TM	<i>Finite Element Transfer Matrix</i>
GM	<i>Gain Margin</i>
ICSD	<i>Integrated Control/Structure Design</i>

IFF	<i>Integral Force Feedback</i>
LFT	<i>Linear Fractional Transformation</i>
LFR	<i>Linear Fractional Representation</i>
LMI	<i>Linear Matrix Inequality</i>
LQR	<i>Linear Quadratic Regulator</i>
LTl	<i>Linear Time Invariant</i>
PCO	<i>Plant-Controller Optimization</i>
PD	<i>Proportional-Derivative</i>
PEA	<i>Piezo-Electric Actuator</i>
PID	<i>Proportional-Integral-Derivative</i>
PPF	<i>Positive Position Feedback</i>
PM	<i>Phase Margin</i>
RM	<i>Rigid Mode</i>
RW	<i>Reaction Wheel</i>
SOF	<i>Second Order Filter</i>
SOTAS	<i>Second Order Template on Acceleration Sensitivity</i>
TITOP	<i>Two-Input Two-Output Port</i>
TMM	<i>Transfer Matrix Method</i>
VM	<i>Validation Model</i>

Nomenclature

Generalized displacements in equations and figures are expressed as follows:

$\{q\}$ column matrix of generalized displacements.

$\{\dot{q}\}$ column matrix of generalized velocities.

$\{\ddot{q}\}$ column matrix of generalized accelerations.

The vector $\{q\}$ of generalized displacements is often decomposed as follows (identically for generalized velocities and generalized accelerations):

$\{x\}$ generalized translations.

$\{\theta\}$ generalized rotations.

Generalized coordinates can be projected in the following directions or frames:

\vec{x} unit vector along x axis.

\vec{y} unit vector along y axis.

\vec{z} unit vector along z axis.

Subscript $_a$ Reference frame or vector associated to body a .

Subscript $_{R_i}$ inertial reference frame or reference frame associated to i -th body when specified.

Subscript $_{R_G}$ reference frame at point G .

The equations of motion and figures may include the following elements:

$[K]$ square matrix of system generalized stiffness.

$[D]$ square matrix of system generalized damping coefficients.

$[M]$ square matrix of system generalized masses.

$\{F\}$ column matrix of generalized loads.

$[\bar{\phi}^R]$ matrix of rigid-body modes.

$[\bar{\phi}^C]$ matrix of constraint modes.

$[\bar{\phi}^N]$ matrix of natural modes.

$\{F_c\}$ vector of externally applied forces at the constraint degrees of freedom.

$\{\tilde{F}_e\}$ vector of loads acting on a substructure as a result of its connection to adjacent substructure at the constraint degrees of freedom.

$\{F_r\}$ vector of externally applied forces at the rigid-body degrees of freedom.

$\{\tilde{F}_r\}$ vector of loads acting on a substructure rigid body degrees of freedom as a result of its connection to adjacent substructure.

where the vectors of loads are usually decomposed in the following sub-vectors:

$\{F_P\}$ Applied point force at point P .

$\{T_P\}$ Applied torque at point P .

$\{\eta\}$ column matrix of normalized displacements.

N_r or subscript r dimension of rigid body modes.

N_e or subscript e dimension of redundant constraint modes.

N_n or subscript n dimension of fixed-constraint modes.

N dimension of total degrees of freedom.

$[\tau_{PG}]$ kinematic model between points P and G .

$[D_G^A]$ Inverse dynamics rigid-body model of a structure \mathcal{A} at point G .

$(*PG)$ Skew-symmetric matrix associated to the vector $\{PG\}$.

The TITOP model uses the following notations:

$\{F_{\mathcal{A}/\mathcal{P},P}\}$ vector of loads exerted by a substructure \mathcal{A} to a substructure \mathcal{P} at point P .

$\{f_{\mathcal{A}/\mathcal{P},P}\}$ force exerted by a substructure \mathcal{A} to a substructure \mathcal{P} at point P .

$\{t_{\mathcal{A}/\mathcal{P},P}\}$ torque exerted by a substructure \mathcal{A} to a substructure \mathcal{P} at point P .

$[G_P^A(s)]$ one-connection-point TITOP model of substructure \mathcal{A} at point P .

$[G_{P,C}^A(s)]$ two-connection-point TITOP model of substructure \mathcal{A} at points P and C .

$[J_P^A]$ rigid body matrix or direct dynamic model of substructure \mathcal{A} at point P .

$[L_P]$ modal participation matrix of natural modes at point P .

$[H_{P,C}^A(s)]$ two-connection-point TITOP model of substructure \mathcal{A} at points P and C with a revolute joint at point P .

Other mathematical notations are:

I_n Identity matrix of size $n \times n$.

0_n Zeros matrix of size $n \times n$.

Part I

Background

Chapter 1

Introduction

“Start by doing what’s necessary; then do what’s possible; and suddenly you are doing the impossible.”
- Francis of Assisi

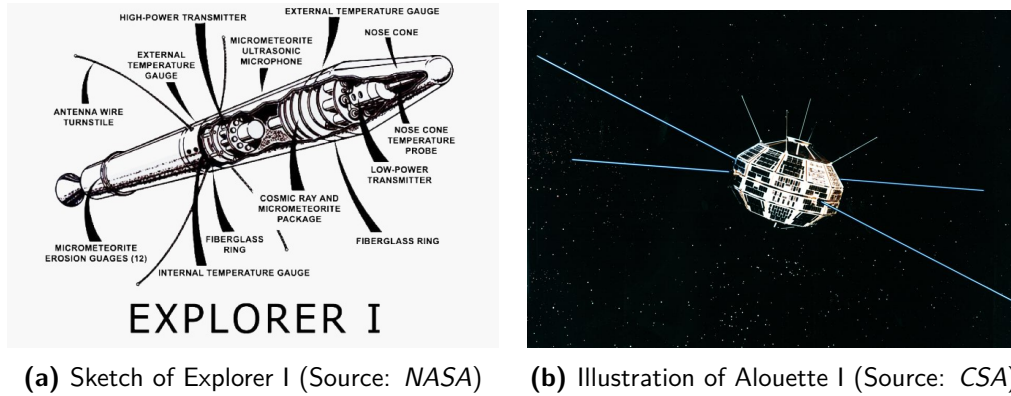
THE objective of this PhD thesis is to perform integrated attitude control/structure design of a large flexible satellite using structured \mathcal{H}_∞ synthesis, by modeling flexible multibody structures and developing a control strategy for the controller’s synthesis of flexible multibody systems. This chapter introduces in Sec. 1.1 the problematic of the control of flexible structures to the reader, and explains in Sec. 1.2 in which way this problem has been addressed in the field of attitude control. Finally, Sec. 1.3 states the main guidelines of the thesis.

1.1 Control of Flexible Space Structures: A Brief History

Since the beginning of the space era, spacecraft have been sent into space to satisfy a wide variety of technological challenges, scientific researches, commercial requirements and defense necessities. Historically, spacecraft attitude control has been considered as the primary objective to be achieved by the spacecraft control system. Spacecraft dynamics are controlled to strict requirements which depend on the pointing budget, spacecraft function mode, orbit environment and onboard sensors and actuators.

During the last decades, space science has been looking for new ways of discovering and analyzing celestial objects in the Universe to understand some aspects of Einstein’s theory of relativity, such as gravitational waves or the origin of the Big Bang. Analysis of the Universe’s most violent events is needed in order to improve our current understanding of physics. The most violent events in the Universe are related to black holes, black holes collisions, supernovas remnants or galaxy clusters, among others. The study of these high-energy celestial objects requires X -ray and Γ -ray instruments which can only work outside Earth’s atmosphere. These instruments require long focal lengths to improve image quality, which can vary from 4 m to more than 20 m long.

There are two ways of fulfilling the requirement of long focal lengths: satellite formation flying and distributed instrumentation. In satellite formation flying the focal distance is equal to the distance between the two satellites, each one containing different parts of the instrumentation, but this require a high-precision attitude control, which considerably increases the spacecraft’s costs. The distributed



(a) Sketch of Explorer I (Source: NASA) (b) Illustration of Alouette I (Source: CSA)

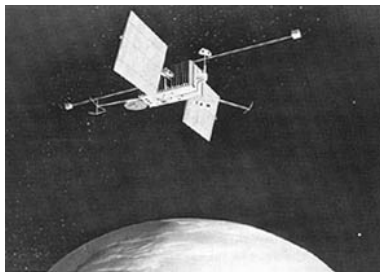
Figure 1.1: First experiences with flexible interaction in space

instrumentation approach uses different deployable parts of the spacecraft to increase the focal length of the instruments, such as extensible benches or deployable booms. This solution is less expensive and more robust since only one satellite is needed and attitude control performances are not prohibitive. In addition, the relatively gentle environment of space, with no air-friction and no self-weight loads, allows the design and construction of spacecraft with complex geometries and large dimensions. As a result, distributed instrumentation is often the final solution.

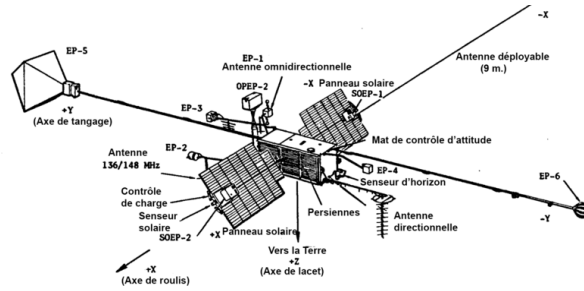
Added to the requirement of long extendable parts, satellites need more and more power supply for the correct functioning of the onboard systems. This is translated into an augmentation of the solar panel's surface, making the satellite larger. Moreover, antennas are becoming larger as well since larger size increase its sensibility for detecting radio waves. As a result, spacecraft structure is discretized in "modules" or substructures which allow a simplification of system's modeling, analysis, production, assembly and integration. Nowadays, a spacecraft is a Flexible Multibody System (FMS) composed of a platform or rigid hub, to which several substructures are attached such as antennas, deployable booms, solar arrays or extendable masts. The mass increase, however, is minimized since satellites' weight is limited to a few tones due to launching rocket maximum take-off weight. Hence, there is a structural tendency of enlarging spacecraft's dimensions and lightening its structure, which makes the spacecraft large and flexible.

Elastic behavior of spacecraft structure is a well known problem since the beginnings of the space race. Flexible interaction with the control of spacecraft dynamics can occur in numerous and subtle ways, worsening the spacecraft dynamics or structure's flexible deformations. The control system designer must be aware of it and consider flexibility in his synthesis models. Although engineers have always been aware of these interactions, some of them may go undetected and may even provoke spacecraft's loss. The first records about flexible interactions go back to the Explorer I and Alouette I, the first artificial satellites of USA and Canada, respectively.

Explorer I (1958) was an Earth-orbiting spacecraft with a long cylindrical body with four flexible antennas extending laterally (see Fig. 1.1a). The vehicle was to be passively spin stabilized about its principal axis of minimum moment of inertia. However, after one orbit it started experiencing precessional motion and after a week the vehicle was stabilized rotating about its axis of maximum moment inertia, which was not suspected before the flight. Rotation about either the maximum or minimum moment of inertia is stable for a rigid body, so engineers started searching which mechanism provoked that change in the rotation axis. The answer was that Explorer I was not rigid because of the whip antennas. The antennas have an associated bending motion coupled with the precessional motion, provoking an energy dissipation process until the minimum-energy state (rotation about the



(a) Artist concept of OGO-III
(Source: NASA)



(b) Sketch of OGO-III (Source: NASA)

Figure 1.2: OGO-III was the first active controlled satellite experiencing boom-bending difficulties

maximum moment of inertia) was achieved [Tutt 69]. Since then, the destabilizing effects of structural energy dissipation in spin-stabilized spacecraft are counterbalanced by an active nutation damper system.

Flexibility can also interact with the environment, as experienced by Alouette I (1962). This vehicle had a compact central body and four antennas, two of them 22.9 meters long and the other two 11.4 meters long (see Fig. 1.1b). The antennas were extendable booms which were deployed after launch. The spacecraft was spin stabilized about its axis of maximum moment of inertia, but since its launch a rate of spin decay was detected. After three years the satellite stopped spinning. Research revealed that the spin brake mechanism was caused by the interaction of the flexible boom with solar and radiation pressure. The solar radiation provoked the asymmetrical bending of the booms by thermal distortion which, with the interaction of the solar pressure, induced a net torque to the body [Tutt 69]. The torque might either help or oppose the spin depending on the vehicle's geometry, but in the case of Alouette I the spin rate was opposed. The following missions solved this problem by adding small metallic reflectors at the ends of the booms, which provided a compensating torque.

When three-axis active attitude control started being implemented, control engineers continued encountering flexible interaction problems. Due to the large dimension and low mass density of some satellites, flexible modes are in the low-frequency band and they may interfere with the attitude control system's bandwidth. Therefore, the control system has to be modified due to nonnegligible structural flexibility, otherwise the action of the spacecraft control system may worsen the structural deformations as well as the spacecraft dynamics. Despite engineers' awareness, some satellites have experienced control-system/structure interaction which caused the failure of their mission.

The first Control-Structure Interaction (CSI) problem was experienced by the OGO-III (Orbiting Geophysical Observatory, 1966) satellite. This vehicle, depicted in Fig. 1.2, had two 6.10-meter boom parallel to the pitch axis and one 9.14-meter boom parallel to the roll axis. In addition, two solar arrays were mounted along the roll axis. It had an active feedback system to control roll attitude, using reaction wheels and gas jets to unload momentum saturation. Ground control noticed that when the satellite approached perigee, roll-axis oscillations of 0.42 Hz were detected, increased in amplitude until the reaction wheels, gas jets and solar-array drive were all excited. However, reaction-wheel and solar-array oscillations were sustained until the vehicle approached apogee of its orbit. Control-system/boom-flexibility was suspected as the cause of the oscillations. Analysis showed that there was a discrepancy in the amount of structural damping assumed in the preflight closed-loop stability analysis. Sustained oscillation of 0.42 Hz could be possible if boom damping ratios of 0.3 % were used, and not the preflight values of 1 % and 2 % [Tutt 69]. The next missions used a different delay logic

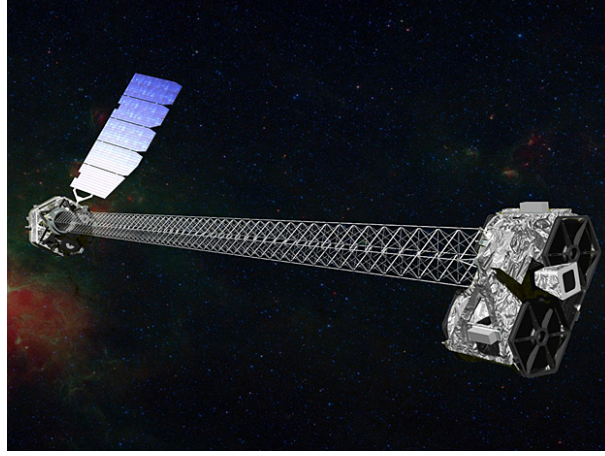


Figure 1.3: Artist concept of the NuSTAR mission

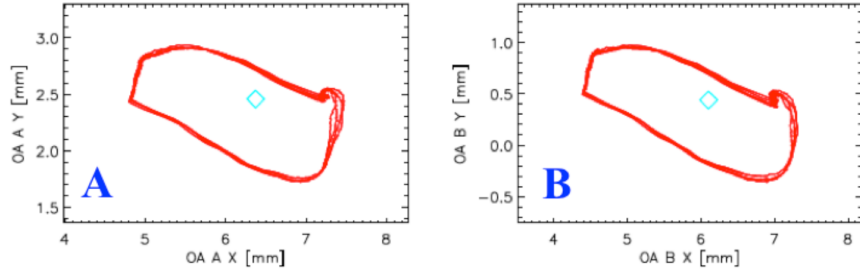


Figure 1.4: Thermal distortion of NuSTAR's optical axis (Source: *NuSTAR Observatory Guide*)

for the reaction wheel control and improved the dynamic model for synthesis.

Yet, many lessons can be drawn from these examples and these lessons retain their value today. Understanding of CSI problems has helped to significantly improve satellite's reliability and life limit. Indeed, there are very few records about CSI problems during the 80s and the 90s, even if modern spacecraft is more complex. An example of the improved know-how is the NuSTAR mission (Nuclear Spectroscopic Telescope Array, 2012), the first focusing high energy X -ray space observatory. NuSTAR employs grazing incidence optics to be able to focus X -rays. For this, a 10.15-meter focal length Wolter telescope is held at the end of a long deployable mast. A laser metrology system is used to determine the exact relative positions of the optics and the focal plane at all times. The spacecraft attitude control system is designed to actively control the attitude to within 1 arcsec during an observation, performing adjustments to keep the spacecraft z axis oriented towards the science target. For that, the control system has been conceived to reject disturbances in a maximized bandwidth subject to maintain gain and phase stability margins in the range of 6-8 dB and 30-45 degrees [Ruth 10]. The mission is achieving all its scientific objectives, even though the induced vibrations due to the thermal flexing of the mast (see Fig. 1.4).

Despite the recent technological advances in control/structure design, even nowadays the attitude control system can fail and provoke spacecraft loss. This is the case of the Hitomi satellite (ASTRO-H, 2016). ASTRO-H (Fig. 1.5) was conceived to reveal the structure and evolution of the universe by observing high-energy objects that are visible in the X -ray and Γ -ray bands. It consisted of an

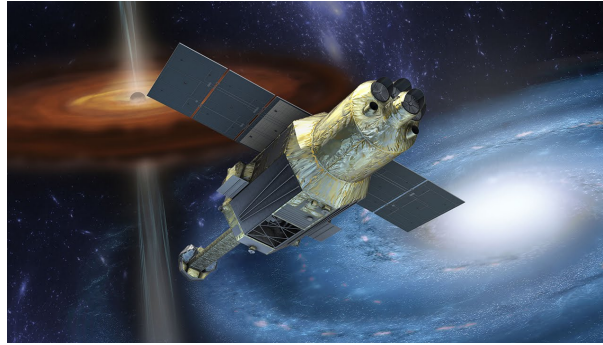


Figure 1.5: Artist concept of the Hitomi (ASTRO-H) satellite (Source: JAXA)

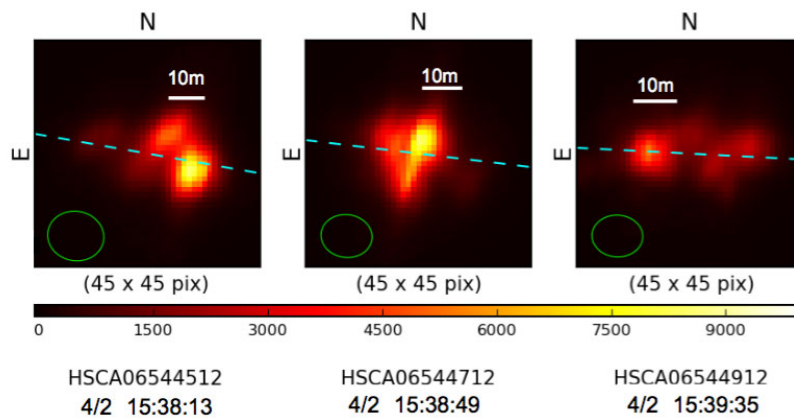


Figure 1.6: ASTRO-H debris spinning at 5.2 revolutions per second as seen by the Subaru Telescope (Source: *National Astronomical Observatory of Japan*)

octagonal platform containing all the basic sensors and actuators (star trackers, reaction wheels, etc), two solar array pads attached and an extensible optical bench up to 12 meters long. One month after launch, on March 26th 2016, the unexpected behavior of the attitude control system caused incorrect determination of its attitude as rotating, although the satellite was not rotating actually. In the result, the reaction wheel was activated and lead to the rotation of satellite. In addition, the magnetic torque believed to avoid the reaction wheel's saturation did not work properly. Judging the situation as critical, the safe hold mode switched on automatically, using the thrusters to stop the rotation. However, the attitude control system provided an atypical command and the spacecraft's rotation was indeed accelerated. Once the satellite's speed exceeded the design values, the most vulnerable parts of the spacecraft (solar arrays, the deployable mast) separated off from the satellite, as it was observed by the Subaru Telescope (see Fig. 1.6). The causes of the attitude control system anomaly are still being inquired, but the lost of all communication with the satellite have made this task almost impossible.

The history of flexible satellite control has demonstrated to be plenty of challenges and technological advances. The larger and lighter modular spacecrafts often imply a rigorous study of the CSI problem in order to minimize the probability of failure. Although a significant improvement has been made since the launch of the first flexible satellites, robust and reliable attitude control systems are needed in order to accomplish successfully future scientific missions. Approaches which simultaneously take into account the structural behavior and the control system actions are an added value when dealing with the CSI problem.

1.2 Thesis Context

In the field of attitude control of large flexible satellites, the main objective is to guarantee system stability against low-frequency perturbations and induced vibrations. Nevertheless, new generation satellites must accommodate high-precision scientific experiments and reduce launching costs, what is making the design of their structure larger and lighter. More precisely, new generation space science experiments need X-ray interferometer benches and long-range telescopes with long focal lengths, both needing long masts clamped to the spacecraft platform. Furthermore, large flexible satellites are now discretized or modularized in several substructures in order to recycle its design for other satellite platforms. The large size and lightness imply low-frequency flexible modes that may interfere with the controller's bandwidth, destabilize the system and eventually provoke its loss, in what is called the Control Structure Interaction (CSI) problem. On the other hand, system modularity implies a lack of knowledge to predict the dynamic behavior of the entire assembled system and, consequently, impedes working directly in pre-design phases of the control/structure system.

In the space sector, this problem is solved with a loop of crossed-information between the control and the structure departments, who have to establish the minimal specifications for each system in order to achieve a successful integration. These specifications include determining a minimum value for frequency of the first flexible mode, fixing a maximal mass for the whole system, a maximal size for several substructures, etc. For these specifications, performance barriers are imposed for each system, ensuring a successful final integration. Nevertheless, these barriers do not allow exploiting the maximum optimal capacities of the two systems working together.

That is the reason why new conception methods, which tie together spacecraft structural dynamics and attitude control laws design, were born. Messac and Malek [Messac 92] designed the structure and the control system of a rotatory flexible spacecraft, addressing system's disturbance rejection and system's command following performance, while optimizing the profile of the flexible appendage for minimum mass. The model used was a FE-model of a simplified flexible spacecraft, controlled by a hub-torque commanded with a full-order controller. Both the structure and the controller were optimized with an algorithm developed by the authors. Messac and Malek thereby demonstrated that control/structure optimization gives better results than control optimization alone in terms of mass costs and control performances. However interesting, their approach had limitations when dealing with real design scenarios and robustness. The authors modeled the whole system without taking account the advantages of modularity, and the controller optimization did not use robust synthesis techniques.

Alazard *et al.* [Alazard 13b] performed integrated attitude control/structure design of an Earth Observation satellite using a genetic algorithm for the system's optimization. The modeling technique allowed modular system assembly by interconnecting the different parts of the system such as the hub and flexible appendages. The models were FE-based, in LFR representation for the optimization of structural parameters. The attitude control system consisted of a low-order controller for each stabilization axis and a roll-off filter. This study supposed the first step to a generic approach to integrated control/structure design since it provided tools for flexible multibody system modeling and an approach for attitude control. However, the proposed modeling technique did not allow the interconnection of different substructures among them. In addition, the optimization process was iterative and several software were involved: NASTRAN for re-computing the FE-models, the genetic algorithm and the μ synthesis. This made the co-design study complex and time-consuming.

Taking advantage of the structured \mathcal{H}_∞ form, Alazard [Alazard 13a] used a multi-model \mathcal{H}_∞ synthesis scheme to design a fixed-structure controller of an earth-observation satellite. Simultaneously, avionic parameters (sensors and actuators delay) were optimized in order to select the ideal actuator

for challenging requirements or standard requirements. This supposed the first study in integrated control/avionics design using structured \mathcal{H}_∞ tools. The study demonstrated that the same level of performance could be achieved with less expensive actuators and sensors when optimizing the control/avionic system simultaneously. Nevertheless, the modeling technique was the same as in [Alazard 13b] and thus the interconnection among flexible substructures was not possible.

Thanks to the aforementioned studies, integrated attitude control/structure design is feasible and useful. Feasibility is the result of the studies using the most modern algorithms for structure/control optimization, such as genetic algorithms or non-smooth \mathcal{H}_∞ optimization. Usefulness since these studies demonstrate that there is always additional benefits when considering the control system and the structure simultaneously for control law and structural design. However, no study provided a modeling technique which takes into account the modularity of flexible multibody systems. In addition, no study has performed integrated control/structure design of flexible multibody systems using structured \mathcal{H}_∞ tools.

1.3 Thesis Overview

The objective of this research is to perform integrated attitude control/structure design of a large flexible satellite using structured \mathcal{H}_∞ synthesis, by modeling flexible multibody structures and developing a control strategy for the controller's synthesis of flexible multibody systems. This study involves a multidisciplinary research in which the modeling of mechanical systems, control law synthesis and control law validation must be integrated. Furthermore, the approach must be able to isolate and manage the parameters to be optimized, either mechanical parameters or control law parameters. Therefore, the thesis approach starts dealing with the modeling techniques of large flexible structures, the modeling of actuators and sensors for control of flexible structures and the implementation of parametric variation in those models. The thesis continues with the evaluation of the different control strategies which can be used using the models provided in this study, to conclude with the implementation of the integrated/control design scheme in structured \mathcal{H}_∞ form and the application of this scheme to a flexible satellite.

Chapters 1, 2 and 3 recall the background of this study. Chapter 2 explains and situates the different studies carried on modeling, control and integrated design of flexible structures. Chapter 3 recalls briefly some concepts of general mechanics, structural mechanics and control theory which are used in this study.

Chapter 4 is entirely devoted to setting the framework for the modeling of FMS. The objective is to propose a general theoretical framework for the modeling of FMS using finite element (FE) data and use it for integrated control/structure design. The foundations of the framework are developed according to the needed kinematic description, the needed overlapping mechanism and the required form of equation of motion. This chapter has motivated the publication of [Alazard 15].

Chapter 5 uses the framework stated in Chap. 4 to develop the theory for the modeling of FMS for use in automatic control. The chapter provides straightforward mechanical models for modeling starlike or chainlike flexible structures, piezoelectric substructures and revolute joints. Parameterization possibilities are also evaluated. A part of the results of this chapter have been published in the *ASME Journal of Dynamic Systems, Measurement and Control* [Perez 16b] and in several international conferences: EURO GNC 2015 [Perez 15a], IFAC ACNAAV 2015 [Perez 15b] and IFAC ACA 2016 [Perez 16a].

Chapter 6 provides a set of applications of the developed modeling technique for FMS stated in Chap. 5. The modeling method is explained and validated in representative examples of FMS modeling. A comparison of the proposed modeling technique with the *Assumed Modes Method* (AMM) is provided and its advantages are highlighted. These examples can also be found in the produced publications [Perez 16b], [Perez 15a], [Perez 15b] and [Perez 16a].

Chapter 7 evaluates the different control strategies that can be applied for the attitude control/vibration suppression of flexible multibody structures. Collocated/non-collocated damping and centralized/decentralized synthesis schemes are compared and discussed. The control strategies are explained through an academic example and applied for the developed models of Chaps. 5 and 6 in order to chose the most adequate control architecture for the integrated control/structure design.

Chapter 8 is devoted to explain how to implement the integrated control/structure design problem in structured \mathcal{H}_∞ form. The general framework is explained and guidelines for imposing the rigid-body motion and the flexible motion specifications are given. Other utilities, as minimization of command energy and roll-off specification, are illustrated. The implementation is illustrated with the co-design of an academic model of a flexible spacecraft.

Chapter 9 uses the knowledge developed in the precedent chapters to perform the integrated attitude control/structure design of a flexible satellite. The flexible satellite is modeled with the proposed flexible multibody system technique, performing integrated design according to mission specifications. Part of the results have been published in the international conference IFAC ACA 2016 [Perez 16c].

The last part, consisting of Chaps. 10 and 11, is dedicated to discuss and resume the main contributions of the PhD, and to provide the guidelines that may help other future studies in the domain. The manuscript is supplemented by a set of appendixes which provide further notions in finite elements, more figures and the Matlab code of the most used functions during the study.

Chapter 2

Literature Review

“Be sure you put your feet in the right place, then stand firm.”
- Abraham Lincoln

Contents

2.1	Studies on the Modeling of Large Flexible Structures	12
2.1.1	General Framework	12
2.1.2	FMD using floating rotating frame	13
2.1.3	FMD using corotational rotating frame and inertial frame	16
2.1.4	Actuator/Sensor Models for Flexible Structures Control	17
2.2	Studies on Control of Large Flexible Structures	18
2.2.1	Attitude Control of Large Flexible Structures	19
2.2.2	Vibrations Suppression of Large Flexible Structures	19
2.3	Studies on Integrated Control/Structure Design	21

Integrated Control/Structure Design is a vast domain which comprehends two major engineering fields: modeling and control of flexible structures. This chapter aims to explain the different modeling approaches which can be used and the main applications in control of flexible structures. The chapter reviews and merges these two different domains with the discussion of what has been accomplished so far in the integrated design domain.

IN this chapter, the state-of-the-art of the problematic associated with integrated control/structure design is summarized. Integrated control/structure design comprehends two clearly distinguished areas: modeling and control. First, the existing modeling techniques that deal with large flexible structures are explained. In addition, the modeling of the actuators and sensors used to control these kind of systems is addressed. Second, studies on control of large flexible structures are presented, focusing on attitude control and vibration suppression applications. Finally, a review of the integrated structure/control design is explained.

2.1 Studies on the Modeling of Large Flexible Structures

Modeling of large flexible structures has been a major concern in control applications for the last thirty years due to the development of larger and lighter structures [Wasfy 03]. Large size and reduced mass imply lower natural frequencies which are typically closely spaced [Schoen 09]. Low natural frequencies may interfere with controller's bandwidth, affecting the whole dynamical behavior of the system. Simple and accurate models for large flexible structures which predict these characteristics are indispensable for designing, optimizing and controlling engineering systems. In Sec. 2.1.1, the method for dealing with the modeling of large flexible structures and a widely used classification of modeling techniques are established. Next, Secs. 2.1.2 and 2.1.3 present the most representative studies of the different modeling types. In Sec. 2.1.4, a short review of the different existing models of actuator and sensors for flexible structure control is presented.

2.1.1 General Framework

The study of large flexible structures implies dealing with large dynamics models. This is mainly attributed to the high amount of degrees of freedom (DOF) which have to be considered for an accurate modeling of the structure, making their analysis complex and time-consuming. In order to reduce the complexity and facilitate structural understanding, the so-called *substructuring techniques* are used, consisting of the *macrodiscretization* of the large system into a set of subsystems known as substructures, appendages or modules, which in turn are separately modeled. This strategy considers then the large flexible structures as a *Flexible Multibody System* (FMS) or *Flexible Multibody Structure* (FMS); i.e., a group of interconnected rigid and deformable components, each of which undergoing translational and rotational motions [Wasfy 03].

In order to analyze the dynamic response of FMS due to external conditions, it is necessary to compute the *Flexible Multibody Dynamics* (FMD). FMD has a significant importance for the design, optimization and control of many practical systems such as space vehicles [Masoudi 11, Guy 14] or robot manipulators [Chatlat. 09, Boscariol 10]. In design, FMD can be used to calculate the system parameters such as dimensions, configuration, and materials that minimize the system cost while satisfying the design safety constraints such as strength,

rigidity, and static/dynamic stability. FMD is used in control applications for predicting the response of the multibody system to a given control action and for calculating the changes in control actions necessary to direct the system towards the desired response.

However, obtaining the FMD of a FMS is not a simple task. It is the result of a long and tedious process. First, it is mandatory to choose the kinematic description of the motion of the different elastic bodies experiencing small or large displacements. This kinematic description can be done in three different ways according to the chosen reference frame: using either a *floating frame*, a *corotational frame* or an *inertial frame*. Second, the semi-discrete equations governing the elastic and rigid motion of each substructure are derived, depending on the particular nature of each component: beam models are used for 1D components, plate and shell models for 2D members and continuum models for 3D components. The equations can be obtained either analytically, semi-analytically or using any kind of discretization method, like the *finite element* (FE) discretization. Third, the constraints between the different substructures are established as constraint equations. These constraints can be in the form of prescribed motion (one or several DOF are forced to follow a given motion), joints (several DOF are related) or contact/impact (one or several DOF are constrained to a value within a given interval). To conclude, implicit or explicit solution assembly procedures are used to solve the semi-discrete equations of motion along with the constraint equations, obtaining the desired FMD.

As it has been shown, getting the FMD is the result of the multiple possible choices to derive the model. In this review the publications on FMD are mainly divided according to the kinematic description of the motion (floating frame, corotational frame or inertial frame) since they are directly related to the different type of applications. Other categories can be done according to the different steps along the FMD computation, but they are not revised here. The reader might head to [Shabana 97] or [Wasfy 03] if a more detailed review of modeling of multibody systems is desired.

2.1.2 FMD using floating rotating frame

The floating frame is currently the most widely used method in the simulation of FMD. Developed in the early 1970s, the floating frame is an intermediate reference frame which is attached to a flexible component and follows the average local rigid body motion. The total displacement is evaluated by superimposing small elastic deformations on the large rigid body motion. This simplifies the calculation of the internal forces, leading to rapid computation of the FMD. It is the most efficient method for the simulation of FMS undergoing small elastic deformations and slow rotational speeds such as satellites and space structures, a domain in which it has been systematically applied. In [Kane 80], Kane and Levinson made use of the floating frame to derive the FMD of a complex spacecraft with seven different kinematic formulations (momentum principle, Lagrange's equations, D'Alembert Principle or Hamilton Canonical Equations, among others) and then in [Kane 81] they added the elastic displacements considering constrained and unconstrained beam elements in order to analyze and simulate large displacements. In [Likins 69], Likins also made use of the floating frame

to derive the kinematic description of flexible space vehicles. Since then, Kane's and Likin's formulations have been applied in many studies. For example, in [Masoudi 11] Masoudi and Mahzoon applied the Kane's approach in order to derive a model of a free-floating space robot with four linkages and to perform maneuvering and vibration control.

The main advantage of the floating frame approach resides on its usage to extend modal analysis and experimental modal identification techniques to FMS. This is performed by identifying the mode shapes and frequencies of each flexible component. Then, the first n modes (where n is determined by the required accuracy and the nature of the problem) are superposed on the rigid body motion of the component represented by the motion of the floating frame. This is what is called the *Assumed Modes Method* (AMM). In [Likins 67], Likins was one of the first authors which used the modal analysis within a floating reference frame in order to derive the equations of motion of a free rotating spacecraft. In [Hughes 74], Hugues superimposed the natural modes and constrained modes of the different flexible appendages to the rigid motion of a space vehicle in order to study the implications of the flexibility on the attitude dynamics, and obtained the so-called *impedance matrix* of the spacecraft, a tool to analyze the influence of spacecraft flexibility. In [Pascal 88], Pascal extended the work of [Hughes 74] by performing the dynamic analysis of a system of hinge-connected flexible bodies, obtaining the reduced dynamic impedance matrix of a generic tree-structure. In [Turner 80], Turner and Junkins also used the AMM in addition to a kinematic description obtained with the Hamilton's Principle in order to compute the optimal single-axis reorientations of a flexible vehicle.

Furthermore, the effect of inertial forces, as the centrifugal stiffness, can be taken into account in this approach in a non-linear way, because accelerations are measured with respect to a rotating frame (the floating frame attached to the appendage). In [Likins 73] this is performed for a spinning flexible spacecraft, and showed the influence of centrifugal stiffness on the flexible appendage modes shapes and natural frequencies. Besides flexible space vehicles modeling, other uses of the floating frame approach include modeling of flexible robot manipulators [Chatlat. 09, Boscariol 10, Usono 86] and rotorcraft modeling [Zhu 97, Choura 91].

However, in the majority of FMD literature on floating frame approach, the flexible components are discretized using the FE method. FE-based models are the most powerful tool for structural analysis [Usono 86, Rong 11, Bokhari 08]. This has lead to develop direct substructuring techniques based on the FE method, taking for granted the use of a floating frame to superpose rigid and elastic displacement, and with constraint equations established through boundary conditions to the FE models. Among these techniques, two methods have drawn researchers' attention for decades: the *Finite Element Transfer Matrix* (FE-TM) method and the *Component Modes Synthesis* (CMS) Method. It should be noticed that in the literature, these techniques are not directly mentioned as floating-frame-based techniques, they are conceived as independent techniques for substructuring large FE models.

2.1.2.1 Component Modal Synthesis Techniques

The CMS method has received significant attention in the aerospace industry since its idea of matrix condensation lends itself particularly well to the concept of substructuring. It is an extension of modal analysis that is particularly applicable to large flexible systems [Ersal 08]. First, it uses modal analysis to obtain a proper model of each subsystem. Then it assembles these subsystem models conforming the whole structure, taking into account the different frames for the different substructures. Among the available dynamic substructuring methods, CMS stands the most systematic and efficient procedure for developing a satisfactory decomposed model [Dhingra 94, Craig Jr 00, Ersal 08].

CMS techniques are divided in three main categories, depending on the selection of component modes for the substructure's assembly. There is a wide choice of component modes [Craig Jr 00]: normal modes (which can be fixed-interface normal modes, free-interface normal modes and loaded-interface normal modes) constraint modes, rigid-body modes, attachment modes, residual flexibility modes and residual flexibility attachment modes. The reader might head to [Craig Jr 00] if more information about component modes is required. The three main categories are:

- Methods based on constraint and fixed-interface normal modes. These approaches use a combination of *constraint modes* (which include rigid-body modes) and *fixed-interface normal modes* for substructure coupling. The most known methods are the Hurty's method [Hurty 65] and the Craig-Bampton's method [Craig 68]. The Imbert's method (also called effective-mass method, [Imbert 79, Alazard 08]) is included in this category as well. The main aspects of these methods will be discussed and compared in Chap. 4.
- Methods based on residual flexibility and free-interface normal modes. More difficult to implement, especially when a substructure has rigid-body freedom. Hintz [Hintz 75] and Macneal [MacNeal 71] have developed methods which fall into this category.
- Methods based on loaded-interface normal modes. Mainly used for acquisition of the substructure's data for FE model verification.

CMS techniques have been a widely used for modeling and assembling flexible substructures. Several research articles have studied how to obtain representations of substructures modeled with FE. In [Young 90], Young substructured the complete FE model of a two-dimensional truss in order to synthesize a distributed control law. Nevertheless, here the substructure assembly process was mainly based on the overlapping between the inertia and stiffness matrices provided by the substructures' FE model. This required deep knowledge of the FE theory and impeded straightforward concatenation of complex structures. Shortly after, Sunar [Sunar 92] started studying FE models substructuring at a more general level applying Guyan static condensation, a specific type of CMS. Later, Su [Su 95] proposed a CMS-based method to decompose a structure into a collection of substructures to synthesize decentralized controllers, and called it Substructural Controller Synthesis. However, the

overlapping between systems was done at the matrix level, presenting the same practical disadvantages as in [Young 90].

The aforementioned studies did not compute the substructure's state-space representation and did not develop a more intuitive overlapping method. Guy [Guy 14], based on Alazard [Alazard 08] and Cumer [Cumer 01], came up with a state-space representation from the substructure's FE model in order to represent the linear dynamics of a spacecraft with flexible appendages in star-like structure. Imbert's method was used in order to transfer the influence of flexible appendages to the spacecraft main hub. However, it did not allow for the representing of flexible substructures in chain-like assembly and the results were not compared with other methods.

2.1.2.2 Finite Element Transfer Matrix Method

The FE-TM method has not enjoyed the same degree of application as the CMS method, but it has been proved a powerful tool for the analysis of structures. Leckie [Leckie 60] stated the fundamentals of the transfer matrix method, which can be seen as a continuity function for a flexible system with transferable boundaries among the substructures. Later, Dokainish [Dokainish 72] merged the FE method with the transfer matrix method for the dynamic analysis of plates and presented it as the FE-TM method. Since then, many researchers extended the technique and used it for many different applications. MacDaniel [McDaniel 77] applied the method for orthogonally stiffened structures and demonstrated the efficiency of the FE-TM by computing the frequency response of a two row-five span plate structure. Sankar [Sankar 80] used the method to show fast convergence for obtaining natural frequencies of a cantilevered plate. Ohga [Ohga 83] extended and applied the method for the dynamic analysis of space frame structures, demonstrating the accuracy and efficiency of the method with numerical examples compared to classic FE substructure assembly. Rong [Rong 11] modified the FE-TM Method and its algorithms to solve the eigenvalue problem simply and conveniently, validating it on a plane wing model.

Other authors, like Yousuff [Yousuff 86] and Tan [Tan 90], modified the FE-TM method in order to create suitable models for flexible structures control. This method continues being improved by the works of authors such as Rui [Rui 08], who partially uses FE-TM to compute FMD of FMS, and enriched with other control applications as in Krauss [Krauss 10], where a non-collocated feedback is applied using the transfer matrix method.

2.1.3 FMD using corotational rotating frame and inertial frame

The corotational frame follows an average rigid body motion of an individual finite element within the flexible component. In this approach, the motion of a finite element is divided into a rigid body motion and natural deformation modes. The approach is used for static modeling of structures undergoing large displacements and small deformations. Some non-linear effects such as centrifugal stiffness are naturally included, and it has no limits on the magnitude

of angular velocities. Representative works with this kinematic description are the ones of Housner in [Housner 84], where he analyzed the maneuver and deployment of flexible multi-member trusses and frames with convected coordinate frame, and in [Housner 88], where Housner developed a three dimensional finite element formulation of truss-like structures without superimposing the rigid modes thanks to the convected coordinate frame. In [Wu 92], Wu and Housner continued to enlarge the approach of convected coordinate system to joint-dominated structures. Banerjee and Nagarajan [Banerjee 97] also made advantage of the corotational frame in order to simulate the large overall motion of flexible beams undergoing large deflections.

In many articles, intermediate frames are not used, instead the global inertial frame is directly used for measuring deformations. In this approach, the motion of an element consists of a combination of rigid body motion and deformation and the two types of motion are not separated. Vu-Quoc and Simo [Vu-Quoc 87] were one of the first authors to formulate this type of kinematic description for FMS experiencing large deformations. Wasfy and Noor [Wasfy 00] used this approach to compute the numerical model for simulation of a large space telescope. Dignath and Schiehlen [Dignath 00] computed the model of a tethered satellite system with this approach in order to perform vibration control. Leamy [Leamy 01] simulated the dynamic response of a tethered satellite system using this technique.

2.1.4 Actuator/Sensor Models for Flexible Structures Control

Actuators and sensors are an essential part of a control system because they produce the necessary forces to move the FMS and the necessary measurements to compute command actions. Actuators convert a form of energy such as electrical, chemical, or mechanical into mechanical energy that produces forces or moments on the FMS. Among all types of actuators, piezoelectric actuators and sensors (PEAs) have been the most used in control design of large flexible structures. The design of control systems involving PEAs requires an accurate knowledge of the electro-mechanical behavior of the system for vibration dynamics, transfers between the inputs and the outputs and non-linear effects such as hysteresis and creep effect. In order to integrate PEAs in the controlled structure, a design procedure including virtual prototyping of piezoelements integrated with the structure needs to be developed. This is why they have been meticulously studied in the literature of FMS.

Macroscopic PEAs models are divided in two main categories. In the first category, the behavior of a PEAs is decoupled in several contributions such as hysteresis, vibration dynamics and creep based on physical laws. The most well-known model structure of PEAs is the electro-mechanical model proposed by Goldfarb and Celanovic [Goldfarb 97], where piezoelectric stack actuators for control manipulation were modeled using a Maxwell resistor capacitor to represent hysteresis. Inspired by this approach, Adriaens [Adriaens 00] modified the model with charge steering to avoid the necessity of including hysteresis effects.

In the category of decoupled dynamics models, other models only consider vibration dynamics with FE models [Piefort 01] or transfer matrix models [Worak. 11]. In [Piefort 01],

Piefort and Preumont modeled piezoelectric shell structures with finite elements and validated the model experimentally. Worakitjaroenphon [Worak. 11] derived the transfer function of a piezoelectric material from its FE formulation. Other models only include static behaviour, as in Smits [Smits 91], where a bimorph piezoelectric component is modeled. However, this review has not found piezoelectric actuator/sensor modeling in the form of state space representation.

The second category does not decouple the different behaviors of the PEA, all effects are considered simultaneously. However, they are only accurate over small frequency ranges, what seriously limits their usage. One example of this kind of models is the one of Dang and Tan [Dang 05], where a rate-dependent neural-network-based hysteresis model is directly used as a model of the PEA.

2.2 Studies on Control of Large Flexible Structures

The area of control of large flexible structures has been and continues to be a very active research area due to its applications in flexible robotic manipulators and large space structures. The control laws implemented must account for control/structure interaction, and thereby account for the modification of the system dynamics stability and performance due to the presence of structural flexibility.

As it has been stated before, the modeling of large flexible structures plays a crucial role to accomplish this objective. The modeling process has to include the necessary control inputs/outputs that vary the dynamical behavior of the system in order to be controlled, as well as the most accurate dynamical behavior. Once the FMD has been derived, control techniques can be applied in order to find the most suitable control law for the required application. The FMD model can be used in two ways: to design a centralized control law or to design a decentralized control law. In the centralized approach, the controller is designed based on a reduced version of the entire FMD model. In the decentralized approach, the system to be controlled is viewed as a collection of subsystems. Controller design is carried out on the subsystem level, and the individual controllers are then applied in some manner to the complete system. The decentralized approach takes greater advantage of the substructured nature of the FMD model, while the centralized approach only uses the final assembled model of the FMD.

Either with a centralized or decentralized architecture, the control applications which are performed on space structures comprehend retargetting of flexible appendages, active vibration control, attitude control and deployment control. In this review, only attention to attitude and vibration control is paid, since they are the closest applications to this study.

2.2.1 Attitude Control of Large Flexible Structures

In attitude control applications, the orientation of the entire space structure should be controlled at all time to maintain the desired orientation. Disturbances are typically caused by the motion of an onboard appendage, the docking or separation of another structure, thermal deflections or solar radiation pressure. The action of the attitude control system on the spacecraft must not worsen the structural deformation as well as the spacecraft attitude dynamics. Attitude control is achieved using control moment gyros or reaction control jets. The orientation of the space structure is obtained either by referring to a fixed earth target (Earth Sensors), fixed stars (Star Trackers), or by using high-speed gimballed inertial navigation gyros.

Therefore, the attitude control system ensures system orientation against perturbations. Many authors have focused their research efforts on this subject, particularly in the flexible case. Park [Park 02] developed a modified positive position feedback control to reduce thermally induced attitude disturbances for a spacecraft with a flexible boom. For the Shuttle Radar Topography Mission in [Hamelin 01], Hamelin modified the attitude control system of the Shuttle to mitigate the impact of the 200-foot deployable mast on the stability and performance. They modified the control system to control the damper system which ensured that mast tip motion remained within the limits of the outboard antenna that mapped the Earth. Zheng [Zheng 05] performed the complex task of optimal attitude control of a flexible spacecraft with time-varying LQR taking into account non-linearities. Meiyu [Meiyu 10] also performed optimal attitude control of a flexible spacecraft, but this time ensuring minimum vibration by the implementation of an optimal forward position feedback controller.

Many controller synthesis techniques can be used: PID, adaptive control, pseudo - linearization, LQR, fuzzy control, etc. However, most studies opt for robust control techniques such as the \mathcal{H}_∞ synthesis. For instance, it was used by Bennani [Bennani 11] as the robust control synthesis technique for the attitude control system of the BIOMASS Satellite. However, \mathcal{H}_∞ synthesis often results in high-order controllers which must be reduced later, complicating the design task.

The development of structured \mathcal{H}_∞ control [Gahinet 11, Burke 06] opened the gates for a new age in robust attitude control. This technique allowed to synthesize robust low-order structured controllers, which is very pertinent in attitude control since the problematic often implies structured solutions (PIDs, roll-off filters). Guy [Guy 12] demonstrated its suitability for flexible structures control. Alazard [Loquen 12] used a structured \mathcal{H}_∞ approach to synthesize the attitude control system of a satellite with cantilevered flexible appendages. Falcoz [Falcoz 15] successfully applied structured \mathcal{H}_∞ control to refine the Rosseta's orbit controller.

2.2.2 Vibrations Suppression of Large Flexible Structures

In vibration suppression applications, the control system must be able to damp structure oscillations due to disturbances because they can reduce the precision of onboard instruments.

Although active control of structural vibrations can be considered an independent control application domain by itself, it is intimately related with attitude control in particular and control of large flexible structures in general. Indeed, damping could enhance stability and performance of the attitude control system since the spacecraft behave somewhat like a rigid spacecraft [Woerkhom 93]. Active control of structural vibrations is called simply stabilization, as the deformations are to be stabilized with respect to their steady state values.

Stabilization is closely related to the concept of positivity, a characteristic which ensures system stability when the system is closed with negative feedback. Benhabib [Benhabib 81] explained this concept and deduced that the transfer matrix of a structure is positive real if collocated actuators and sensors are used. With this result, he designed controllers for vibration suppression of a large flexible structure. McLaren and Slater [McLaren 87] also made advantage of the positivity concept and applied it to design robust controllers for the DRAPER space telescope, a large space structure. This has immediately separated the control strategies in two large domains: collocated and non-collocated control.

Collocated approaches have been largely used in the literature for damping of space structures. Fanson [Fanson 90] demonstrated the feasibility of using Positive Position Feedback (PPF) as a vibration control strategy for damping of large space structures. Preumont compared in [Preumont 02] collocated acceleration feedback and collocated integral force feedback for active damping of flexible structures, demonstrating that integral force feedback guaranteed closed-loop stability in all circumstances. Lately, Preumont used integral force feedback in [Preumont 11] for active vibration damping of a flexible space truss. Robust \mathcal{H}_∞ control synthesis has also been used for active damping of space structures by authors as Safonov [Safonov 91], who, using collocated sensors/actuators, designed a robust multivariable controller for active vibration suppression of a large space structure. On the contrary, fewer studies exist about non-collocated active damping of large space structures. Damaren [Damaren 00] studied the possibilities of achieving positivity of non-collocated FMS, obtaining a theory for controlling flexible structures with non-collocated feedback. Krauss [Krauss 10] also studied the problem of non-collocated feedback with the transfer matrix modeling technique. Smith [Smith 94] designed \mathcal{H}_∞ controllers for active vibration damping of a space truss with non-collocated actuators/sensors, developing an eigenvalue perturbation model.

It should be mentioned that it is within this field where the greatest efforts for decentralized control have been made. Many works have made advantage of using the CMS technique in FMD for decentralized vibration control purposes. One of the first authors who merged FE modeling of FMS, state-space modeling and decentralized control was Young [Young 90], who substructured the complete FE model of a two-dimensional truss in order to synthesize a distributed control law. Young demonstrated the feasibility of controlled component synthesis for structures with an open chain topology. Subsequently, Su [Su 95] proposed a method to decompose a structure into a collection of substructures in order to design a controller for each substructure, called *Substructural Controller Synthesis*, and applied the method to a plane truss example. Finally, Butler and Dhingra [Butler 03] studied integrated structure and control design using substructure decomposition based on CMS as well, designing LQR controllers for each substructure.

2.3 Studies on Integrated Control/Structure Design

Integrated Control/Structure Design (ICSD) arises as a solution in early design phases of large space structures. As previously stated, increasing complexity of large space structures makes Control-Structure Interaction (CSI) problem more critical, urging the need of developing new methods which tie together spacecraft structural dynamics and control laws. These methods are also called *Plant-Controller Optimization* (PCO) or *co-design* (CD). In the majority of ICSD studies, the structure model and the control techniques are closely related: FMD model is used in model-based control as an integral part of the controller as well as in controller design for optimizing the controller/FMS parameters. Therefore, this field merges modeling and control theory, the control system does not deal anymore with a *fixed* structure, it can be modified and optimized in order to achieve higher performances such as maximized dimensions, lighter materials that minimize the system cost, increment of strength and robust static/dynamic stability.

ICSD methods began being studied in the 80s as an opposite technique to the current method of separated iterative sequences within the structural and control disciplines. The first integrated design methodologies were those which used optimization algorithms in Hale [Hale 85], Onoda [Onoda 87] and Khot [Khot 88]. Hale [Hale 85] performed optimal simultaneous structural and control design of a maneuvering flexible spacecraft, minimizing a cost function composed of the weighted mass and control force, deducing the necessary and sufficient conditions for an optimum. Later, Onoda and Haftka [Onoda 87], developed an approach using nested optimization technique for optimization of total cost of a flexible structure and control system, constraining at the same time the magnitude of response to a given disturbance. Khot [Khot 88] also developed an optimization algorithm with nonlinear mathematical programming approach for designing an optimal damping law and optimizing structural parameters of a truss structure, finding that the optimized truss had a better closed-loop behavior than the nominal truss.

Optimization algorithms continued to be improved in the 90s using nonlinear dynamics and optimizing more complicated structures. Messac and Malek [Messac 92] designed the structure and the control system of a rotatory flexible spacecraft, addressing disturbance rejection and command following performance of the system, while optimizing the profile of the flexible appendage for minimum mass of the system. Messac and Malek thereby demonstrated that control/structure optimization gives better results than control optimization alone in terms of mass costs and control performances. Maghami [Maghami 96] posed the ICSD problem as a nonlinear programming problem to minimize the control effort required to maintain a specified line-of-sight pointing performance, under persistent white noise disturbance, of an evolutionary model called CEM. CEM was composed of eight flexible substructures (trusses) and the pointing performance was validated numerically and experimentally. Ou and Kikuchi [Ou 96] extended the application building an independent modal space control algorithm for an integrated design procedure composed of structural design, control design, and actuator locations design. Oliver and Asokanthan [Oliver 97] performed ICSD for a satellite undergoing maneuvers modeled including the nonlinear orbital dynamics and analyzed the influence

of parameters such as the mass in the final dynamic behavior of a maneuver.

In the late 90s ICSD methods started using \mathcal{H}_∞ control approach to design robust controllers against parameter uncertainties. Tsujioka [Tsujioka 96] used genetic and nonlinear optimization algorithms to compute the \mathcal{H}_∞ control system and optimize structure parameters and actuator/sensor location of a FE model. Savant [Savant 99] proposed an iterative method to bound the truncation errors and to optimize robustness margin of the closed loop system changing structural design parameters, finding controllers of lower order than those obtained with standard μ -synthesis methods, achieving the same robust-performance. Kajiwara and Nagamatsu [Kajiwara 99] also performed ICSD with \mathcal{H}_2 and \mathcal{H}_∞ optimization for vibration control mechanisms. This approach continues to be used nowadays in studies as Alazard *et al.* [Alazard 13b], where optimization of the attitude control system of an Earth Observation satellite and the FE model were performed using a genetic algorithm.

However, the aforementioned general algorithms for integrated design were constructed under the premise of a full-order and unstructured control law (eg., LQ, \mathcal{H}_2 and \mathcal{H}_∞ control laws) which could be obtained in an analytic manner. The integrated design problem with a specified controller structure (e.g., a low-order PID and decentralized controllers etc) had not been studied that far except for a quite limited and simple control laws like velocity feedback control. In real control problems, like large space structures, the structure (or the order) of the controller is limited since the scale of the controlled system itself is high-order dimension. With the development of the Linear Matrix Inequality (LMI) approach [Boyd 94, Scherer 97], structured control laws began being feasible in ICSD. Hiramoto [Hiramoto 06, Hiramoto 09] described the ICSD problem as polynomial matrix on the Laplace variable s and constrained the closed-loop stability region of the feedback system by solving LMIs. Hiramoto was able to optimize an arbitrary (low-order, PID and decentralized control) structure for the feedback controller, while ensuring robustness against parameter uncertainty given in the standard \mathcal{H}_∞ based control schemes. In [Hiramoto 06], the algorithm and the methodology are presented and demonstrated through illustrative examples. In [Hiramoto 09] the complexity of the design was increased by adding optimal actuator/sensor placement, and ICSD was performed to compute optimal structural parameters, collocated actuator placement and vibration control of a supported beam.

Nowadays, the structured \mathcal{H}_∞ synthesis algorithms developed in [Gahinet 11] or [Burke 06], allow to optimize structured controllers and other tuneable parameters of the system. The ICSD problem is posed in a multi-channel \mathcal{H}_∞ scheme where constraints to controller structure and parameters variability are set in the frequency domain. Taking advantage of this form, Alazard [Alazard 13a] used a multi-model \mathcal{H}_∞ synthesis scheme to design a fixed-structure controller of an earth-observation satellite. Simultaneously, avionic parameters (sensors and actuators delay) were optimized in order to select the ideal actuator for challenging requirements or standard requirements.

This chapter has reviewed the state-of-the-art of the methods concerning the modeling, control and co-design of large flexible structures. As stated in Chap. 1, the field lacks of studies which involve simultaneously modeling and integrated control/structure design of flexible multibody structures. Regarding the modeling of FMS, only a few studies (those in [Guy 14], [Alazard 08] and [Cumer 01]) provided state-space representations of FE-based models of substructures. These studies only can assemble substructures in star-like configuration. Furthermore, there is also a shortage of linear models of substructures actuated through piezoelectric materials for control purposes. Concerning the integrated attitude control/structure design, only one study has been done using structured \mathcal{H}_∞ synthesis [Alazard 13a], where only the actuator avionics were optimized. The study of this thesis is focused on providing the necessary foundations for performing integrated control/structure design of flexible multibody structures, with strong emphasis on the flexible spacecraft application.

Chapter 3

Materials and Methods

“What we observe is not nature itself, but nature exposed to our method of questioning.”
- Werner Heisenberg

Contents

3.1	Introduction to Mechanics	26
3.1.1	Satellite Attitude Dynamics	26
3.1.2	Flexible Structural Dynamics	30
3.2	Introduction to Robust Control Theory	31

This chapter explains the main methods and preliminary concepts that somehow are used throughout the study. Since the thesis seeks to perform integrated design developing a flexible multibody linear modeling technique and to use structured \mathcal{H}_∞ synthesis, the main concepts on mechanics and control theory are recalled.

An integrated control/design study requires merging the knowledge of two complex fields: rigid and flexible system mechanics and linear control theory. This chapter recalls in Sec. 3.1 the main mechanical concepts that are used for satellite attitude dynamics and flexible dynamics. In Sec. 3.2, the main aspects of robust control theory are exposed with special emphasis on the structured \mathcal{H}_∞ theory, the method which is used throughout the entire study.

3.1 Introduction to Mechanics

In order to understand the attitude control/structure interaction problem, previous concepts about flexible mechanics and attitude dynamics are needed. The first section, Sec. 3.1.1, recalls the linearized equations used to express the attitude dynamics of a satellite with the approach and notation of [Alazard 08]. In Sec. 3.1.2 the most fundamental equations and properties of flexible structures are presented.

3.1.1 Satellite Attitude Dynamics

Generally speaking, the satellite attitude dynamics equations are three second-order nonlinear equations. Automatic control theory does not provide exact analytical solutions and design procedures for such dynamic plants, so linearization of these equations is necessary if the satellite control engineer wishes to use standard automatic control techniques. The linearization used throughout this study is based on the equations of motion proposed in [Alazard 08], where a 6-DOF model which describes the rotations and translations of the hub of a multi-body spacecraft are described as follows at its center of mass G :

$$\begin{Bmatrix} \mathbf{F}_G \\ \mathbf{T}_G \end{Bmatrix} = [D_G^H] \begin{Bmatrix} \ddot{\mathbf{x}}_G \\ \ddot{\boldsymbol{\theta}}_G \end{Bmatrix} = \begin{bmatrix} m^H I_3 & 0 \\ 0 & J_G^H \end{bmatrix} \begin{Bmatrix} \ddot{\mathbf{x}}_G \\ \ddot{\boldsymbol{\theta}}_G \end{Bmatrix} \quad (3.1)$$

In Eq. (3.1) the hub's three translational accelerations, $\{\ddot{\mathbf{x}}_G\}$, and the three angular accelerations, $\{\ddot{\boldsymbol{\theta}}_G\}$, are considered together. Note that for the rotation dynamics, the relation $\mathbf{T}_G = J_G^H \ddot{\boldsymbol{\theta}}_G$ is a linear approximation of the actual nonlinear dynamic equation which reads:

$$\{\mathbf{T}_G\} = \frac{d\{L_G^H\}}{dt} \Big|_{R_i} \quad (3.2)$$

where $\{L_G^H\} = [J_G^H]\{\dot{\boldsymbol{\theta}}_G\}$ is the angular momentum of the hub H at point G . Then, using time domain derivation in the body frame of the hub H (in which J_G^H is constant) it comes:

$$\{\mathbf{T}_G\} = \{L_G^H\} = [J_G^H]\{\dot{\boldsymbol{\theta}}_G\} + \{\dot{\boldsymbol{\theta}}\} \times ([J_G^H]\{\boldsymbol{\theta}_G\}) \quad (3.3)$$

The nonlinear term $([J_G^H]\{\dot{\boldsymbol{\theta}}_G\})$ in Eq. (3.3) can be neglected for small angular velocities

$\{\dot{\theta}_G\}$, which is a common characteristic of spacecraft dynamics.

The relation between velocities between the hub's points P and G is given by:

$$\{\dot{x}_P\} = \{\dot{x}_G\} + \{PG\} \times \{\dot{\theta}_G\} \quad (3.4)$$

$$\{\dot{\theta}_G\} = \{\dot{\theta}_P\} \quad (3.5)$$

and with the notation given in [Alazard 08], Eqs. (3.4) and (3.5) can be expressed in the following compact form:

$$\begin{Bmatrix} \dot{x}_G \\ \dot{\theta}_G \end{Bmatrix} = \underbrace{\begin{bmatrix} I_3 & (*GP) \\ 0 & I_3 \end{bmatrix}}_{\tau_{GP}} \begin{Bmatrix} \dot{x}_P \\ \dot{\theta}_P \end{Bmatrix} \quad (3.6)$$

where τ_{GP} is called the 6×6 kinematic model between points G and P and $(*GP)$ is the skew-symmetric matrix associated with the vector $\{PG\} = \{x \ y \ z\}^T|_{R_G}$:

$$(*GP) = \begin{bmatrix} 0 & -z & y \\ z & 0 & -x \\ -y & x & 0 \end{bmatrix}_{R_G} ; \quad (*PG) = \begin{bmatrix} 0 & z & -y \\ -z & 0 & x \\ y & -x & 0 \end{bmatrix}_{R_G} \quad (3.7)$$

If the dynamic equations have to be derived in another point of the hub, as for example point P , the acceleration at that point, $\{\ddot{x}_P\}$ reads:

$$\{\ddot{x}_P\} = \{\ddot{x}_G\} + \{\ddot{\theta}_G\} \times \{GP\} + \{\dot{\theta}_G\} \times \left(\frac{d\{GP\}}{dt} \Big|_{R_G} + \{\dot{\theta}_G\} \times \{GP\} \right) \quad (3.8)$$

where $d\{GP\}/dt = 0$ for a rigid body. For small angular rates the nonlinear terms in the right side of Eq. (3.8) can be neglected. The acceleration at point P is then deduced from the acceleration at point G by the linear relation:

$$\{\ddot{x}_P\} = \{\ddot{x}_G\} + (*PG)\{\ddot{\theta}_G\} \quad (3.9)$$

from which the following kinematic relationship can be derived:

$$\begin{Bmatrix} \ddot{x}_G \\ \ddot{\theta}_G \end{Bmatrix} = \underbrace{\begin{bmatrix} I_3 & (*GP) \\ 0 & I_3 \end{bmatrix}}_{\tau_{GP}} \begin{Bmatrix} \ddot{x}_P \\ \ddot{\theta}_P \end{Bmatrix} \quad (3.10)$$

Expressing the external force power, P_{ext} , computed along a virtual velocity field:

$$P_{ext} = \begin{Bmatrix} \dot{x}_G \\ \dot{\theta}_G \end{Bmatrix}^T \begin{Bmatrix} F_G \\ T_G \end{Bmatrix} = \begin{Bmatrix} \dot{x}_P \\ \dot{\theta}_P \end{Bmatrix}^T \begin{Bmatrix} F_P \\ T_P \end{Bmatrix} \quad (3.11)$$

Combining Eqs. (3.10) and (3.11) the relation between loads at different points of the hub can be expressed as:

$$\begin{Bmatrix} F_P \\ T_P \end{Bmatrix} = [\tau_{GP}^T] \begin{Bmatrix} F_G \\ T_G \end{Bmatrix} = \begin{bmatrix} I_3 & 0 \\ -(*GP) & I_3 \end{bmatrix} \begin{Bmatrix} F_G \\ T_G \end{Bmatrix} \quad (3.12)$$

Finally, using Eq. (3.12) in Eq. (3.1) the linearized equation of motion at point P is derived:

$$\begin{Bmatrix} F_P \\ T_P \end{Bmatrix} = [\tau_{GP}^T] \begin{bmatrix} m^H I_3 & 0 \\ 0 & J_G^H \end{bmatrix} [\tau_{GP}] \begin{Bmatrix} \ddot{x}_G \\ \ddot{\theta}_G \end{Bmatrix} = [D_P^H] \begin{Bmatrix} \ddot{x}_G \\ \ddot{\theta}_G \end{Bmatrix} \quad (3.13)$$

where the transport of the inverse dynamic model of the hub H from a the point G to point P is written as follows:

$$[D_P^H] = [\tau_{GP}^T][D_G^H][\tau_{GP}] = \begin{bmatrix} m^H I_3 & m^H(*GP) \\ -m^H(*GP) & J_G^H - m^H(*GP)^2 \end{bmatrix} \quad (3.14)$$

Expressions in Eqs. (3.1) and (3.13) are useful to model the system as interconnected subsystems. Let suppose that a rigid appendage or subsystem, named A , is characterized by its own dynamic model D_P^A at point P :

$$\begin{Bmatrix} F_{H/A} \\ T_{H/A,P} \end{Bmatrix} = [D_P^A] \begin{Bmatrix} \ddot{x}_P \\ \ddot{\theta}_P \end{Bmatrix} \quad (3.15)$$

where $F_{H/A}$ is the reaction force transmitted from the hub H to the appendage A and $T_{H/A,P}$ is the reaction torque transmitted from the hub H to the appendage A at point P . The hub experiences the same loads in opposite senses, giving

$$\begin{Bmatrix} F_G - F_{H/A} \\ T_G - T_{H/A,P} \end{Bmatrix} = [D_P^H] \begin{Bmatrix} \ddot{x}_P \\ \ddot{\theta}_P \end{Bmatrix} \quad (3.16)$$

and introducing Eq. (3.15) in Eq. (3.16) the equation of motion of the whole system at point P is obtained:

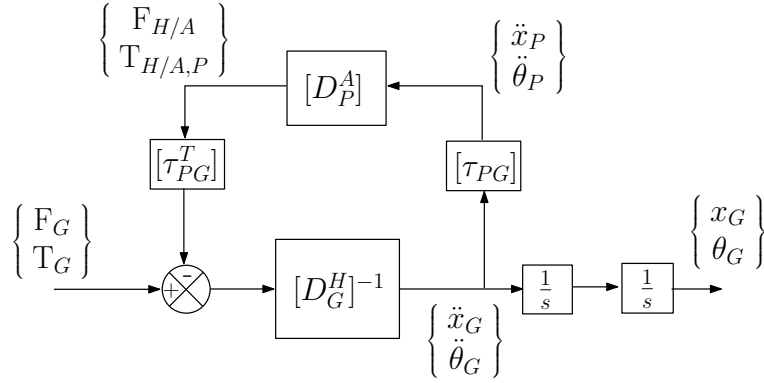


Figure 3.1: Block diagram of the direct dynamic model of a satellite composed of a hub H and an appendage A

$$\begin{Bmatrix} F_P \\ T_P \end{Bmatrix} = ([D_P^A] + [D_P^H]) \begin{Bmatrix} \ddot{x}_P \\ \ddot{\theta}_P \end{Bmatrix} = ([D_P^A] + [\tau_{PG}^T][D_G^H][\tau_{PG}]) \begin{Bmatrix} \ddot{x}_P \\ \ddot{\theta}_P \end{Bmatrix} \quad (3.17)$$

It is more practical to express the whole dynamic model at the center of mass G of the hub H , since the external forces $\{F_G\}$ and torques $\{T_G\}$ will correspond to the outputs of the Attitude and Orbit Control System (AOCS) which is mounted in the hub. Then, the transporting Eq. (3.17) to point G one gets

$$\begin{Bmatrix} F_G \\ T_G \end{Bmatrix} = ([D_G^H] + [D_G^A]) \begin{Bmatrix} \ddot{x}_G \\ \ddot{\theta}_G \end{Bmatrix} = ([D_G^H] + [\tau_{PG}^T][D_G^A][\tau_{PG}]) \begin{Bmatrix} \ddot{x}_P \\ \ddot{\theta}_P \end{Bmatrix} \quad (3.18)$$

Equation (3.18) introduces the inverse dynamics model of the satellite (accelerations as inputs, forces as outputs). For AOCS purposes, it is more convenient to derive the direct dynamic model (forces as inputs, accelerations as outputs):

$$\begin{Bmatrix} \ddot{x}_G \\ \ddot{\theta}_G \end{Bmatrix} = ([D_G^H] + [D_G^A])^{-1} \begin{Bmatrix} F_G \\ T_G \end{Bmatrix} = [D_G^{satellite}]^{-1} \begin{Bmatrix} F_G \\ T_G \end{Bmatrix} \quad (3.19)$$

This formulation can be represented as a block diagram scheme (see Fig. 3.1) and it can be easily used with a graphical programming environment (Mathworks Simulink) for simulation purposes. Once the system is assembled, the relation between the external loads (F_G and T_G , like thrust force or reaction wheel torque) applied to the system and the system's acceleration is set, describing the linearized attitude and translation dynamics. In practice, the attitude dynamics equations of the satellite are more complicated than those shown in Eqs.(3.1), (3.13) and (3.19). There may exist side effects such as structural dynamics of the body or of the appended solar panels, sloshing effects in the fuel tanks, and sensor noise. The consideration of structural dynamics of the different bodies is addressed in this study. Concerning the remaining effects, although the basic form of these equations remains unaffected, the control

equations will need filters to handle them.

3.1.2 Flexible Structural Dynamics

The general form of the equation of motion describing the dynamic balance between the external, elastic, inertia and damping forces acting on a discrete flexible structure with a finite number of degrees of freedom (DOF) is:

$$[M]\{\ddot{q}\} + [D]\{\dot{q}\} + [K]\{q\} = \{F\} \quad (3.20)$$

where $\{q\}$ and $\{F\}$ are the vectors of generalized displacements (translations and rotations) and forces (point forces and torques) and $[M]$, $[K]$ and $[D]$ are respectively the mass, stiffness and damping matrices; they are symmetric and semi positive definite. Matrices $[M]$ and $[K]$ are obtained from the discretization of the structure, usually with finite elements (FE). The damping matrix $[D]$ represents the various dissipation mechanisms in the structure. It is generally assumed that the existence of damping does not cause coupling of the undamped natural modes of vibration [Hurty 65, Kraker 93]. Natural modes are obtained considering the free response of the following undamped (conservative) equation:

$$[M]\{\ddot{q}\} + [K]\{q\} = 0 \quad (3.21)$$

Trying solutions of the form $q = \phi_i e^{j\omega_i t}$, ϕ_i and ω_i must satisfy the following eigenvalue problem:

$$(K - \omega_i^2 M)\phi_i = 0 \quad (3.22)$$

Since $[M]$ and $[K]$ are symmetric and semi definite positive (or definite positive) the eigenvalue ω_i^2 is real and non negative. The eigenvalue ω_i^2 is called the *natural frequency* and ϕ_i it is called the *mode shape* associated with that frequency. The number of modes is lower or equal to the number of DOF, and the number of mode shapes are equal to the number of DOF.

The mode shapes of distinct natural frequencies are orthogonal with respect the orthogonal matrix, $\phi_j^T [M] \phi_i = 0$, and they are also orthogonal with respect to the stiffness matrix. The orthogonality conditions are often written as follows:

$$\{\phi_i^T\} [M] \{\phi_j\} = \mu_i \delta_{ij} \quad (3.23)$$

$$\{\phi_i^T\} [K] \{\phi_j\} = \mu_i \omega_i^2 \delta_{ij} \quad (3.24)$$

where δ_{ij} is the Kronecker delta index and μ_i is the model mass of mode i . Since mode

shapes can be scaled arbitrarily, it is usual to normalize the mode shapes in such a manner that $\mu_i = 1$. The orthogonality properties of mode shapes are used in order to derive the modal decomposition of the EOM in Eq. (3.20). Performing a change of variables from the physical coordinates $\{q\}$ to modal coordinates $\{\eta\}$ according to the following relation:

$$\{q\} = [\phi]\{\eta\} \quad (3.25)$$

where $[\phi]$ is the matrix of mode shapes defined as $[\phi] = [\phi_1 \phi_2 \dots \phi_n]$. Substituting Eq. (3.25) in Eq. (3.20) and premultiplying by $[\phi]^T$ the following transformation is obtained:

$$diag(\mu_i)\{\ddot{\eta}\} + [\phi]^T[D][\phi] + diag(\mu_i\omega_i^2)\{\eta\} = [\phi]^T\{F\} \quad (3.26)$$

Modal decomposition is the most general transformation of the EOM of a flexible structure. However, it must be applied in different approach either if rigid body modes ($\omega_i = 0$) are considered or not in the flexible structures. A different approach is needed in order to model flexible multibody systems and include the influence on the linearized attitude dynamics described in Eq. (3.19). This study uses a technique for transforming the EOM based on the component modes synthesis, which classifies the different mode shapes depending on their nature. The understanding of the modal synthesis decomposition is crucial for understanding the component mode synthesis approach.

3.2 Introduction to Robust Control Theory

This study demonstrates the applicability of structured robust control tools for integrated design. Thus, the basic concepts of robust control theory have to be recalled. Robust control is a type of optimal control synthesis which ensures performance and stability of a system encountering environment perturbations or model uncertainties. Robust control synthesis was first introduced by Doyle and Glover [Doyle 81, Doyle 89], and since then it has evolved into several fields: robust control using \mathcal{H}_2 norm, robust control using \mathcal{H}_∞ , structured \mathcal{H}_∞ synthesis, μ -analysis, etc. This section presents the main results on robust control theory and explains the structured \mathcal{H}_∞ so that the reader can be familiar with this method hereafter.

In robust control, the dynamic model is set into the *standard form* (see Fig. 3.2), which includes the following inputs/outputs:

- The transfers between the inputs w_{perf} and the outputs z_{perf} which characterize the channel to optimize.
- The commands u and the measurements y which are used for the control law $K(s)$

The matrix transfer of the standard form of a dynamic model $P(s)$ can be decomposed in the following manner:

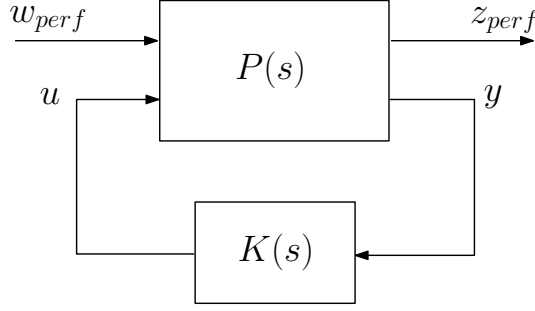


Figure 3.2: Standard form representation

$$\begin{Bmatrix} z_{perf} \\ y \end{Bmatrix} = \begin{bmatrix} P_{11}(s) & P_{12}(s) \\ P_{21}(s) & P_{22}(s) \end{bmatrix} \begin{Bmatrix} w_{perf} \\ u \end{Bmatrix} \quad (3.27)$$

The objective is then to optimize the control law $K(s)$ such as the closed loop is stabilized according to the optimization channel $w_{perf} \rightarrow z_{perf}$. However, a system can present uncertainties which can be the result of neglected dynamics and non-linearities, which in the standard form they are represented by the block Δ . Closed-loop stability is sensitive to these uncertainties, compromising the stability of the system. It is then imperative to guarantee the stability of all the models derived from the possible perturbations of Δ . This is called robust stability. The small-gain theorem allows ensuring closed-loop stability under certain conditions:

Theorem 3.1. *Assume two stable systems with transfer functions $P_1(s)$ and $P_2(s)$ are connected in a feedback loop, then the closed loop system is input-output stable if $\|P_1(s)\| \cdot \|P_2(s)\| < 1$.*

The norm can be the \mathcal{H}_∞ norm, that is the size of the largest singular value of the transfer function over all frequencies. Also any induced norm will lead to the same results. If the system P_2 is identified as the uncertainty block $\Delta(s)$ and it is restricted to the domain of stable linear systems of norm $\|\Delta(s)\|_\infty < 1$, then the system $P_1(s)$ is stable if and only if $\|P_2(s)\|_\infty < 1$.

In the illustration provided in Fig. 3.3, closed loop stability is guaranteed against every uncertainty $\Delta(s)$ satisfying $\|\Delta(s)\|_\infty < 1$ if and only if $\|G(s)K(s)(I + G(s)K(s))^{-1}\|_\infty < 1$. Thus, the robust stability of this system implies the transfer $T = G(s)K(s)(I + G(s)K(s))^{-1}$, called the complementary sensitivity function. Minimizing the complementary sensitivity function will make the system robust stable, but since the sensitivity function takes the form $S = (I + G(s)K(s))^{-1}$, it results that always $T + S = 1$, which obliges to find a good trade-off between robustness and performance.

Finding the control law $u = K(s)y$ which robustly stabilizes the system is called the standard \mathcal{H}_∞ problem. For that, it minimizes the \mathcal{H}_∞ norm between w_{perf} and z_{perf} of the closed loop, i.e., it minimizes the impact of the perturbations w_{perf} on the performance outputs z_{perf} while ensuring the internal stability of the system.

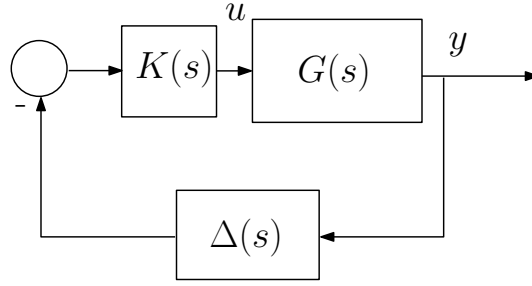


Figure 3.3: Small-gain theorem diagram when $P_1(s) = K(s)G(s)$ and $P_2(s) = \Delta(s)$

Definition 3.2. Optimal \mathcal{H}_∞ Problem. It minimizes $\|\mathcal{F}(P, K)\|_\infty$ among the set of controllers $K(s)$ which internally stabilize the system. The minimum is noted γ_{opt} and it is called “ \mathcal{H}_∞ -optimal” gain.

Definition 3.3. Sub-Optimal \mathcal{H}_∞ Problem. It finds the compensator $K(s)$ which internally stabilizes the system and at the same time ensures $\|\mathcal{F}(P, K)\|_\infty < \gamma$ with $\gamma > 0$.

This synthesis approach obtains a full-order compensator, i.e., the order of the compensator is equal to the order of the system plus the order of the weighting filters needed with such synthesis approaches. This is an important inconvenience for large flexible structures, since their associated models are usually high-order due to the presence of flexible modes. To avoid this inconvenience, structured \mathcal{H}_∞ synthesis was developed [Gahinet 11, Burke 06]. This technique allows the imposition of the controller’s order and its architecture, the selection the transfers to be minimized and the use of several models at the same time.

As in the standard \mathcal{H}_∞ problem, the structured \mathcal{H}_∞ problem also uses the standard form. Therefore, it can be found:

- A linear time invariant model (LTI), $P(s)$.
- A structured controller $K(s) = \text{diag}(K_1(s), \dots, K_N(s))$ which combines all the modifiable elements of the controller. Each controller’s element $K_j(s)$ is supposed to be a LTI with a given structure (proportional gain, proportional-derivative, second-order transfer function, state-space of a fixed order m , etc).

With this, two kind of synthesis can be performed: the multi-channel synthesis and the multi-model synthesis. Let consider the synthesis of a controller of a model with two channels for the performance inputs/outputs:

$$w_{perf} = \begin{Bmatrix} w_1 \\ w_2 \end{Bmatrix} \quad z_{perf} = \begin{Bmatrix} z_1 \\ z_2 \end{Bmatrix} \quad (3.28)$$

Whereas the standard \mathcal{H}_∞ problem has to minimize γ such that:

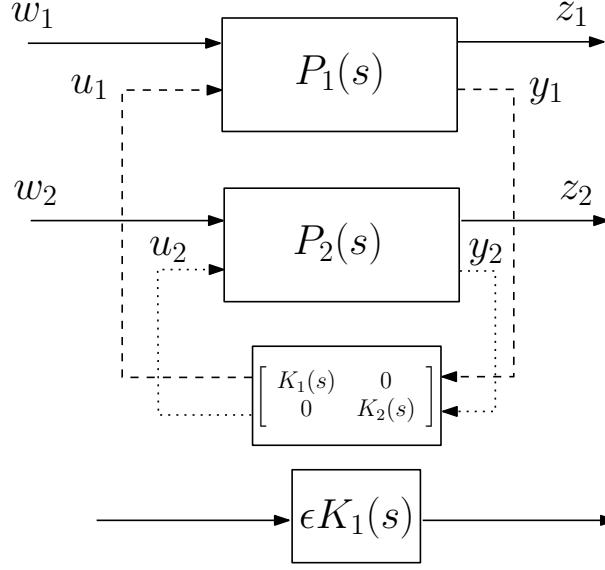


Figure 3.4: Standard form for multichannel \mathcal{H}_∞ synthesis

$$\left\| \begin{bmatrix} \mathcal{F}(P, K)_{11} & \mathcal{F}(P, K)_{12} \\ \mathcal{F}(P, K)_{21} & \mathcal{F}(P, K)_{22} \end{bmatrix} \right\|_\infty < \gamma \quad (3.29)$$

the structured \mathcal{H}_∞ problem minimizes γ such that

$$\left\| \begin{bmatrix} \mathcal{F}(P, K)_{11} & 0 \\ 0 & \mathcal{F}(P, K)_{22} \end{bmatrix} \right\|_\infty < \gamma \quad (3.30)$$

since the crossed terms $\mathcal{F}(P, K)_{12} = T_{w_1 \rightarrow z_2}$ and $\mathcal{F}(P, K)_{21} = T_{w_2 \rightarrow z_{21}}$ do not suppose performance specifications. Therefore, the structured \mathcal{H}_∞ synthesis search the minimum of

$$\max(\|\mathcal{F}(P, K)_{11}\|_\infty, \|\mathcal{F}(P, K)_{22}\|_\infty) \quad (3.31)$$

This feature can be exploited in many different manners. Besides already imposing controller's structure and architecture, controller's stability can be forced as well by adding a new fictive channel with a static gain ϵ (see Fig. 3.4). Furthermore, the controller's frequency response (roll-off) can also be established substituting the static gain by a filter with the desired frequency response. In the same manner, given two different systems $P_1(s)$ and $P_2(s)$, the structured \mathcal{H}_∞ multi-model synthesis allows getting a controller $K(s)$ with ensures stability and performance of both systems (see Fig. 3.4).

Part II

Study

Setting the Modeling Framework of Flexible Multi-Body Structures in Automatic Control

“High achievement always takes place in the framework of high expectation.”
 - Charles Kettering

Contents

4.1	Selection of the Motion’s Kinematic Description	39
4.2	The Double-Port Approach as an Overlapping Mechanism	41
4.3	Substructure’s EOM Manipulation	48
4.3.1	Hurty’s Method	48
4.3.2	The Craig-Bampton’s Method	52
4.3.3	Imbert’s Method or Effective Mass Method	54
4.3.4	EOM’s Transformations Discussion	55

The first step for developing a control-oriented flexible multibody system modeling technique is to determine the modeling framework. This framework is the starting point since it sets the reference frames, equations of motion and constraints that are used in order to derive flexible substructure models for automatic linear control. The setting of the framework allows the development and use of the models in the next chapters.

THIS chapter develops, explains and discusses the different foundations which form the general framework created for the control-oriented modeling of flexible multibody systems (FMS). The foundations of the modeling framework have to meet several requirements, such as the available data for the equations of motion, the model's simplicity and the needed properties for integrated control/structure design.

In Fig. 4.1, a generic flexible substructure of a FMS is depicted. The flexible body (substructure), named \mathcal{A} , is linked to the parent structure, named \mathcal{P} , at the point P and to a child substructure, named \mathcal{C} , at the point C . Therefore, only two connection points are assumed in this study. The external loads applied to \mathcal{A} are the interactions with \mathcal{P} at point P and with \mathcal{C} at point C . The equations of motion (EOM) of the flexible substructure are obtained through the finite element (FE) modeling technique which, written in terms of generalized coordinates q , have the following matrix form:

$$[M] \{\ddot{q}\} + [D] \{\dot{q}\} + [K] \{q\} = \{F\} \quad (4.1)$$

Equation (4.1) describing the dynamics of the substructure alone, the flexible substructure's model for FMS assembly has to transform Eq. (4.1) in order to take into account the interactions with the neighboring substructures \mathcal{P} and \mathcal{C} , preserving a state-space form so that linear control tools can be used. In addition, for integrated control/structure design purposes the models should be parameterized with the variables that are required for optimization, such as mass, length, surface, density or Young's modulus.

These requirements introduce a set of difficulties that the modeling technique must be able to manage. These problems are described as follows:

- Substructure interconnection: the assembly between the different substructures must describe the interactions between them. This is what is named the **overlapping** problem.
- Substructure linear independence and completeness: the substructure's model must contain all the necessary information so that the model can be used independently of the other substructures to which it is connected. This implies:
 - The substructure's boundary conditions must be externalized outside the model.
 - The substructure's model must be defined by its own dynamic parameters.
- Substructure parameterization: variables liable to be optimized in an integrated control/structure design should be traceable.
- Substructure linear model with the required properties: linear control tools (such the ones that use structured \mathcal{H}_∞ optimization) need models in state-space representation or equivalent transfer matrices. Therefore, the EOM, obtained with FE analysis, must be cast into a **state-space representation** which includes the aforementioned properties. This model must include the rigid and flexible motion of the substructure so that the FMS has all the degrees of freedom required for integrated control/structure design.

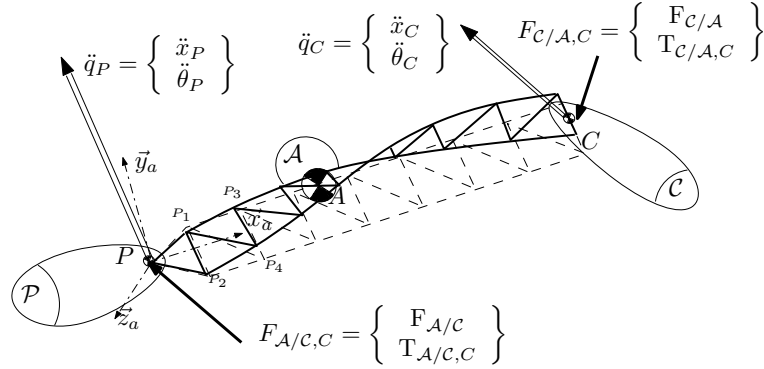


Figure 4.1: Substructure \mathcal{A} linked to structure \mathcal{P} and substructure \mathcal{C} in chain-like assembly

In this chapter a framework which helps solving these issues is proposed. The framework consists of three pillars: the choice of the modeling frame, the selection of the interaction mechanism which allows the substructure's assembly and the study of the different EOM's transformations to cast the model in state-space form. First, the modeling frame is chosen. Second, the interactions among substructures are translated in acceleration-load transfer among substructures, in what is called the Double-Port Approach (DPA), solving the substructure's interconnection and independence issue. Third, several transformation of the substructure's EOMs have been analyzed in order to find the most suitable one for state-space representation and variable parameterization. This chapter has allowed the publication of the Double-Port Approach in [Alazard 15]. Moreover, the discussion of the component modes synthesis techniques is the base of other publications of the thesis.

4.1 Selection of the Motion's Kinematic Description

The first step for flexible substructure modeling is the selection of the modeling frame in which the kinematic description of the system is going to be developed. The study's approach searches models that reproduce the rigid body motion taking into account the small perturbations due to the flexible motion of the system. This motion is described using FE models as input data. The modeling approach will be done in a **floating rotating frame**. Thus, the total displacement is computed by superimposing small elastic deformations on the large rigid body motion. In addition, as stated in Chap. 2, this is the most efficient method for the simulation of flexible multibody systems undergoing small elastic deformations and slow rotational speeds, such as satellites and space structures.

The floating frame approach is illustrated in this work in a simplified way without deriving the kinematic description directly. The objective here is simply to highlight the main points of the modelling framework and to show why it is well-suited to our modelling problem. If a more rigorous floating frame approach is desired, the reader might consult [Shabana 97]. Let us consider a generic FMS such as the one depicted in Fig. 4.2, in which substructures are linked using one connection point among them. Let us consider the inertial global frame

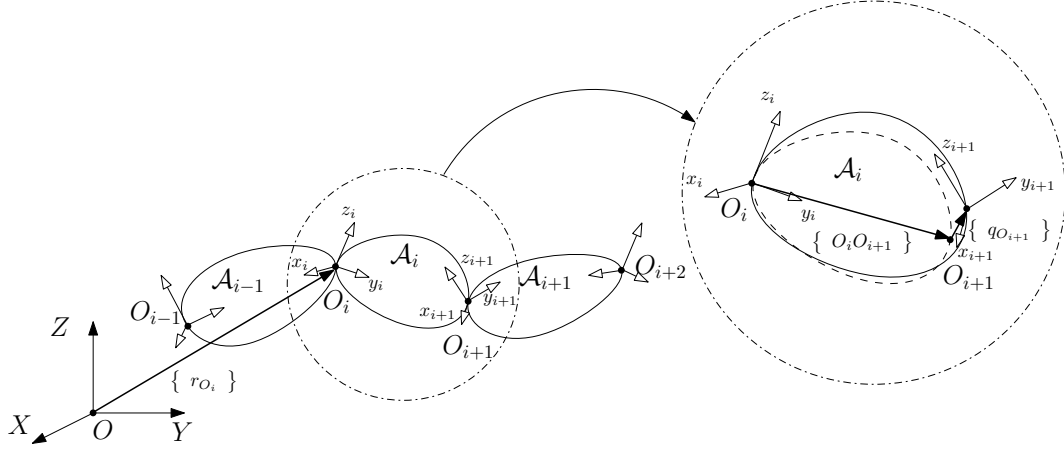


Figure 4.2: Generic FMS with floating frame approach notation

$\{O, X, Y, Z\}$ in which the absolute coordinates $\{r\}$ of a point are expressed. Let us consider the set of body reference frames attached to each substructure \mathcal{A}_i , $\{O_i, x_i, y_i, z_i\}$ as depicted in Fig. 4.2. Each body reference frame is related to the global inertial frame through the rotation matrix $[R_i]$. Given the absolute position of the connection point O_i of a substructure \mathcal{A}_i , the absolute position of the connection point O_{i+1} , $\{r_{O_{i+1}}\}$, can be written as:

$$\{r_{O_{i+1}}\} = \{r_{O_i}\} + [R_i] \left\{ \{O_i O_{i+1}\} + \{q_{O_{i+1}}\} \right\} \quad ; \quad O_{i+1} \in \mathcal{A}_i \quad (4.2)$$

where $\{r_{O_i}\}$ is the absolute position of the connection point O_i , $\{O_i O_{i+1}\}$ is the body frame position of the connection point O_i without elastic displacement and $\{q_{O_{i+1}}\}$ is the vector of elastic displacements around the equilibrium/rigid position of point O_{i+1} , which can be extracted from the FE formulation of the substructure's EOM in Eq. (4.1). The absolute position of point O_{i+1} is imposed as a constraint for the next substructure of the FMS, \mathcal{A}_{i+1} , but if the orientation is different the following coordinate change must be performed:

$$\{r_{O_{i+1}}\}_{i+1} = [R_{i+1}]^{-1} \{r_{O_{i+1}}\} \quad ; \quad O_{i+1} \in \mathcal{A}_{i+1} \quad (4.3)$$

In Sec 4.2 the interest of using accelerations as interconnection constraints is highlighted. In a floating reference frame, accelerations can be written as follows:

$$\{\ddot{r}_{O_{i+1}}\} = \{\ddot{r}_{O_i}\} + [R_i] \{\ddot{q}_{O_{i+1}}\} \quad ; \quad O_{i+1} \in \mathcal{A}_i \quad (4.4)$$

under the hypothesis of neglecting the nonlinear terms, such as the Coriolis contribution, since the framework supposes small elastic displacements and slow rigid body motion, what is the case of satellites and space structures. The same frame change can be applied for the acceleration of point O_{i+i} as in Eq. (4.3).

The floating frame approach sets a framework that enables the achievement of several requirements. First, a linear model can be derived since small elastic displacements are added to large rigid body motion, with no coupling terms. Second, each substructure's is independent from the others since they have their own body reference frame and is defined by its own EOM. Therefore, the choice of using a floating frame approach for the modeling framework is made. The next section sets the overlapping technique that interconnects the different substructures of a FMS under the floating frame assumption.

4.2 The Double-Port Approach as an Overlapping Mechanism

When dealing with models of substructures forming a FMS, the main difficulty lies on the consideration of the mechanical interactions among them. This is what is named the **overlapping** among substructures: the constraints which express the relations between the various components of the FMS. The overlapping among substructures has been addressed in literature in three different ways:

- Through the introduction of additional constraint equations [Shabana 97, Wasfy 03]. Constraint equations express the relations between the various components of the system. They have the form $\phi(q, \dot{q}, t) \geq 0$ where ϕ is the vector of algebraic constraint equations, q is the vector of generalized system coordinates, t is the time, and \dot{q} its time derivative. In the floating frame approach, constraint equations are usually written such that the flexible body coordinates are expressed in a floating frame and the rigid body coordinates (which define the motion of the floating frames) are expressed in the inertial frame as in Eq. (4.4).
- Through the overlapping of the mass and stiffness matrices [Young 90, Sunar 92]. The FE models of the different substructures are assembled by adding the different contributions of the mass and stiffness matrices to the interface nodes. In a floating frame approach, this method is equivalent as the constraint equations, but it is performed at the matrix level.
- Through the transfer matrix method [Leckie 60, Mucino 81]. Described in Sec 2.1.2.2, this method allows to transfer the imposed displacements and velocities to the neighboring substructures through the substructure's transfer matrix.
- Through a transfer of linear momentum and power when using *Port Hamiltonian systems* [Schaft 06]. This method is recommended for nonlinear systems where different physic descriptions are involved, such as fluid mechanics, electromagnetism or elasticity.

The above overlapping approaches are suitable for mechanical applications, but they are not suitable for applications in automatic control. The pursued technique must express the interactions between structures in a simple and intuitive way, in a single block in which there is no need of additional equations, manipulating mass and stiffness matrices or determining

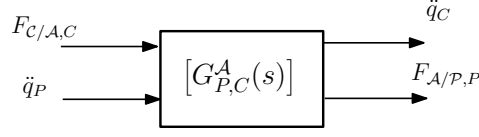


Figure 4.3: Block diagram of a model in Double-Port form

linear momentum or mechanic power. This has been accomplished by developing the **Double-Port (DP)** approach.

The DP approach uses a double input-output port transfer to model each substructure. The overlapping mechanism is expressed as an acceleration/load transfer between the connection points. The double input-output port model is a multi-input multi-output transfer with two channels. The first channel represents the direct dynamic model (forces as inputs and accelerations as outputs) at the connecting point between the substructure and the child structure. The second channel represents the invert dynamic model (accelerations on input and forces on output) at the connecting point between the substructure and the parent structure. The generic form of a substructure's model using the DP approach is written as:

$$\begin{Bmatrix} \ddot{q}_C \\ F_{A/P,P} \end{Bmatrix} = [G_{P,C}^A(s)] \begin{Bmatrix} F_{C/A,C} \\ \ddot{q}_P \end{Bmatrix} \quad (4.5)$$

where $\{\ddot{q}_C\}$ is the substructure's acceleration at the connection point C , $\{F_{A/P,P}\}$ is the load exerted at connection point P by the substructure, $\{\ddot{q}_P\}$ is the substructure's acceleration at the connection point P and $\{F_{C/A,C}\}$ is the load received by the substructure at connection point C . This transfer is also depicted as a block diagram in Fig. 4.3.

In the DP approach, the rigid body motion is imposed to the substructure by the acceleration input of the inverse dynamic channel, $\{\ddot{q}_P\}$, coming from the parent structure \mathcal{P} . The rigid body motion plus the flexible motion induced by the substructure are transmitted with the transferred acceleration at point C , $\{\ddot{q}_C\}$, to the child substructure \mathcal{C} . In the opposite direction, the load received by the substructure at point C from the child structure \mathcal{C} , $\{F_{C/A,C}\}$, enters through the direct dynamic model channel and, after interacting with the substructure, the load $\{F_{A/P,P}\}$ is transmitted to the parent structure \mathcal{P} . This mechanism is repeated throughout the chain of substructures to the end.

The morphology of a model using the DP approach offers straightforward means to meet a wide set of the established requirements. The DP approach allows, with the correct transformation of the EOM:

- The externalization of the substructure's boundary conditions. The computation of the model does not require specific boundary conditions (clamped-free, pinned-clamped, etc) since they are imposed by the connections to other substructures, which constraint the transfer channels.
- The modeling of each substructure's behavior by its own dynamic parameters.

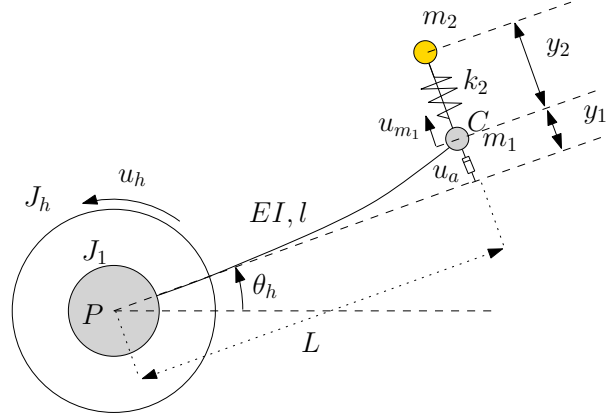


Figure 4.4: A simplification of a flexible pointing system composed of a rigid hub and two flexible appendages

- An intuitive and automatic assembly process by interconnecting the transferred loads and accelerations to the neighboring substructures.

Therefore, the DP approach will be used as the overlapping mechanism to perform substructure interconnection. It should be noted that the DP approach also fixes the necessary inputs/outputs for the state-space representation of the model. The next step is to look for an appropriate way of transforming the EOM so that they can be cast in a state-space representation with the inputs/outputs required by DP. A study of the possible EOM transformations is presented in Sec. 4.3. The following paragraphs are dedicated to show an illustrative example of the DP model.

Illustrative Example on DP form: the flexible pointing system

As an illustrative example of the DP form for flexible substructure modeling, let consider the simplified flexible pointing system depicted in Fig. 4.4. This system is composed of a rotatory hub with inertia J_h , solidary with a disc of inertia J_1 . The disc J_1 is a part of the Appendage 1 (gray color), composed of the disc, a flexible bar attached to the disc and a lumped mass at the end of the bar, m_1 . The mass of the bar can be neglected with respect to m_1 . Appendage 2 (yellow) is connected to Appendage 1 at m_1 through a spring of stiffness k_2 and its mass is modeled as m_2 .

The system can be decomposed (or separated) in different substructures (or appendages), as illustrated in Fig. 4.5. The objective is to model the modular system by interconnecting the different appendages using a double-port approach. A double port dynamic model $[Z_1(s)]$ is developed to represent the middle appendage, Appendage 1. The block-diagram representation of this dynamic model is presented in Fig. 4.6 and highlights that acceleration and force are both on the inputs or the outputs of $[Z_1(s)]$:

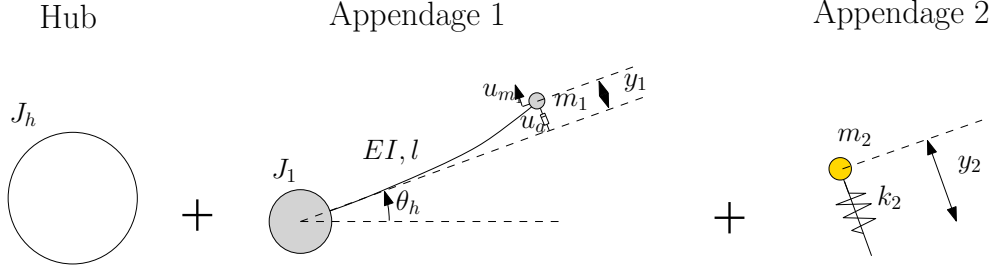


Figure 4.5: Decomposition in hub and appendages of the flexible pointing system

$$\begin{Bmatrix} \ddot{Y}_{abs}(s) \\ F_{1/h}(s) \end{Bmatrix} = [Z_1(s)] \begin{Bmatrix} F_{2/1}(s) \\ \ddot{\theta}_h(s) \end{Bmatrix} \quad (4.6)$$

where $F_{1/h}(s) = \mathcal{L}[f_{1/h}(t)]$ is the force applied by Appendage 1 on the parent substructure h , the rotatory hub; $F_{2/1}(s) = \mathcal{L}[f_{2/1}(t)]$ is the force applied by the child substructure, Appendage 2, to the Appendage 1; $\ddot{\theta}_h(s) = \mathcal{L}[\ddot{\theta}_h(t)]$ is the inertial acceleration of the connecting point (interface) between the rotatory hub and Appendage 1; $\ddot{Y}_{abs}(s) = \mathcal{L}[\ddot{y}_{abs}(t)]$ is the inertial acceleration of the connecting point between Appendage 1 and the child substructure Appendage 2; i.e, $\ddot{y}_{abs} = \ddot{y}_1 + \ddot{\theta}_h L$.

In order to get the relation between the desired inputs/outputs, the system's EOM must be derived. Using either the *Newton* principle or the *Lagrange* method, the following equations that govern the dynamical behavior of each system's substructure are derived:

$$J_h \ddot{\theta}_h = u_h + F_{1/h} \quad (4.7)$$

$$\begin{bmatrix} J_1 + m_1 L^2 & m_1 L \\ m_1 L & m_1 \end{bmatrix} \begin{Bmatrix} \ddot{\theta}_h \\ \ddot{y}_1 \end{Bmatrix} + \begin{bmatrix} 0 & 0 \\ 0 & c_1 \end{bmatrix} \begin{Bmatrix} \dot{\theta}_h \\ \dot{y}_1 \end{Bmatrix} + \begin{bmatrix} 0 & 0 \\ 0 & k_{eq} \end{bmatrix} \begin{Bmatrix} \theta_h \\ y_1 \end{Bmatrix} = \begin{bmatrix} 1 & L & 0 \\ 0 & 1 & 1 \end{bmatrix} \begin{Bmatrix} F_{h/1} \\ u_{m_1} \\ u_a \end{Bmatrix} \quad (4.8)$$

$$F_{2/1} = m_2 \ddot{y}_2 + c_2 \dot{y}_2 + k_2 y_2 + m_2 \ddot{y}_1 \quad (4.9)$$

Equation (4.7) corresponds to the rotatory hub's dynamics, Eq. (4.8) to the Appendage 1 dynamics and Eq. (4.9) to the Appendage 2 dynamics. The parameter $k_{eq} = 12EI/l^3$ is the equivalent stiffness at the end of the beam. Thus, for the Appendage 1 dynamics, $[Z_1(s)]$ is a second order transfer and can be represented by the following equivalent DP forms:

- The state-space representation associated to the state $x = \{y_1 \quad \dot{y}_1\}^T$, with the input-

s/outputs depicted in Fig. 4.6:

$$\begin{bmatrix} \dot{y}_1 \\ \ddot{y}_1 \\ \ddot{y}_{abs} \\ F_{1/h} \end{bmatrix} = \left[\begin{array}{cc|cc} 0 & 1 & 0 & 0 \\ -k_{eq}/m_1 & -c_1/m_1 & 1/m_1 & -L \\ -k_{eq}/m_1 & -c_1/m_1 & 1/m_1 & 0 \\ k_{eq}L & c_1L & 0 & -J_1 \end{array} \right] \begin{bmatrix} y_1 \\ \dot{y}_1 \\ F_{2/1} = u_{m_1} \\ \ddot{\theta}_h \end{bmatrix} \quad (4.10)$$

- The matrix of transfers between the acceleration-load transmission at points P and C :

$$[Z_1(s)] = \frac{\begin{bmatrix} s^2 & L(k_{eq} + c_1s) \\ L(k_{eq} + c_1s) & -(J_1m_1s^2 + c_1(m_1L^2 + J_1)s + k_{eq}(m_1L^2 + J_1)) \end{bmatrix}}{m_1s^2 + c_1s + k_{eq}} \quad (4.11)$$

where the pulsations $\omega_f = \sqrt{\frac{k_{eq}(m_1L^2 + J_1)}{J_1m_1}}$ and $\omega_{pc} = \sqrt{\frac{k_{eq}}{m_1}}$ can be distinguished as the zero and pole pulsations respectively. The pulsation ω_f is the free pulsation of Appendage 1, whereas ω_{pc} is the *parent cantilevered* pulsation; i.e, when the disc J_1 is clamped to the inertial frame and it cannot rotate.

Equations (4.10) and (4.11) can be represented by the block diagram depicted in Fig. 4.6. The lower channel of $[Z_1(s)]$ (from $\ddot{\theta}_h$ to $F_{1/h}$) is equivalent to the *inverse dynamic model* and can be expressed in kg·m and the upper channel of $[Z_1(s)]$ (from $F_{2/1}$ to \ddot{y}_{abs}) is equivalent to the *direct dynamic model* and can be expressed in kg⁻¹. Regarding the overlapping mechanism, the interactions with other substructures are carried by the channels wired to other blocks. These interactions are in fact the constraints or boundary conditions on the inputs of the $[Z_1(s)]$ block. Since both channels are invertible, two additional models can be extracted:

- The inversion of the upper channel, $[Z_1(s)]^{-1u}$, gives the inverse dynamic model of Appendage 1, where applied forces can be computed from the induced accelerations:

$$[Z_1(s)]^{-1u} / \begin{bmatrix} \dot{y}_1 \\ \ddot{y}_1 \\ F_{2/1} \\ F_{1/h} \end{bmatrix} = \left[\begin{array}{cc|cc} 0 & 1 & 0 & 0 \\ 0 & 0 & 1 & -L \\ k_{eq} & c_1 & m_1 & 0 \\ k_{eq}L & c_1L & 0 & -J_1 \end{array} \right] \begin{bmatrix} y_1 \\ \dot{y}_1 \\ \ddot{y}_{abs} \\ \ddot{\theta}_h \end{bmatrix}. \quad (4.12)$$

- The inversion of the lower channel, $[Z_1(s)]^{-1l}$, which gives the direct dynamic model of Appendage 1, where the resulting accelerations can be computed from the applied forces:

$$[Z_1(s)]^{-1l} / \begin{bmatrix} \dot{y}_1 \\ \ddot{y}_1 \\ \ddot{y}_{abs} \\ \ddot{\theta}_h \end{bmatrix} = \left[\begin{array}{cc|cc} 0 & 1 & 0 & 0 \\ -\omega_f^2 & -c_1\omega_f^2/k_{eq} & \frac{J_1+m_1L^2}{J_1m_1} & L/J_1 \\ -k_{eq}/m_1 & -c_1/m_1 & \frac{J_1+m_1L^2}{J_1m_1} & 0 \\ k_{eq}L/J_1 & c_1L/J_1 & 0 & -1/J_1 \end{array} \right] \begin{bmatrix} y_1 \\ \dot{y}_1 \\ F_{2/1} \\ F_{1/h} \end{bmatrix}. \quad (4.13)$$

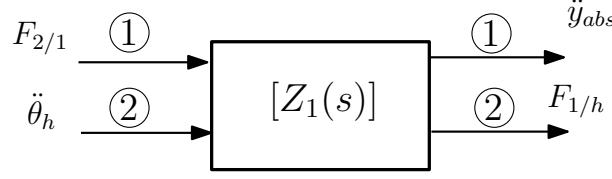


Figure 4.6: Block diagram representation of the DP model of Appendage 1, $Z_1(s)$

The lower channel inversion in Eq. (4.13) is the most used form in control design since it provides the dynamic response for the applied external forces $F_{2/1}$ and $F_{1/h}$. The matrix of transfers can be written as follows:

$$[Z_1(s)]^{-1_l} = \frac{\begin{bmatrix} \frac{J_1+m_1L^2}{J_1}(J_1s^2 + cL^2s + k_{eq}L^2) & -L(k_{eq} + c_1s) \\ L\frac{J_1+m_1L^2}{J_1}(k_{eq} + c_1s) & -(m_1s^2 + c_1s + k_{eq}) \end{bmatrix}}{J_1m_1s^2 + (J_1 + m_1L^2)c_1s + (J_1 + m_1L^2)k_{eq}} \quad (4.14)$$

In Eq. (4.14) the *child cantilevered* pulsation $\omega_{cc} = \sqrt{\frac{k_{eq}L^2}{J_1}}$ (when mass m_1 is clamped in the inertial frame) can be found as a zero of the transfer $F_{2/1} \rightarrow \ddot{y}_{abs}$. The free pulsation ω_f appears as a pole in this case and the *parent cantilevered* pulsation ω_{pc} appears as a zero of the transfer $F_{1/h} \rightarrow \ddot{\theta}_h$. These pulsations are consistent with [Preumont 11], where it is stated that transmission zeros are identical to the natural frequencies of a modified system in which a support has been added instead of an actuator. Consequently, when the transfer $F_{2/1} \rightarrow \ddot{y}_{abs}$ is observed, the transmission zeros are the same ones as if the system was clamped at the DOF \ddot{y}_1 .

The DP model together with the inversion operations allow the management of various constraints and boundary conditions. Indeed, these constraints and boundary conditions must be specified on the inputs of the subsystem model. The following conditions can be imposed:

- The substructure is clamped to the parent structure and loaded or connected to another substructure on the side of the child structure. In this case, the DP model of Eq. (4.10), $[Z_1(s)]$, can be used directly.
- The substructure is clamped to the child structure and loaded or connected to another substructure on the side of the parent structure. This case is provided by the inverse DP model of Eq. (4.10), $[Z_1(s)]^{-1}$.
- The substructure is clamped to the parent structure and to the child structure. This case is solved by using the upper channel inversion model $[Z_1(s)]^{-1_u}$. The forces are now free outputs and they represent the lock force.
- The substructure is loaded at both connection points. This case is solved by using the lower channel inversion model $[Z_1(s)]^{-1_l}$. The accelerations are now free outputs and they can be used to compute the system's trajectory.

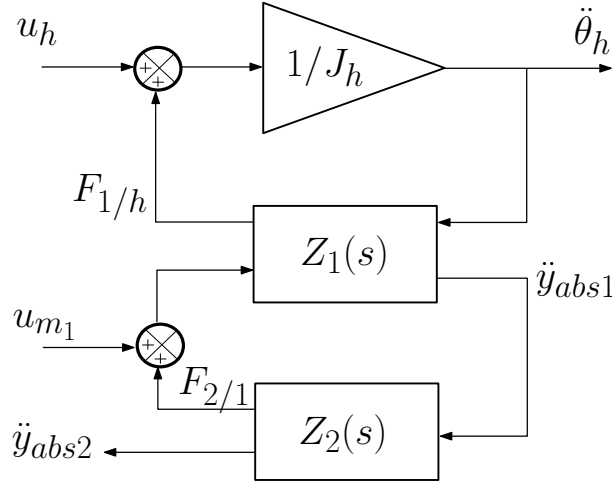


Figure 4.7: Block diagram representation of the interconnection among the different system's substructures

In order to model the whole system, the dynamics of the hub and Appendage 2 must be expressed in terms of acceleration-load transfer. However, the hub and Appendage 2 cannot be modeled with DP form since they are only connected to Appendage 1, being considered as terminal substructures (one connection point only). An analog acceleration-load transfer can be build for the one-connection-point case, which in the case of the hub it results in a static gain:

$$\ddot{\theta}_h = \begin{bmatrix} 1/J_h & 1/J_h \end{bmatrix} \begin{Bmatrix} u_h \\ F_{1/h} \end{Bmatrix} \quad (4.15)$$

For Appendage 2, it results in a Single-Input Single-Output (SISO) system which receives the acceleration at the base and gives the induced force at the connection point:

$$\begin{bmatrix} Z_2(s) \end{bmatrix} / \begin{Bmatrix} \dot{y}_2 \\ \ddot{y}_2 \\ \ddot{y}_{abs2} \\ F_{2/1} \end{Bmatrix} = \left[\begin{array}{cc|c} 0 & 1 & 0 \\ -k_2/m_2 & -c_2/m_2 & -1 \\ -k_2/m_2 & -c_2/m_2 & 0 \\ k_2 & c_2 & 0 \end{array} \right] \begin{Bmatrix} y_2 \\ \dot{y}_2 \\ \ddot{y}_1 \end{Bmatrix} \quad (4.16)$$

Then, the model of the flexible pointing system presented in Fig. 4.4 can be described by a block diagram interconnection (see Fig. 4.7) involving three blocks: $1/J_h$, Z_1 and $Z_2(s)$. The interactions among these three blocks are directly transmitted by the channels between the blocks as accelerations-loads. The interconnection presented in Fig. 4.7 results in the direct dynamic model of the flexible pointing system. The corresponding inversions in the upper or lower channels can be performed as well in order to impose different constraints or boundary conditions to the whole system.

4.3 Substructure's EOM Manipulation

The interconnection mechanism and consequently the desired input/outputs of the substructure's model have been established in Sec 4.2. Nevertheless, the mechanism requires a formulation in which the invert and direct dynamics of the substructure can be extracted without losing the flexible and rigid motion behavior. This implies a formulation of the equations of motion which allows establishing the correct relation between applied forces and accelerations to the substructure under study.

Since it is generally assumed that the existence of damping does not cause coupling of the undamped natural modes of vibration [Hurty 65], Eq. (4.1) can be rewritten in an undamped form:

$$[M] \{\ddot{q}\} + [K] \{q\} = \{F\} \quad (4.17)$$

Equation (4.17) will be used across this section to apply the different possibilities in EOM manipulation. In this research the re-formulation of the equations of motion has been studied through component modal synthesis techniques, particularly those techniques based on constraint and fixed-interface modes for substructure coupling. Three re-formulations have been analyzed in order to choose the most appropriate one: the Hurty's Method [Hurty 65], the Craig-Bampton decomposition [Craig 68] and the Imbert's Method [Imbert 79, Alazard 08]. These methods are discussed in the following sections.

4.3.1 Hurty's Method

The Hurty's Method [Hurty 65] proposes a component modes synthesis method using rigid-body modes, redundant-interface constraint modes and fixed-constraint modes. If the substructure is not constrained, six independent rigid-body displacements modes exist, corresponding to three translations and three rotations with respect to a set of fixed orthogonal coordinate axes (the set $\mathcal{R} = \{r_i\}$). The modes produced in this way are called rigid-body modes. Fewer than six rigid modes may exist if the substructure is partially or totally constrained. The constrained system is statically indeterminate with the redundant constraints (denoted by the set $\mathcal{E} = \{e_i\}$). These constraints are the cause of the attachment to other substructures of the system, and they produce the called constraint modes. Finally, the displacements of other points of the structure relative to the constraints are given by a set of independent modes in which all constraints are fixed, called fixed-constraint natural modes of vibration of the structure (set $\mathcal{I} = \{i_i\}$). Therefore, an arbitrary displacement of the constraints can be divided into rigid-body, constrained and fixed-constraint displacements.

This decomposition is exemplified in Fig. 4.8, where the different displacements are shown for a rectangular plate at the middle point A . In three dimensions, the plate has six rigid degrees of freedom (three displacements, three rotations) and they are determined by the set r_i , located at the front corners of the plate. The displacements of point A can be derived using

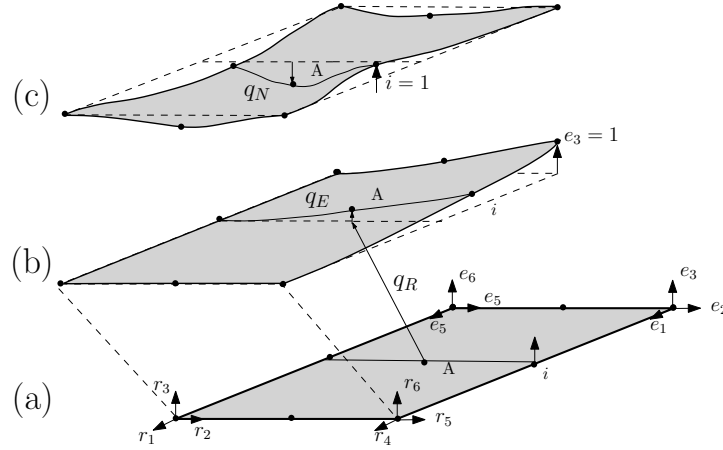


Figure 4.8: Decomposition of a substructure's displacements; adapted from [Hurty 65]

the theory of solid mechanics (Fig. 4.8-a). If these DOF are constrained, the plate cannot translated as a rigid body and the remaining possible displacements are the ones given by the theory of elasticity. If the plate is redundantly constrained in the remaining two corners, the set e_i , the motion of the plate given by the elasticity theory will vary since the boundary conditions are no longer the same. For example, if the displacement e_3 is set to 1, point A will be displaced according to the plate's corner bending (Fig. 4.8-b). Either constrained or unconstrained, there are always interior points, denoted by i , which can move according to elasticity theory if a load is applied on them. If a displacement is imposed at the interior point i , point A will move accordingly (Fig. 4.8-c).

Consequently, the displacement of any point $P(x, y, z)$ is given by the the superposition of these three displacements:

$$\bar{q}(x, y, z) = \bar{q}_R(x, y, z) + \bar{q}_E(x, y, z) + \bar{q}_N(x, y, z) \quad (4.18)$$

When the equations of motion are obtained with FE analysis, which is the case in this study, the substructure is discretized so that the displacements are defined at only a set of points. In this case the displacement at each point can be written as a component of a column vector, and Eq. (4.18) becomes:

$$\{q\} = \{q_r\} + \{q_e\} + \{q_n\} \quad (4.19)$$

The number of coordinates in these sets are N_r for rigid-body modes, N_e for redundant constraint modes and N_n for natural vibration modes, respectively, with $N = N_r + N_e + N_n$. In component-mode synthesis, each of these displacements is expressed as a superposition of discretized mode functions in the form of modal matrices $[\bar{\phi}]$ and a set of generalized coordinates $\{\eta\}$. Thus, the term $[\bar{\phi}_{ij}]$ represents the displacement at point i in the j th mode. Consequently the three types of displacements take the following matrix form in what is called

the Rayleigh-Ritz coordinate transformation:

$$\begin{aligned}\{q_r\} &= [\bar{\phi}^R] \{\eta_r\} \\ \{q_e\} &= [\bar{\phi}^E] \{\eta_e\} \\ \{q_n\} &= [\bar{\phi}^N] \{\eta_n\}\end{aligned}\tag{4.20}$$

The substructure's physical displacements can be expressed in terms of substructure generalized coordinates $\{\eta\}$ by the substituting Eq. (4.20) into Eq. (4.19). Then, the total displacement may be written as

$$\{q\} = [\bar{\phi}] \{\eta\}\tag{4.21}$$

where the complete transformation matrix reads as follows:

$$[\bar{\phi}] = [\bar{\phi}^N \quad \bar{\phi}^E \quad \bar{\phi}^R]\tag{4.22}$$

The component-mode matrix $[\bar{\phi}]$ is a matrix of preselected component modes including: fixed-constraint modes, constraint modes and rigid-body modes. Then the matrix $[\bar{\phi}]$ is obtained as follows:

- a) Using a set of N_n substructure fixed-constraint normal modes, $[\bar{\phi}^N]$, obtained from the solution of the eigenproblem:

$$[K_{nn} - \omega_j^2 M_{nn}] \{\phi_n\}_j = [0], \quad j = 1, 2, \dots, N_n\tag{4.23}$$

$$[\bar{\phi}^N]_{N \times N_n} = \begin{bmatrix} \phi_{nN} \\ 0_{eN} \\ 0_{rN} \end{bmatrix}\tag{4.24}$$

- b) Using a set of redundant constraint modes, defined relative to the redundant boundary coordinate set:

$$[\bar{\phi}^E]_{N \times N_e} \equiv \begin{bmatrix} \phi_{ne} \\ I_{ee} \\ 0_{re} \end{bmatrix} = \begin{bmatrix} -K_{nn}^{-1} K_{ne} \\ I_{ee} \\ 0_{re} \end{bmatrix}\tag{4.25}$$

- c) Using a set of rigid-body modes, obtained by solving the equation resulting from restraining the rigid-body motion of the substructure:

$$\begin{bmatrix} \bar{\phi}^R \\ \bar{\phi}^E \end{bmatrix}_{N \times N_r} \equiv \begin{bmatrix} \phi_{nr} \\ \phi_{er} \\ I_{rr} \end{bmatrix} = \begin{bmatrix} - \begin{bmatrix} K_{nn} & K_{ne} \\ K_{en} & K_{ee} \end{bmatrix}^{-1} \begin{bmatrix} K_{nr} \\ K_{er} \end{bmatrix} \\ I_{rr} \end{bmatrix} \quad (4.26)$$

The set of N_n fixed - interface normal modes can be reduced to a smaller set of kept normal modes, denoted as $[\phi_k]$. The combined set $[\bar{\phi}^R \ \bar{\phi}^E]$ spans the static response of the substructure to interface loading and allows for arbitrary interface displacements $\{q_b\}$. These interface displacements can be accompanied by the displacements of the interior of the substructure as shown in Fig. 4.8.

As a consequence of classifying the modes in three categories, namely, rigid-body modes, constraint modes, and normal modes, the Eq. (4.17) can be partitioned as follows:

$$\begin{bmatrix} M_{nn} & M_{ne} & M_{nr} \\ M_{en} & M_{ee} & M_{er} \\ M_{rn} & M_{re} & M_{rr} \end{bmatrix} \begin{Bmatrix} \ddot{q}_n \\ \ddot{q}_e \\ \ddot{q}_r \end{Bmatrix} + \begin{bmatrix} K_{nn} & K_{ne} & K_{nr} \\ K_{en} & K_{ee} & K_{er} \\ K_{rn} & K_{re} & K_{rr} \end{bmatrix} \begin{Bmatrix} q_n \\ q_e \\ q_r \end{Bmatrix} = \begin{Bmatrix} F_n \\ F_e + \tilde{F}_e \\ F_r + \tilde{F}_r \end{Bmatrix} \quad (4.27)$$

where $[M]$, $[K]$, $\{q\}$ and $\{F\}$ are the substructure's mass matrix, stiffness matrix, vector of generalized coordinates and vector of externally applied forces, respectively. The “tilde” load term denotes the force resulting from the connection to adjacent structures at the boundary points [Craig Jr 00]. Applying the modal transformation given in Eq. (4.21) and pre-multiplying by $[\bar{\phi}^T]$, and considering that neither interior forces nor external forces apply ($F_n = F_e = F_r = 0$) Eq. (4.27) yields:

$$\begin{bmatrix} \hat{M}_{nn} & \hat{M}_{ne} & \hat{M}_{nr} \\ \hat{M}_{en} & \hat{M}_{ee} & \hat{M}_{er} \\ \hat{M}_{rn} & \hat{M}_{re} & \hat{M}_{rr} \end{bmatrix} \begin{Bmatrix} \ddot{\eta}_n \\ \ddot{\eta}_e \\ \ddot{\eta}_r \end{Bmatrix} + \begin{bmatrix} \hat{K}_{nn} & \hat{K}_{ne} & \hat{K}_{nr} \\ \hat{K}_{en} & \hat{K}_{ee} & \hat{K}_{er} \\ \hat{K}_{rn} & \hat{K}_{re} & \hat{K}_{rr} \end{bmatrix} \begin{Bmatrix} \eta_n \\ \eta_e \\ \eta_r \end{Bmatrix} = \begin{Bmatrix} 0 \\ \tilde{F}_e \\ \tilde{F}_r + \phi_{er}^T \tilde{F}_e \end{Bmatrix} \quad (4.28)$$

Equation (4.28) is the partitioned transformed form of the equations of motion. It should be noted that for the transformed stiffness matrix several submatrices are null matrices. The submatrix $[\hat{K}_{rr}]$ is null since the work done by a self-equilibrating force system on a rigid-body displacement is zero [Hurty 65]. The same occurs to the submatrix $[\hat{K}_{en}]$ since the work done by the constraint forces on a normal mode displacement is zero because in normal mode the constraints are fixed. In the same way, submatrix $[\hat{K}_{er}]$ is a null matrix.

In consequence of the foregoing results, the partitioned transformed equation of motion takes on a simpler form:

$$\begin{bmatrix} \hat{M}_{nn} & \hat{M}_{ne} & \hat{M}_{nr} \\ \hat{M}_{en} & \hat{M}_{ee} & \hat{M}_{er} \\ \hat{M}_{rn} & \hat{M}_{re} & \hat{M}_{rr} \end{bmatrix} \begin{Bmatrix} \ddot{\eta}_n \\ \ddot{\eta}_e \\ \ddot{\eta}_r \end{Bmatrix} + \begin{bmatrix} \hat{K}_{nn} & 0 & 0 \\ 0 & \hat{K}_{ee} & 0 \\ 0 & 0 & 0 \end{bmatrix} \begin{Bmatrix} \eta_n \\ \eta_e \\ \eta_r \end{Bmatrix} = \begin{Bmatrix} 0 \\ \tilde{F}_e \\ \tilde{F}_r + \phi_{er}^T \tilde{F}_e \end{Bmatrix} \quad (4.29)$$

Equation (4.29) presents then submatrices which are more attractive for modeling purposes since the stiffness matrix is no longer coupled with the rigid body motion. Physical interpretations can be derived from several submatrices. The square submatrix $[\hat{K}_{nn}]$ is a diagonal matrix containing the fixed-constraint natural vibration modes, and related with $[\hat{M}_{nn}]$ by the relationship of Eq. (4.23). The square submatrix $[\hat{K}_{ee}]$ is the stiffness matrix associated with the redundant constraints, and its order is equal to the number of redundant constraints. The square matrix $[\hat{M}_{rr}]$ is the rigid body matrix; i.e, the mass matrix if the substructure is considered as rigid. It contains the whole mass of the system, gravity center position and rotatory inertia with respect to the rigid body boundaries. The submatrices $[\hat{M}_{rn}]$ and $[\hat{M}_{re}]$ are the modal participation matrices of the natural modes and constraint boundaries on the rigid-body motion ; i.e, how the natural modes and constraint boundaries affect the rigid dynamics.

If damping is taken into account, the damping matrix $[D]$ may be partitioned in the same way as the mass and stiffness matrices:

$$[\hat{D}] = \begin{bmatrix} \hat{D}_{nn} & \hat{D}_{ne} & \hat{D}_{nr} \\ \hat{D}_{en} & \hat{D}_{ee} & \hat{D}_{er} \\ \hat{D}_{rn} & \hat{D}_{re} & \hat{D}_{rr} \end{bmatrix} \quad (4.30)$$

In general, all of the submatrices are not null as in the case of the mass matrix. However, if all damping forces are internal, then rigid body motions are not damped and in this case the third row and the third column of Eq. (4.30) are null matrices [Hurty 65]. In this case, Eq. (4.29) is written with viscous damping as:

$$\begin{bmatrix} \hat{M}_{nn} & \hat{M}_{ne} & \hat{M}_{nr} \\ \hat{M}_{en} & \hat{M}_{ee} & \hat{M}_{er} \\ \hat{M}_{rn} & \hat{M}_{re} & \hat{M}_{rr} \end{bmatrix} \begin{Bmatrix} \ddot{\eta}_n \\ \ddot{\eta}_e \\ \ddot{\eta}_r \end{Bmatrix} + \begin{bmatrix} \hat{D}_{nn} & \hat{D}_{ne} & 0 \\ \hat{D}_{en} & \hat{D}_{ee} & 0 \\ 0 & 0 & 0 \end{bmatrix} \begin{Bmatrix} \dot{\eta}_n \\ \dot{\eta}_e \\ \dot{\eta}_r \end{Bmatrix} + \begin{bmatrix} \hat{K}_{nn} & 0 & 0 \\ 0 & \hat{K}_{ee} & 0 \\ 0 & 0 & 0 \end{bmatrix} \begin{Bmatrix} \eta_n \\ \eta_e \\ \eta_r \end{Bmatrix} = \begin{Bmatrix} 0 \\ \tilde{F}_e \\ \tilde{F}_r + \phi_{er}^T \tilde{F}_e \end{Bmatrix} \quad (4.31)$$

Equation (4.31) is the final form of the EOM transformed with the Hurty's Method. This equation shows a clear distinction between the rigid body motion, the redundant constraint motion and the fixed-constraint modes. Since the rigid-body motion's contribution to the stiffness matrix has been uncoupled, it is easy to establish a relation between the interconnection loads and transmitted accelerations, as desired in a DP model.

4.3.2 The Craig-Bampton's Method

The Craig-Bampton's Method [Craig 68] is a simplification of the Hurty's Method. It considers the rigid-body modes and the redundant-constraint modes as a single block, simplifying the transformation process. Following the dynamic substructuring explained in [Craig 68], the set of the substructure's DOF, noted as $\{q\}$ can be partitioned in two sets: interfaced or

supported boundary nodes (j index) and the interior elastic nodes (i index). Therefore the corresponding dynamic matrices vectors can be rewritten in this case as follows:

$$\{q\} = \begin{Bmatrix} q_i \\ q_j \end{Bmatrix} \quad \{F\} = \begin{Bmatrix} F_i \\ F_j \end{Bmatrix} \quad [K] = \begin{bmatrix} K_{ii} & K_{ij} \\ K_{ij}^T & K_{jj} \end{bmatrix} \quad [M] = \begin{bmatrix} M_{ii} & M_{ij} \\ M_{ij}^T & M_{jj} \end{bmatrix} \quad (4.32)$$

The Craig-Bampton transformation transforms the set of elastic physical coordinates $\{q_i\}$ to a set of modal coordinates $\{\eta_m\}$ as in the Hurty's method. The set of physical coordinates $\{q\}$ is transformed to a hybrid set of physical coordinates at the interface, $\{q_j\}$, and modal coordinates at the interior, $\{\eta_m\}$, as stated in Eq. (4.33). Thus, the coordinate transformation can be written as:

$$\{q\} = \begin{Bmatrix} q_i \\ q_j \end{Bmatrix} = \begin{bmatrix} \phi_{ij} & \varphi_{im} \\ I & 0 \end{bmatrix} \begin{Bmatrix} q_j \\ \eta_m \end{Bmatrix} = [\Psi] \begin{Bmatrix} q_j \\ \eta_m \end{Bmatrix} \quad (4.33)$$

with the Craig-Bampton Transformation $[\Psi]$ which can be partitioned as:

$$[\Psi] = [\Phi_j \quad \Phi_m]; \quad \Phi_j = \begin{bmatrix} \phi_{ij} \\ I \end{bmatrix} \quad \Phi_m = \begin{bmatrix} \varphi_{im} \\ 0 \end{bmatrix} \quad (4.34)$$

where $[\Phi_j]$ is usually referred to as the Interface Node Functions and $[\Phi_m]$ to as the Fixed Base Mode Shapes [Young 00]. These modes are similar to the ones employed in the Hurty's method but with the difference that this time there is no distinction between rigid-body modes and fixed-constraint modes:

- The Interface Node Functions, $[\Phi_j]$, where $[\phi_{ij}]$ is the Static Constraint Modes Matrix, relate physical displacements at the interface, $\{q_j\}$, to physical displacements of the elastic degrees of freedom, $\{q_i\}$. It describes the static response of the substructure to excitation coming from neighbouring substructures through the interface degrees of freedom. It can be obtained by the following expression, obtained with the static problem of Eq. (4.1):

$$[\phi_{ij}] = -K_{ii}^{-1} K_{ij} \quad (4.35)$$

Rigid modes are embedded in these functions. Thus, for a substructure with an isostatic interface (exactly 6 degrees of freedom) the Static Constraint Modes Matrix will lapse into the rigid modes matrix at the interface point.

- The Fixed Base Mode Shapes, $[\Phi_m]$, with $[\varphi_{im}]$ relating the modal responses $\{\eta_m\}$ to

the physical displacements of the elastic degrees of freedom $\{q_i\}$. They have the same meaning as the fixed-constraint modes in the Hurty's method. They are obtained from the equations of motion with the interface degrees of freedom ($q_j = 0$) constrained and with no force acting in the interior points ($F_i = 0$):

$$[K_{ii}] [\varphi_{im}] = \omega^2 [M_{ii}] [\varphi_{im}] \quad (4.36)$$

Solving the substructure eigenvalues ω^2 and mode shapes $[\varphi_{im}]$ the transformation of physical displacements to modal responses is accomplished by the relation $\{q_i\} = [\Phi_{ij}]\{q_j\} + [\varphi_{im}]\{\eta_m\}$.

The Craig-Bampton method rewrites the substructure motion in Eq. (4.17) from the set of physical coordinates to a set of coordinates consisting of physical coordinates of physical interface points and modal or generalized coordinates, so the equation of motion of a linear substructure is:

$$\begin{bmatrix} M_{ii} & M_{ij} \\ M_{ij}^T & M_{jj} \end{bmatrix} \begin{Bmatrix} \ddot{q}_i \\ \ddot{q}_j \end{Bmatrix} + \begin{bmatrix} K_{ii} & K_{ij} \\ K_{ij}^T & K_{jj} \end{bmatrix} \begin{Bmatrix} q_i \\ q_j \end{Bmatrix} = \begin{Bmatrix} F_i \\ F_j \end{Bmatrix} \quad (4.37)$$

Equation (4.37) can be rewritten using the Craig-Bampton Transformation Matrix Ψ and obtaining a new linear system in terms of the physical boundary displacements q_j and generalized coordinates η_m . Therefore, introducing (4.33) in Eq. (4.37), pre-multiplying by Ψ^T the equation becomes:

$$\begin{bmatrix} \bar{M}_{jj} & \bar{M}_{jm} \\ \bar{M}_{jm}^T & m_m \end{bmatrix} \begin{Bmatrix} \ddot{q}_j \\ \ddot{\eta}_m \end{Bmatrix} + \begin{bmatrix} \bar{K}_{jj} & 0 \\ 0 & k_m \end{bmatrix} \begin{Bmatrix} q_j \\ \eta_m \end{Bmatrix} = \begin{Bmatrix} \phi_{ij}^T F_i + F_j \\ \varphi_{im}^T F_i \end{Bmatrix} \quad (4.38)$$

Equation (4.38) decouples the interior elastic nodes stiffness contribution from the interface nodes stiffness contribution, which is useful for establishing an acceleration-load transfer between boundaries. This decoupling is similar to the one expressed in Eq. (4.31) by the Hurty's Method, but in this case interface nodes contain the rigid body motion and the redundant constraint motion.

4.3.3 Imbert's Method or Effective Mass Method

The Imbert's Method has been the first component modes technique used in automatic control modeling [Imbert 79, Alazard 08]. It can be considered as a simplification of either the Craig-Bampton's Method or the Hurty's Method. In this case the interface node functions, $[\Phi_j]$,

only consider the isostatic case (three degrees of freedom for a 2D problem, six degrees of freedom for a 3D problem) the static constraint modes matrix $[\phi_{ij}]$ lapses into the rigid modes matrix at the connection point, making $j = r$, what leads to the following rigid body modes:

$$[\phi_{ir}] = -K_{ii}^{-1}K_{ir} \quad (4.39)$$

With the same process as in the Craig-Bampton's Method in Sec 4.3.2, the EOM can be partitioned in rigid body DOF and interior DOF:

$$\begin{bmatrix} M_{ii} & M_{ir} \\ M_{ir}^T & M_{rr} \end{bmatrix} \begin{Bmatrix} \ddot{q}_i \\ \ddot{q}_r \end{Bmatrix} + \begin{bmatrix} K_{ii} & K_{ir} \\ K_{ir}^T & K_{rr} \end{bmatrix} \begin{Bmatrix} q_i \\ q_r \end{Bmatrix} = \begin{Bmatrix} F_i \\ F_r \end{Bmatrix} \quad (4.40)$$

Equation (4.40) is rewritten using the Imbert Transformation Matrix $[\Psi]$ (with the same form as the Craig-Bampton's one but with using $[\phi_{ir}]$ instead) and obtaining a new linear system in terms of the physical boundary displacements associated to the rigid body motion, $\{q_r\}$, and generalized coordinates $\{\eta_m\}$. Therefore, introducing Eq. (4.33) in Eq. (4.40), pre-multiplying by $[\Psi^T]$ the equation becomes:

$$\begin{bmatrix} \bar{M}_{rr} & \bar{M}_{rm} \\ \bar{M}_{rm}^T & m_m \end{bmatrix} \begin{Bmatrix} \ddot{q}_r \\ \ddot{\eta}_m \end{Bmatrix} + \begin{bmatrix} 0 & 0 \\ 0 & k_m \end{bmatrix} \begin{Bmatrix} q_r \\ \eta_m \end{Bmatrix} = \begin{Bmatrix} \phi_{ir}^T F_i + F_r \\ \varphi_{im}^T F_i \end{Bmatrix} \quad (4.41)$$

In this case the resulting term $[K_{jj}] = [K_{rr}]$ is null for the same reasons explained in Sec 4.3.1. With this formulation, only interactions between the rigid body motion and the interior body motion can be analyzed, since the redundant constraint motion is not considered in this method.

4.3.4 EOM's Transformations Discussion

Three component modes synthesis techniques using fixed-interface modes for substructure coupling have been presented throughout this section: the Hurty's Method, the Craig - Bampton's Method and the Imbert's Method. In this section, the three transformations are evaluated in order to choose the most suitable one for flexible substructure model derivation.

The Imbert's Method has been the most used EOM form for flexible substructure modeling until now. The studies [Alazard 08, Guy 14] have been based on this form of EOM's transformation in order to evaluate the loads of a flexible appendage connected to a central rigid body. It offers means for the parameterization of the substructure since the transformation shows the substructure's rigid body matrix $[M_{rr}]$ and the natural frequencies $[k_m]$. However, this kind of transformation only allows the assembly of FMS in star-like structures

or chain-like structures where only the last appendage can be flexible. Indeed, redundant constraint motion is not taken into account. As this study aims at assembling FMS with flexible substructures in chain-like structure, this transformation is not suitable for a DP form.

The Craig-Bampton's Method is largely used in FE substructuring techniques [Craig Jr 00] since it takes into account the physical displacements of the interface for both the isostatic and not-isostatic constraints. Nevertheless, the embedding of the rigid modes in the Interface Nodes Functions $[\Phi_j]$ makes more difficult the task of distinguishing the rigid body motion from the redundant constraint motion. This formulation also complicates the finding of the rigid body matrix for parameterization. The interface DOF $\{q_j\}$ are coupled and the resulting EOM is more difficult to manipulate to build a DP model. An additional manipulation is needed in order to impose a rigid body constraint among the displacements $\{q_j\}$, as performed in [Perez 15a], making the transformation even more tedious.

The Hurty's Method is the most general approach for EOM transformation. Indeed, all the previous methods can be derived from it with the pertinent simplifications. In addition, it offers a clear distinction between the motions that will be assigned to a DP model: rigid body motion, redundant constraint motion and interior displacements. The stiffness and damping matrices are decoupled and the rigid-body motion can be transferred from one point to another without additional manipulation since the transformation naturally includes this constraint. The rigid body matrix $[M_{rr}]$, fixed constraint frequencies $[K_{nn}]$ and the kinematic model from connection point P (parent structure) to connection point C (child structure), $[\phi_{er}]$ are accessible for future parameterization in integrated control/structure optimization.

Therefore, the Hurty's Method is the EOM's transformation which will be used for the FMS modeling proposed in this study. The choice is based on the trade-off between its generality and the possibilities of casting the uncoupled equations in a DP form. This form of EOM is used in order to derive the state-space representation of flexible substructures in Chap. 5.

This chapter has established the framework for FMS modeling. The kinematic description is done under the floating frame approach hypothesis. The interconnection among substructures (overlapping) is performed with the double-port approach, which allows the consideration of different constraints (boundary conditions) in the substructure using acceleration-load transfer. In order to find the most suitable EOM form for the double-port model, different component modes synthesis techniques have been pondered and the Hurty's Method has been selected. The following chapter uses the concepts developed here to explain the FMS modeling technique.

Chapter

5

Modeling of Flexible Multibody Structures
for Integrated Control/Structure Design

“There are no rules, no models; rather, there are no rules other than the general laws of Nature.”
- Victor Hugo

Contents

5.1	One Connection Point	58
5.2	Two Connection Points	61
5.3	Extension to Revolute joint	64
5.4	Extension to Piezoelectric Actuators	66
5.5	Implementation of Parametric Variations	71
5.5.1	Localization of Varying Parameters	71
5.5.2	Obtaining the LFT Model of the Substructure	73
5.5.3	Tunable Block Transformation	74
5.6	TITOP Modeling of Flexible Multibody Systems	74

With the modeling framework established in Chap. 4, the modeling technique for FMS is developed. FMS could have star-like or chain-like substructures, revolute joints or embedded piezoelectric actuators. A set of generic flexible substructure models are developed in order to provide all the required tools for automatic control and integrated design of FMS. These models conform the Two-Input Two-Output Port (TITOP) modeling technique, which allows the assembly of FMS for automatic linear control purposes.

THE properties of the partitioned equations of motion in Eq. (4.31), obtained in Sec. 4.3, can be used for simple, accurate and intuitive modeling of FMS. The advantages of this transformation are maximized when they are applied to build the model of a substructure with one connection point or two connection points with other substructures. More connection points are possible to model as well, but this case is not illustrated in this study since the connection complexity obliges to manipulate the FE model itself and the problem becomes rather a structural problem than a control modeling problem.

The different usages of Hurty's EOM are explained in this chapter. First, the case of one connection point is explained. Second, the case of two connection points is addressed. Third, the modeling case of a revolute joint at a connection point is described. Next, the method is expanded to take into account piezoelectric effects, allowing the modeling of piezo-actuated substructures. The parameterization possibilities are explained as well in order to gauge the potential of this modeling technique for integrated control/structure design. To conclude the chapter, the assembly technique of FMS is described.

5.1 One Connection Point

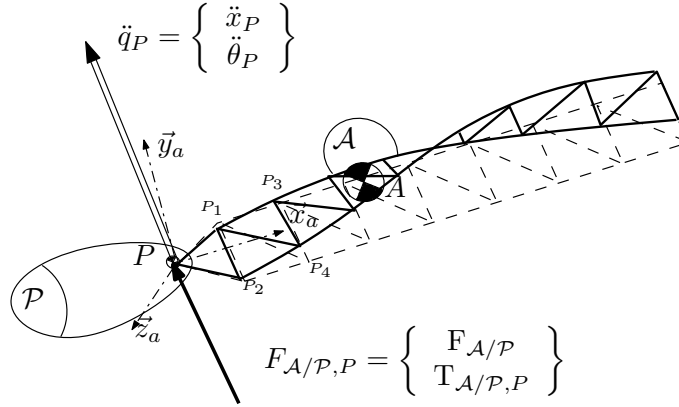
In this section, the modeling of a flexible substructure connected to another structure through one connection point is explained. As shown in Fig. 5.1, let us consider a flexible body (substructure) \mathcal{A} linked to the parent structure \mathcal{P} at the point P . It is assumed that the only external loads applied to \mathcal{A} are the interactions with \mathcal{P} at point P .

The problem is thus how to consider the coupling between structures \mathcal{P} and \mathcal{A} . As stated in Sec. 4.2, the coupling is made by an exchange between loads and accelerations through the connection point. Therefore, the coupling transfer between \mathcal{P} and \mathcal{A} is expressed as an acceleration-load transfer through the connection point P . Equation (4.31) offers the advantage of casting the FE Model of substructure \mathcal{A} in the state-space representation using accelerations and loads as inputs and outputs through the boundaries. This is possible thanks to the decoupling of the stiffness matrix when CMS transformation is performed. In the case of one connection point, there are no redundant constraint displacements besides the rigid-body displacements. This implies that the rigid body displacements (translations and rotations) are directly associated with point P , which constraints the substructure \mathcal{A} to be always fixed to \mathcal{P} , sharing the rigid-body motions of the ensemble. As there are not redundant constraint displacements, second row and second column of Eq. (4.31) can be removed leading to:

$$\begin{bmatrix} \hat{M}_{nn} & \hat{M}_{nr} \\ \hat{M}_{rn} & \hat{M}_{rr} \end{bmatrix} \begin{Bmatrix} \ddot{\eta}_n \\ \ddot{\eta}_r \end{Bmatrix} + \begin{bmatrix} \hat{D}_{nn} & 0 \\ 0 & 0 \end{bmatrix} \begin{Bmatrix} \dot{\eta}_n \\ \dot{\eta}_r \end{Bmatrix} + \begin{bmatrix} \hat{K}_{nn} & 0 \\ 0 & 0 \end{bmatrix} \begin{Bmatrix} \eta_n \\ \eta_r \end{Bmatrix} = \begin{Bmatrix} 0 \\ \tilde{F}_r \end{Bmatrix} \quad (5.1)$$

The coupling is established as an exchange acceleration-load through the connection point:

$$\{F_{\mathcal{A}/\mathcal{P},P}\} = [G_P^{\mathcal{A}}(s)] \{\ddot{q}_P\} \quad (5.2)$$

Figure 5.1: Substructure \mathcal{A} linked to structure \mathcal{P}

where $\{F_{\mathcal{A}/\mathcal{P},P}\}$ is the load transmitted to the structure \mathcal{P} by the appendage \mathcal{A} , $[G_P^{\mathcal{A}}(s)]$ is the linear model of the appendage \mathcal{A} when connected at point P , and $\{\ddot{q}_P\}$ the acceleration of the displacements, $\{\ddot{x}_P\}$, and rotations, $\{\ddot{\theta}_P\}$, at point P . In the 3D case, where 6 degrees of freedom are needed to describe rigid body motion, $[G_P^{\mathcal{A}}(s)]$ is a 6×6 transfer matrix (i.e. $r = 6$). The loads experienced by \mathcal{A} due to adjacent connections, $\{\tilde{F}_r\}$, are in the opposite direction of the loads experienced by \mathcal{P} , $\{F_{\mathcal{A}/\mathcal{P},P}\}$. Identifying terms of Eq. (5.2) with Eq. (5.1):

$$\{\tilde{F}_r\} = \{-F_{\mathcal{A}/\mathcal{P},P}\}; \quad \{\ddot{\eta}_r\} = \{\ddot{q}_P\}; \quad [\hat{M}_{rn}] = [L_P^T]; \quad [\hat{M}_{rr}] = [J_P^{\mathcal{A}}] \quad (5.3)$$

In the case of one connection point, normalized rigid-body accelerations are equal to the acceleration at point P . The matrix $[L_P]$ is the modal participation matrix of natural modes at point P ; i.e, it expresses how the motion of P is affected by the natural modes of vibration and vice-versa. The square matrix $[J_P^{\mathcal{A}}]$ is the direct dynamic model, at point P , of the substructure \mathcal{A} assumed rigid [Alazard 15] taking the following form for $r = 6$:

$$[J_P^{\mathcal{A}}] = [\tau_{AP}^T] \begin{bmatrix} m^{\mathcal{A}} I_3 & 0_3 \\ 0_3 & \mathbb{I}_A^{\mathcal{A}} \end{bmatrix} [\tau_{AP}] \quad (5.4)$$

where $m^{\mathcal{A}}$ is the substructure's total mass, $\mathbb{I}_A^{\mathcal{A}}$ is the substructure's total inertia at its mass center and matrix $[\tau_{AP}]$ is the kinematic model between the mass center of substructure \mathcal{A} , point A , and the connection point P , written as:

$$[\tau_{AP}] = \begin{bmatrix} I_3 & (*AP) \\ 0_3 & I_3 \end{bmatrix} \quad (5.5)$$

with $[(*AP)]$ being the skew-symmetric matrix associated to the vector $\{AP\}$. Considering that the natural vibration modes are normalized with respect to the mass matrix, the

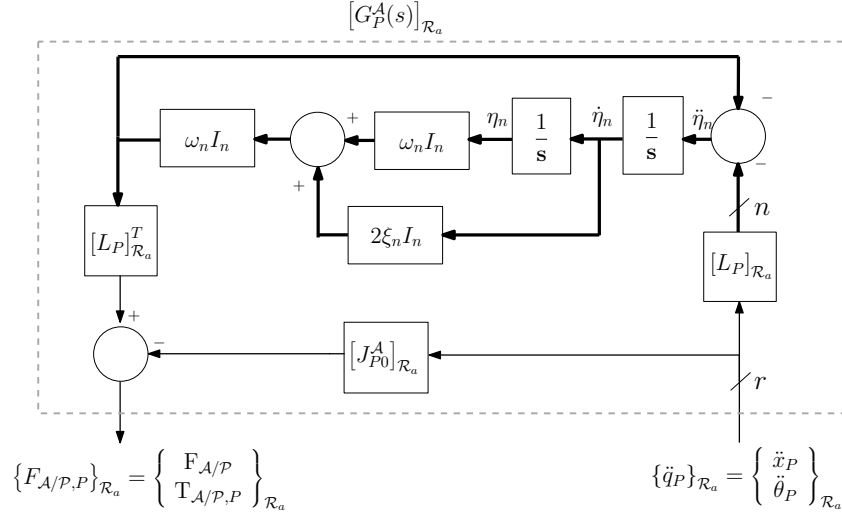


Figure 5.2: Block diagram representation of the connections of appendage \mathcal{A} , projected in the frame \mathcal{R}_a

submatrix $[\hat{M}_{nn}]$ becomes the identity matrix, $[\hat{K}_{nn}]$ is a diagonal matrix containing the natural modes (fixed-constraint natural frequencies squared, ω_n^2) and $[\hat{D}_{nn}]$ a diagonal matrix expressed with a damping ratio ξ_n . Consequently, the linear model of the appendage \mathcal{A} reads:

$$\left\{ \begin{array}{l} \left\{ \begin{array}{l} \dot{\eta}_n \\ \ddot{\eta}_n \end{array} \right\} = \begin{bmatrix} 0_n & I_n \\ -\omega_n^2 I_n & -2\omega_n \xi_n I_n \end{bmatrix} \left\{ \begin{array}{l} \eta_n \\ \dot{\eta}_n \end{array} \right\} + \begin{bmatrix} 0 \\ -L_P \end{bmatrix} \left\{ \ddot{q}_P \right\} \\ \left[F_{\mathcal{A}/\mathcal{P},P} \right] = L_P^T \begin{bmatrix} -\omega_n^2 I_n & -2\omega_n \xi_n I_n \end{bmatrix} \left\{ \begin{array}{l} \eta_n \\ \dot{\eta}_n \end{array} \right\} - \underbrace{\left[J_P^A - L_P^T L_P \right]}_{J_{P0}^A} \left\{ \ddot{q}_P \right\} \end{array} \right. \quad (5.6)$$

The physics lying within Eq. (5.6) can be interpreted from the control domain point of view. The rigid-body displacements of the appendage \mathcal{A} are transmitted by its connection point P through the whole of the appendage, and that excites the fixed-boundary natural modes (the modes obtained when clamping the appendage at point P) through the modal participation matrix $[L_P]$. This natural modes produce a load transmitted to substructure \mathcal{P} modifying the load that appendage \mathcal{A} will induce to \mathcal{P} , which is the residual mass of the appendage $[J_{P0}^A]$ times the acceleration at point P . This can be seen schematically as the rigid-body displacement of appendage \mathcal{A} perturbed with a feedback of its own natural vibration modes as shown in Fig. 5.2.

The model in Eq. (5.6) is commonly used in space engineering to connect a flexible appendage to a rigid body considered as the main hub [Alazard 08]. Nevertheless, the model does not take into account what happens if substructure \mathcal{A} is connected to another substructure at the opposite end, since there is no information about its displacement. In Sec. 5.2 an approach is proposed for the case of two connection points, which is sufficient for modeling chain-like substructures.

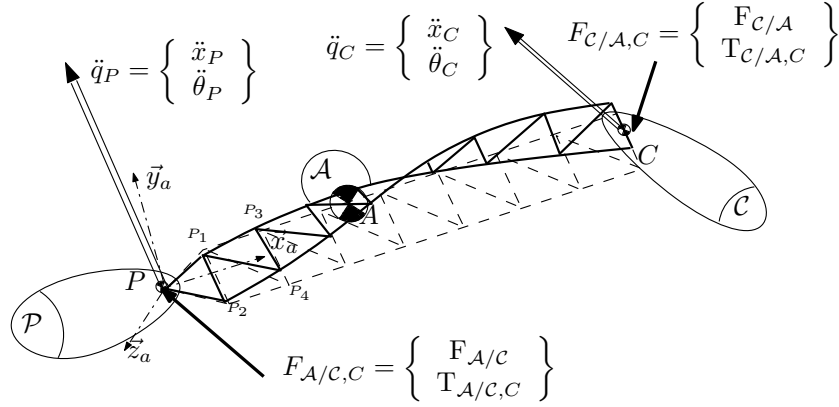


Figure 5.3: Substructure \mathcal{A} linked to structure \mathcal{P} and substructure \mathcal{C}

5.2 Two Connection Points

In this section, the modeling of a substructure connected to two different structures through two connection points, one for each structure, is explained. As shown in Fig. 5.3, the flexible body (substructure) \mathcal{A} is linked to the parent structure \mathcal{P} at the point P and to a child substructure \mathcal{C} at the point C . It is assumed that the only external loads applied to \mathcal{A} are the interactions with \mathcal{P} at point P and with \mathcal{C} at point C .

As seen in Sec. 5.1, the main problem is how to consider the coupling between substructures \mathcal{P} , \mathcal{A} and \mathcal{C} . Again, the overlapping between substructures is expressed as an acceleration-load transfer through the common boundaries under the framework of a DP model seen in Sec. 4.2. In this case, both points, P and C , suffer an acceleration-load transfer, in such a way that the acceleration is transferred to the next substructure in the chain (\mathcal{C} in this case) and the load is transmitted to the previous substructure in the chain (the parent \mathcal{P} structure). Therefore the objective is to build a double-port model of the substructure \mathcal{A} such that:

$$\begin{Bmatrix} \ddot{q}_C \\ F_{A/P,P} \end{Bmatrix} = [G_{P,C}^{\mathcal{A}}(s)] \begin{Bmatrix} F_{C/A,C} \\ \ddot{q}_P \end{Bmatrix} \quad (5.7)$$

As there are only two connection points, the assignment of degrees of freedom is simple: rigid-body displacements to connection point P and the redundant constraint displacements to connection point C . Thus the accelerations read:

$$\{\ddot{q}_P\} = \{\ddot{\eta}_r\}; \quad \{\ddot{q}_C\} = \{\ddot{\eta}_e\} + [\phi_{er}]\{\ddot{\eta}_r\} \quad (5.8)$$

where $[\phi_{er}]$ is described in Eq. (4.26) and it has the same form as the kinematic model between connection point P and connection point C , $[\tau_{PC}]$. Equation (5.8) implies that the rigid motion is supported by point P and the constrained motion of connection point C is a

result of the rigid body motion in P transported to point C ($[\phi_{er}]\{\ddot{\eta}_r\}$) plus the constrained motion due to flexibility ($\{\ddot{\eta}_e\}$). In the same way, loads are received and transmitted by appendage \mathcal{A} with the following directions:

$$\begin{aligned} F_{\mathcal{A}/\mathcal{P},P} &= -\tilde{F}_r \\ F_{\mathcal{C}/\mathcal{A},C} &= \tilde{F}_e \end{aligned} \quad (5.9)$$

Using the relations given in Eq. (5.8) and (5.9) in combination with Eq. (4.31), a state-space representation can be obtained for the substructure \mathcal{A} :

$$\begin{cases} \begin{Bmatrix} \dot{\eta}_n \\ \dot{\eta}_e \\ \ddot{\eta}_n \\ \ddot{\eta}_e \end{Bmatrix} = A \begin{Bmatrix} \eta_n \\ \eta_e \\ \dot{\eta}_n \\ \dot{\eta}_e \end{Bmatrix} + B \begin{Bmatrix} F_{\mathcal{C}/\mathcal{A},C} \\ \ddot{q}_P \end{Bmatrix} \\ \begin{Bmatrix} \ddot{q}_C \\ F_{\mathcal{A}/\mathcal{P},P} \end{Bmatrix} = C \begin{Bmatrix} \eta_n \\ \eta_e \\ \dot{\eta}_n \\ \dot{\eta}_e \end{Bmatrix} + (D + D_\delta) \begin{Bmatrix} F_{\mathcal{C}/\mathcal{A},C} \\ \ddot{q}_P \end{Bmatrix} \end{cases} \quad (5.10)$$

where A , B , C , D and D_δ are the short hand notation of the following state-space matrices:

$$A = \begin{bmatrix} 0_{n+e} & I_{n+e} \\ -\hat{M}_Q^{-1} \hat{K}_Q & -\hat{M}_Q^{-1} \hat{D}_Q \end{bmatrix} \quad (5.11)$$

$$B = \begin{bmatrix} 0_{n+e,e+r} \\ \hat{M}_Q^{-1} \begin{bmatrix} 0_{ne} & -\hat{M}_{nr} \\ I_{ee} & -\hat{M}_{er} \end{bmatrix} \end{bmatrix} \quad (5.12)$$

$$C = \begin{bmatrix} \begin{bmatrix} 0_{en} & I_{ee} \end{bmatrix} \begin{bmatrix} -\hat{M}_Q^{-1} \hat{K}_Q & -\hat{M}_Q^{-1} \hat{D}_Q \end{bmatrix} \\ \begin{bmatrix} \hat{M}_{rn} & \hat{M}_{re} \end{bmatrix} \begin{bmatrix} \hat{M}_Q^{-1} \hat{K}_Q & \hat{M}_Q^{-1} \hat{D}_Q \end{bmatrix} \end{bmatrix} \quad (5.13)$$

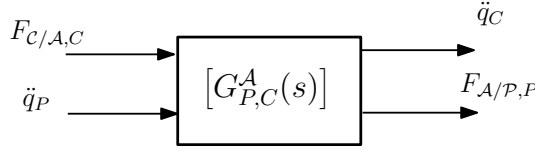


Figure 5.4: Block diagram of the Two-Input Two-Output Port (TITOP) Model

$$D = \begin{bmatrix} \begin{bmatrix} 0_{en} & I_{ee} \end{bmatrix} \hat{M}_Q^{-1} \begin{bmatrix} 0_{ne} & -\hat{M}_{nr} \\ I_{ee} & -\hat{M}_{er} \end{bmatrix} \\ -\begin{bmatrix} \hat{M}_{rn} & \hat{M}_{re} \end{bmatrix} \hat{M}_Q^{-1} \begin{bmatrix} 0_{ne} & -\hat{M}_{nr} \\ I_{ee} & -\hat{M}_{er} \end{bmatrix} \end{bmatrix} \quad (5.14)$$

with

$$\begin{aligned} \hat{M}_Q &= \begin{bmatrix} \hat{M}_{nn} & \hat{M}_{ne} \\ \hat{M}_{en} & \hat{M}_{ee} \end{bmatrix}; \quad \hat{K}_Q = \begin{bmatrix} \hat{K}_{nn} & 0 \\ 0 & \hat{K}_{ee} \end{bmatrix}; \\ \hat{D}_Q &= \begin{bmatrix} \hat{D}_{nn} & \hat{D}_{ne} \\ \hat{D}_{en} & \hat{D}_{ee} \end{bmatrix}; \quad D_\delta = \begin{bmatrix} 0_{er} & \phi_{er} \\ \phi_{er}^T & -\hat{M}_{rr} \end{bmatrix}; \end{aligned} \quad (5.15)$$

Equation (5.10) with Eqs. (5.11), (5.12), (5.13), (5.14) and (5.15) form the double-port model, $[G_{P,C}^A(s)]$, of the flexible substructure \mathcal{A} in chain-like assembly, called **Two-Input Two-Output Port (TITOP) model**. This model allows to interconnect different flexible substructures in chain-like assembly taking into account flexible motions. A simplified scheme of the TITOP model is shown in Fig. 5.4. In the six degrees of freedom case, $[G_{P,C}^A(s)]$, of the flexible substructure \mathcal{A} is a 12×12 state-space model (that is, $r = 6$, $e = 6$). The TITOP model explained here, being derived from the Hurty's Method, uses fixed-constraint natural modes. A different type TITOP model, using cantilevered modes and the mode shapes at connection point C , is derived in [Alazard 15], showing another form of building TITOP models. The transformation of the FE equations and the computation of the state-space model can be easily encoded in any programming language, as shown in Sec. D.2, where a matlab function performing this task is described.

The physical interpretation of Eq. (5.10) is similar to the one connection point case. In this case rigid-body displacements of the appendage \mathcal{A} are transmitted by its connection point P through the whole of the appendage, and this excites the fixed-boundary natural modes (the modes obtained when clamping the appendage at point P and C) through the modal participation matrices, $[\hat{M}_{rn}]$ and $[\hat{M}_{re}]$, and thus the constraint point C . These natural modes produce a load transmitted to substructure \mathcal{P} modifying the load that appendage \mathcal{A} will induce to \mathcal{P} , which depends on the load received at point C , $\{F_{C/A,C}\}$, the acceleration received at point P , $\{\ddot{q}_P\}$ and the natural modes. It can be observed that the rigid-body

matrix of substructure \mathcal{A} , $[\hat{M}_{rr}]$, influences the transfer as well.

As stated in Sec. 4.2, the DP form allows the consideration of different boundary conditions on the substructures by inversion of the upper or lower channels. By setting inputs to 0, $[G_{P,C}^{\mathcal{A}}(s)]$ represents the clamped (at P)- free (at C) model of \mathcal{A} . In the same way, $[G_{P,C}^{\mathcal{A}}(s)]^{-1}$ represents the free (at P) - clamped (at C) model of \mathcal{A} . Both channels are invertible and thus the following equations

$$[G_{P,C}^{\mathcal{A}}(s)]^{-1^u} \rightarrow \begin{Bmatrix} F_{C/\mathcal{A},C} \\ F_{\mathcal{A}/\mathcal{P},P} \end{Bmatrix} = [G_{P,C}^{\mathcal{A}}(s)]^{-1^u} \begin{Bmatrix} \ddot{q}_C \\ \ddot{q}_P \end{Bmatrix} \quad (5.16)$$

$$[G_{P,C}^{\mathcal{A}}(s)]^{-1^l} \rightarrow \begin{Bmatrix} \ddot{q}_C \\ \ddot{q}_P \end{Bmatrix} = [G_{P,C}^{\mathcal{A}}(s)]^{-1^l} \begin{Bmatrix} F_{C/\mathcal{A},C} \\ F_{\mathcal{A}/\mathcal{P},P} \end{Bmatrix} \quad (5.17)$$

can be used to take into account boundary conditions at P or C . Indexes u and l are used to describe the “upper” channel and “lower” channel respectively. It should be noted that removing connection point C the same model as for the one connection point case is found. Thus Eqs. (5.16) and (5.17) correspond to the clamped-clamped and free-free models, respectively.

The TITOP model of a flexible substructure is the most general model for FMS assembly. Given the FE model of a substructure and selecting the corresponding nodes for connection to other substructures, a TITOP model can be derived for control purposes. In the following sections extensions of the TITOP technique are presented for the revolute joint modeling, piezoelectric coupling and substructure’s parameterization. A wide variety of examples using this model are shown in Chap. 6.

5.3 Extension to Revolute joint

The double-port approach allows taking into account constraints at the connection points by simply restricting or releasing degrees of freedom. Taking advantage of this property, a revolute joint at the connection point P between the bodies \mathcal{A} and \mathcal{P} , as depicted in Fig. 5.5, can be modeled for the two connection point case.

For this purpose, the double port model $[G_{P,C}^{\mathcal{A}}(s)]_{\mathcal{R}_a}$ of the body \mathcal{A} projected in its associated frame \mathcal{R}_a must be augmented. Let $\{e_a\} = \{x_{e_a} y_{e_a} z_{e_a}\}_{\mathcal{R}_a}^T$ be a unit vector along the revolute joint axis, then:

$$\begin{Bmatrix} \begin{Bmatrix} \ddot{q}_C \\ F_{\mathcal{A}/\mathcal{P},P} \end{Bmatrix}_{\mathcal{R}_a} \\ t_{rj,P} \end{Bmatrix} = \underbrace{\begin{bmatrix} I_{12} \\ E_a \end{bmatrix} [G_{P,C}^{\mathcal{A}}(s)]_{\mathcal{R}_a} \begin{bmatrix} I_{12} & E_a^T \end{bmatrix}}_{[H_{P,C}^{\mathcal{A}}(s)]_{\mathcal{R}_a}} \begin{Bmatrix} \begin{Bmatrix} F_{C/\mathcal{A},C} \\ \ddot{q}_P \end{Bmatrix}_{\mathcal{R}_a} \\ \ddot{\alpha} \end{Bmatrix} \quad (5.18)$$

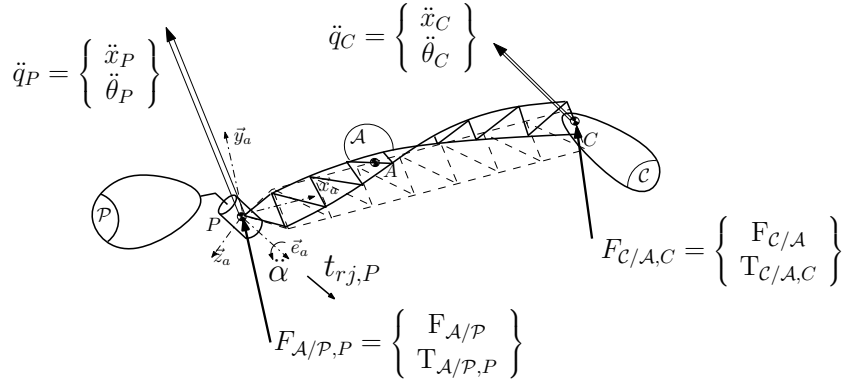


Figure 5.5: Appendage \mathcal{A} connected to \mathcal{P} through a revolute joint along \vec{e}_a

with the selection matrix:

$$E_a = - \begin{bmatrix} 0_{1 \times 9} & x_{e_a} & y_{e_a} & z_{e_a} \end{bmatrix} \quad (5.19)$$

where $[H_{P,C}^A(s)]_{\mathcal{R}_a}$ is the double port model augmented with a 13th input: $\ddot{\alpha}$, the angular acceleration inside the revolute joint and a 13th output: $t_{rj,P}$ the torque applied by an actuator located inside the revolute joint. Therefore, the state-space model $[H_{P,C}^A(s)]_{\mathcal{R}_a}$ is the Two-Input Two-Output Port (TITOP) model of a flexible substructure with a revolute joint at the connection point P .

This augmentation allows to release the desired degrees of freedom (setting $t_{rj,P} = 0$) or to take into account the model $K(s)$ of a local mechanism inside an actuated revolute joint as it can be seen in Fig. 5.6. In this case, the system $[H_{P,C}^A(s)]_{\mathcal{R}_a}$ has to be inverted between its 13th input and its 13th output, defining a new inversion operation: $[H_{P,C}^A(s)]_{\mathcal{R}_a}^{-1_p}$, the operation corresponding to the inversion of the 13-th input output channel of $[H_{P,C}^A(s)]_{\mathcal{R}_a}$ such that:

$$\left\{ \begin{bmatrix} \ddot{q}_C \\ F_{A/P,P} \\ \ddot{\alpha} \end{bmatrix}_{\mathcal{R}_a} \right\} = [H_{P,C}^A(s)]_{\mathcal{R}_a}^{-1_p} \left\{ \begin{bmatrix} F_{C/A,C} \\ \ddot{q}_P \\ t_{rj,P} \end{bmatrix}_{\mathcal{R}_a} \right\} \quad (5.20)$$

The effect of $K(s)$ on the boundary condition at point P is strictly taken into account. An application of this modeling extension is shown in Chap. 6 for the case of a two-link flexible manipulator driven by actuators at its joints. It should be highlighted that the obtained TITOP model for the revolute joint is valid for small variations around a given configuration of the revolute joint.

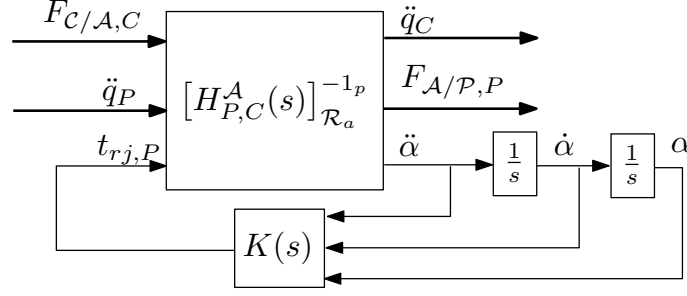


Figure 5.6: Local mechanism model $K(s)$ in the double port model of a body \mathcal{A}

5.4 Extension to Piezoelectric Actuators

The TITOP modeling technique explained in the precedent sections can be expanded to the case in which the flexible substructure presents an embedded piezoelectric material for vibration control. As stated in [IEEE 88], the constitutive linear equations of an element piezoelectric material read:

$$\{T\} = [c^E]\{S\} - [e]^T\{E\} \quad (5.21)$$

$$\{D\} = [e]\{S\} + [\epsilon^S]\{E\} \quad (5.22)$$

where $\{T\}$ is the stress vector, $\{S\}$ the deformation vector, $\{E\}$ the electric field, $\{D\}$ the electric displacement, $[c]$ the elasticity constants matrix, $[\epsilon]$ the dielectric constants matrix, $[e]$ the piezoelectric constants, with superscripts E , S and T indicating static conditions for E , S and T respectively.

The dynamic equations of a piezoelectric continuum can be discretized in elements and written in the finite element formulation as follows [Piefort 01]:

$$[\mathcal{M}_{xx}]\{\ddot{x}\} + [\mathcal{K}_{xx}]\{x\} + [\mathcal{K}_{x\phi}]\{\phi\} = \{f\} \quad (5.23)$$

$$[\mathcal{K}_{\phi x}]\{x\} + [\mathcal{K}_{\phi\phi}]\{\phi\} = \{\gamma\} \quad (5.24)$$

where the element coordinates $\{x\}$, the applied voltage $\{\phi\}$, the electric charge $\{\gamma\}$ and external forces $\{f\}$ are related through the element mass matrix, $[\mathcal{M}_{xx}]$, the element stiffness matrix, $[\mathcal{K}_{xx}]$, the piezoelectric coupling matrix $[\mathcal{K}_{x\phi}]$ and the capacitance matrix $[\mathcal{K}_{\phi\phi}]$. Upon carrying out the assembly of each piezoelectric element, we get the global system of equations:

$$[M_{qq}]\{\ddot{q}\} + [K_{qq}]\{q\} + [K_{qv}]\{v\} = \{F\} \quad (5.25)$$

$$[K_{vq}]\{q\} + [K_{vv}]\{v\} = \{g\} \quad (5.26)$$

where the global coordinates $\{q\}$, the global applied voltage $\{v\}$, the electric charge $\{g\}$ and external forces $\{F\}$ are now related through the global mass matrix, $[M_{qq}]$, the global stiffness matrix, $[K_{qq}]$, the piezoelectric coupling matrix $[K_{qv}] = [K_{vq}]^T$ and the capacitance matrix $[K_{vv}]$.

In order to obtain the TITOP model of the piezo-actuated substructure, the global coordinates $\{q\}$ are then partitioned into three main sets: rigid-body coordinates, r , redundant boundary coordinates, e , and fixed-interface normal modes, n . Applying this division, Eqs. (5.25) and (5.26) result:

$$\begin{bmatrix} M_{nn} & M_{ne} & M_{nr} \\ M_{en} & M_{ee} & M_{er} \\ M_{rn} & M_{re} & M_{rr} \end{bmatrix}_{qq} \begin{Bmatrix} \ddot{q}_n \\ \ddot{q}_e \\ \ddot{q}_r \end{Bmatrix} + \begin{bmatrix} K_{nn} & K_{ne} & K_{nr} \\ K_{en} & K_{ee} & K_{er} \\ K_{rn} & K_{re} & K_{rr} \end{bmatrix}_{qq} \begin{Bmatrix} q_n \\ q_e \\ q_r \end{Bmatrix} + \begin{bmatrix} K_{nv} \\ K_{ev} \\ K_{rv} \end{bmatrix} \{v\} = \begin{Bmatrix} F_n \\ F_e + \tilde{F}_e \\ F_r + \tilde{F}_r \end{Bmatrix} \quad (5.27)$$

$$\begin{bmatrix} K_{vn} & K_{ve} & K_{vr} \end{bmatrix} \begin{Bmatrix} q_n \\ q_e \\ q_r \end{Bmatrix} + [K_{vv}]\{v\} = \{Q\} \quad (5.28)$$

where $[M]$, $[K]$, $\{q\}$ and $\{F\}$ have been partitioned into their contributions to rigid-body, redundant boundaries and fixed-boundary displacements. The “tilde” load term, $\{\tilde{F}_e\}$ and $\{\tilde{F}_r\}$, denotes the force resulting from the connection to adjacent structures at the boundary points. Proceeding like in the Hurty’s Method, Eq. (4.21) is substituted into Eqs. (5.27) and (5.28), which are pre-multiplied by $[\Phi^T]$. Considering that neither interior forces nor external forces apply ($F_n = F_e = F_r = 0$), Eq. (5.27) yields:

$$\begin{bmatrix} \hat{M}_{nn} & \hat{M}_{ne} & \hat{M}_{nr} \\ \hat{M}_{en} & \hat{M}_{ee} & \hat{M}_{er} \\ \hat{M}_{rn} & \hat{M}_{re} & \hat{M}_{rr} \end{bmatrix}_{\eta\eta} \begin{Bmatrix} \ddot{\eta}_n \\ \ddot{\eta}_e \\ \ddot{\eta}_r \end{Bmatrix} + \begin{bmatrix} \hat{K}_{nn} & 0_{ne} & 0_{nr} \\ 0_{en} & \hat{K}_{ee} & 0_{er} \\ 0_{rn} & 0_{re} & 0_{rr} \end{bmatrix}_{\eta\eta} \begin{Bmatrix} \eta_n \\ \eta_e \\ \eta_r \end{Bmatrix} + \begin{bmatrix} \hat{K}_{nv} \\ \hat{K}_{ev} \\ \hat{K}_{rv} \end{bmatrix} \{v\} = \begin{Bmatrix} 0 \\ \tilde{F}_e \\ \tilde{F}_r + \phi_{er}^T \tilde{F}_e \end{Bmatrix} \quad (5.29)$$

$$\begin{bmatrix} \hat{K}_{nv} & \hat{K}_{ev} & \hat{K}_{rv} \end{bmatrix} \begin{Bmatrix} \eta_n \\ \eta_e \\ \eta_r \end{Bmatrix} + [K_{vv}]\{v\} = \{G\} \quad (5.30)$$

with the new coupling matrix coefficients:

$$\hat{K}_{nv} = \phi_{nn} K_{nv} \quad (5.31)$$

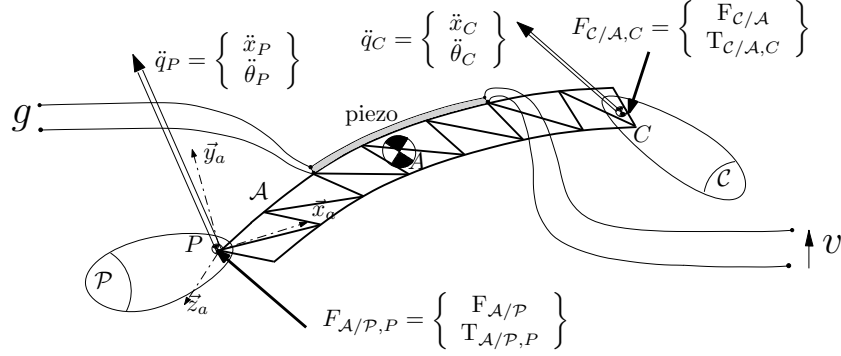


Figure 5.7: Illustration of a generic substructure with bonded piezoelectric material

$$\hat{K}_{ev} = K_{ev} + \phi_{en} K_{nv} \quad (5.32)$$

$$\hat{K}_{rv} = K_{rv} + \phi_{re} K_{ev} + \phi_{rn} K_{nv} \quad (5.33)$$

Equations (5.29) and (5.30) are the most generalized expression for a FE model of a piezoelectric component transformed through the Hurty's method. No previous studies have been found regarding the application of a component modes synthesis technique to the FE EOM of a piezoelectric material. This is probably the first time that the Hurty's method is applied to the FE model of a piezoelectric component.

In order to derive the state-space representation, a substructure as the one shown in Fig. 5.7 is considered. The flexible piezoelectric component \mathcal{A} is linked to the parent structure \mathcal{P} at the point P and to a child substructure \mathcal{C} at the point C . It is assumed that the only external loads applied to \mathcal{A} are the interactions with \mathcal{P} at point P and with \mathcal{C} at point C , as hypothesis on Eq. (5.29) states. Voltage v can be applied to the piezo in order to provoke a electric field, and the electric charge g is an available measurement.

The main problem is how to consider the electro-mechanical coupling between \mathcal{P} , \mathcal{A} , \mathcal{C} and electric states. The mechanical overlapping between substructures is expressed as an acceleration-load transfer through the common boundaries, always respecting the DP form. With this approach, both points, P and C , suffer an acceleration-load transfer, in such a way that the acceleration is transferred to the next substructure in the chain (\mathcal{C} in this case) and the load is transmitted to the previous substructure in the chain (the parent \mathcal{P} structure). The existing electro-mechanical coupling between loads-accelerations and voltage-charge is considered through the augmentation of the classic double-port model with an additional electric input, the applied voltage v , and with an additional electric output, the electric charge, g , such that:

$$\begin{Bmatrix} \ddot{q}_C \\ F_{A/P,P} \\ g \end{Bmatrix} = [G_{P,C}^A(s)] \begin{Bmatrix} F_{C/A,C} \\ \ddot{q}_P \\ v \end{Bmatrix} \quad (5.34)$$

Therefore Eq. (5.34) relates the accelerations suffered at connection point P , loads at con-

nection point C and the applied voltage v to the acceleration at connection point C , transmitted force to the previous substructure \mathcal{P} and the measured electric charge g . An assignment of the different degrees of freedom is performed in order to distribute the acceleration-load transfer: rigid-body displacements are those of connection point P and the redundant constraint displacements those of connection point C . Thus the accelerations read:

$$\begin{aligned}\ddot{q}_P &= \ddot{\eta}_r \\ \ddot{q}_C &= \ddot{\eta}_e + \phi_{er}\ddot{\eta}_r\end{aligned}\tag{5.35}$$

Equation (5.35) implies that the rigid motion is supported by point P and the constrained motion of connection point C is a result of the rigid body motion in P transported to point C ($\phi_{er}\ddot{\eta}_r$) plus the constrained motion due to flexibility ($\ddot{\eta}_e$).

In the same way, loads are received and transmitted by appendage \mathcal{A} with the following directions:

$$\begin{aligned}F_{\mathcal{A}/\mathcal{P},P} &= -\tilde{F}_r \\ F_{C/\mathcal{A},C} &= \tilde{F}_e\end{aligned}\tag{5.36}$$

Using the relations given in Eqs. (5.35) and (5.36) in combination with Eq. (5.29), a state-space representation can be obtained for the piezoelectric component \mathcal{A} :

$$\left\{ \begin{array}{l} \begin{Bmatrix} \dot{\eta}_n \\ \dot{\eta}_e \\ \ddot{\eta}_n \\ \ddot{\eta}_e \end{Bmatrix} = A \begin{Bmatrix} \eta_n \\ \eta_e \\ \dot{\eta}_n \\ \dot{\eta}_e \end{Bmatrix} + B \begin{Bmatrix} F_{C/\mathcal{A},C} \\ \ddot{q}_P \\ v \end{Bmatrix} \\ \begin{Bmatrix} \ddot{q}_C \\ F_{\mathcal{A}/\mathcal{P},P} \\ g_c \end{Bmatrix} = C \begin{Bmatrix} \eta_n \\ \eta_e \\ \dot{\eta}_n \\ \dot{\eta}_e \end{Bmatrix} + (D + D_\delta) \begin{Bmatrix} F_{C/\mathcal{A},C} \\ \ddot{q}_P \\ v \end{Bmatrix} \end{array} \right.\tag{5.37}$$

where A , B , C , D and D_δ are the short hand notation of the following state-space matrices:

$$A = \begin{bmatrix} 0_{n+e} & I_{n+e} \\ -\hat{M}_Q^{-1}\hat{K}_Q & -\hat{M}_Q^{-1}\hat{D}_Q \end{bmatrix}\tag{5.38}$$

$$B = \begin{bmatrix} 0_{n+e,e+r+v} \\ \hat{M}_Q^{-1} \begin{bmatrix} 0_{ne} & -\hat{M}_{nr} & -\hat{K}_{nv} \\ I_{ee} & -\hat{M}_{er} & -\hat{K}_{ev} \end{bmatrix} \end{bmatrix} \quad (5.39)$$

$$C = \begin{bmatrix} \begin{bmatrix} 0_{en} & I_{ee} \end{bmatrix} \begin{bmatrix} -\hat{M}_Q^{-1} \hat{K}_Q & -\hat{M}_Q^{-1} \hat{D}_Q \end{bmatrix} \\ \begin{bmatrix} \hat{M}_{rn} & \hat{M}_{re} \end{bmatrix} \begin{bmatrix} \hat{M}_Q^{-1} \hat{K}_Q & \hat{M}_Q^{-1} \hat{D}_Q \end{bmatrix} \\ \begin{bmatrix} \hat{K}_{vn} & \hat{K}_{ve} \end{bmatrix} \begin{bmatrix} I_{n+e,n+e} & 0_{n+e,n+e} \end{bmatrix} \end{bmatrix} \quad (5.40)$$

$$D = \begin{bmatrix} \begin{bmatrix} 0_{en} & I_{ee} \end{bmatrix} \hat{M}_Q^{-1} \begin{bmatrix} 0_{ne} & -\hat{M}_{nr} & -\hat{K}_{nv} \\ I_{ee} & -\hat{M}_{er} & -\hat{K}_{ev} \end{bmatrix} \\ \begin{bmatrix} \hat{M}_{rn} & \hat{M}_{re} \end{bmatrix} \hat{M}_Q^{-1} \begin{bmatrix} 0_{ne} & -\hat{M}_{nr} & -\hat{K}_{nv} \\ I_{ee} & -\hat{M}_{er} & -\hat{K}_{ev} \end{bmatrix} \\ 0_{ve} \quad 0_{vr} \quad K_{vv} \end{bmatrix} \quad (5.41)$$

with

$$\begin{aligned} \hat{M}_Q &= \begin{bmatrix} \hat{M}_{nn} & \hat{M}_{ne} \\ \hat{M}_{en} & \hat{M}_{ee} \end{bmatrix}; \quad \hat{K}_Q = \begin{bmatrix} \hat{K}_{nn} & 0_{ne} \\ 0_{en} & \hat{K}_{ee} \end{bmatrix}; \\ \hat{D}_Q &= \begin{bmatrix} \hat{D}_{nn} & 0_{ne} \\ 0_{en} & \hat{D}_{ee} \end{bmatrix}; \quad D_\delta = \begin{bmatrix} 0_{ee} & \phi_{er} & 0_{ev} \\ -\phi_{er}^T & \hat{M}_{rr} & \hat{K}_{rv} \\ 0_{ve} & 0_{vr} & 0_{vv} \end{bmatrix}; \end{aligned} \quad (5.42)$$

Equation (5.37) with Eqs. (5.38), (5.39), (5.40), (5.41) and (5.42) form the double-port model, $[G_{P,C}^A(s)]$, of the flexible piezoelectric component \mathcal{A} in chain-like assembly, called **actuated Two-Input Two-Output Port (TITOP)** model. This model allows to interconnect different flexible substructures in chain-like assembly taking into account flexible motions. A simplified scheme of the TITOP model is shown in Fig. 5.8. In the 6 degrees of freedom case with one piezoelectric strip, $[G_{P,C}^A(s)]$, of the flexible substructure \mathcal{A} is a 13×13 state-space model (that is, $r = 6$, $v = 1$, $e = 6$, $g = 1$). It should be noticed that the measured charge is denoted g_c and not g because only relative displacement between connection point P and connection point C is measured for the sake of input/output simplicity.

The physical interpretation of Eq. (5.37) is as follows. The rigid-body displacements of the appendage \mathcal{A} are transmitted by its connection point P through the whole of the appendage, and this excites the fixed-boundary natural modes (the modes obtained when clamping the appendage at point P and C) through the modal participation matrices, $[\hat{M}_{rn}]$ and $[\hat{M}_{re}]$, and

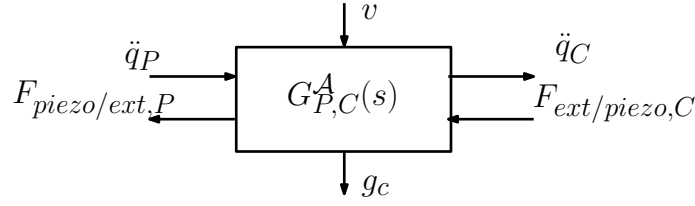


Figure 5.8: Block diagram of TITOP modeling of a substructure actuated with piezoelectric materials

thus the constraint point C . These natural modes produce a load transmitted to substructure \mathcal{P} modifying the load that appendage \mathcal{A} will induce to \mathcal{P} , which depends on the load received at point C , $F_{C/\mathcal{A},C}$, the acceleration received at point P , $\{\ddot{q}_P\}$ and the natural modes. In addition, voltage v modifies these transfers by increasing or reducing the transferred loads at P and C , and the measured electric charge g_c responds to displacements changes either by mechanical interaction (through load application) or by electric field application (voltage). This behavior is illustrated in Chap. 6 with the modeling of flexible beam with bonded piezoelectric material.

5.5 Implementation of Parametric Variations

This section underlines another attribute of the TITOP model which relates it to integrated control/structure design. The model can be parameterized as a function of structural configuration parameters open to vary along an optimization process or uncertainty analysis. For a structure with varying configuration or varying mass and stiffness properties, like most space structures, the TITOP modeling technique may be especially efficient since it can take into account such variations (see [Guy 14] as an illustrative example). It can also be used for structural/control integrated design allowing structural sizing parameters to be simultaneously optimized with the attitude control gains [Murali 15].

The explicit form of the EOM transformed with the Hurty's Method allows the identification of sensitive parameters of optimization/ uncertainty analysis such as the mass, position of the mass center, geometric dimensions, frequency modes, damping coefficients, etc. The identification is followed by the creation of a LFT form of the TITOP model in order to use it either for integrated design or for uncertainty analysis. The LFT form is converted into a set of tuneable parameters for integrated control/structure design.

5.5.1 Localization of Varying Parameters

Physical parameters are accessible in the TITOP model through the rigid-body matrix, denoted as $[\hat{M}_{rr}]$ or $[J_P^A]$ in Eq. (5.4). Indeed, total system mass, m^A , the substructure's inertia, \mathbb{I}_A^A , and the center of mass' position, $\{AP\}$, can be parameterized by accessing to this matrix:

$$[\hat{M}_{rr}] = [J_P^A] = [\tau_{AP}^T] \begin{bmatrix} m^A I_3 & 0_3 \\ 0_3 & \mathbb{I}_A^A \end{bmatrix} [\tau_{AP}] = \begin{bmatrix} m^A I_3 & m^A (*AP) \\ -m^A (*AP) & \mathbb{I}_P^A \end{bmatrix} \quad (5.43)$$

where $\mathbb{I}_P^A = \mathbb{I}_A^A - m^A (*AP)^2$ is the appendage's inertia at connection point P . These variations change the behavior of the direct feed-through matrix of the TITOP model, D_δ , so the variations are transmitted across the whole FMS.

Matrix $[\phi_{er}]$ reflects the geometric properties of the appendage, since it transports the kinematics from point P to C . It is strictly equivalent to the transport kinematic matrix $[\tau_{PC}]^T$, but in FE notation. The parameter which can be varied is the relative position from the connection point P to the connection point C , which can be seen as the length of a mast, for example.

$$[\phi_{re}] = [\tau_{PC}] = \begin{bmatrix} I_3 & (*PC) \\ 0_3 & I_3 \end{bmatrix} = \begin{bmatrix} 1 & 0 & 0 & 0 & -(z_C - z_P) & y_P - y_C \\ 0 & 1 & 0 & z_C - z_P & 0 & -(x_C - x_P) \\ 0 & 0 & 1 & -(y_P - y_C) & x_C - x_P & 0 \\ 0 & 0 & 0 & 1 & 0 & 0 \\ 0 & 0 & 0 & 0 & 1 & 0 \\ 0 & 0 & 0 & 0 & 0 & 1 \end{bmatrix} \quad (5.44)$$

Natural modes can be parameterized by accessing to matrix $[\hat{K}_{nn}]$ in the two-connection-point case or $[I_n \omega_n]$ in the one-connection-point case. Usually, after applying the Hurty's method transformation, the modes appear diagonally ordered from the lowest frequency to the highest one. Lowest frequency modes are the most open to be varied since they are the ones that may interfere with the controller's bandwidth. This is also useful for frequency mode truncation: the highest flexible modes can be removed for model simplification when their associated mass function can be neglected [Imbert 79]. Furthermore, if the natural modes have an explicit equation which relates its value to other geometric or mass parameters, it is straightforward to vary the natural modes as a function of those parameters. For example, the natural fixed modes of a cantilevered square plate of side a and thickness h are well known:

$$\omega_n = \frac{\beta_n}{a^2} \sqrt{\frac{Eh^2}{12(1 - \nu^2)\rho}} \quad (5.45)$$

So if the size of a solar array has to be varied with a value of δ_a in an integrated control/structure design and its influence on the first flexible mode has to be taken into account, the varied frequency can be written as follows:

$$\omega_1(\delta_a) = \omega_1 \frac{a^2}{(a + \delta_a)^2} \quad (5.46)$$

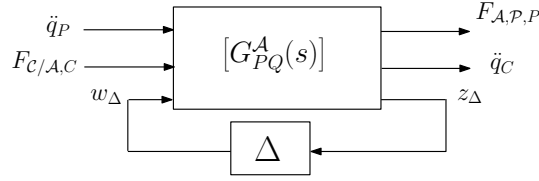


Figure 5.9: The TITOP LFR model, which takes into account parametric variations inside the block Δ

Equation (5.47) shows the simplest way to include parametric variations in already known data such as the frequency modes. From this it is deduced that it is not absolutely necessary to know the exact expression of the flexible modes. For example, if modes are known to vary proportionally to the root of the appendage's cross section inertia I_z (such in the case of a mast), the insertion of the parameter variation will read as follows:

$$\omega_1(\delta_I) = \omega_1 \frac{\sqrt{I_z}}{\sqrt{I_z + \delta_I}} \quad (5.47)$$

The damping coefficients can also be parameterized when the values across the diagonal of matrix $[\hat{D}_{nn}]$ are managed. The damping coefficients associated to each flexible mode appear in the form of $2\xi_n\omega_n$. Adding variations to ξ_n will take into account damping variation through $[\hat{D}_{nn}]$. However, if flexible modes are varied through $[\hat{K}_{nn}]$, variations must be added to $[\hat{D}_{nn}]$ as well in order to properly variate the system.

It can be noticed that not all parameters are easily accessible in the TITOP formulation, as for example the cross-section area or the Young's modulus. Furthermore, there is no *full parameterization*; i.e, it is not possible to know before hand how parameter variations will affect other submatrices which compose the TITOP model. This is the case of modal participation matrices ($[\hat{M}_{rn}]$, $[\hat{M}_{en}]$) or crossed-stiffness matrix ($[\hat{K}_{ee}]$). However, for elementary substructures like a mast or a boom, Murali [Murali 15] proposes the analytic TITOP model which can be used to obtain a fully parameterized model with length, cross-section inertia, young modulus, etc. Parameter variations are taken into account at all system levels, guaranteeing all the dynamic variations. This model, called *superelement* and recalled in Appendix A, is used in Sec. 6.2 for parameter variations of the masts of a rotatory spacecraft.

5.5.2 Obtaining the LFT Model of the Substructure

When a parameter is varied inside the substructure's TITOP model, either for integrated design or for uncertainty analysis purposes, the next step is to transform the model into LFT (Linear Fractional Transformation) form. The TITOP LFT model will then be composed of a nominal model, without variations, and the Δ block, which takes into account the model's variations. An example is provided for better understanding of the process.

If length L has to be varied to analyze its influence in the FMS, its variation δ can be

modelled in the skew symmetric matrix $(*PC)$ associated with the vector $\{PC\}$ (see Fig. 5.3) in the following way:

$$(*PC)(\delta) = (L + \delta)\vec{x}_a = \begin{bmatrix} 0 & 0 & 0 \\ 0 & 0 & -(L + \delta) \\ 0 & L + \delta & 0 \end{bmatrix}_{\mathcal{R}_a} = F_l\left(\begin{bmatrix} 0 & 0 & 0 & 0 & 0 \\ 0 & 0 & -L & 1 & 0 \\ 0 & L & 0 & 0 & 1 \\ 0 & 0 & -1 & 0 & 0 \\ 0 & 1 & 0 & 0 & 0 \end{bmatrix}, \Delta\right) \quad (5.48)$$

where $F_l(N, \Delta)$ is the lower Linear Fractional Transformation (LFT) of N by Δ , and $\Delta = \delta I_2$ [Belcastro 99]. Such a Linear Fractional Representation (LFR) of $(*PC)(\delta)$ can be propagated in $[\phi_{cr}(\delta)] = [\tau_{PC}(\delta)]$ and in the whole state-space model using standard functions of robust control theory [Balas 05]. The final LFR model contains the nominal model, $[G_{P,C}^A(s)]$, and the Δ block, as depicted in Fig. 5.9. Such a formalism of parametric variations is commonly used in control system theory for sensitivity analysis [Ferreres 99, Belcastro 99]. Therefore, the variations inside the model are contained in the Δ block, which changes the system's dynamics when the nominal parameters are modified.

5.5.3 Tunable Block Transformation

The Δ block obtained in Sec. 5.5.2 is used in the literature as a tool for robust analysis (μ -analysis tools), worst case determination or robust control synthesis. It is a diagonal matrix containing all the system's variations, known or unknown.

If these variations cannot be managed, then the problem can be seen as a robust control problem: uncertainty analysis, robust performance, worst case, etc. However, if variations are consciously applied to the system, that is, the variations are known, then the problem can be regarded as an optimization problem: finding the optimal variation which improves the system's performance. This is what is called the integrated control/structure design problem.

Therefore, if integrated design is desired, the Δ block has to be regarded as a set of tuneable parameters. The Δ block has to be treated then with different tools, mainly those provided in [Gahinet 11] where tuneable gains, state-space models and transfer functions are developed in order to apply structured \mathcal{H}_∞ schemes to the models. The tuneable block transformation is then a problem of tools for manipulation, not a conceptual problem.

5.6 TITOP Modeling of Flexible Multibody Systems

The state-space realizations found for FE models transformed with the Hurty's decomposition in the double-port form serve as elemental bricks for building FMS undergoing small deflections. Indeed, the one-connection-point TITOP model can be used to model flexible sys-

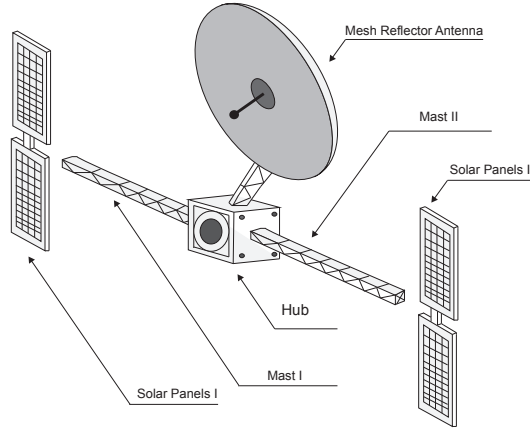


Figure 5.10: Example of Flexible Multibody System (FMS)

tems in star-like structures or to end chain-like structures. The two-connection-point TITOP model can be used to connect every type of chain-like structures between them, taking into account its flexibility. The revolute joint model can be used to model rotating substructures of the FMS, such as solar panels or pointing antennae. The piezoelectric model can be used to take into account the influence of bonded piezoelectric materials along booms or masts in the substructure's dynamics. The channels which connect the substructures among them can be modified to add perturbations to acceleration measurements or load disturbances at the connection points.

For instance, the FMS shown in Fig. 5.10 can be modeled as different TITOP models interacting among them as depicted in Fig. 5.11. The flexible multibody spacecraft is composed of a rigid main body or hub in which other appendages are attached such as an antenna, masts and solar panels. For control purposes, it is useful to choose as inputs the loads applied to the hub, F_G and as outputs the induced accelerations at the hub, $\{\ddot{q}_G\}$, which comprehend the rigid body motion of the spacecraft. These accelerations are transported to the connection point P_i (P_1 for the antenna connection point, P_2 for one of the masts) through the kinematic model $[\tau_{P_i G}]$ [Alazard 08], where they are transmitted to the TITOP models of the flexible appendages. For the masts, the masts' TITOP models transfer the acceleration $\ddot{q}_{Mast/SP}$ to the solar panels and they receive the corresponding connection force $F_{SP/Mast}$. This transfer results in a “disturbance” load applied to the hub which is added to F_G . Eventually, rotation matrices $[R_i]$ as the ones explained in Sec. 4.1 can be included in the diagram in order to change from the hub's frame to the appendage's frame.

The TITOP assembly maps the dynamic interactions of the FMS. This is an advantage at all levels: modeling, control and integrated control design:

- **Modeling.** The substructures' TITOP models are linear, self-completed and are obtained with FE data. No additional data other than the substructure's FE model is needed. If a substructure is no longer needed, it can be removed from the diagram and the FMS will be modified accordingly without further analysis of the remaining substructures. Furthermore, the assembly process lend itself particularly well-suited for

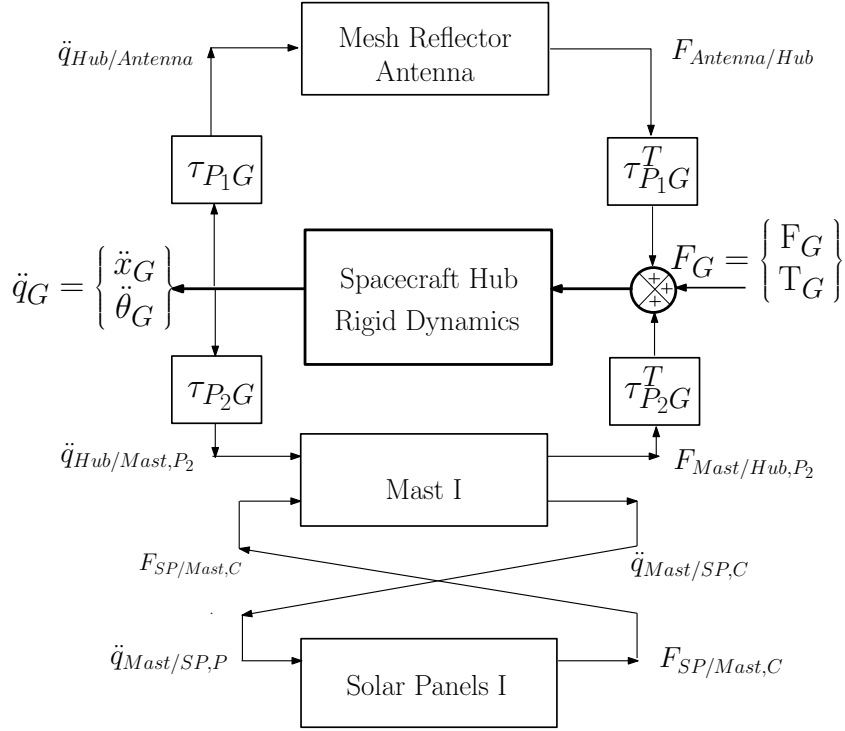


Figure 5.11: FMS assembly using TITOP models (mast II is not represented for simplicity)

implementation in a graphical programming environment for modeling, simulating or analyzing multidomain dynamic systems, such as Marthworks Simulink.

- **Control.** The TITOP scheme of a FMS offers straightforward means for analyzing centralized or decentralized control schemes. Furthermore, it allows the simulation of accelerator and force measurements, the introduction of system's disturbances at different points of the FMS and to take into account other control mechanisms such as revolute joints or piezoelectric actuators.
- **Integrated Design.** The TITOP models can be used independently of the boundary conditions linking the FMS. In addition, the models can be parameterized in order to be optimized in an integrated control/structure design.

This chapter has presented the Two-Input Two-Output Port (TITOP) modeling technique for modeling of FMS in star-like or chain-like configuration. Star-like configurations can be assembled using one-connection-point TITOP models. Chain-like configurations are assembled using two-connection-point TITOP models. The models have been extended to take into account the effect of a revolute joint and a bonded piezoelectric material, which offers even more possibilities for the modeling of FMS. The next chapter will use these models in a variety of applications so that the utility of the TITOP modeling technique can be gauged.

Chapter

6

Application and Validation of the TITOP Technique for the Modeling of Flexible Multibody Systems

“My powers are ordinary. Only my application brings me success.”
 - Isaac Newton

Contents

6.1	Beam-like Substructures	78
6.1.1	Beam Concatenation	78
6.1.2	Beam with Bonded Piezoelectric Material	81
6.1.3	Beam Parametric Variations	85
6.2	Planar Rotatory Flexible Spacecraft	90
6.2.1	Spacecraft System description	90
6.2.2	Spacecraft System modeling	90
6.2.3	Comparison of the Modeling Methods	94
6.2.4	Spacecraft System Parameterization	96
6.3	Two-Link Flexible Manipulator	98
6.3.1	TITOP modeling of the planar two-link flexible arm	99
6.3.2	Modeling and simulation results	101

This section shows the most representative cases of the many different FMS modeling problems that the TITOP modeling method can solve. Three kinds of FMS modeling problems are explained: beam-like substructures, a system composed of rigid and flexible bodies (rotatory flexible spacecraft) and a system with revolute joints (two-link flexible arm). All problems are validated with respective reference models and in two of them parameterization is performed.

ONCE the TITOP modeling framework has been developed in Chaps. 4 and 5, the technique has been applied to several illustrative examples in order to gauge its potential. Three different FMS modeling problems are presented within this chapter to estimate the accuracy of the method when compared to other FMS linear models, non-linear models and parameterized models.

The first example consists of the application of the TITOP technique to beam-like substructures. These examples aim at showing how the modeling technique can be applied to one of the most used shapes in structure assembly. Concatenation between several beams in chain-like assembly is explained and the resulting model is validated with a reference model. Then, another example using beams with bonded piezoelectric materials is addressed as seen in Sec. 5.4. Finally, a study involving several parameterization approaches is performed in order to figure the potential of parameterization of the TITOP technique.

The second example is a rotatory spacecraft with four flexible masts with lumped masses located at their ends. This example shows the application of the TITOP modeling technique when the substructures involved in the FMS have different behavior (flexible masts, rigid hub and rigid lumped masses). The modeling process is addressed with the TITOP modeling method and then compared with the model provided by a widely used approach, the Assumed Modes Method (AMM). Then, accuracy between both methods is evaluated for different boundary conditions. Finally, parametric variations are induced to the system to analyze the system's behavior.

The third example is a planar two-link flexible arm, a conventional FMS modeling problem where kinematic nonlinearities can be large. This modeling technique is applied to a revolute joint as seen in Sec. 5.3, extending it to the case of a joint with associated mass and inertia. The accuracy of the modes in different configurations is compared with a non-linear model, and a dynamic simulation of the system driven by actuators is performed in order to evaluate the differences between the TITOP model and the non-linear model.

6.1 Beam-like Substructures

6.1.1 Beam Concatenation

As an illustrative and validation example of the TITOP modeling technique, a chain of flexible beams attached to a hub is considered. The main objectives are (i) to model the dynamics of the flexible FMS chain and (ii) express the dynamic coupling between the chain and the hub. The system is depicted in Fig. 6.1. Let a 3D beam of length L be substructured in four parts or child-beams 1, 2, 3 and 4 of lengths $L/8$, $L/4$, $L/2$ and $L/8$ respectively. Each substructure has identical cross-section properties (rectangular section of width b and height h) and identical material composition (density ρ and constant elastic module E). For each child-beam a 7-element FE model is derived for obtaining the input data for the TITOP modeling technique.

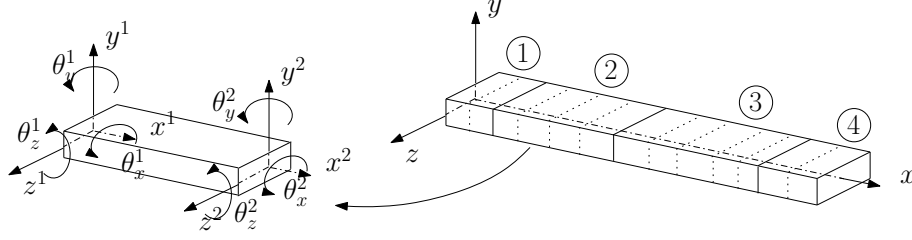


Figure 6.1: Chain of Flexible Beams for TITOP Modeling and the corresponding parametrization of the FE model

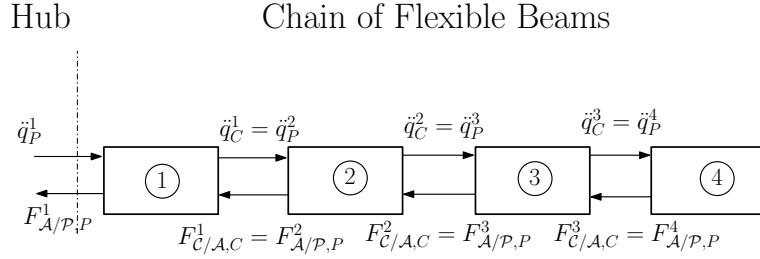


Figure 6.2: TITOP modeling of a chain of flexible beams

The TITOP models of each substructure, once concatenated, must present the same dynamic behavior as an entire beam of length L and must transmit an identical load to the connection point located at the hub. The system is assembled as shown in Fig. 6.2. The child-beams' TITOP models are connected following the transfer load/acceleration of each model. The transmitted acceleration at point C of the i -th child-beam is the acceleration at point P of the $i + 1$ -th child beam. In the same manner, the transmitted load at point P of the i -th childbeam is the load at point C of the $i+1$ -th child-beam. All the child-beams are two-connection-points TITOP models except for the fourth child-beam, which is a one connection-point TITOP model. The resulting model is compared with a complete 50-element FE model of the beam of length L .

The frequency response of the transfer $\ddot{q}_P \rightarrow F_{A,P,P}$, which represents the transfer between the hub dynamics and the induced loads of the chain, is compared. Particularly, the transfer between the angular acceleration induced to the chain's root, $\ddot{\omega}_y$, and the force F_z and torque M_y received by the hub is analyzed. Figure 6.3 shows the dynamic behavior of the system: when the hub rotates counter-clockwise, the flexible chain of appendages follows the movement, and by the action-reaction principle a load is induced to the hub, opposed to this movement.

In Fig. 6.4 the frequency response of the induced torque M_y and force F_z to a counter-wise rotation around the y axis (the fifth element of the coordinate vector $\{\ddot{q}_P\}$, $\ddot{\omega}_y$) is shown. As it can be evaluated, the frequencies of the resonances and anti-resonances of both systems are in perfect agreement for the first nine modes. For the static case ($f = 0$ Hz), the exact gain values are obtained, which demonstrates that the assembled system has identical total mass, total inertia and center of mass as the reference model. For frequencies beyond the tenth mode, the TITOP modeling technique shifts with respect to the reference model. This is

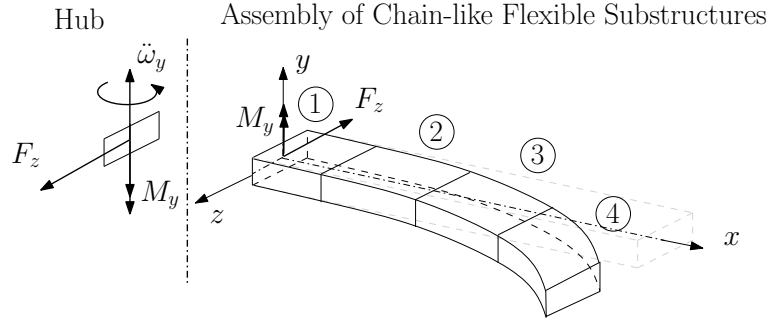


Figure 6.3: Illustration of the dynamic behavior of a chain of flexible beams connected to a hub when inducing a counter-clockwise rotation along the y axis to the root

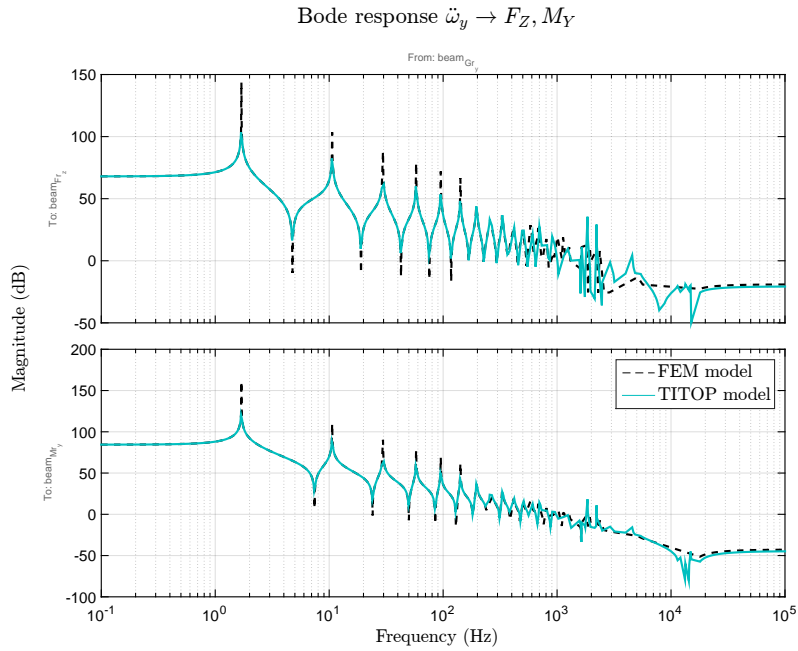


Figure 6.4: Frequency Response of the transmitted torque and force to the hub by the chain of flexible beams when spun counter-clockwise along the y axis (see Fig. 6.3)

caused by the less quantity of input data used by the TITOP models, a 7-element FE model for each child-beam. If more elements were used, the TITOP modeling technique would behave exactly as the reference model for high frequencies.

Identical results are found when analyzing the transfer of the acceleration of the vertical translation of the hub, \ddot{q}_y , and the received force F_y and torque M_z . The dynamics are illustrated in Fig. 6.5 and the frequency response is shown in Fig. 6.6.

The TITOP modeling technique has been applied and validated for a chain of flexible 3D beams. This exemplifies the use of the TITOP modeling technique to model FMS undergoing small displacements and rotations. The beam configuration proposed in this section can be changed in order to model more complex systems. For instance, if the orientation of the

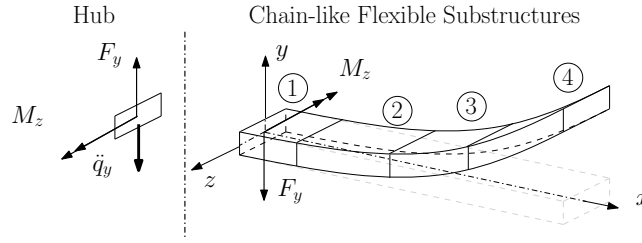


Figure 6.5: Illustration of the dynamic behavior of a chain of flexible beams connected to a hub when vertical accelerations are applied to the root

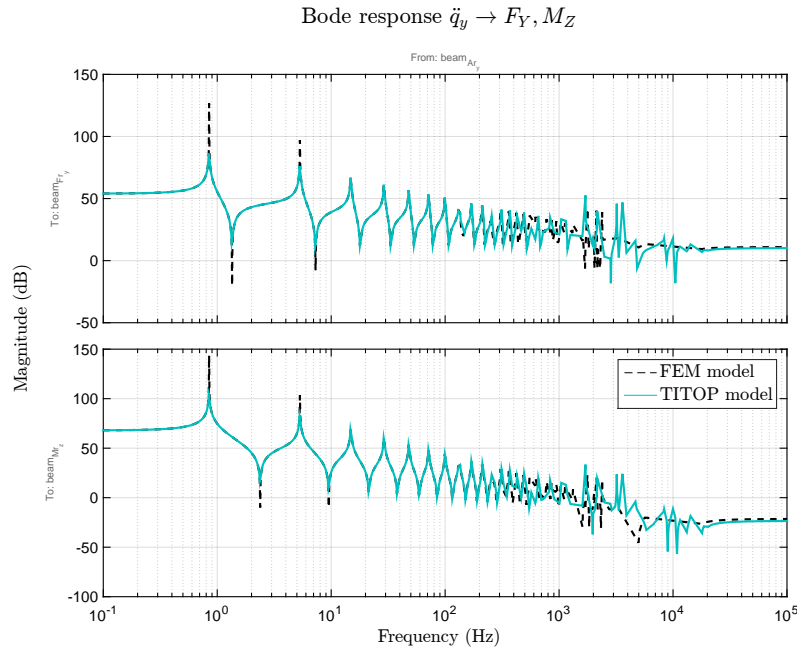
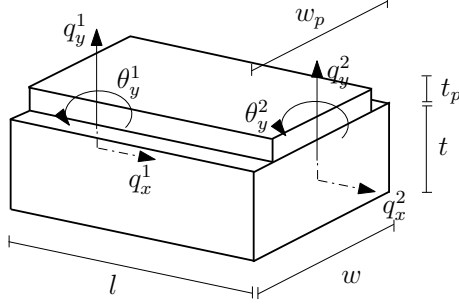


Figure 6.6: Frequency Response of the transmitted torque and force to the hub by the chain of flexible beams when vertical accelerations are applied to the root (see Fig. 6.5)

child-beams is changed through the addition of rotation matrices at the connection points, $[R_i]$, a more complex geometry can be obtained. The introduction of rotation matrices is better shown in the two-link flexible arm example provided in Sec. 6.3.

6.1.2 Beam with Bonded Piezoelectric Material

As an illustrative example of the extension to piezoelectric materials, let us consider a beam linking two substructures at both ends with a piezoelectric strip which has been appropriately bonded to one side, as seen in Fig. 6.7. The thickness of the piezoelectric strip is t_p , with a width denoted by w_p , Young's modulus E_p , density ρ_p and cross-section inertia I_p . The piezoelectric strip is used as an actuator by controlling the voltage v applied to the electrodes, creating a constant electric field $E_3 = v/t_p$ across the thickness of the laminate.

**Figure 6.7:** Piezoelectric beam element

Beam Parameters	Symbol	Value
Number of Elements	n	3
Total length	L	0.50 m
Element length	$l = L/n$	0.17 m
Thickness	t	9.53 mm
Width	w	30.00 mm
Volumetric Density	ρ	2600 kg/m ³
Elastic modulus	E	60 GPa
Piezo Parameters	Symbol	Value
Number of Elements	n	0.5
Element length	$l = L/n$	0.17 m
Thickness	t_p	2 mm
Width	w_p	30 mm
Volumetric Density	ρ_p	7600 kg/m ³
Elastic modulus	E_p	50 GPa
Piezoelectric Constant	d_{31}	-150×10^{-12} m/V
Dielectric Constant	ϵ_{33}^T	1.59×10^{-12} F/m

Table 6.1: Table of beam and piezoelectric parameters

The beam is modeled with a classic FE decomposition in several beam elements of length l . The beam has the same geometric properties as the piezoelectric strip but denoted without the p subindex: t, w, E, ρ and I . Since the piezoelectric laminate is glued to the beam, the mass and stiffness matrices of a beam element can be obtained as a sum of the contributions of the beam and the piezoelectric material. Thus:

$$[\mathcal{M}_{qq}] = [\mathcal{M}_{qq}]_{beam} + [\mathcal{M}_{qq}]_{piezo} \quad (6.1)$$

$$[\mathcal{K}_{qq}] = [\mathcal{K}_{qq}]_{beam} + [\mathcal{K}_{qq}]_{piezo} \quad (6.2)$$

The matrices of Eqs. (6.1) and (6.2) are detailed in Appendix B, computed with classical FE decomposition with beam elements. With further FE decomposition to the piezoelectric strip, the following coupling matrix and capacitance matrix are obtained:

$$[\mathcal{K}_{qv}] = \begin{bmatrix} -d_{31}E_p w_p \\ 0 \\ -d_{31}E_p w_p(t + \frac{t_p}{2}) \\ d_{31}E_p w_p \\ 0 \\ d_{31}E_p w_p(t + \frac{t_p}{2}) \end{bmatrix} \quad [\mathcal{K}_{vv}] = \frac{w_p l}{t_p} (\epsilon_{33}^T - d_{31}^2 E_p) \quad (6.3)$$

where d_{31} is the piezoelectric constant under constant stress which relates the shrinkage observed in the direction 1 when an electric field E_3 is applied along the direction of

polarization 3. The coefficient ϵ_{33}^T is the dielectric constant of the material.

The global mass, stiffness, coupling and capacitance matrices are obtained by appending the elements matrices along the diagonal. Common node points between two points are simply added together. As an example the casting of stiffness matrices is given bellow for a 2×2 case:

$$[\mathcal{K}_{qq}]^1 = \begin{bmatrix} k_{11}^1 & k_{12}^1 \\ k_{21}^1 & k_{22}^1 \end{bmatrix}; \quad [\mathcal{K}_{qq}]^2 = \begin{bmatrix} k_{11}^2 & k_{12}^2 \\ k_{21}^2 & k_{22}^2 \end{bmatrix} \rightarrow [K_{uu}] = \begin{bmatrix} k_{11}^1 & k_{12}^1 & 0 \\ k_{21}^1 & k_{22}^1 + k_{11}^2 & k_{12}^2 \\ 0 & k_{21}^2 & k_{22}^2 \end{bmatrix} \quad (6.4)$$

Obtaining the global piezoelectric coupling matrix is more complicated since it depends on the desired profile of voltages for the piezoelectric strips. If the same voltage is applied among all the strips then the assembly is straightforward:

$$[\mathcal{K}_{qv}]^1 = \begin{bmatrix} k_{1v}^1 \\ k_{2v}^1 \end{bmatrix}; \quad [\mathcal{K}_{qv}]^2 = \begin{bmatrix} k_{1v}^2 \\ k_{2v}^2 \end{bmatrix} \rightarrow [K_{uv}] = \begin{bmatrix} k_{1v}^1 \\ k_{2v}^1 + k_{1v}^2 \\ k_{2v}^2 \end{bmatrix} \quad (6.5)$$

$$[\mathcal{K}_{vv}]^1 = [k_{vv}^1]; \quad [\mathcal{K}_{vv}]^2 = [k_{vv}^2] \rightarrow [K_{vv}] = [k_{vv}^1 + k_{vv}^2] \quad (6.6)$$

However, if a different voltage is applied for each strip on each element then one has:

$$[\mathcal{K}_{qv_1}]^1 = \begin{bmatrix} k_{1v_1}^1 \\ k_{2v_1}^1 \end{bmatrix}; \quad [\mathcal{K}_{qv_2}]^2 = \begin{bmatrix} k_{1v_2}^2 \\ k_{2v_2}^2 \end{bmatrix} \rightarrow [K_{uv}] = \begin{bmatrix} k_{1v_1}^1 & 0 \\ k_{2v_1}^1 & k_{1v_2}^2 \\ 0 & k_{2v_2}^2 \end{bmatrix} \quad (6.7)$$

$$[\mathcal{K}_{vv}]^1 = [k_{vv}^1]; \quad [\mathcal{K}_{vv}]^2 = [k_{vv}^2] \rightarrow [K_{vv}] = \begin{bmatrix} k_{vv}^1 & 0 \\ 0 & k_{vv}^2 \end{bmatrix} \quad (6.8)$$

In this last case, the applied voltage is a vector containing the different voltages applied along the assembled beam, whereas in the first case voltage is a scalar. The second option might be more suitable when a voltage profile has to be applied along the beam.

After FE assembly, the complete FE model of the beam with bonded piezoelectric material is obtained. The Hurty's Method is applied to the FE model as explained in Sec 5.4 and the TITOP model is obtained. Properties are extracted from the data of Table 6.1. Three beam segments with piezoelectric strips are concatenated in two different manners: one considering the same voltage applied to the strips (single-voltage case), the other one considering that different voltages can be applied to the strips (multi-voltage case).

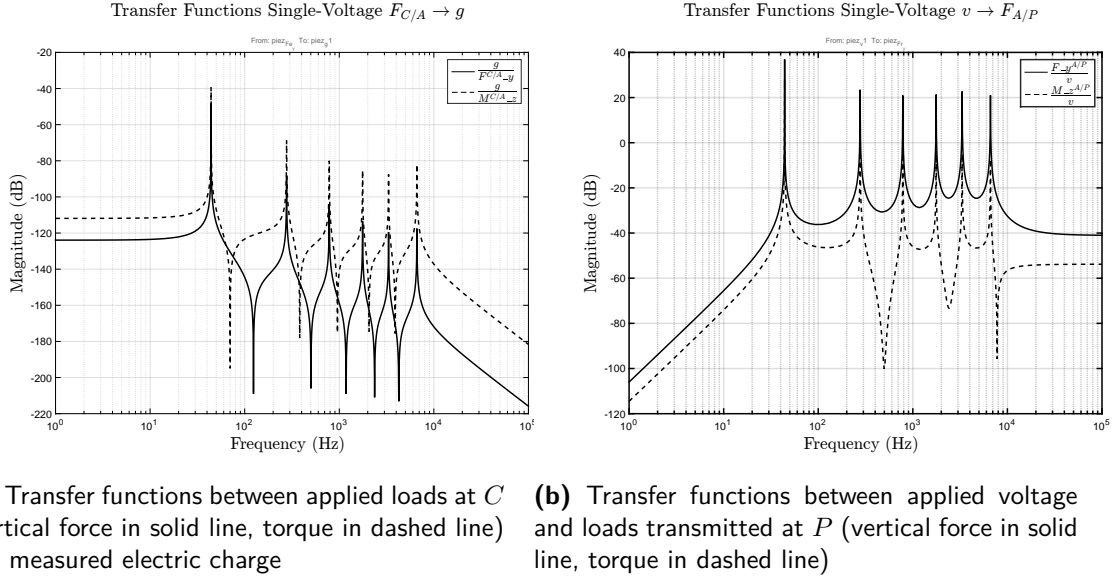
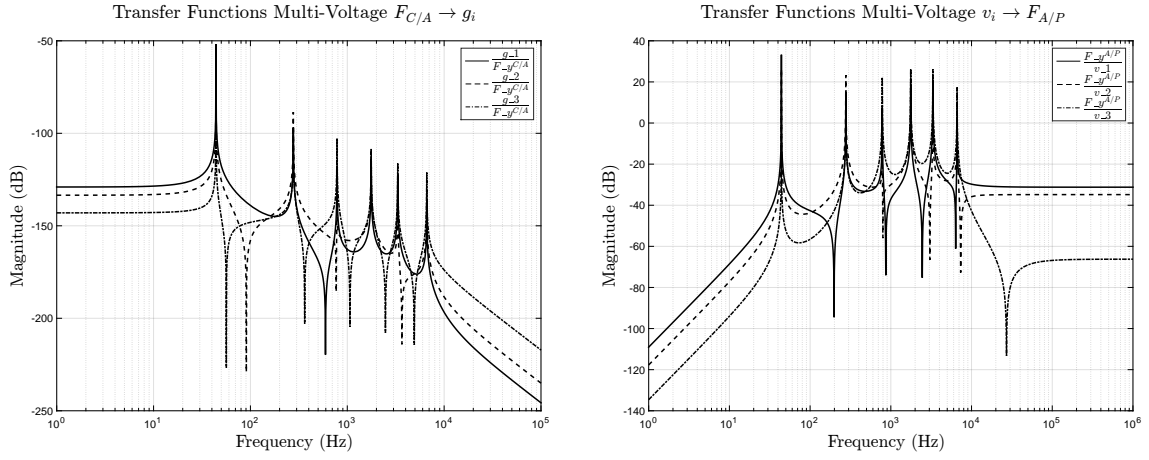


Figure 6.8: Transfer functions of the single voltage case

Figures 6.8a and 6.8b show the frequency response of the beam when one single-voltage is applied. Figure 6.8a shows the frequency response of the measured electric charge when a force/torque is applied at the end C of the concatenation of beams. Figure 6.8b shows the frequency response of the transmitted force/load at point P when voltage is applied. The first resonant frequency appears at 68 Hz, fast enough for the majority of large flexible systems. It can be evaluated that the transfer voltage/load is non-collocated (no alternance of poles/zeros) whereas the transfer load/charge is. This will affect the evaluation of control strategies in Chap. 7.

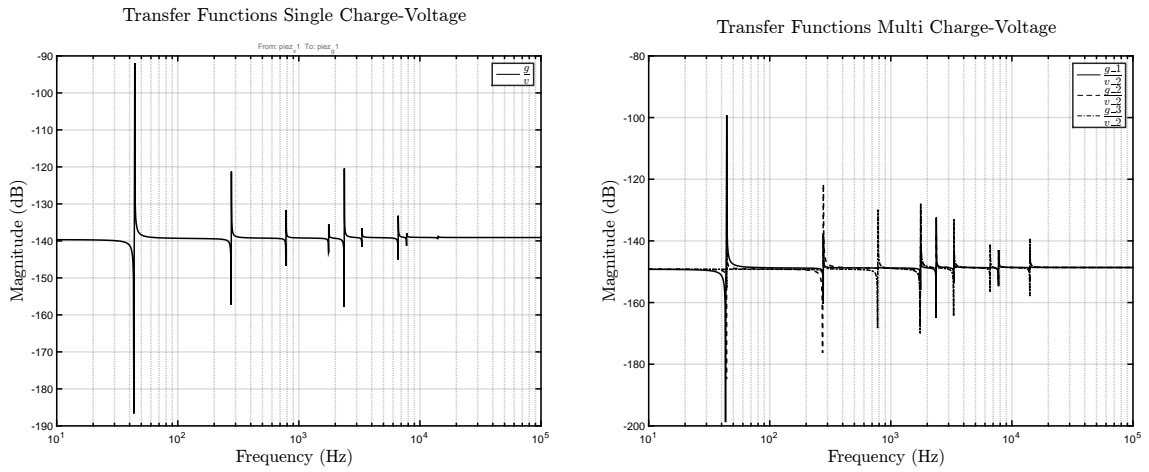
Figures 6.9a and 6.9b show the frequency response of the beam for the multi-voltage case. The first resonant frequency continues to be 68 Hz, but this time versatility is increased because there are more different voltage profiles which can be used. Figure 6.9a shows the frequency response of the electric charge of the i -th strip, g_i , when a vertical force is applied at the end, $F_{C/A}$. Figure 6.9b shows the frequency response of the transmitted vertical force at point P , $F_{A/P}$, when applying a voltage v_i to the i -th piezoelectric strip. In Fig. 6.9b, it can be evaluated that the strip located near connection point P (associated voltage v_1) has the highest gain, whereas the one located near connection point C (associated voltage v_3) has the lowest gain.

Finally, the transfer between the measured electric charges and the applied voltages can be computed. This is shown in Fig. 6.10a for the single-voltage case and in Fig. 6.10b for the multi-voltage case. It can be seen that the poles/zeros alternate, offering possibilities of collocated control schemes. However, the separation between poles and zeros is negligible, so the system does not present a good controllability with this strategy. This concept will be recalled in Chap. 7, and it is a direct consequence of the DP form of the TITOP model. Since the beam is symmetric, the poles of the system, which is considered as *clamped-free*, coincide with the transmission zeros, which correspond to the system *free-clamped*. Other



(a) Transfer functions between applied loads at C and measured electric charge (multi-voltage case) (b) Transfer functions between applied voltage and loads transmitted at P (multi-voltage case)

Figure 6.9: Transfer functions of the multi- voltage case



(a) Single Voltage \rightarrow Charge transfer function (b) Multi-Voltage \rightarrow Charge transfer functions

Figure 6.10: Charge-Voltage transfer functions of the concatenated flexible piezoelectric beam

measurements should be used if an increased controllability is desired.

6.1.3 Beam Parametric Variations

This section studies the parameterization possibilities of beam-like structures using the TITOP modeling technique. This is needed to gauge the potential use of this model for integrated control/structure design purposes. The parameterization is done in two different ways: considering length variation without constraints (length variation of a single flexible beam) and restraining total length variation (length variation of a chain of flexible beams). Complemen-

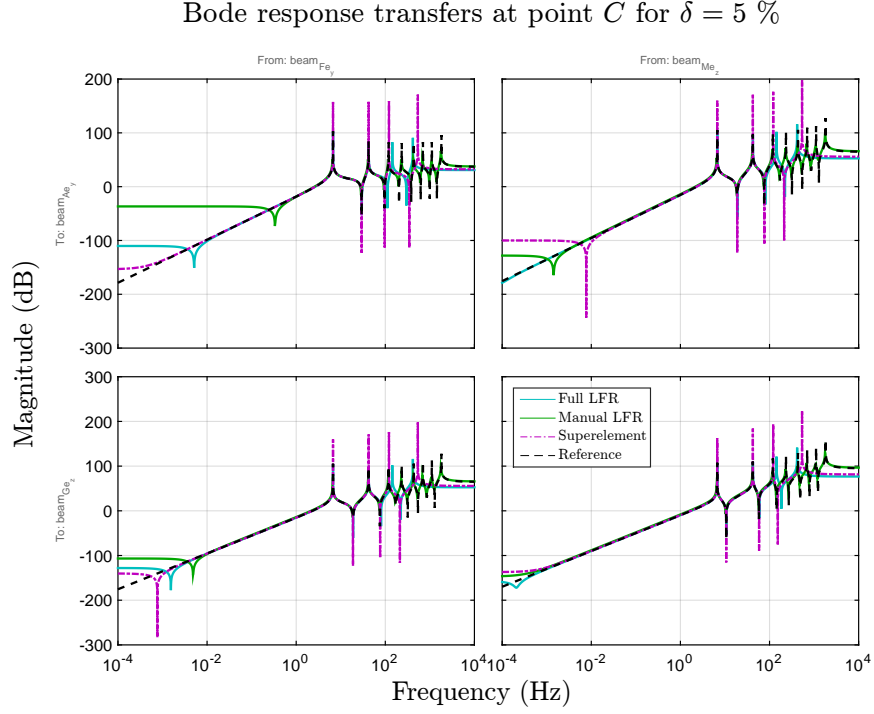


Figure 6.11: Transfer Functions at point C for small variations on the beam's length

tary figures for this section can be found in Appendix E. Only the most representatives are presented hereafter for the two cases.

Length Variation of a Single Beam

For this case, the length variation of a single beam in TITOP model form is studied with different approaches. One approach is the one stated in Sec. 5.5, localizing the different matrices where the length L appears as a parameter. This approach is called *manual LFR*, since the parameterization is done “manually”. Another approach is the one called “full LFR”, where a classic 3rd order analytic FE model is derived as a function of L . The last approach for comparison is the superelement technique (see Appendix A), which uses analytic 5th order FE decomposition to derive the parametric TITOP model of a beam.

Simulations are run for a beam of total length $L = 1$ m, which can vary freely within the interval $\delta_l \in [0.5, 1.5]$, that is, a 50% of variation range. LFR models are derived for each approach (manual, full and superelement), sampled for a set of different random lengths and then compared with a reference model which consists of a FE model developed for each sampled length. A set of one hundred samples was used to evaluate the approaches' error in Table 6.2. The mean error, μ , and the standard deviation, σ , have been computed for the first five frequencies of the beam. As it can be evaluated, the full and superelement LFR models are more accurate than the manual LFR, as expected. Particular attention has been

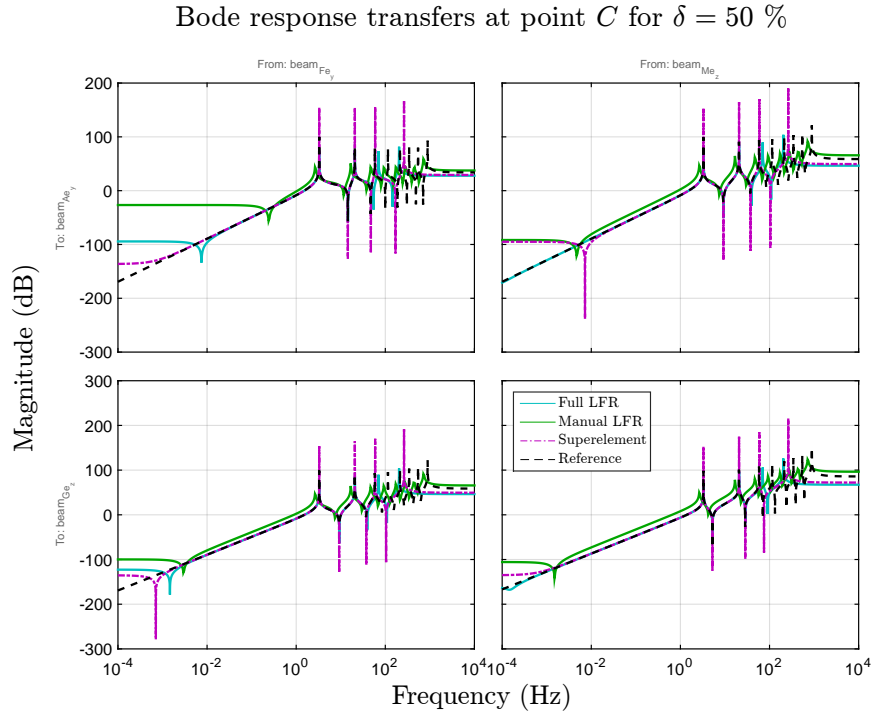


Figure 6.12: Transfer Functions at point C for large variations on the beam's length

Value	Reference	Full LFR	Manual LFR	Superelement
Mean Error μ	-	0.002	0.0654	0
Standard Deviation σ	-	$0.41 \cdot 10^{-8}$	0.05	$0.13 \cdot 10^{-8}$
Δ size	-	28	20	19
f_1 ($L = 1.05$ m)	6.71	6.71	6.71	6.71
f_1 ($L = 1.50$ m)	3.29	3.29	2.84	3.29

Table 6.2: Error analysis single beam parameterization for 100 samples

given to the computation of the first flexible mode, f_1 , since in control applications it may interfere with the system's bandwidth. It is noticed that for small variations (10% range) all models predict almost the exact frequency. However, for large variations (maximum range variation) the manual LFR approach completely misses the targeted first flexible mode.

The importance of small/large variations is depicted in Figs. 6.11 and 6.12. Figure 6.11 shows the transfer functions load-acceleration at connection point C for small variations. In this case, all approaches are in agreement. However, when large variations are desired (see Fig. 6.12) manually added parameterization fails to predict the exact behavior of the system. Full and superelement models are more desirable when accuracy is required in a large variation range.

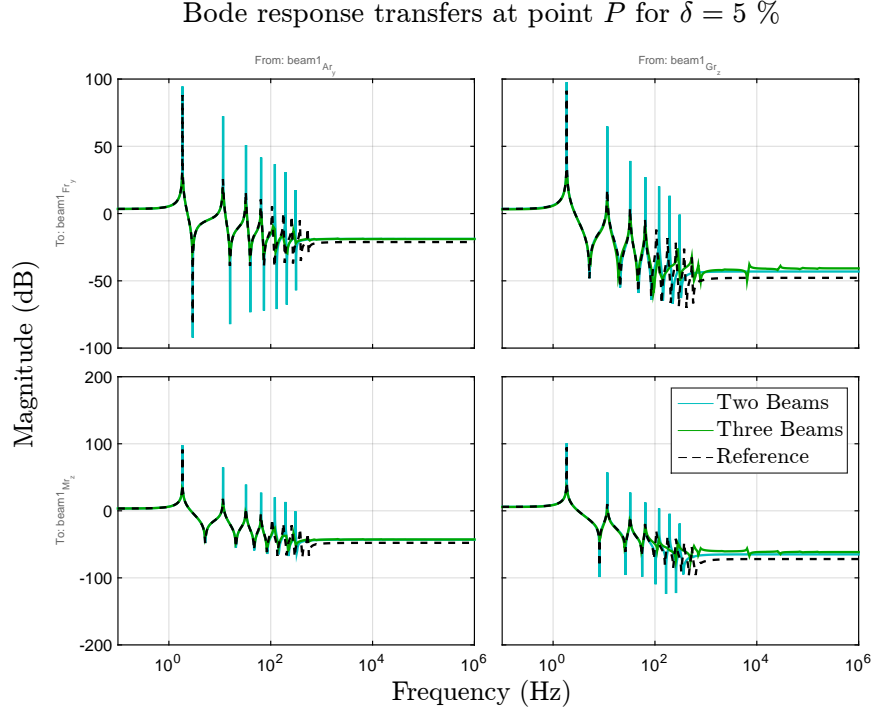


Figure 6.13: Transfer Functions at point P for small variations on the beam's length inside the chain of beams

Constrained Length Variation in a Chain of Beams

This illustration is motivated by a future usage of varying the length L of a beam: piezoelectric strip placement along a deployable mast, while the total mast's length is constant. For this purpose, a fixed total length of $L = 2$ m is considered for the linking of two flexible beams, i.e., the connection among the beams must always be equal to 2 m. Two different configurations are proposed: two and three flexible beams concatenation.

For the case of concatenation of two flexible beams while the total length is restricted to $L = 2$ m, one beam is allowed to vary within the range of $\delta_l \in [0.5, 1.5]$, while the other one is parameterized as $L - \delta_l$. Obviously, since the two beams sum up $L = 2$ m, the flexible modes must always be the same ones and the variation of δ_l indicates only at what point one beam ends and the next one starts. The three flexible beams concatenation consists of three flexible beams, one can vary with $\delta_l \in [0.5, 1.5]$, the one at the middle of the chain has a fixed length of $l_p = 0.2$ m and the remaining one is parameterized as $L - \delta_l - l_p$. Since all beams have identical properties, flexible modes must be always equal, and the parameterization only indicates at what location the beam of length l_p can be found in the chain.

Figures 6.13 and 6.14 show the frequency response at connection point P (the root of the chain) for small and large variations respectively. The parameterized models are obtained with full parameterization approach. The reference model is a 10-nodes FE model of a beam

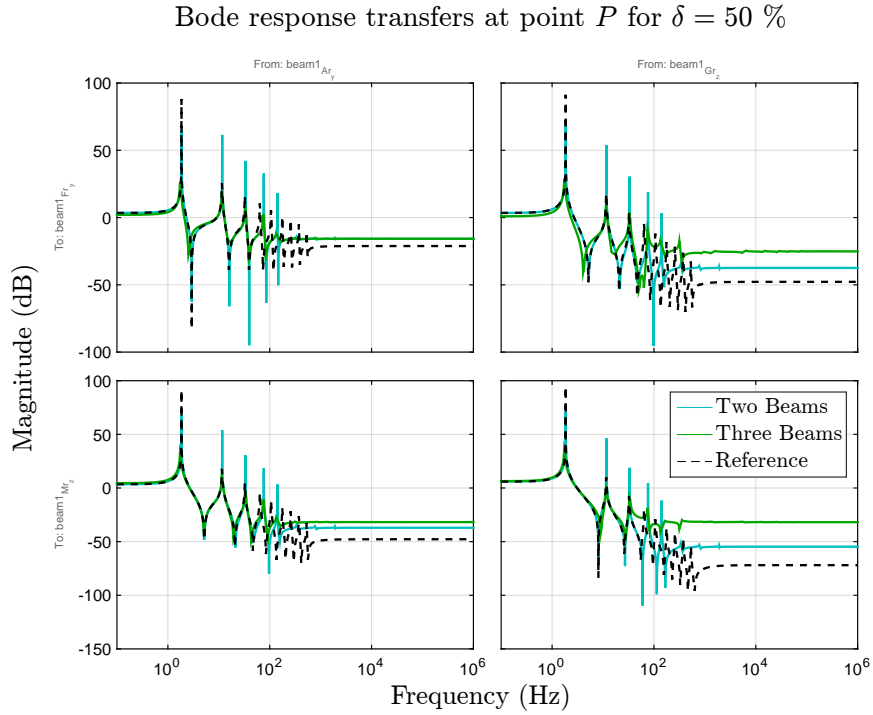


Figure 6.14: Transfer Functions at point P for large variations on the beam's length inside the chain of beams

two meters long. It is shown that flexible modes are always located at the same values for both large and small variations of δ_l . Therefore, varying δ_l is equivalent as translating longitudinally the beam of length l_p . This can be useful for parameterizing piezoelectric strips location along a mast, for example. However, the size of the associated Δ blocks of the associated LFR models is larger than the ones of the single beam variation. The two-beams case has a Δ block with 48 occurrences of δ_l , while the three-beams case has 51. Indeed, these values are the almost the double of the single beam case.

Other possible variations

Only length variation has been explained throughout this section since it is the most representative parameter for beam-like structures. Varying this parameter not only significantly affects the first flexible modes, but also the total mass of the system. In addition, this parameterization can be constrained to a constant value of total length so that different distributions of the child beams can be modeled.

Other parameters can be variated as well. The most interesting ones are the geometric properties of the beam's cross-section, since they are directly correlated with the stiffness and total mass. The geometric shape of the cross-section (solid rectangular, solid circular, hollow cylindrical, I-section, etc) play a crucial role on the value of the parameter EI and the total

mass. Beam's density or Young's modulus can also be varied, but these parameters have usually have been set before hand.

However, these parameters could imply a larger Δ block, which can quickly become computationally expensive. For example, the parameterization of a solid rectangular cross-section of height t and width b gives a LFR model with a 71×71 Δ block, 52 occurrences for t and 19 occurrences for b . If length variation is desired as well, the Δ block results in a more than 100×100 Δ block.

6.2 Planar Rotatory Flexible Spacecraft

To demonstrate the validity of the TITOP modeling method for a FMS modeling problem with rigid and flexible bodies, a maneuvering flexible spacecraft is presented. A rotating flexible spacecraft is often modeled as a coupled rigid hub and flexible beam-like structures with tip masses at their ends. This section provides a generic approach for modeling such a system, which can be expanded to every kind of FMS. Results will be compared with another modeling approach based on the largely accepted AMM [Junkins 93], demonstrating the less sensitivity of the TITOP modeling method to changes in boundary conditions.

6.2.1 Spacecraft System description

The system is composed of a rigid main hub with four identical cantilevered flexible appendages and tip masses as shown in Fig. 6.15. The configuration parameters are provided in Table 6.3. Under normal operation, the spacecraft undergoes planar rotational maneuvers about the inertially fixed axis \vec{z} . The spacecraft body frame is attached to the center of mass of the rigid hub, and it is denoted by a right-handed triad \vec{x} , \vec{y} and \vec{z} . The rotation about the axis \vec{z} is denoted by the angle θ and the translational deformation of each tip by w_{tip}^i , with superscript i denoting the beam number.

The system is actuated by three different torques. The main torque, t_{hub} is provided by the main hub about the axis \vec{z} . Two additional input torques, $t_{tip,1}$ and $t_{tip,2}$, are applied at the tip masses 1-3 and 2-4 respectively. These torques can be applied purposely for control reasons or can be the result of environment disturbances.

6.2.2 Spacecraft System modeling

The modeling problem of a single axis rotating flexible spacecraft is addressed extensively using two modeling schemes: TITOP method and AMM method.

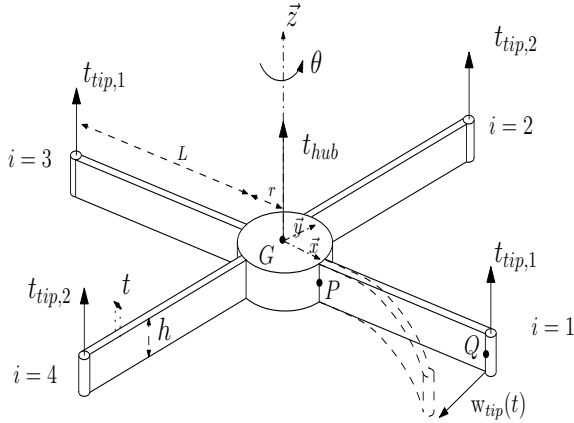


Figure 6.15: Rotatory Flexible Spacecraft

Parameters	Symbol	Value
Hub radius	r	0.31 m
Hub mass	m_h	233.50 kg
Hub inertia	J_h	10.85 kg/m ²
Beam Mass Density	ρ	1.30 kg/m
Beam Elastic modulus	E	75.84 GPa
Beam length	L	1.22 m
Beam thickness	t	3.18 mm
Beam height	h	0.15 m
Tip mass	m_t	2.29 kg
Tip mass inertia	J_t	2.44 g/m ²
Nodes beam FEM	nod	11
Number of AM	asm	13

Table 6.3: Spacecraft configuration parameters

TITOP approach

The TITOP approach needs two sets of data. The first one corresponds to structural data: rigid body matrices of the hub and tip masses, and a FE model for the beams. The second one corresponds to connection matrices: for each appendage, the kinetic transportation matrix τ_{GP} and the rotation frame matrix R must be provided.

The rigid body matrices are straightforward for the planar case:

$$J_G^{Hub} = \begin{bmatrix} m_h & 0 & 0 \\ 0 & m_h & 0 \\ 0 & 0 & J_h \end{bmatrix} \quad J_Q^{Tip} = \begin{bmatrix} m_t & 0 & 0 \\ 0 & m_t & 0 \\ 0 & 0 & J_t \end{bmatrix} \quad (6.9)$$

The kinematic models between points G and P_i , being i the appendage number i , are in the planar case:

$$\tau_{P_1G} = \begin{bmatrix} 1 & 0 & 0 \\ 0 & 1 & r \\ 0 & 0 & 1 \end{bmatrix} \quad \tau_{P_2G} = \begin{bmatrix} 1 & 0 & 0 \\ 0 & 1 & -r \\ 0 & 0 & 1 \end{bmatrix} \quad \tau_{P_3G} = \begin{bmatrix} 1 & 0 & -r \\ 0 & 1 & 0 \\ 0 & 0 & 1 \end{bmatrix} \quad \tau_{P_4G} = \begin{bmatrix} 1 & 0 & r \\ 0 & 1 & 0 \\ 0 & 0 & 1 \end{bmatrix} \quad (6.10)$$

and the rotation matrices can be written as follows:

$$R_i = \begin{bmatrix} \cos \beta_i & -\sin \beta_i & 0 \\ \sin \beta_i & \cos \beta_i & 0 \\ 0 & 0 & 1 \end{bmatrix}_{App \rightarrow Hub} \quad (6.11)$$

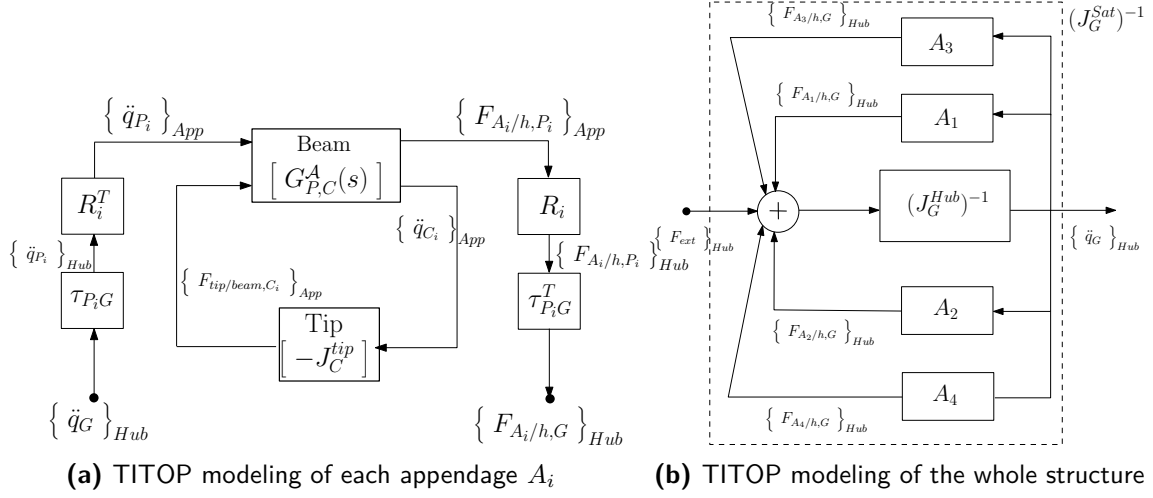


Figure 6.16: TITOP Modeling of the rotatory spacecraft

where β_i is the angle of the i th appendage i with \vec{x} . Beam's FE model is obtained with classical FE discretization in five elements. Mass and stiffness matrices are transformed as explained in Sec. 5.2 to get the TITOP model of the beam. As the tip mass is considered as rigid, there is no need of applying CMS to this substructure, Eq. (6.9) is used for such a purpose.

The assembly for each appendage is done as shown in Fig. 6.16a. Accelerations at the hub are transmitted to the attachment point P_i through the kinematic model $\tau_{P_i G}$, and then changed to the appendage frame through R_i^T . The acceleration of the hub, together with the load exerted by the tip mass at the opposite end, are the inputs of the beam TITOP model, which delivers the acceleration transmitted to the tip mass and the load transmitted to the hub, which has to be transported to the hub and change its frame.

TITOP being a generic six degrees of freedom approach, it is restricted to the three planar degrees of freedom. Thus, the acceleration and loads vectors used in Figs. 6.16a and 6.16b have three components corresponding to the two translations in the plane $\pi(\vec{x}, \vec{y})$ and one rotation around \vec{z} .

The same process is performed to the four appendages, obtaining the final assembly shown in Fig. 6.25b. It can be observed that the resulting system, $(J_G^{Sat})^{-1}$, has the applied torques as inputs when the following inputs are assigned the following values: $(F_{ext} = \{0 \ 0 \ t_{hub}\}^T)$, and the hub accelerations as outputs ($\ddot{q}_G = \ddot{\theta}$). Tip acceleration can be observed through the signal transmitted from the beam to the tip and tip torques $t_{tip,1}$ and $t_{tip,1}$ can be added to $F_{tip/beam,C_i}$ loads with the help of a sum block.

AMM Approach

For the comparison objective, the classical assumed modes (AM) solution is exploited. Although AMM can be applied in many different ways, the most general case is deriving the hub-beam-tip equations.

The AMM assumes a decoupled spatial and time deformation approximated by the series:

$$w(x, t) = \sum_{i=1}^{asm} \phi_i(x) q_i(t) \quad (6.12)$$

where $\phi_i(x)$ denotes the assumed mode shape, $q_i(t)$ denotes the i -th generalized coordinate, asm denotes the number of terms retained in the approximation and x the distance from the considered point in the beam to the attachment point.

Then, the kinetic and potential energy of the spacecraft, containing space and time partial derivatives of $w(x, t)$, are derived using the approximation in Eq. (6.12) and performing the integration with respect to x , writing the kinetic energy and potential energy in the quadratic forms:

$$T(t) = \frac{1}{2} \sum_{i=1}^{asm} \sum_{j=1}^{asm} M_{ij} \dot{q}_i(t) \dot{q}_j(t) = \frac{1}{2} \{\dot{q}(t)\}^T [M] \{\dot{q}(t)\} \quad (6.13)$$

$$V(t) = \frac{1}{2} \sum_{i=1}^{asm} \sum_{j=1}^{asm} K_{ij} q_i(t) q_j(t) = \frac{1}{2} \{q(t)\}^T [K] \{q(t)\} \quad (6.14)$$

where M_{ij} denotes the (i, j) -th element of the symmetric mass matrix $[M]$ (respectively for the stiffness matrix $[K]$). The equations of motion follow on introducing T and V into Lagrange's equations:

$$\frac{d}{dt} \left(\frac{\delta T}{\delta \dot{q}_r} \right) - \frac{\delta T}{\delta q_r} + \frac{\delta V}{\delta q_r} = Q_r, \quad r = 1, \dots, asm \quad (6.15)$$

where Q_r denotes the generalized non-conservative forces, the applied torques. The following equations of motion are obtained:

$$\sum_{j=1}^{asm} M_{rj} \ddot{q}_j(t) + \sum_{j=1}^{asm} K_{rj} q_j(t) = Q_r, \quad r = 1, \dots, asm \quad (6.16)$$

which written in matrix compact form gives:

$$[M]\{\ddot{q}(t)\} + [K]\{q(t)\} = \{Q(t)\} \quad (6.17)$$

The analytic formulation of mass and stiffness submatrices in Eq. (6.17) for the rotatory spacecraft can be found in Junkins [Junkins 93], which have been developed with the following admissible functions satisfying the boundary conditions for clamped-free appendages:

$$\phi_i(x) = 1 - \cos\left(\frac{j\pi x}{L}\right) + \frac{1}{2}(-1)^{j+1}\left(\frac{j\pi x}{L}\right)^2 \quad (6.18)$$

The admissible functions in Eq. (6.18) are known to produce very accurate results and have been adopted widely [Elgohary 15]. Equation (6.17) provides thus the desired equations of motion in which the time-varying amplitudes are generalized coordinates. Given the instantaneous vector $\{q(t)\}$, the instantaneous deformation of the structure is approximated by the assumed modes expansion.

6.2.3 Comparison of the Modeling Methods

A comparison between the TITOP modeling technique and the numerical AMM is presented. The TITOP model uses FE models of five elements for each beam, and the AMM uses 13 modes per beam. Both methods are compared with the reference FE model (FEM) of the whole structure which can be found in [Junkins 93], considered to be the most accurate.

Accuracy

First, the accuracy of the proposed TITOP modeling technique is verified. A comparison of all methods (AMM, TITOP and FEM) among the first six flexible modes is shown in Table 6.4. The computed frequencies converge accurately for the 8-DOF per appendage TITOP solution, whereas the AMM solutions are not accurate for modes 4-6, as previously seen in the frequency response. The Relative Mean Square (RMS) error of these values is shown in Fig. 6.21, showing that for the same number of degrees of freedom the TITOP modeling technique is slightly more accurate. Therefore, the TITOP modeling is able to provide accurate models which have less degrees of freedom and achieves more accurate results than the AMM.

Robustness to variations in boundary conditions

Figure 6.19a presents the effect of flexible appendages on the main hub motion, $\ddot{\theta}_{hub}$. Figure 6.19b shows the dynamic response of the tip accelerations to the hub torque, t_{hub} . Both figures are in perfect agreement with the frequency response of the reference model, FEM, until the fourth flexible mode, located at around 50 Hz. At that point, the response $t_{hub} \rightarrow \ddot{w}_{tip}$ of the AMM presents a significant error in the first anti-resonance frequency.

Mode	AMM			TITOP			Reference
No	$N = 5$	$N = 10$	$N = 15$	$N = 8$	$N = 18$	$N = 28$	$N = 100$
1	4.3731	4.3723	4.3722	4.3722	4.3722	4.3722	4.3722
2	7.9084	7.9070	7.9067	7.9066	7.9066	7.9066	7.9066
3	51.7234	51.4518	51.4259	51.4286	51.3999	51.3989	51.3987
4	53.0829	52.8066	52.7797	52.7819	52.7525	52.7515	52.7513
5	160.2661	157.5591	156.7351	156.4701	155.7516	155.7257	155.7203
6	161.0962	158.3683	157.5382	157.2609	156.5407	156.5147	156.5094

Table 6.4: Table showing the natural frequencies (ω_i , rad/s) corresponding to the first six flexible modes for each modeling method. N denotes the number of degrees of freedom per appendage. The reference frequency (ω_i^{ref}) is obtained with a FE model of 100 degrees of freedom per appendage.

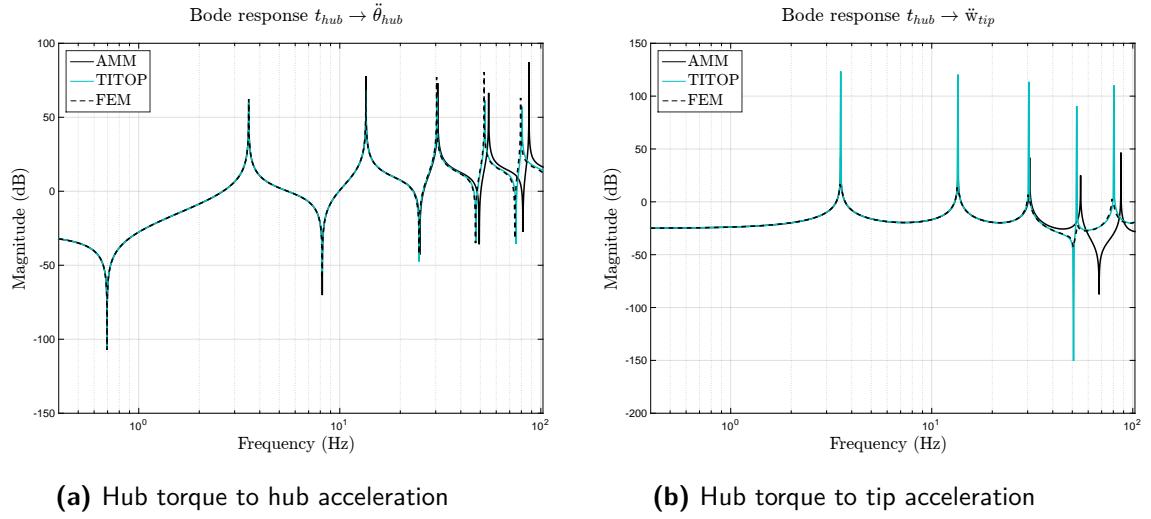


Figure 6.17: Frequency response comparison for $M_t = 2.290$ kg

As it can be evaluated, the AMM is no longer accurate for frequencies beyond the third flexible mode for this spacecraft configuration. The TITOP method, however, is accurate for the considered frequency range. This difference is due to the AMM assumption of clamped-free mode shapes, whereas real mode shapes of a hub-beam-mass system are different from a clamped-free system, as theoretically demonstrated in Elgohary [Elgohary 15]. The TITOP modeling technique does not make any approximation of mode shapes, they naturally arise when the whole system is assembled. This demonstrates that the TITOP method is less sensitive to the imposed boundary conditions, while AMM remains more sensitive due to the choice of the mode shapes. As a result, the TITOP method is valid for every type of configuration, whereas AMM is limited by the selected mode shapes.

Such sensitivity to boundary conditions is highlighted by studying the influence of a mass at the tip of each beam. Figure 6.18 shows the frequency response $t_{hub} \rightarrow \ddot{w}_{tip}$ when there is no mass at the tip of the beam, $M_t = 0$ kg, whereas Fig. 6.19 shows the same frequency response with a heavy mass at the tip, $M_t = 114.5$ kg. When there is no tip mass, the AMM

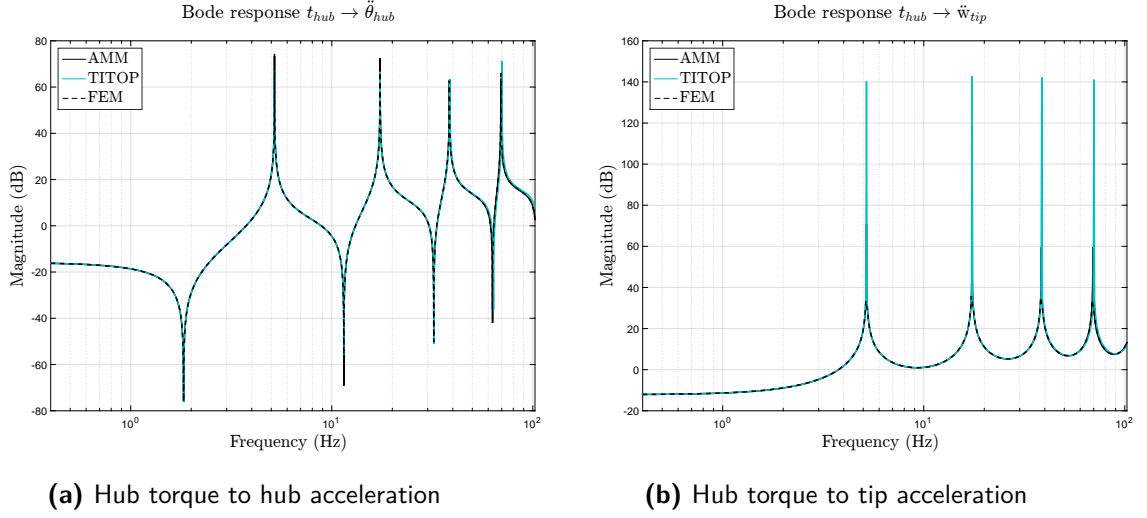


Figure 6.18: Frequency response comparison for $M_t = 0.00$ kg

is perfectly valid and coincides with the reference model, since its admissible functions fully respect the *clamped-free* boundary conditions. However, when a heavy mass is located at the tip, the clamped-free boundary conditions no longer apply, which makes AMM fail in predicting the frequency response. On the other hand, the TITOP method perfectly fits the frequency response of the reference model in all cases.

6.2.4 Spacecraft System Parameterization

The TITOP modeling technique allows taking into account the variations of certain structural parameters inside the model, since they can be easily found inside the state-space representation of the substructures. In this section parametric variations are performed to the rotatory spacecraft, including variations on beams' lengths and tip masses.

Considering the appendage as a beam, its length variations are introduced through the superelement model explained in Murali [Murali 15] and recalled in Appendix A. As demonstrated in Sec. 6.1.3, a full LFR parameterization will have the same accuracy. Tip mass variations are introduced through the rigid-body matrix of the tip mass, Eq. (6.9), as follows:

$$J_C^{Tip}(\delta_m) = \begin{bmatrix} m_t + \delta_m & 0 & 0 \\ 0 & m_t + \delta_m & 0 \\ 0 & 0 & J_t(\delta_m) \end{bmatrix} \quad (6.19)$$

After assembly, the system appears as the model shown in Fig. 6.20, with variations in tip mass Δ_{m_i} and beam's length Δ_{L_i} included in the Δ -block.

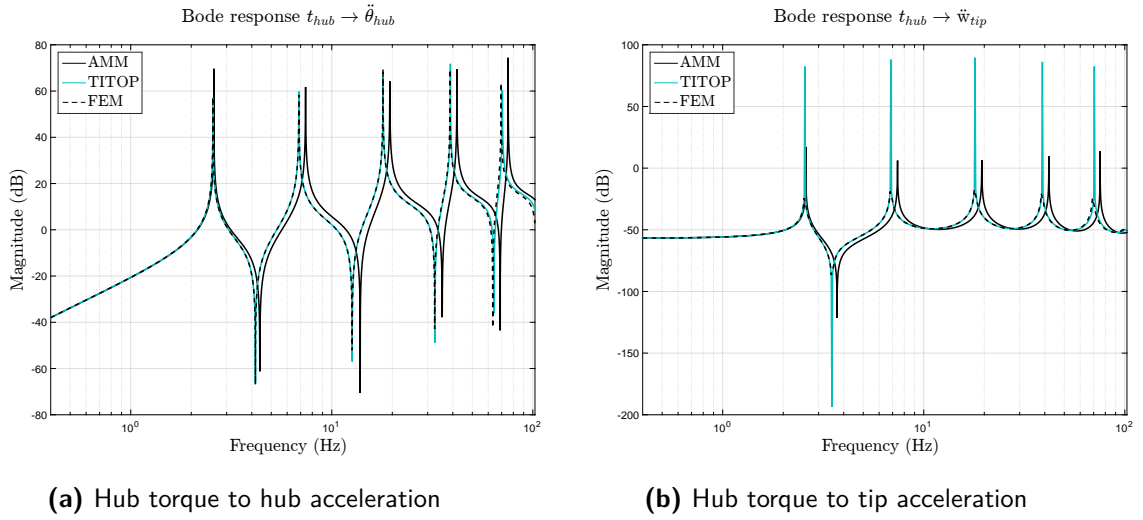
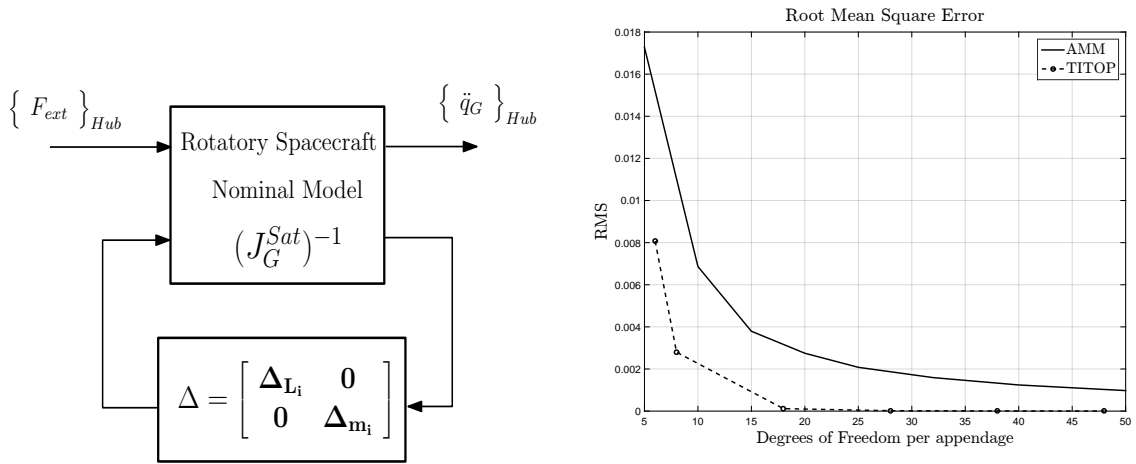
Figure 6.19: Frequency response comparison for $M_t = 114.5$ kg

Figure 6.20: Rotatory spacecraft with variations

Figure 6.21: RMSE¹ for each method (six modes)

Using this approach, dynamic behavior sensitivity analysis can be performed. As it can be seen in Fig. 6.22, the first natural frequency of the system decreases by either increasing length or increasing tip mass in all appendages in the same manner.

Nevertheless, the most interesting remark can be done when only one appendage varies its beam's length and tip's mass. As it can be appreciated in Fig. 6.23, a new frequency mode appears, not present in the case where all appendages varied their length and tip mass simultaneously. Indeed, if all appendages are identical the symmetric modes of the appendages are uncontrollable from the hub's torque and they do not appear in the frequency response. In the case of only one appendage variation, however, the asymmetry due to the variation of one single appendage makes these modes now controllable and can be found in the frequency

¹Root Mean Square Error $RMSE = \sqrt{\frac{1}{6} \sum_{i=1}^6 \left(\frac{\omega_i - \omega_i^{ref}}{\omega_i^{ref}} \right)^2}$

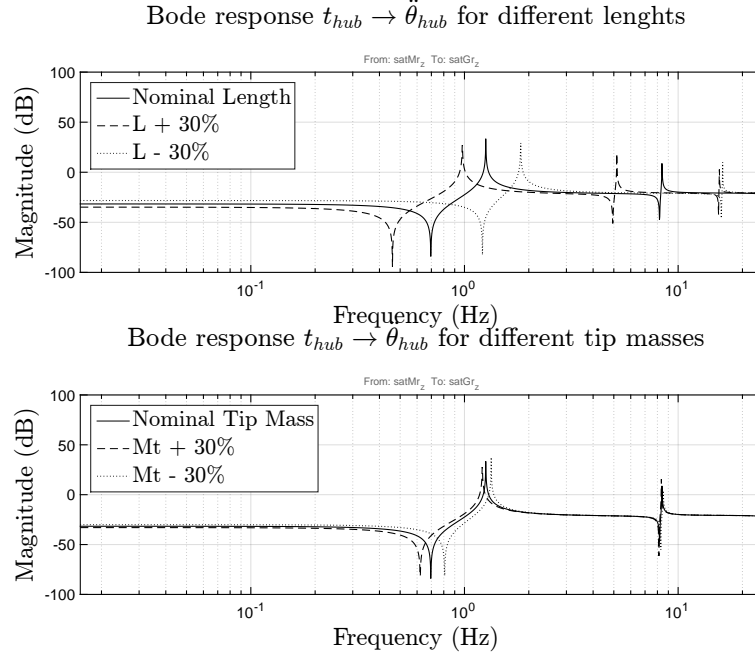


Figure 6.22: Bode system comparison when varying length and tip mass for all the appendages simultaneously

response.

As it has been demonstrated, parametrization can be easily taken into account with the TITOP method. For this problem AMM approach of Junkins [Junkins 93] considers several simplifications for the model, such as symmetric displacements between appendages. If such kind of variations were done with the AMM approach, the whole model would have been changed, re-initializing the modeling process. On the contrary, this step is avoided with the TITOP modeling technique. The TITOP model does not require re-formulating the problem since all the variations are considered from the beginning of the modeling process and individually for each appendage. The TITOP model represents simultaneously the spacecraft nominal configuration with all the possible parameter variations, whereas the AMM approach needs to compute a new model for each parameter variation.

6.3 Two-Link Flexible Manipulator

In this section, the TITOP modeling technique is compared to a nonlinear modeling technique for the case of a planar two-link flexible arm, a flexible multi-chain example where the kinematic non-linearities can be large. The objective is to evaluate the accuracy of the TITOP linear model for a control application and to determine if the non-linear terms could restrict its usage. In addition, the modeling process is explained for taking into account the revolute joint's actuator with mass and inertia at the connection points.

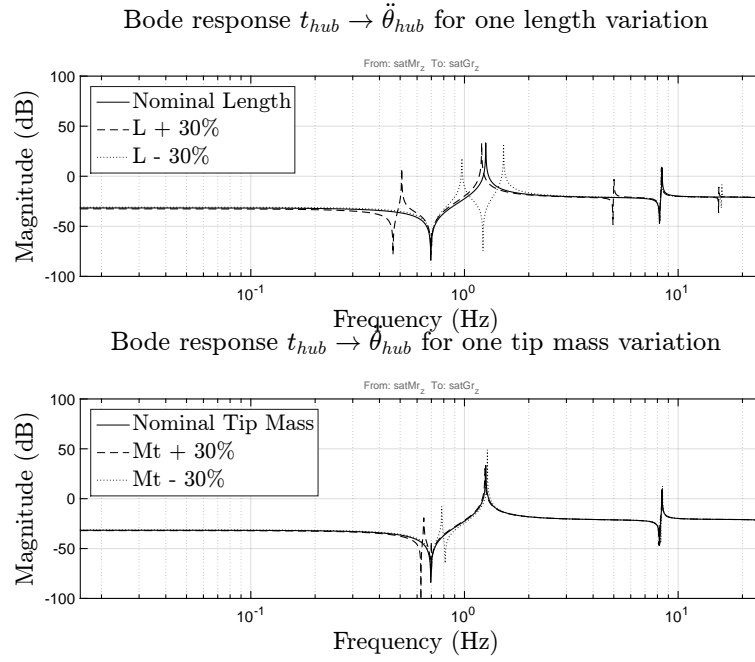


Figure 6.23: Bode system comparison when varying length and tip mass for one appendage only

The nonlinear model of the planar two-link flexible arm can be found in its explicit closed-form in Luca [Luca 91]. It consists of two flexible arms with a payload at the end of the second arm. This system is illustrated in Fig. 6.24 and its corresponding parameters are described in Table 6.5.

6.3.1 TITOP modeling of the planar two-link flexible arm

The TITOP modeling of a n -link flexible arm composed of a chain of n link flexible segments and joints starts with the individual assembly of each flexible segment to the joint. The rigid body matrix of the joint can be derived straightforward for the planar case as stated in Sec. 6.2.2:

$$J_{G_i}^{Joint_i} = \begin{bmatrix} m_{h_i} & 0 & 0 \\ 0 & m_{h_i} & 0 \\ 0 & 0 & J_{h_i} \end{bmatrix} \quad (6.20)$$

The inverse dynamics TITOP model of the flexible link i is obtained as depicted in Fig. 6.25a. The connections follow the same principles explained in Sec. 5.3, where the angular acceleration induced by the revolute joint to the system is added to the angular acceleration of the hub (the joint's rigid body matrix). The total acceleration (the one received by the joint and the one imposed by the joint's rotation) is transmitted to the channel which corresponds

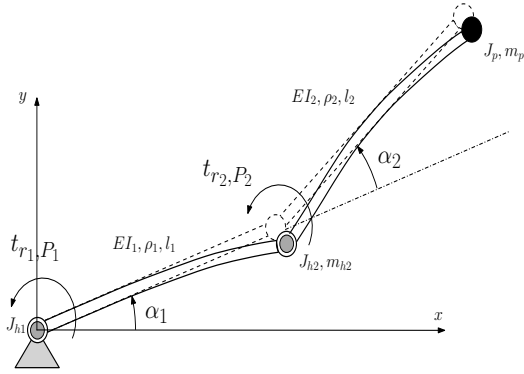


Figure 6.24: The planar two-link flexible arm

Parameters	Symbol	Value
Link 1 Inertia	J_{h1}	0.1 kg/m ²
Link 2 Inertia	J_{h2}	0.1 kg/m ²
Link 2 Mass	m_{h2}	1.0 kg
Beam 1 Density	ρ_1	0.2 kg/m
Beam 2 Density	ρ_2	0.2 kg/m
Beam 1 Cross section	EI_1	1 N·m ²
Beam 2 Cross section	EI_2	1 N·m ²
Beam 1 length	l_1	0.5 m
Beam 2 length	l_2	0.5 m
Payload Mass	m_p	0.1 kg
Payload Inertia	J_p	0.5 g/m ²

Table 6.5: Arm configuration parameters

to the acceleration at point P of the i -th flexible arm's TITOP model. The load transmitted by the i -th flexible arm to the joint at point P is subtracted from the inertial load obtained at the joint to get the resulting load to the $i - 1$ -th flexible arm, $F_{i/i-1,P_i}$. It is assumed that the flexible arm is perfectly connected to the center of the joint; i.e., no kinematic transport matrix is needed since $G_i \equiv P_i$. Finally, the applied joint's torque, t_{r_i,P_i} , is obtained as the third component of the transmitted loads for the planar case. The second channel, the one which exchanges acceleration-load at the other end of the segment (point C_i) remains unchanged for future connection to the next flexible link.

Once the TITOP models of the n flexible links have been derived, they can be assembled following the same patterns as in Secs. 5.6 and 6.2.2. The connections between the flexible arms are preceded by the rotation matrices $R_{i-1 \rightarrow i}$ or $R_{i-1 \rightarrow i}^T$, which take into account the orientation of one segment respect to the previous one. Since the TITOP technique is linear, these matrices are set with a constant value corresponding to the orientation of the structure in nominal configuration, $\alpha_i(0)$.

$$R_{i-1 \rightarrow i} = \begin{bmatrix} \cos(\alpha_i(0)) & \sin(\alpha_i(0)) & 0 \\ -\sin(\alpha_i(0)) & \cos(\alpha_i(0)) & 0 \\ 0 & 0 & 1 \end{bmatrix} \quad (6.21)$$

In Fig. 6.25, the particular case for $n = 2$ is depicted. The payload effect is fed back as in the case of the rotatory spacecraft's tip mass as in section 6.2.2. The assembled model gives the inverse dynamic model of the two-link flexible arm:

$$\begin{Bmatrix} t_{r1,P1} \\ t_{r2,P2} \end{Bmatrix} = [J_{P1,P2}^{arm}(s)] \begin{Bmatrix} \ddot{\alpha}_1 \\ \ddot{\alpha}_2 \end{Bmatrix} \quad (6.22)$$

The direct dynamics of the two-link flexible arm can be obtained with the inversion of Eq. (6.22).

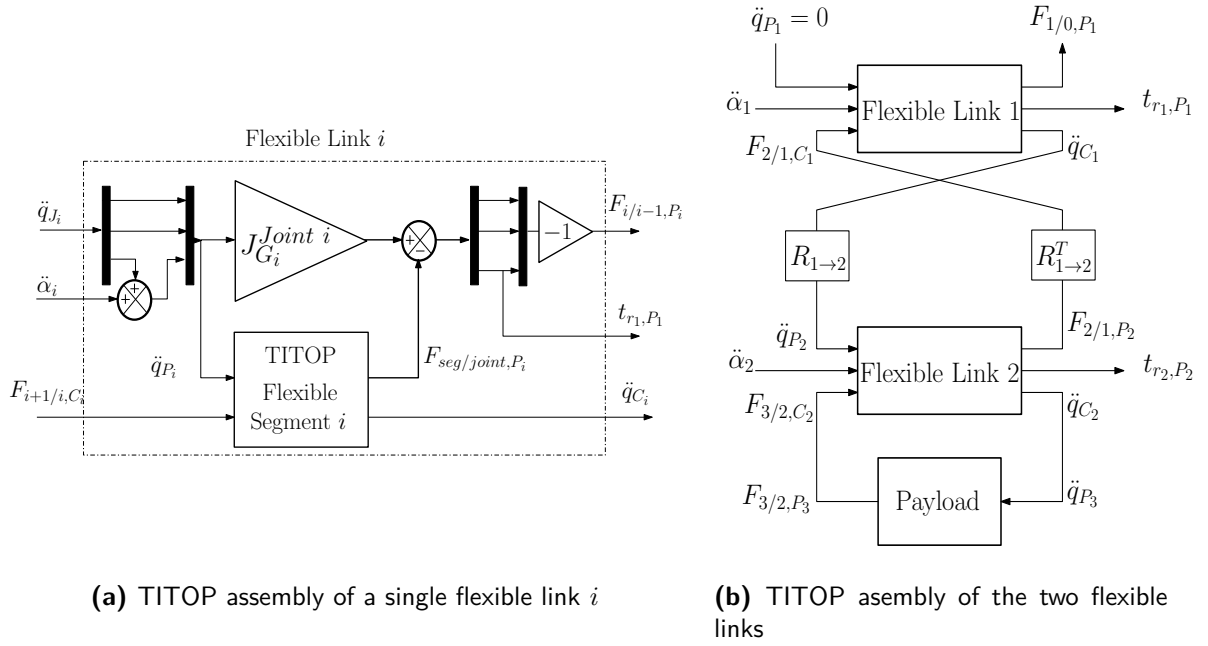


Figure 6.25: TITOP assembly of the inverse dynamics model of the two-link flexible arm

Mode	Nonlinear			TITOP		
No	$\alpha_2(0) = 0^\circ$	$\alpha_2(0) = 30^\circ$	$\alpha_2(0) = 90^\circ$	$\alpha_2(0) = 0^\circ$	$\alpha_2(0) = 30^\circ$	$\alpha_2(0) = 90^\circ$
1	8.8335	8.8348	8.8392	8.9215	8.9227	8.9284
2	16.6209	16.3947	15.7827	16.6341	16.4060	15.7884
3	101.2585	100.9695	100.2199	101.4696	101.1769	100.4178
4	144.3649	144.3386	144.2713	140.2959	140.2595	140.1671

Table 6.6: Table showing the natural frequencies (ω_i , rad/s) corresponding to the first fourth flexible modes for each modeling method of the two-link flexible arm. Three initial configurations are considered: $\alpha_2(0) = 0^\circ$, $\alpha_2(0) = 30^\circ$ and $\alpha_2(0) = 90^\circ$

6.3.2 Modeling and simulation results

In order to test the system's TITOP model, the planar two-link flexible arm with the physical parameters described in Table 6.5 is compared with the nonlinear closed-form model found in Luca [Luca 91]. The TITOP model uses a two-element FE model for each flexible segment. The FE model takes into account translations along the x and y axis of the segment, and rotations around the z axis. The model of [Luca 91] only considers translations along the y axis and the rotation around z , and it uses two assumed modes for each segment.

First, the natural frequencies of the system are compared for different nominal configurations. The comparison is shown in Table 6.6. It can be noticed that the error is not larger than 1.0% of the non-linear value for the first frequency mode, 0.01% for the second frequency mode and 0.2 % for the third frequency mode. The fourth frequency shows a discrepancy of 2.8 %. However, nothing can be concluded regarding the accuracy of the frequency modes

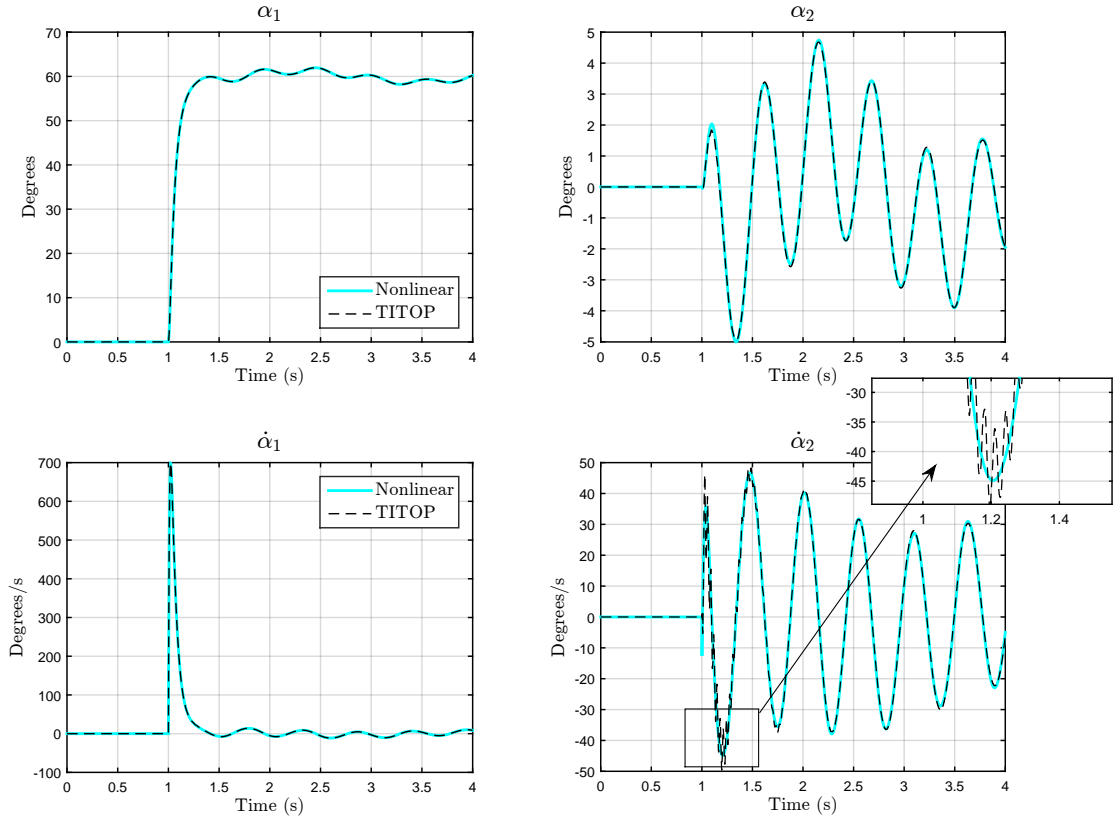


Figure 6.26: Dynamic evolution of link 1 (α_1) and link 2 (α_2) under step input ($\alpha_{ref1} = 60^\circ$) and fully extended arm ($\alpha_2(0) = 0^\circ$)

since the non-linear model uses four assumed modes computed for the nominal configuration $\alpha_2(0) = 0^\circ$. This could be an error source for the highest frequency modes. On the other hand, the TITOP model considers translations along the x axis, which might explain the differences, and it is more robust to changes in the nominal configuration (since it is equivalent to changes in the boundary conditions).

Once the models have been proved to have the same dynamics, a numerical simulation is performed to validate the direct dynamics TITOP model with the non-linear direct dynamics model in controlled evolution. The joints' rotation of the flexible arm is controlled through a Proportional-Derivative (PD) controller for each joint, taking the angular position and rate as inputs as shown in Eq. (6.23) and Fig. 5.6.

$$\begin{aligned} t_{r1,P1} &= k_{p1}(\alpha_{ref1} - \alpha_1) - k_{v1}\dot{\alpha}_1 \\ t_{r2,P2} &= k_{p2}(\alpha_{ref2} - \alpha_2) - k_{v2}\dot{\alpha}_2 \end{aligned} \quad (6.23)$$

A numerical simulation has been performed for a $\alpha_{ref1} = 60^\circ$ step command given to the first joint when the arm is fully extended ($\alpha_2(0) = 0^\circ$). The controller's gains are $k_{p1} = 160$ N·m, $k_{v1} = 11$ N·m·s, $k_{p2} = 60$ N·m and $k_{v2} = 1.1$ N·m·s. The non-linear equations of motion have been integrated via a fourth order adaptive Runge-Kutta (Dormand-Prince) method. Figure 6.26 shows the dynamic response of the joints for the first four seconds. The non-linear model and the TITOP model are in perfect agreement, even when the non-linearities are expected to be large ($\dot{\alpha} \gg 1$ rad/s). In the sub-plot corresponding to $\dot{\alpha}_2$, an additional frequency can be observed at the peaks over the first cycle, which it is not present in the non-linear model.

Therefore, the linear model provided by the TITOP modeling technique can be used as an approximation even when the non-linear terms can be large, as in the case of a two-link flexible arm. Furthermore, for the same level of modeling complexity, the TITOP model is able to provide additional frequency modes which have a more significant impact than the non-linear terms in the system's response.

This chapter has developed three representative examples of FMS modeling with the TITOP technique. The assembly, the introduction of piezoelectric effects and the consideration of parametric variations have been explained and validated for beam-like substructures. The assembly of rigid and flexible bodies has been explained throughout the flexible rotatory spacecraft example, validated through comparison with the AMM, and parameterized to evaluate the influence of asymmetric and symmetric variations in its flexible appendages. In addition, the TITOP model has demonstrated being more robust against changes in boundary conditions. Finally, assembly of substructures including revolute joints has been addressed through the example of a two-link flexible manipulator. The TITOP modeling technique has demonstrated, again, being accurate even when kinematic non-linearities are expected to be large. Chapters 4, 5 and 6 have stated and applied the modeling framework for FMS. The next chapters will be focused on developing the framework for integrated control/structure design by evaluating the different control strategies which can be studied with the TITOP modeling technique, setting the desired specifications for integrated control/structure design with \mathcal{H}_∞ control and finally applying all the concepts in the case of a flexible satellite.

Chapter

7

Control Strategies Evaluation for Control of Flexible Multibody Structures

“However beautiful the strategy, you should occasionally look at the results. ”
- Winston Churchill

Contents

7.1	Control of Rigid Body Motion	106
7.1.1	Standard Synthesis Techniques	106
7.1.2	Robust Synthesis Techniques	109
7.1.3	Synthesis Techniques Including Active Damping	110
7.1.4	Decentralized VS Centralized Control and Optimization	111
7.2	Control of Flexible Modes	113
7.2.1	Acceleration Feedback	114
7.2.2	Integral Force Feedback	116
7.2.3	Other Controller Architectures	117
7.2.4	Robustness to Pole/Zero Flipping	118
7.2.5	Real Actuator/Sensor Dynamics	119

This chapter is devoted to the evaluation of different control strategies which lead to the synthesis of a controller satisfying spacecraft dynamics' specifications. A discussion of the different procedures for controlling rigid body and flexible motion is provided throughout the chapter, highlighting the control architectures that could be more advantageous for integrated control/structure design.

SINCE the structured \mathcal{H}_∞ synthesis allows the choice of controller's architecture, a set of different control strategies must be evaluated in order to select the architecture which offers more possibilities for successful optimization. The controller architecture has to address the control of rigid and flexible motion in order to ensure attitude control pointing performance and robustness. This chapter shows the main strategies for controlling rigid body motion and damping of flexible modes, applying them to practical examples and piezoelectric TITOP models. In Sec. 7.1 the control of the rigid body motion is explained, where standard, robust and centralized/decentralized synthesis techniques are discussed and evaluated. In Sec. 7.2, the active damping of flexible modes with collocated actuator/sensor pairs is evaluated with several strategies and tested against pole/zero flipping and real actuator dynamics.

7.1 Control of Rigid Body Motion

The attitude control of a flexible space structure implies, in the first place, controlling spacecraft's motion as a rigid body, i.e., the control of the angles about the roll, φ , pitch, θ , and yaw, ψ , axis. In addition, the analysis must include the effects that structural flexibility could have in those angles so that they can always meet pointing requirements. Sometimes only the control of the rigid body motion via the use of reaction wheels, thrusters and magnetotorquers located at the satellite's platform is enough for the mission's success. However, when flexibility starts being highly coupled with the rigid body motion, additional active damping control could be required in order to satisfy pointing requirements. In this section, the different ways of improving the control of the rigid body motion are highlighted with the help of the flexible pointing system described in Sec. 4.2.

7.1.1 Standard Synthesis Techniques

As stated before, the attitude control is performed by controlling the angle position about the roll, yaw and pitch axis. This is achieved by using proportional-derivative (PD) or proportional-derivative-integral (PID) controllers. These controllers allow the control of the time-response (proportional term), damping (derivative term) and tracking error (integral term) of the dynamic response. They can be combined with filters in order to make more emphasis on controlling a specified frequency or notching flexible modes.

Attitude control pointing specifications are usually four: two specifications that state the closed-loop dynamic response and two specifications concerning the robustness of the control law. Hence, desired damping ξ_{des} and desired bandwidth ω_{des} are specified to determine the closed-loop second order dynamics. Gain and phase stability margins, GM and PM, of the open loop are specified to ensure an adequate level of robustness of the closed-loop response. Usually pitch, roll and yaw dynamics are uncoupled, which allows addressing the different specifications separately. However, there is a trade-off between robustness specifications and dynamic performance specifications: although high gains imply a more reactive and agile system, they cause a loss of robustness against noise and torque perturbations. A compromise

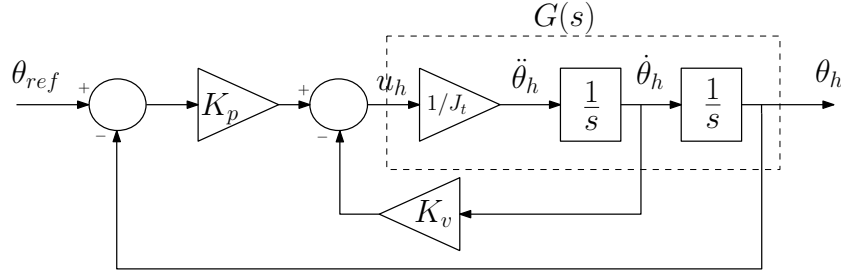


Figure 7.1: PD controller applied to the *rigid* flexible pointing system

must be chosen in order to propose the optimal solution.

The presence of flexible modes affects the achievement of these specifications. When the frequencies of the flexible modes are placed near the closed-loop desired bandwidth, robustness specifications can be significantly altered. Adding a control law which provides additional flexible modes damping could benefit the attitude control system's performance.

To demonstrate that damping of flexible modes can improve attitude control's robustness, let us consider the example of the simplified flexible pointing system illustrated in Fig. 4.4 and modeled in Sec. 4.2. The flexible pointing system can be governed through two actuators, one reaction wheel located at the hub providing the torque u_h , and one piezoelectric stack providing an internal force u_a used to isolate tip vibrations (m_1) from the payload (m_2). Therefore, there is one actuator for each type of motion (the attitude of the hub and the vibration of the tip).

The control of the hub's rotation θ_h is performed by introducing a PD which exploits θ_h and $\dot{\theta}_h$ as measurements to compute the command torque u_h . In a standard controller synthesis, the gains are computed considering the desired closed-loop dynamics, CL_{des} , of the system considered as rigid:

$$den(CL_{des}) = s^2 + 2\xi_{des}\omega_{des}s + \omega_{des}^2 \quad (7.1)$$

Figure 7.1 shows the controller interconnection with the rigid model. Identifying terms with Eq. (7.1) the gains K_p and K_v of the PD controller can be determined as follows:

$$K_p = J_t\omega_{des}^2; \quad K_v = 2J_t\xi_{des}\omega_{des} \quad (7.2)$$

where J_t is the total system inertia ($J_t = J_h + J_b + L^2(m_1 + m_2)$ in this example). According to Eq. (7.2), the proportional gain depends quadratically on the desired bandwidth ω_{des} , being very sensitive to its augmentation. Indeed, the augmentation proportional gain is strongly correlated with the loss of robustness, since the controller risks to increase the unknown outcomes (noise, unmodeled dynamics) of the system when its proportional gain is high. An evaluation of the system's robustness depending on the chosen bandwidth is done

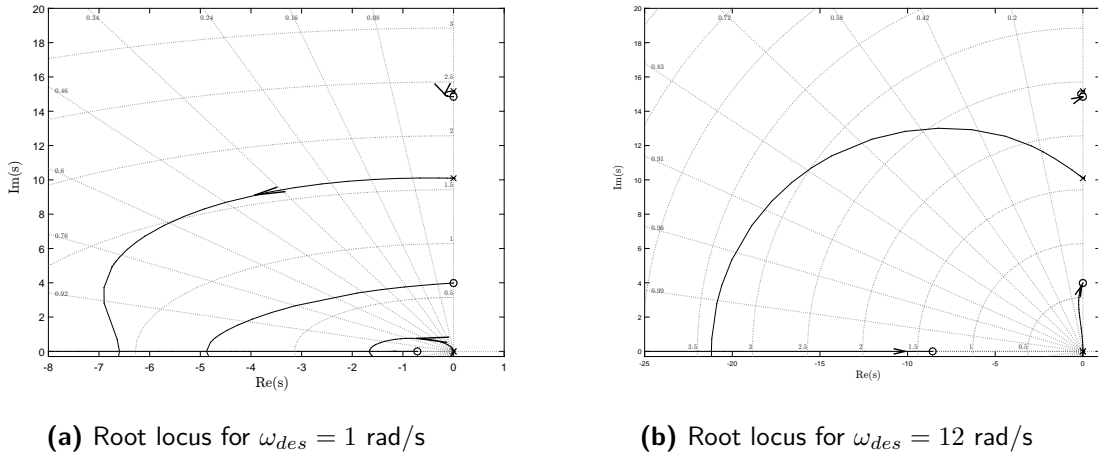


Figure 7.2: Root Locus of the transfer $u_h \rightarrow u_c$

in the following paragraphs.

Let us suppose that a low frequency bandwidth is desired, i.e, much lower than the first flexible mode. In a numerical application of the flexible pointing system, with $m_1 = 0.6$ kg, $m_2 = 0.4$ kg, $J_h = 0.05$ kg/m², $J_b = 0.005$ kg/m², $L = 0.56$ m, $k_1 = 16.8$ N·m, $k_2 = 50$ N·m and $c_1 = c_2 = 1.0 \times 10^{-4}$ N·m·s, the resulting flexible modes pulsations are $\omega_1 = 10.09$ rad/s and $\omega_2 = 15.17$ rad/s. Hence, a bandwidth ten times lower is chosen, giving $\omega_{des} = 1$ rad/s. When considering a desired damping of $\xi_{des} = 0.5$ the gains result in $K_p = 0.3686$ N·m and $K_v = 0.3686$ N·m·s.

The corresponding tuning in the root locus is depicted in Fig. 7.2a, where the rigid body poles are located at the desired dynamics and the gain margin is infinite since the root locus always remains on the left-half of the complex plane. This is due to the collocation between the hub's actuator and sensor. As previously mentioned in Sec. 4.2, it can be evaluated that the poles are located at the free pulsations of the system, ω_f , and the zeros at the corresponding cantilevered pulsations, ω_{pc} , corresponding to the natural pulsations of the modified system in which supports have been added instead of accelerometers at \ddot{y}_{abs1} and \ddot{y}_{abs2} .

Now let us consider the case of a very high bandwidth in which the first flexible mode interferes, $\omega_{des} = 12$ rad/s. The resulting gains are $K_p = 53.0784$ N·m and $K_v = 4.4232$ N·m·s. The root locus is shown in Fig. 7.2b, and again the gain margin is infinite, since the root locus is always located in the left-half of the complex plane. However, the rigid mode is not assigned to the specification and exhibits a low damping ratio which can create oscillations on the spacecraft rigid motion.

From the point of view of stability, nothing will impede the augmentation of the gains in order to achieve a faster closed-loop response. However, the introduction of real actuator dynamics shows that higher gains result in a less robust system. Figure 7.3 shows the Nichols

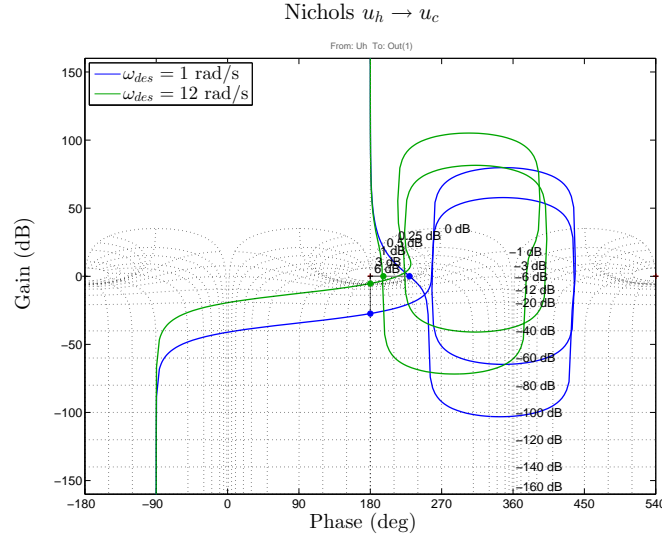


Figure 7.3: Nichols Diagram for the controlled system with real actuator dynamics (10 ms delay)

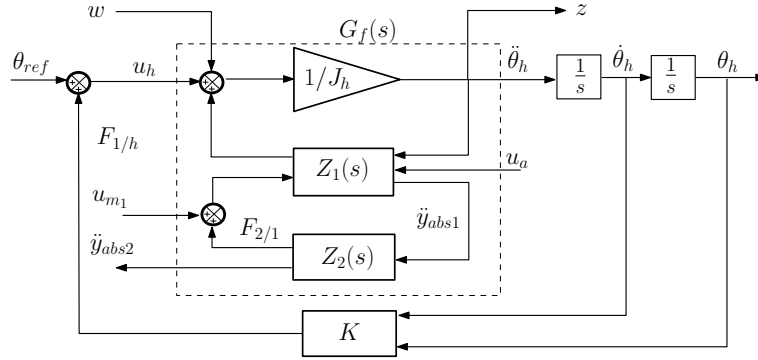


Figure 7.4: PD controller robust synthesis applied to the flexible pointing system

plot for the low-bandwidth controller and the high-bandwidth controller when the torque actuator has a delay of 10 ms. It can be evaluated that robustness performances have been more degraded in the high-bandwidth controller case (GM = 5.35 dB, PM = 15.5 degrees) than in the low-bandwidth controller case (GM = 27.4 dB, PM = 49.5 degrees).

7.1.2 Robust Synthesis Techniques

The standard controller synthesis technique is therefore limited by the bandwidth requirements in presence of flexible modes and real actuator dynamics. Robust control techniques give more robust controllers since they search for the maximization of robust specifications. Let us consider a structured \mathcal{H}_∞ synthesis of the same PD controller which minimizes the transfer between the disturbance torque w and the performance output z corresponding to the hub angular acceleration as seen in Fig. 7.4.

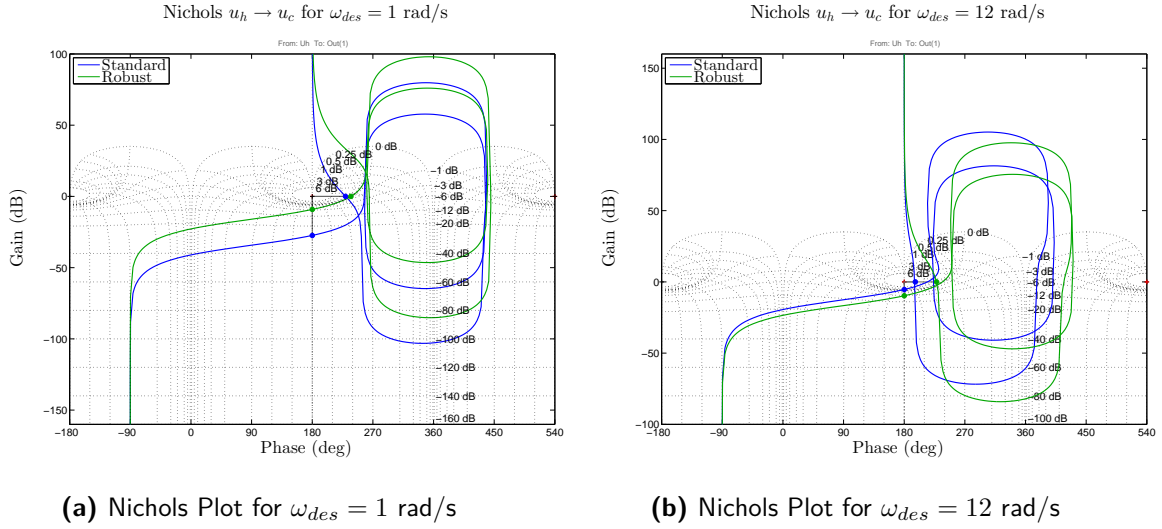


Figure 7.5: Nichols plots comparing robust synthesis with standard rigid approach

The open loop response of the obtained controllers, considering torque delay of 10 ms, is shown in Fig. 7.5a for the low bandwidth case and in Fig. 7.5b for the high bandwidth case. A comparison with the controllers obtained by the standard technique is also depicted. There is no improvement for the low-bandwidth case, but there is an enhancement of gain and phase margins of the high bandwidth case. For a required bandwidth of $\omega_{des} = 12$ rad/s, there is a gain of 5 dB in the gain margin and of 30 degrees in the phase margin (GM = 10.5 dB, PM = 44.8 degrees). It can be concluded that robust synthesis can be more beneficial for bandwidth requirements near the flexible modes.

7.1.3 Synthesis Techniques Including Active Damping

The foregoing sections did not employ any particular damping technique, only the rigid body motion was controlled. This section highlights the importance of active damping to improve the attitude control response and robust performance.

Now let us suppose an active damping control law is used to command the torque u_a of the flexible pointing system. Among all the laws which could be used, described in Sec. 7.2, direct velocity feedback is used for this case. The feedback gain is tuned to maximize the damping of the first flexible mode, giving a value of $K_a = 2.44$:

$$u_a = \frac{K_a}{s} \ddot{y}_{abs1} \quad (7.3)$$

The resulting dynamic behavior of the commanded response is shown in Fig. 7.6. Again, there is no improvement for the low bandwidth requirement (see Fig. 7.6a) but the high bandwidth requirement exhibits a slight enhancement of 15 degrees in the phase margin (PM = 35.2 degrees, see Fig. 7.6b). Active damping can thus be an interesting approach to achieve

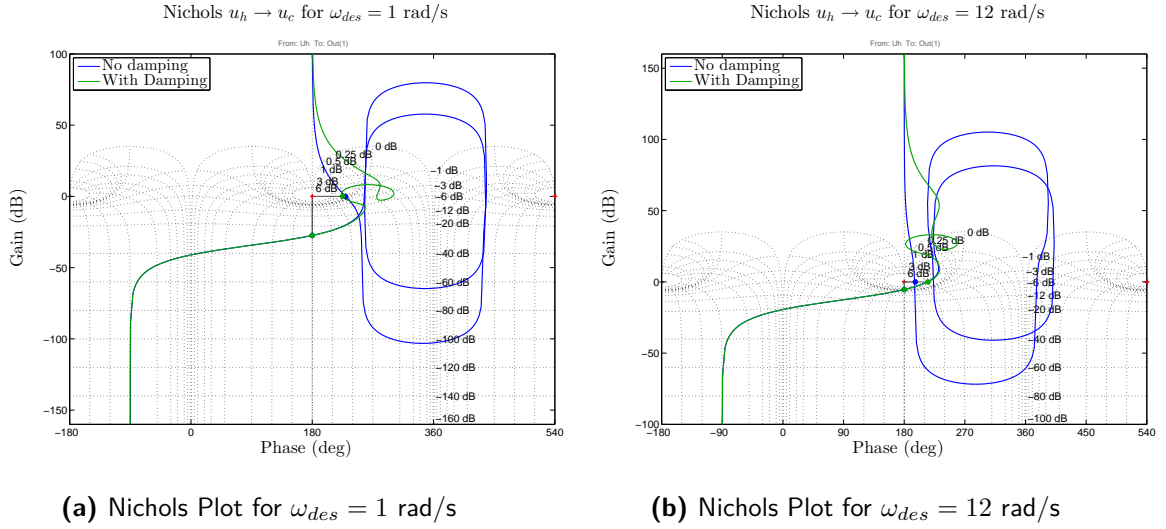


Figure 7.6: Nichols plots comparing standard rigid approach alone and with closed-loop active damping

challenging bandwidth requirements of the attitude control system.

7.1.4 Decentralized VS Centralized Control and Optimization

Since flexible substructures are not in the satellite's platform, a new control dilemma arises: decentralized or centralized control. In the conventional approach to structure control, a controller is designed based on a centralized control model that is created by reducing a larger evaluation model. The final controller is then verified with the evaluation model.

Another approach for designing controllers for flexible structures is through decentralized control. In this approach, the system to be controlled is viewed as a collection of subsystems. Controller design is carried out on the subsystem level, and the individual controllers are then applied in some manner to the complete system. FMSs lend themselves particularly well to decentralized control approaches since the system has already been decomposed in several subsystems.

Although decentralized control schemes are suitable for FMS control, system's stability is not guaranteed after interconnecting all the controllers and substructures. This is the main problem of decentralized control [Siljak 11]. Furthermore, attempts to formulate decentralized control strategies by extending standard optimization concepts and methods have not been successful; the simple reason is that nonclassical decentralized information structure does not lend itself to a manageable formulation of any kind of optimality principle. This fact is responsible for a relatively large gap between theory and practice of optimal decentralized control.

In this thesis, the theoretical requirements for decentralized control stability and optima are not addressed since they are out of the scope. The approach, however, consists of using

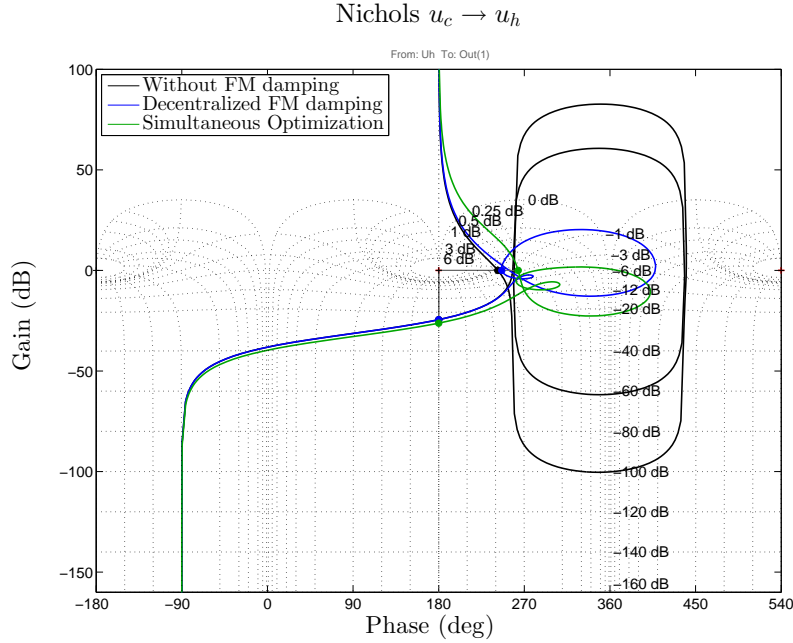


Figure 7.7: Nichols Plot comparing decentralized optimization to centralized optimization

decentralized control architectures and guaranteeing the stability of the FMS through the optimization performed with structured \mathcal{H}_∞ techniques. Therefore, the approach is *centralized* regarding the optimization process (the entire model is used) but *decentralized* regarding the controller's architecture (each subsystem has its own independent controller).

The advantage of this *hybrid* approach is shown in Fig. 7.7. Three different approaches have been applied to control the hub's rotation of the flexible pointing system through the hub's torque u_h . All the three approaches had low bandwidth requirements ($\omega_{des} = 1$ rad/s). The black solid line represents an approach without active damping, presenting the worst robust performance (GM = 24.5 dB, PM = 62.2 degrees). The blue solid line represents an approach with decentralized active damping, tuned to maximally damp the first flexible mode (GM = 24.5 dB, PM = 63.3 degrees). The green solid line represents open loop response of the system with a controller synthesized with simultaneous (centralized) optimization of the rigid body motion controller and the active damping controller. The simultaneous optimization improves the robust performances (GM = 26.2 dB, PM = 83.5 degrees), even if in the foregoing sections the improvement of robust performances in the low bandwidth requirements was demonstrated to be harder.

Hence, a decentralized controller architecture merged with a centralized optimization approach can be beneficial in order to improve system robust performance. Using structured \mathcal{H}_∞ synthesis, the controllers' values of the decentralized architecture can be optimized globally for the required dynamic behavior and performance of the FMS. If an architecture is "suitable" for optimization (i.e., a stabilizing solution can be found for the proposed architecture), then the synthesis will be able to find a solution for the optimization problem. The

next section will give guidelines in order to propose the most “suitable” architectures for the active damping of flexible modes.

7.2 Control of Flexible Modes

Structural vibrations are an essential characteristic in the dynamics of large flexible spacecraft. The question arises whether they can be damped out by active control. If successful, the spacecraft thus damped would behave somewhat more like a rigid spacecraft. This could lead to simplified and robust design of the attitude controller for the spacecraft, as exemplified in the foregoing section. Thus, attitude control performance, in terms of closed-loop dynamics and robustness, could be enhanced by the active damping of the flexible modes. In this section, a set of control architectures for active damping is explained and applied to the TITOP models developed in Chaps. 5 and 6. Only attention is paid to control strategies with guaranteed stability. They can be implemented in a decentralized manner, with each actuator interacting only with the collocated sensor. In this case, the control system consists of independent SISO loops, whose stability can be established from the root locus of

$$K(s)G_f(s) \quad (7.4)$$

where $G_f(s)$ is the structure transfer function between the actuator and the collocated sensor and $K(s)$ is the active damping controller. According to Preumont [Preumont 11], for practical reasons the active damping $K(s)$ should have enough roll-off at high frequency, so that vibrations are not amplified beyond actuator’s bandwidth. Another important aspect is the **collocation** between actuators and sensors.

Collocated actuator and sensor pairs *always* lead to alternating poles and zeros near the imaginary axis, which is translated into an unconditionally stable system. This is because the root locus plot keeps the same general shape, and remains entirely within the left half plane when the system parameters are changed from their nominal values. In order to take advantage of this property, this section revises collocated control strategies. However, it will be shown that a noncollocated configuration can occur if the designer is not aware of the chosen inputs/outputs. Noncollocated control is not the most adequate strategy since it is related to poor robust performance, but in some applications it can be the only available option for flexible mode damping (not all systems can have collocated actuator and sensor pairs).

The different possibilities for $K(s)$ are presented as follows. In Sec. 7.2.1, acceleration feedback controllers are explained. In Sec. 7.2.2, integral force feedback is explained. In Sec. 7.2.3, other strategies which cannot be directly applied to the TITOP model are explained. Finally, in Secs. 7.2.4 and 7.2.5 these control strategies are tested against the collocation/non collocation of the internal forces and measurements and the presence of real actuator dynamics.

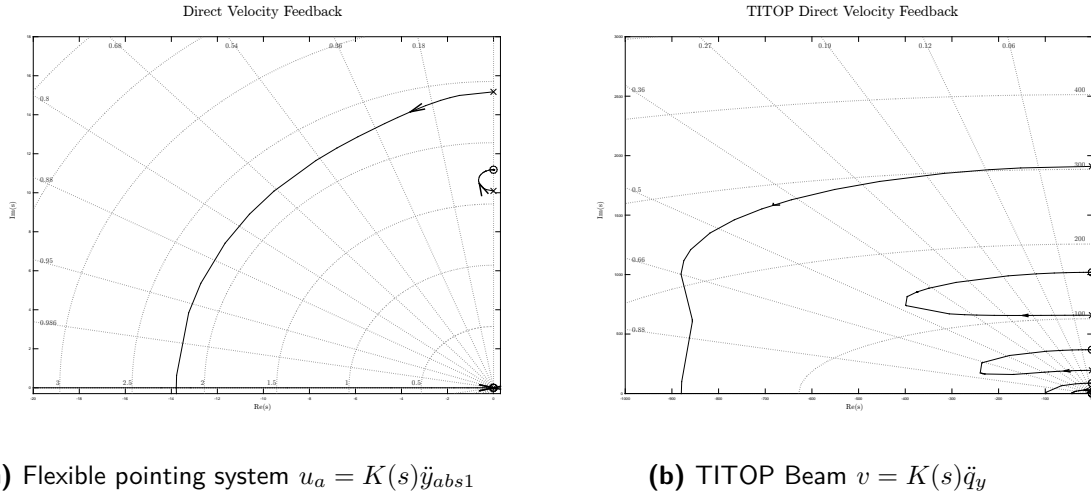


Figure 7.8: Acceleration Feedback applied to the different systems

Throughout this section the control strategies are illustrated with their application to the flexible pointing system and a flexible beam modeled with the TITOP technique. The values used for the flexible pointing system are $m_1 = 0.6$ kg, $m_2 = 0.4$ kg, $J_h = 0.05$ kg/m², $J_b = 0.005$ kg/m², $L = 0.56$ m, $k_1 = 16.8$ N·m, $k_2 = 50$ N·m and $c_1 = c_2 = 1.0 \times 10^{-3}$ N·m·s. The properties of the flexible beam modeled with TITOP are length $L = 1.5$ m, Young's modulus $E = 60 \times 10^9$ N/m², section thickness $t = 9.53$ mm, section width $b = 30$ mm, volumetric density $\rho = 2600$ kg/m³. The properties of the piezoelectric material bonded to the flexible beam are piezoelectric constant $d_{31} = -150 \times 10^{-12}$ m/V, dielectric constant $T_{33} = 1.59 \times 10^{-12}$ F/m, laminate thickness $t_p = 2$ mm, laminate width $w_p = 30$ mm, elastic modulus $E_p = 50 \times 10^9$ and volumetric density $\rho_p = 7600$ kg/m³.

7.2.1 Acceleration Feedback

In a control law based on acceleration feedback, the measured output is an acceleration and the control input is a force. Measuring acceleration in translations is easier than measuring velocities or displacements, specially when the structure is stiff. This is not the case however for angular accelerations, where an angular accelerometer is much more expensive than a gyroscope. The acceleration feedback can be implemented in two ways: direct rate feedback and second order filter feedback.

Direct Rate Feedback

In the direct rate feedback, the measured acceleration is integrated and multiplied by a gain in order to increase the system's damping. The control law is written as follows:

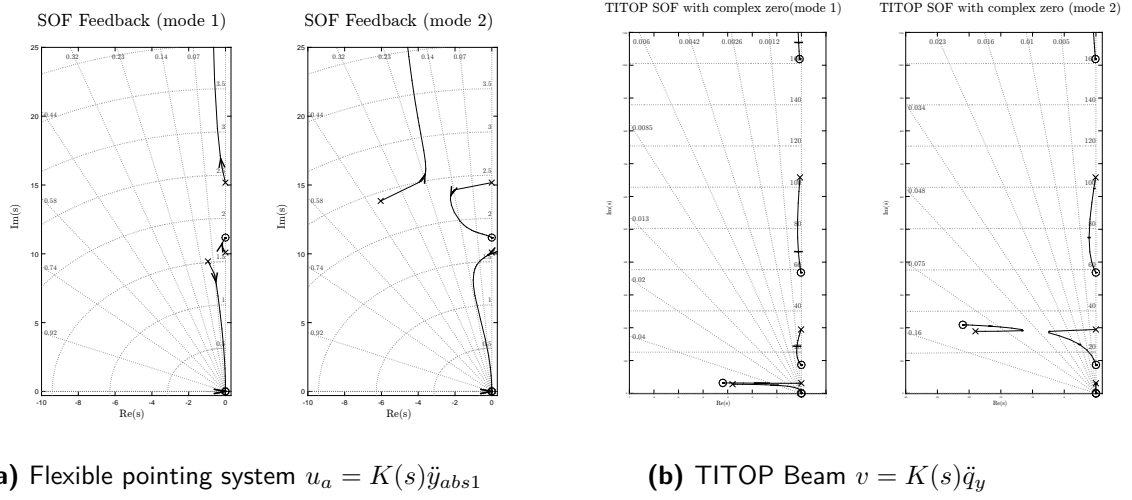


Figure 7.9: Root locus of the second order filter applied to the different systems

$$K(s) = \frac{K_v}{s} ; \quad u = -K(s)\ddot{y} \quad (7.5)$$

The active damping mechanism is guaranteed since the power is being dissipated ($u^T \cdot \dot{y} \leq 0$). In Fig. 7.8a, rate feedback root locus is depicted for the flexible pointing system example. In Fig. 7.8b, rate feedback is applied to a piezoelectric beam, feeding the applied voltage with the measurement of the tip's vertical acceleration, \ddot{q}_y . The stability properties of this controller are guaranteed in both cases thanks to the root locus being always in the left-half of the complex plane, but the TITOP case seems more efficient for damping the flexible modes.

Second Order Filter

This controller passes the acceleration signal through a second order filter with damping to generate a force feedback proportional to the measured output. This controller enjoys guaranteed stability as well, increasing roll-off at high frequencies. The control law can be written as follows:

$$K(s) = \frac{K_p}{s^2 + 2\xi_f\omega_f s + \omega_f^2} ; \quad u = -K(s)\ddot{y} \quad (7.6)$$

where ξ_f and ω_f are respectively the damping coefficient and the natural pulsation of the filter. They are tuned to maximize the damping of a targeted flexible mode. In Fig. 7.9a two second order filters are presented for the flexible pointing system, one targeting mode 1 and the other targeting mode 2. Sometimes, a pair of complex auto-conjugate zeros can be added to the filter to improve the controllability of the targeted mode. This is the case of the TITOP beam model depicted in Fig. 7.9b.

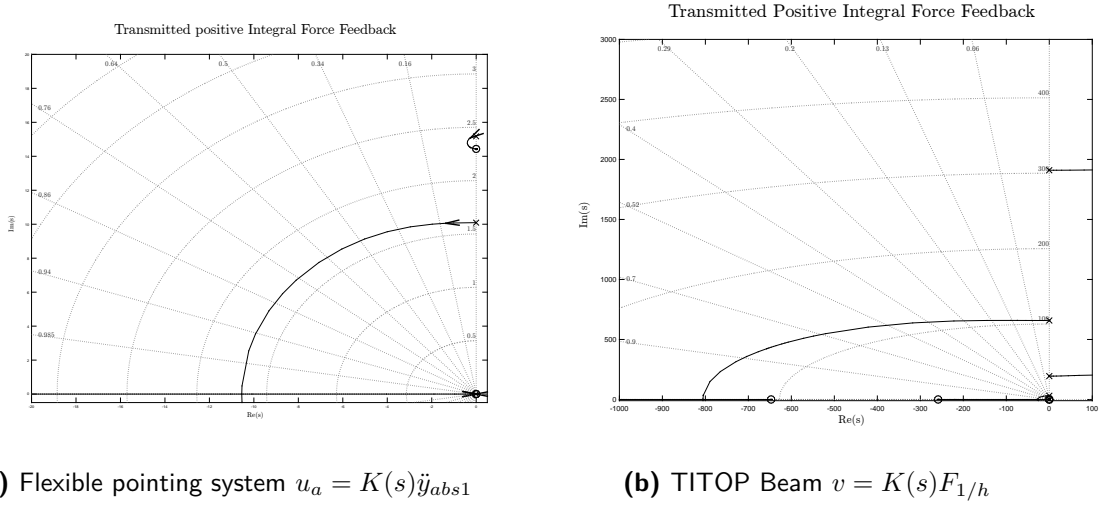


Figure 7.10: Root locus of the *positive Integral Force Feedback* IFF

7.2.2 Integral Force Feedback

This decentralized control strategy considers local controllers connecting their actuators with their collocated force sensor. The controller of a *positive Integral Force Feedback* (IFF) takes the following form:

$$K(s) = -\frac{K_p}{K_a(s + \varepsilon)} ; \quad u = -K(s)F \quad (7.7)$$

where K_p and K_a are proportional gains of the controller and ε is the forgetting factor to avoid saturation that could lead a full integral action. This scheme is unconditionally stable for all values of K_p/K_a since it leads to alternating pole and zeros along the imaginary axis. The negative sign in Eq. (7.7) is combined with the negative sign in the feedback loop to produce a positive feedback.

IFF is applied to the case of the flexible pointing system in Fig. 7.10a. It is shown that the control strategy leads to alternating poles and zeros and therefore it is unconditionally stable. It should be noted as well that the zeros are not located in the same places as in the acceleration feedback, since now the transmission zeros, obtained by enforcing a zero force at the connecting DOF, are identical to the natural frequencies of the system when the controller is disconnected from the system, identical to the natural frequencies of the free system. The transmission zero in the rate feedback case is located at 11 rad/s, whereas the transmission zero in the IFF case is nearby 14 rad/s.

The IFF applied to the TITOP beam is shown in Fig. 7.10b. It can be noted that the root locus is not unconditionally stable, there are no alternating poles and zeros and the root locus steps into the right-half complex plane. The double port form of the TITOP is what causes this disadvantage. Indeed, a TITOP model can have two kinds of IFF: the one

which measures the transmitted load, $F_{A/P,P}$, and the one which measures the received load, $F_{A/C,C}$. It appears to be that the first one is not a collocated effort, leading to unstable configuration. The second one cannot be implemented yet for a single beam since there is no received force to measure, it will be explained in Sec. 7.2.4 where a concatenation case is presented.

7.2.3 Other Controller Architectures

This section revises other collocated control strategies which can be applied for active damping control. Nevertheless, they cannot be directly applied to a TITOP model because they involve measurement of relative displacements and velocities. As a reminder, a TITOP model has as inputs/outputs inertial accelerations and loads transferred through the boundaries of other substructures in the chain. A manipulation of the obtained TITOP's outputs is required in order to obtain relative velocities and displacements.

The remaining strategies are the PD controller and the *Positive Position Feedback* (PPF), both of them based on the measurement of relative position and velocity. In the PD strategy, relative position and velocity are fed back with a proportional gain and a derivative gain respectively in order to produce the control force, as follows:

$$u = K_p y_{rel} + K_v \dot{y}_{rel} = [K_p \quad K_v] \begin{Bmatrix} y \\ \dot{y} \end{Bmatrix}_{rel} \quad (7.8)$$

A PD controller does not have a good roll-off at high frequencies since the derivative term can amplify noise at high frequencies. A PPF controller uses a second order filter to improve the roll-off of the control system, allowing high frequency gain stabilization:

$$K(s) = \frac{-K_p}{s^2 + 2\xi_f \omega_f s + \omega_f^2} ; \quad u = -K(s)y_{rel} \quad (7.9)$$

where the pulsation ω_f is tuned to have a roll-off -40 dB beyond the desired bandwidth. Both approaches are shown in Fig. 7.11 where they have been applied to the flexible pointing system example. Both approaches are unconditionally stable since they are collocated strategies.

Regarding the TITOP model, another control strategy can be used if the measured charge output signal, g_c is used for applied voltage feedback, v . However, as mentioned in Sec. 6.1.2, this configuration offers poor controllability (poles and zeros nearly cancel out). This fact obliges the use of the actuated TITOP model electric inputs and outputs either for control or measurement, but not both at the same time.

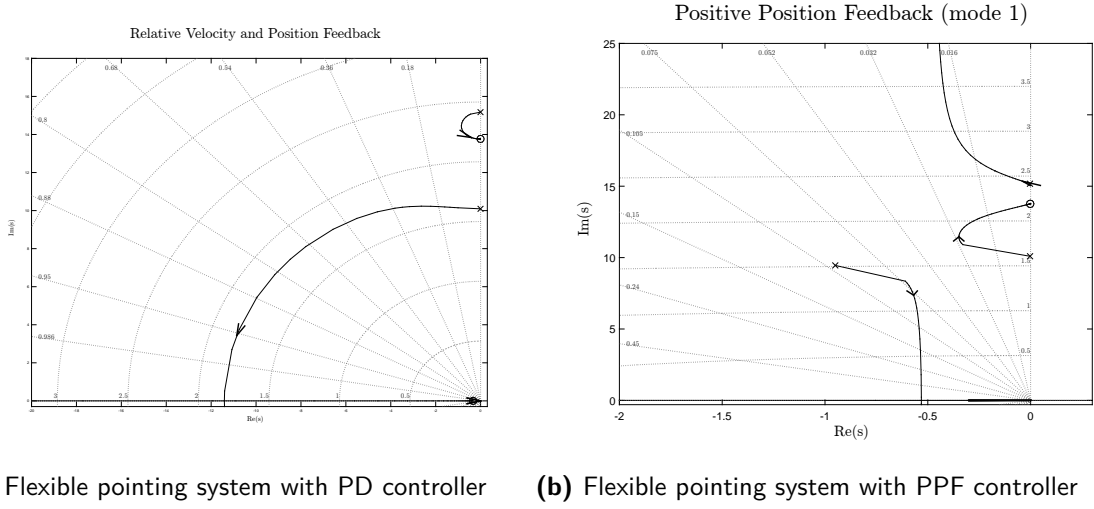


Figure 7.11: Root locus of the PD and PPF controllers

7.2.4 Robustness to Pole/Zero Flipping

In the foregoing sections, the collocation of actuator/sensor pairs has been taken for granted in all the control strategies. However, it should be noted that the actuators and sensors were not *strictly collocated*. The theorem states that the transfer matrix of a structure is positive real (i.e., dissipates energy) if collocated actuators and rate sensors are used, this result being totally independent of the numerical values of the modal frequencies and the mode shapes of the structure [Benhabib 81]. This collocation must be done at the ultimate level, that is, if inertial accelerations are measured, the applied loads must be inertial, and if relative accelerations are measured, the control forces must be internal. If this requirement is not respected, *pole/zero flipping* may occur, i.e., there are no longer alternating poles and zeros along the imaginary axis.

As it can be noted, the control strategies of Secs. 7.2.1 and 7.2.3 were not truly strictly collocated systems, since an inertial measurement (absolute acceleration) was taken to drive an internal applied force, u_a . Nevertheless, for the given values of the system alternating poles and zeros were obtained since the flexible pointing system was stiff enough. Now let us suppose that the value of m_2 is changed to a heavier one, $m_2 = 1.2$ kg, making the system *more flexible*. The new root locus of the acceleration feedback and IFF are shown in Fig. 7.12. It can be observed that the transmission zeros of the acceleration feedback controller are located at a lower frequency (see Fig. 7.12a), since now the cantilevered frequency associated to Appendage 2, $\omega_{cc} = \sqrt{k_2/m_2}$, decreases as the mass m_2 increases. As a consequence, the alternating scheme of poles and zeros is broken and the acceleration feedback is no longer collocated. This is also observed for other acceleration feedback based controllers (See Figs. E.5 and E.6 in Appendix E), due to the fact that the acceleration is measured in the inertial frame whereas the applied force is internal, thus not being truly collocated. In the other hand, IFF remains collocated and unconditionally stable (see Fig. 7.13b), since the controller uses truly collocated inputs/outputs (measured force, internal force actuator).

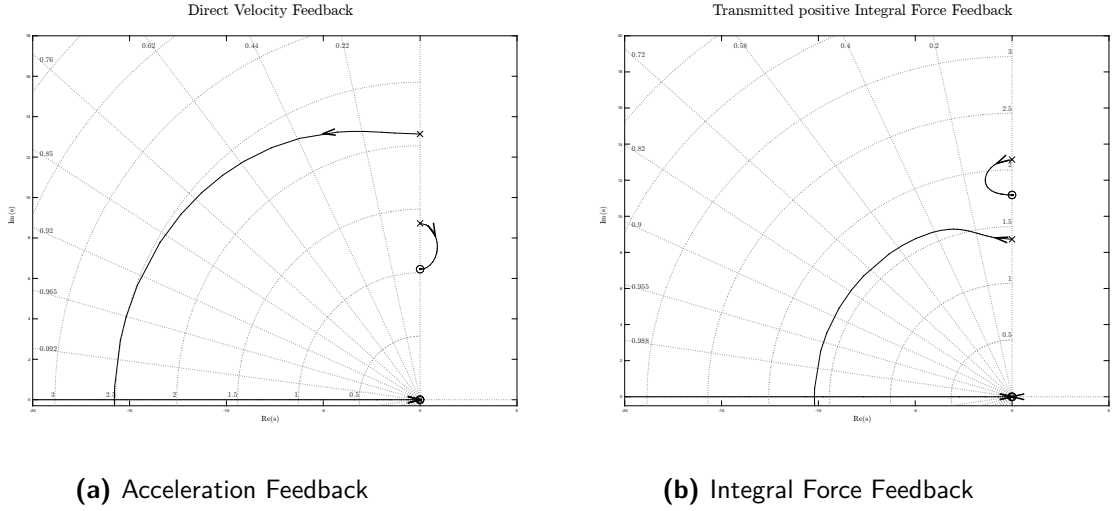


Figure 7.12: Root locus of the flexible pointing system with heavier appendage ($m_2 = 1.2$ kg)

The TITOP model experiences the pole/zero flipping effect when the structure is flexible enough. If a second flexible beam is linked to the flexible beam used in the foregoing sections, acceleration feedback is no longer collocated, even if it is applied at the same location (see Fig. 7.13). This issue is solved either by using relative rate feedback (Fig. 7.14a) or IFF using the measured received force from segment 2 to segment 1 (Fig. 7.14b).

It can be concluded that only *strictly* collocated inputs/outputs lead to unconditionally stable active damping strategies. The term *strictly* refers to the couple inputs/outputs being inertial or non-inertial, but they cannot be mixed. An IFF controller is more robust to pole/zero flipping since the measured output (internal force) is strictly collocated with the applied force.

It should be highlighted that there are other causes for pole/zero flipping. If a controller has zeros near the system's poles, pole zero flipping may occur if the system's model has uncertainties which can vary the position of the pole. This is particularly important when a the controller contains a *notch filter* [Preumont 11], a filter specially designed to induce artificial collocation in a non-collocated system. Other source for pole/zero flipping are actuator/sensor configurations with poor controllability/observability, where the presence of small uncertainties can shift the order of poles and zeros due to their proximity.

7.2.5 Real Actuator/Sensor Dynamics

Actuators play a crucial role in the design of the control system and, in many cases, they constitute the limiting factor. They can be ground-based or structure-based actuators. Ground-based actuators react on a fixed support, e.g. force motors, torque motors or tendons. The structure-based actuators do not have ground support and some examples are reaction wheels, control moment gyros, proof-mass actuators, piezoelectric strips, piezoelectric stacks or other

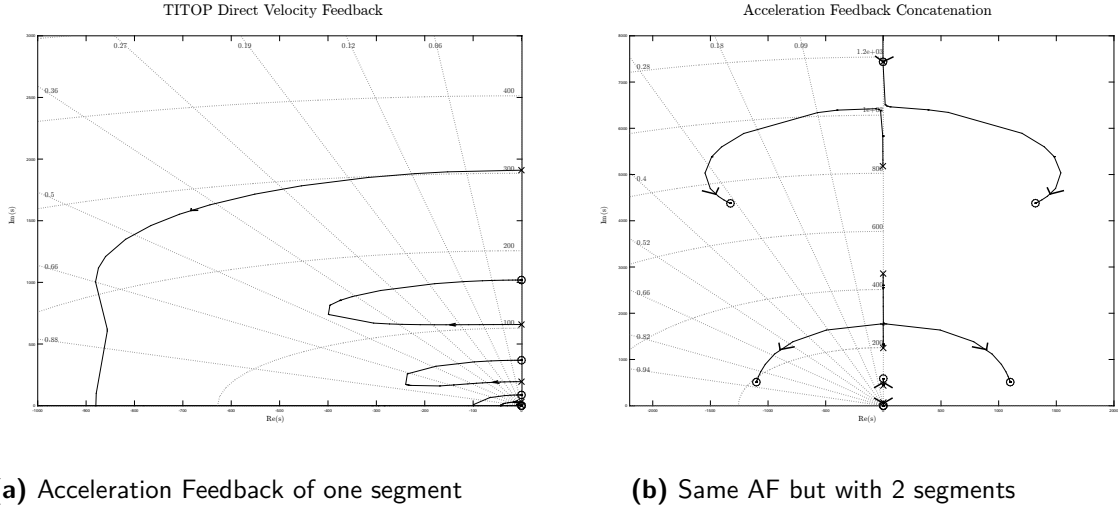


Figure 7.13: For TITOP models, an acceleration feedback control law can lose pole/zero collocation when other appendages are connected

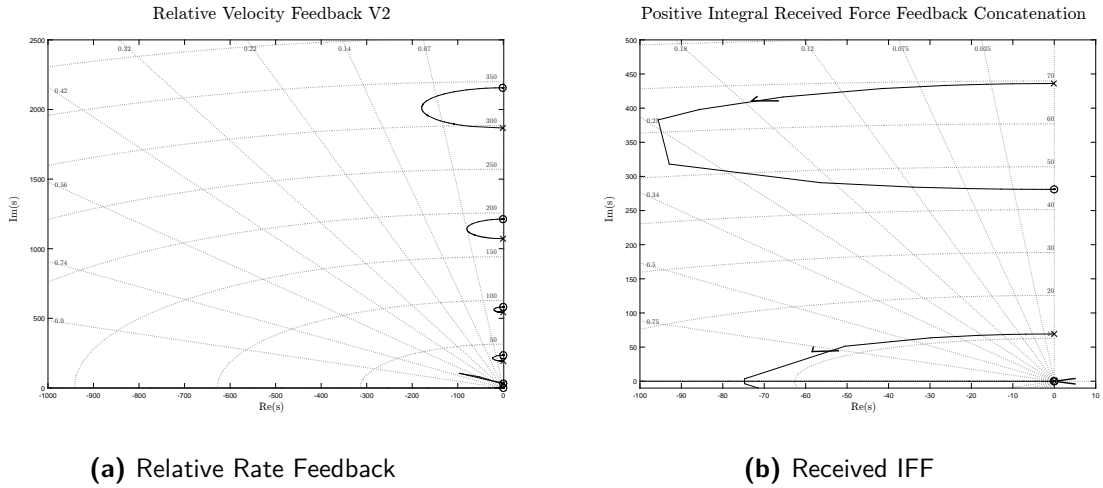


Figure 7.14: If several appendages are connected with the TITOP technique, relative acceleration feedback or IFF can be used as collocated control strategies

active members (revolute joints, extendable parts). All actuating devices involving only internal, self-equilibrating forces, such as piezoelectric actuators, cannot influence the rigid body motion of the structure.

Sensors also play a very important role in the control system. They can limit the control design in three different ways: imposing the measurements which can be measured because not all the variables are within the normally available sensors, limiting the measurement precision because of noise reasons or altering the dynamic behavior of the system.

Due to their importance, actuators and sensors must be modeled in order to take into account their influence on the system's behavior. Throughout this section, it has been as-

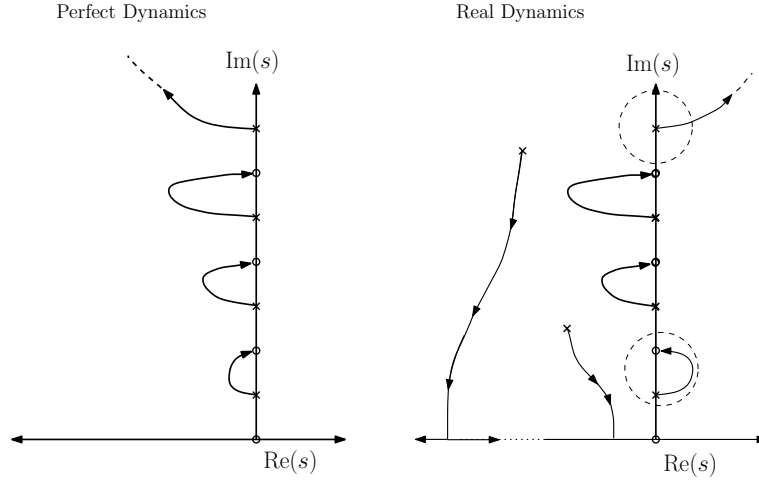


Figure 7.15: Illustration of the changes in the root locus of a collocated control when real actuator dynamics are considered

sumed that actuators and sensors have perfect dynamics. In practice, however, the dynamic behavior of the piezoelectric actuators can be modeled as a pass-band filter in the range of frequencies $\omega \in (\omega_l, \omega_h)$ within they can operate:

$$A(s) = \frac{s^2}{s^2 + 2\xi_l\omega_l s + \omega_l^2} \frac{\omega_h^2}{s^2 + 2\xi_h\omega_h s + \omega_h^2} \quad (7.10)$$

Actuator dynamics $A(s)$ adds four extra poles which are translated in two asymptotes which significantly alter the root locus for $\omega < \omega_l$ and $\omega > \omega_h$. Thus, active damping is no longer unconditionally stable beyond that range of frequencies since it has a destabilizing influence beyond that range (see Fig. 7.15); system's positivity is lost due to the actuator's limited bandwidth. Nevertheless, the controller can still operate at small gains thanks to the natural damping of the structure, which places the poles slightly to the left of the imaginary axis.

An evaluation of the different control strategies for controlling the rigid body motion and the flexible modes of a FMS has been done throughout this chapter. The interest of performing a centralized optimization of a decentralized control system has been highlighted with an example. Since active damping has demonstrated to be beneficial for attitude control performance and robustness, a set of collocated active damping strategies has been presented, and their application to TITOP models has been discussed. The strategies have been focused on collocated actuator/sensor approaches. Acceleration feedback appears to be more problematic than positive integral feedback because of the not strict collocation of actuators and sensors. This problem being discovered, the presented control architectures can be carefully applied later in the integrated control/structure design of FMS, performed in Chaps. 8 and 9.

Chapter

8

Implementation of Integrated Control/Structure Design in Structured \mathcal{H}_∞ Form

“Ideas are easy. Implementation is hard.”
- Guy Kawasaki

Contents

8.1	General Procedure and Scheme for Integrated Design	124
8.2	Implementation of Specifications and Constraints	126
8.2.1	Rigid Motion Specifications	127
8.2.2	Flexible Motion Specifications	130
8.2.3	Structural Specifications	132
8.2.4	Controller Specifications	133
8.3	Co-Design of a Rotatory Spacecraft	134
8.3.1	LFT Model for Co-Design	135
8.3.2	Block Δ Transformation	135
8.3.3	Augmented Controller Architecture	136
8.3.4	Implementation of Design Specifications	137
8.3.5	Optimization and Results	138

This chapter explains how to put an integrated control/structure design problem in structured \mathcal{H}_∞ form so that the synthesis can be performed using structured robust control functions, available in the Matlab Robust Control Toolbox. The specifications for rigid body and flexible motion as well as structure and controller specifications are translated in \mathcal{H}_∞ constraints and applied to the integrated control/structure design of a rotatory spacecraft.

IN this chapter, the main objective is to show the use of structured \mathcal{H}_∞ synthesis as a tool to perform integrated design studies, with special emphasis on the control/structure application, i.e. *transform* the structured \mathcal{H}_∞ synthesis as explained in Chap. 3, in a tool to solve co-design problems. The specifications for the control of the system's dynamics and the structural specifications are converted in \mathcal{H}_∞ constraints so that structured \mathcal{H}_∞ tools can be used. First, an overview of the implementation procedure is described in Sec. 8.1. In Sec. 8.2 the conversion of system's specifications in \mathcal{H}_∞ constraints is shown for the specifications on the system's dynamics, structure and controller. Finally, the co-design of the rotatory flexible spacecraft is performed in Sec. 8.3 to illustrate the concepts explained throughout the chapter.

8.1 General Procedure and Scheme for Integrated Design

The integrated control/structure design (ICSD) method of this study uses structured robust control synthesis. A thorough explanation of structured \mathcal{H}_∞ controller synthesis is given in [Gahinet 11] and [Burke 06], where it is shown how it is possible to impose the order, the structure and stability of the controller thanks to the structured \mathcal{H}_∞ synthesis. Some aspects of this theory have been recalled in Chap. 3 and this section presents the needed modifications to perform integrated design. The integrated control/structure problem needs five steps for implementation under \mathcal{H}_∞ form:

Step 1 : Obtain a LFT model of the system. The FMS under study has to be modeled following the TITOP modeling technique or other preferred approach. The model has to contain the sizing parameters to be tuned, which will result in a LFT with an associated Δ block including parametric variations. The channels of the FMS modeling scheme have to be “broken” in order to incorporate the perturbation inputs w and performance z outputs that will be used lately for requirements implementation in Secs. 8.2.1 and 8.2.2.

Step 2: Conversion of the Δ block into tunable parameters. Once the LFT model of the FMS is obtained, it is separated into the nominal LTI model $G(s)$ and the Δ block. Depending on the software being used, the block Δ is often presented as a *lfr object*. This is the case, for example, of Matlab Robust Control Toolbox functions. Since the block Δ has to be presented as a set of tunable parameters instead of an uncertainty block as used by robust analysis tools, the full block is converted into a diagonal matrix Δ_i with tunable parameters δ_i , respecting the number of occurrences for each parameter. In Sec. D.1 an example of a matlab code to perform this task is presented.

Step 3: Selection of the controller's architecture and creation of an *augmented* controller. Depending on the controller's architecture, $C(s)$, the nominal system $G(s)$ will have to provide to the synthesis scheme of Fig. 8.1 the needed control inputs, y , and the needed control outputs, u that will be used by the controller to stabilize the system in the feedback

$\mathcal{F}_l(G(s), C(s))$. An *augmented* controller, $K(s) = \text{diag}(C(s), \Delta_i)$, is created incorporating the set of tunable parameters, Δ_i , that will act as a feedback between the system outputs y^Δ and system inputs u^Δ , and $C(s)$ being a structured controller that will act as a feedback between the system outputs y and system inputs u .

Step 4: Selection of the weighting functions. A set of weighting filters $[W_z, W_C, W_k]$ has to be obtained in order to state the dynamic behavior of the system, shape the frequency response of the controller and optimize structural parameters. The form of these weighting functions is explained in the next sections.

Step 5: Build the multi-channel \mathcal{H}_∞ synthesis scheme. With the elements obtained in the precedent steps, the synthesis scheme is build by establishing the feedback of the *augmented* controller $K(s)$ with the corresponding inputs/outputs of the nominal system $G(s)$. Additional channels are added in order to weight the controller's frequency response and structural variations.

Figure 8.1 shows the standard multi-channel \mathcal{H}_∞ synthesis problem for ICSD of the system $G(s)$. The synthesis scheme has three different channels:

- One multidimensional channel which connects the perturbations of the system, w , to the performance outputs, z .
- One multidimensional channel which connects the inputs of the control system, y_c , to the outputs, u_c .
- One multidimensional channel which connects the inputs of the constraints of the varying parameters $f_k(\delta_i)$ block, w_k , to its outputs z_k .

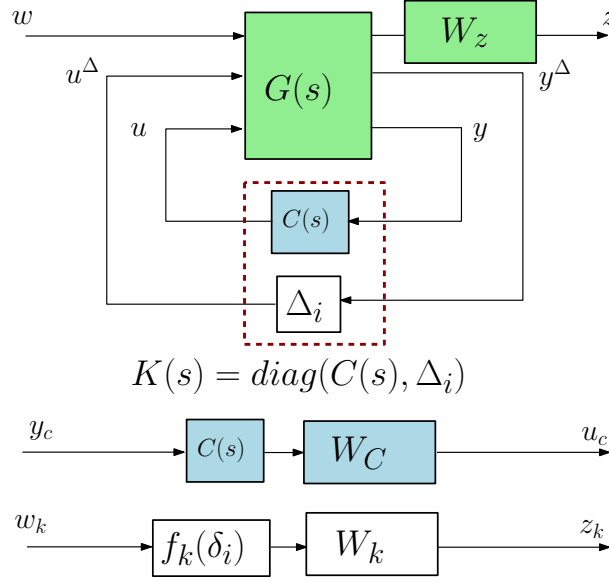
Structured \mathcal{H}_∞ synthesis computes the sub-optimal tuning of the free parameters of $C(s)$ and Δ_i embedded in $K(s)$ to enforce closed-loop internal stability, $\mathcal{F}_l(G(s), K(s))$, such that:

$$\min_{K(s)} \{ \max \{ \|W_k(s)f_k(\delta_i)\|_\infty, \|W_C(s)C(s)\|_\infty \} \}$$

such that

$$\|W_z(s)T_{w \rightarrow z}(s)\|_\infty < \gamma_{perf}$$

i.e., it minimizes the \mathcal{H}_∞ norm between the transfer of the perturbation input w and the performance output z , $T_{w \rightarrow z}(s)$, such that it is constrained to be below $\gamma_{perf} > 0$ to meet the required performances. The problem is in the form of multi-channel \mathcal{H}_∞ synthesis, and it allows the set of desired properties to the augmented controller such as its internal stability [Alazard 13a], frequency template [Loquen 12] or maximum gain values. In substance, the structured \mathcal{H}_∞ integrated design synthesis tunes the free parameters contained in the

**Figure 8.1:** Block Diagram of Integrated Design Optimization

augmented controller $K(s) = \text{diag}(C(s), \Delta_i)$ to ensure closed loop internal stability and meet normalized \mathcal{H}_∞ requirements through W_z , W_C and W_k . The main difficulty lies on how to set the correct normalized \mathcal{H}_∞ requirements so that successful integrated design synthesis is guaranteed. Guidelines for the selection of the needed filters to convert the system's specifications in \mathcal{H}_∞ requirements for the flexible spacecraft case are given in the next section.

8.2 Implementation of Specifications and Constraints

The basic large flexible spacecraft design objectives for the control system are:

1. To obtain sufficiently high bandwidth and satisfactory closed-loop damping ratios for rigid-body structural modes. This arises from the need to provide sufficient error decay when a disturbance torque occurs (such as a sudden thermal distortion when entering in Earth's shadow or a gravity gradient torque)
2. To achieve satisfactory pointing errors. This design objective arises from mission performance requirements (such as alignment specification between two different on-board instruments, Radio Frequency specifications of a large antenna)

These two objectives may not necessarily be compatible: increased feedback gains for obtaining higher bandwidth or damping will in general lead to higher pointing errors since they may have an amplifying effect on sensor noise. In this method, control design objectives are addressed as frequency domain specifications on rigid-body modes and then expanded to the rest of the FMS where flexible motions have to be damped. The rigid modes are assigned to a specific part of the spacecraft, likely the hub or platform, in which rigid-body

actuators, such as reaction wheels or control moment gyros, are usually placed to control attitude motion. The center of gravity of the hub is used as the origin of the frame for the rest of the constraints. Then the constraints which can be imposed to the controller or structural parameters are explained.

8.2.1 Rigid Motion Specifications

Controlling the rigid body motion is the most important task of the attitude control system, keeping the angle position between maximum misalignment values for any given torque disturbance. Such disturbances are produced by aerodynamic drag effects in low-Earth orbits, solar radiation and solar wind torques, parasitic torques created by the propulsion thrusters, gravity gradient torque or thermal distortion torque, which can perturb the attitude position when an observation is being made. The specifications are given in the form of a desired bandwidth in which the disturbance torques have to be rejected, ω_{des} , and a desired damping, ξ_{des} , to ensure enough error decay and maximum value when a disturbance occurs.

In order to impose the desired closed-loop rigid body motion, determined with the couple $(\omega_{des}, \xi_{des})$ for each attitude angle (roll φ , pitch θ and yaw ψ), the synthesis scheme uses the acceleration sensitivity function as the performance output of the rigid body DOF:

Definition 8.1. Acceleration Sensitivity Function. Given the equations of motion of a system as the generic second order differential equation $M\ddot{q} + D\dot{q} + Kq = Fu$ where M , D and K are respectively the mass, damping and stiffness matrices, then the acceleration sensitivity function, $S_{\ddot{q}}$, is defined as the transfer $\ddot{q} = \ddot{q}_{real} + w$, where w is the perturbation acceleration.

The Acceleration Sensitivity Function (ASF), $S_{\ddot{q}}$, was introduced and used by [Fezans 08] in a \mathcal{H}_∞ synthesis scheme which was named Second Order Template on Acceleration Sensitivity (SOTAS). In this scheme, each DOF contained in the vector q has a weighting function $W_{\ddot{q}}$ on the ASF in order to set its closed-loop dynamic response. The obtained controller can thus reject low-frequency acceleration disturbances on the DOF. Furthermore, the robustness of the synthesis is enforced since it will have to minimize the effects of the perturbations in q and \dot{q} , variables used by the controller. A block diagram of the SOTAS synthesis scheme is depicted in Fig. 8.3. Hence, the synthesis has to minimize the \mathcal{H}_∞ norm of the transfer

$$T_{w_{\ddot{q}} \rightarrow z} = W_{\ddot{q}} S_{\ddot{q}} \quad (8.1)$$

The frequency weighting function $W_{\ddot{q}}$ is a second order transfer function obtained straightforward from the rigid body specifications, being a low-pass filter with the specified bandwidth and damping as parameters:

$$W_{\ddot{q}} = \frac{s^2 + 2\xi_{des}\omega_{des}s + \omega_{des}^2}{s^2} \quad (8.2)$$

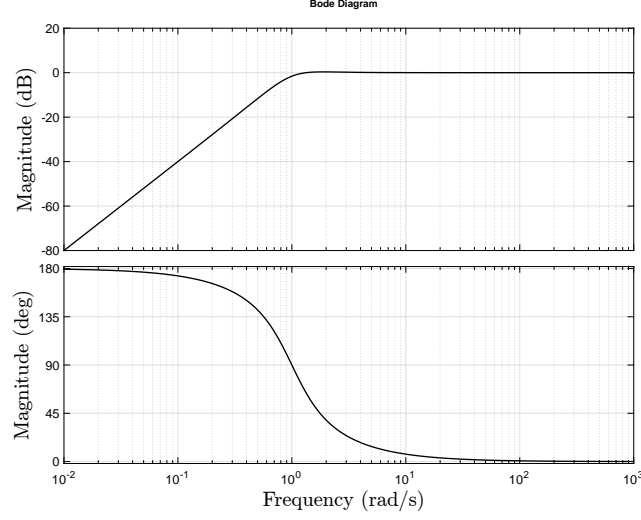


Figure 8.2: Second order template $W_{\ddot{q}}^{-1}$ sets the wished frequency response of the transfer $T_{w \rightarrow z}$ ($\omega_{des} = 1$ rad/s, $\xi_{des} = 0.6$)

The shape of the weighting function (see Fig. 8.2) obliges the ASF to attenuate the sensitivity to acceleration disturbances in the desired bandwidth. Under these conditions, the optimal solution of the SOTAS scheme is defined as follows:

Theorem 8.2. SOTAS Optimal Solution. *Given a second order system $G(s)$ and $P(s)$ its associated SOTAS problem, consisting of the system $G(s)$ and a feedback controller using q and \dot{q} as control inputs, a controller $K(s)$ is considered as the optimal solution of the problem $P(s)$ if and only if $\|\mathcal{F}_l(P, K)\|_\infty = 1$*

This property is the main advantage of the SOTAS synthesis scheme, since by definition the optimal norm γ_{opt} is equal to 1 and therefore any additional constraint implies $\gamma_{perf} \geq 1$, being the distance to 1 considered as a distance to the objective. Therefore, a feedback which gives a performance value close to 1 would fulfill the closed-loop dynamic specifications and will ensure perturbation rejection. Hence the controller can be either rejected or accepted if its associated γ_{perf} is either much greater or less greater than 1.

The SOTAS scheme allows the synthesis of controllers which control the rate and position of the attitude angles against disturbances, which is achieved with PD controllers. If a PID controller is desired in order to ensure null steady-state error, an integral term of the variable q can be added to the weighting function and as control input. The integral term will then considered the integral effect on the ASF:

$$W_{\ddot{q}} = \frac{s^2 + 2\xi_{des}\omega_{des}s + \omega_{des}^2}{s^2} \cdot \frac{s + \lambda_i}{s} \quad (8.3)$$

where λ_i determines the desired integral effect, and it is often chosen as one tenth of

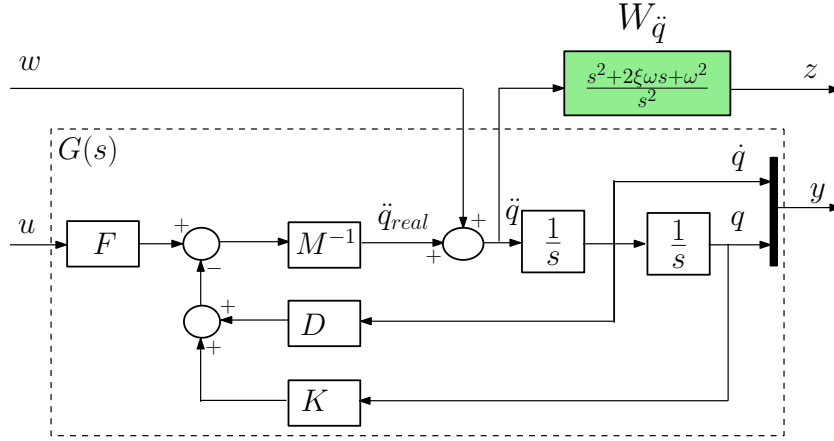


Figure 8.3: SOTAS synthesis scheme

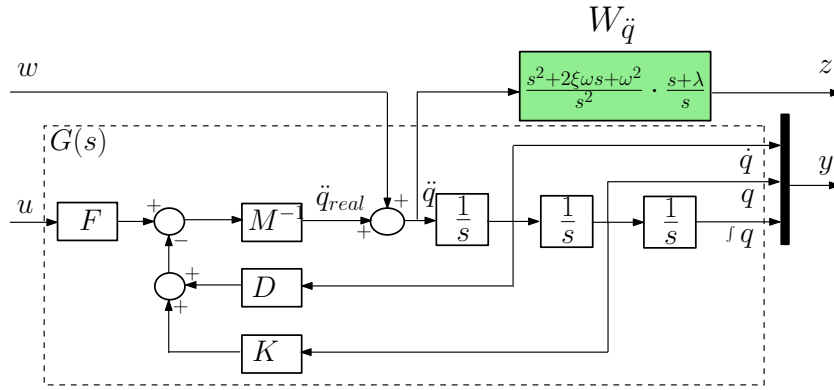


Figure 8.4: SOTAS synthesis scheme taking into account integral effect

the desired bandwidth. The SOTAS scheme with the integral term is depicted in Fig. 8.4. The additional integrators added by the SOTAS scheme through the weighting function can make the synthesis process fail. Particularly, the function *hinfstruct* needs a minimal representation of the SOTAS problem, i.e., a representation which avoids uncontrollable poles and unobservable zeros. The representation of this minimal form is explained with detail in [Guy 12]. Modern structured robust synthesis functions, such as *systune*, can impose the frequency constraints without needing a minimal representation of the weighting functions.

Once the SOTAS scheme has been explained for generalized second order systems, it can be implemented in the more particular TITOP modeling scheme of flexible multibody spacecraft. Following the FMS TITOP modeling example given in Sec. 5.6, the scheme is modified in order to accomodate the SOTAS scheme for controlling the rigid body motion of the platform at its center of gravity G , $\{\ddot{q}_G\}$ (see Fig. 8.5). A perturbation disturbing the acceleration measurements at point G , w_G , is introduced before the transfer of acceleration to the flexible appendage. By doing this, the synthesis process takes into account the flexible motion since the perturbation excites the flexible modes. Then the total acceleration (the real one plus the perturbation) is weighted by the filter $W_{\ddot{q}_G}$ to give the performance output z_G .

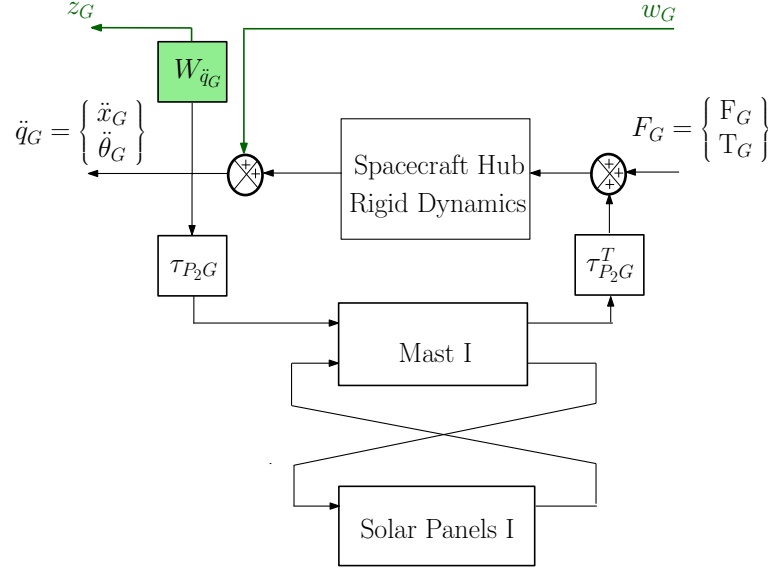


Figure 8.5: SOTAS synthesis scheme applied to the control of rigid body modes of the FMS of Fig. 5.11 (the antenna is not represented for simplicity)

Therefore, the TITOP modeling scheme is used in the SOTAS template in order to control the rigid body dynamics (attitude position) of the spacecraft's platform. One weighting filter is used for each output control axis i , being three the number of filters needed to state the control specifications for the spacecraft's orientation in 3D motion, one filter only for in-plane 2D motion. Hence, the rigid motion specifications form the sub-set W_{z_G} of the performance output weighting functions W_z :

$$W_{z_G} = \text{diag}(W_{z_\theta}, W_{z_\psi}, W_{z_\varphi}) \quad (8.4)$$

8.2.2 Flexible Motion Specifications

The constraints for damping the flexible motion of the FMS are derived from the SOTAS scheme. The specifications regarding the control of flexible modes (e.g. maximum line-sight misalignment or damping for vibration attenuation) are implemented as an extension of the rigid body motion field to the rest of the system. Therefore, constraints in other points of the FMS are assigned as the *desired behavior of the point if the structure was rigid*. Hence, for a point P of the FMS located with the position vector $\{GP\}$ in the spacecraft's frame, the desired acceleration would be the one corresponding to the rigid body field associated to the spacecraft, i.e., the acceleration that point P would have if the spacecraft was infinitely rigid. Since the transmission of the rigid body motion is given by the kinematic transport matrix ϕ_{GP} , the weighting filter for a given point on a FMS can be written as follows:

$$W_{z_P} = \phi_{GP} \cdot W_{z_G}^{-1} = \phi_{GP} \cdot \frac{s^2}{s^2 + 2\xi_{des}\omega_{des}s + \omega_{des}^2} \quad (8.5)$$

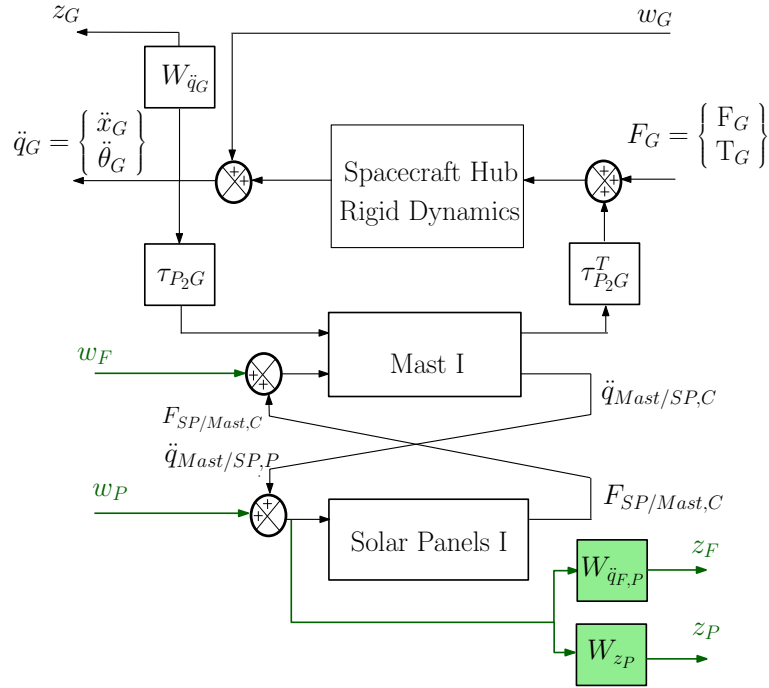


Figure 8.6: SOTAS synthesis scheme with the constraints applied to the flexible motion of the FMS of Fig. 5.11 (the antenna is not represented for simplicity)

Equation (8.5) automatically constraints the controller to increase the system's natural damping, since only a rigid structure is able to satisfy the template. The weighting function can be *relaxed* with a factor greater than 1 in order to simplify the search of a stabilizing controller. As in the rigid body motion case, the acceleration perturbation w_P is added at the measurement of the acceleration of point P , the sum is retrieved and weighted with W_{z_P} to obtain the performance output z_P , as depicted in Fig. 8.6.

An additional constraint can be added in order to ensure the damping effect against disturbance loads. As depicted in Fig. 8.6, a disturbance load w_F is added on the channel of the force transmission from the solar pannels to the mast, which is retrieved up-stream at the measured acceleration at point P . This load perturbation-acceleration transfer excites the flexible modes of Mast I. If the desired damping for the flexible modes of the mast is ξ , the filter $W_{\ddot{q}_{F,P}}$ is a constant value corresponding to the infinity norm of a second order function with the desired damping:

$$W_{\ddot{q}_{F,P}} = \left\| \frac{\omega^2}{s^2 + 2\xi\omega s + \omega^2} \right\|_{\infty}^{-1} \quad (8.6)$$

It should be noted that the value in Eq. (8.6) does not depend on the parameter ω , the value is the inverse of the maximum peak of the second order transfer function, which is directly related with the desired damping ξ . Hence, the filter states an upper limit for the resonances of the transfer function $w_F \rightarrow z_F$.

Although theoretically an infinite number of constraints to flexible motion can be imposed (as much as available sensors in the required points), the author's experience reveal that only one or two constraints per substructure are enough. More constraints increase the number of failed searches of a stabilizing controller and the optimization time. Furthermore, some constraints can be ill-conditioned or could be incompatible with other substructure's constraints.

8.2.3 Structural Specifications

The structural specifications can be established by adding channels that provide additional constraints for the variations included in the Δ_i block. The normalization process expresses the parameter's variation within the $\delta_i \in [-1, +1]$ interval, with the 0 value indicating the nominal configuration of the plant $G(s)$.

A structural constraint k which involves a set of structural parameters δ_i are imposed through the weighting filter W_k and a cost function consisting of one or several parameter variations δ_i , $f_k(\delta_i)$. Only maximization or minimization can be imposed since the structured \mathcal{H}_∞ only allows the minimization of the performance outputs, so other different types of constraints (as for example equality with other parameters) cannot be implemented. If a parameter δ_i has to be maximized, the constraint k is expressed to the transfer $z_k \rightarrow w_k$ as:

$$f_k(\delta_i) = (1 - \delta_i); \quad W_k = \beta_k \quad (8.7)$$

where $\beta_k \geq 1$ is a user-defined value which gives more or less emphasis for the maximization of the associated variation of a parameter i , δ_i . Therefore, since structured \mathcal{H}_∞ synthesis will attempt the minimization of the \mathcal{H}_∞ norm of the channel z_k/w_k to achieve a value below β_k , the parameter δ_i is constrained to have positive values to reduce the coefficient $(1 - \delta_i)$ below β_k . Negative values are thus penalized since they make the sum greater than β_k . The increase of β_k augments the sensibility of that constraint since the value will be farther from the objective. A minimization can be expressed in the opposite sense with $f_k(\delta_i) = \delta_i$, where the synthesis will look for the minimum value of δ_i for the transfer. Another function for maximization can be written if the parameter variations can be presented as a percentage of $[-p\%, +p\%]$:

$$f_k(\delta_i) = \frac{1}{1 + \delta_i \frac{p}{100}}; \quad W_k = \beta_k \quad (8.8)$$

Equation (8.8) also constraints the parameter δ_i to be maximized, but in this case the slope of the function is lower than the slope of the linear expression in Eq. (8.7), as seen in Fig. 8.7. Therefore, for positive values of δ_i , the ones which maximize the i -th parameter, the constraint of Eq. (8.8) gives higher value of the performance index for the same parameter variation, encouraging the optimization process to look for a large maximization for reducing

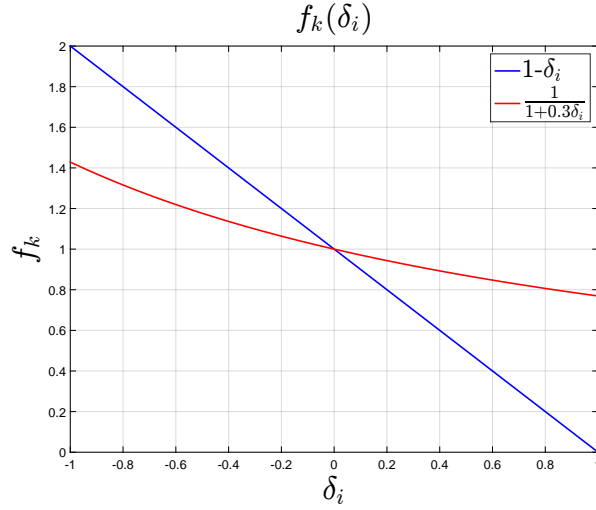


Figure 8.7: Comparison of the cost functions expressed in Eq. (8.7) and Eq. (8.8)

that value.

It should be highlighted that there is no additional *cost function* associated to the optimization of structural parameters. The *cost* of optimizing one parameter in relation to another will depend on how the parameter affects the dynamic behavior of the system, which is constrained by the rigid and flexible constraints that have been established in Secs. 8.2.1 and 8.2.2. If the variation of the parameter significantly affects the fulfillment of rigid body or flexible body requirements, stability or robustness, it will be penalized by the synthesis process.

8.2.4 Controller Specifications

Added to the constraints in the rigid motion, flexible motion and structural parameters, the frequency response of the rigid body motion controller can be improved through the addition of a roll-off channel in the synthesis scheme. This may be necessary to add a cut-off effect in the controller, avoiding the interaction with flexible frequencies which are close to the controller's bandwidth and that have not been damped by the active damping controller (the *spill-over* effect). Within the controller's channel, a weighting filter is added in order to shape the controller's frequency response. For each controlled axis the filter can be set as:

$$W_{ro} = \frac{1}{\sqrt{2}J_{G_i}\omega_{des}^2} \cdot \frac{s + \omega_{ro}}{s/100 + \omega_{ro}} \quad (8.9)$$

where ω_{ro} is the desired roll-off pulsation of the controller ($\omega_{ro} > \omega_{des}$) and J_{G_i} is the system's inertia at its center of gravity around the i -th axis. If the cut-off effect has to be improved, a second order template can be used:

$$W_{ro} = \frac{1}{\sqrt{2}J_{G_i}\omega_{des}^2} \cdot \frac{s^2 + 1.4\omega_{ro}s + \omega_{ro}^2}{(s/100)^2 + 1.4\omega_{ro}(s/100) + \omega_{ro}^2} \quad (8.10)$$

The reader might have guessed that a standard damping of $\xi = 0.7$ was assigned for completion of the required second order parameters. These roll-off templates can be modified in order to satisfy the roll-off requirements of the active damping controller. Then the controller must incorporate a roll-off filter in order to satisfy the roll-off constraint:

$$C(s) = C_0(s) \frac{a_0}{s^2 + b_1s + b_0} \quad (8.11)$$

where $C_0(s)$ is the original controller, and the roll-off filter parameters a_0, b_1, b_0 are to be tuned by the function for structured \mathcal{H}_∞ synthesis. Once the roll-off filters have been assigned for each type of controller, the weighting function for the controller channel will be a diagonal matrix of roll-off filters one for each output control axis:

$$W_C = \text{diag}(W_{ro1}, W_{ro2} \dots W_{ron}) \quad (8.12)$$

Added to the roll-off specification, the applied commands computed by the controller can be minimized taking advantage of a particular constraint that can only be implemented in the *systune* matlab tool. This exclusivity resides on the fact that the constraint for energy minimization involves a \mathcal{H}_2 norm, and the mixing of \mathcal{H}_2 and \mathcal{H}_∞ constraints (time and frequency domains) can only be implemented with the *systune* function. The constraint to minimize the applied commands is:

$$\|T_{w \rightarrow u}\|_2 \leq e \quad (8.13)$$

where $T_{w \rightarrow u}$ is the transfer between the perturbation w , u is the applied control command and e the maximum value of the integral of the transfer with $t \rightarrow \infty$. To implement this constraint is necessary to modify the integrated design scheme in order to incorporate the channel u as an output.

8.3 Co-Design of a Rotatory Spacecraft

As an academic application, ICSD (Integrated Control/Structure Design) is performed to the rotatory spacecraft modeled in Sec. 6.2. The main objective is to control the rigid body mode associated to the hub's rotation, provide additional damping with the incorporation of a piezoelectric laminate and to maximize the length and payload mass of one appendage only. The ICSD of the rotatory spacecraft is then performed following the five steps described in Sec. 8.1.

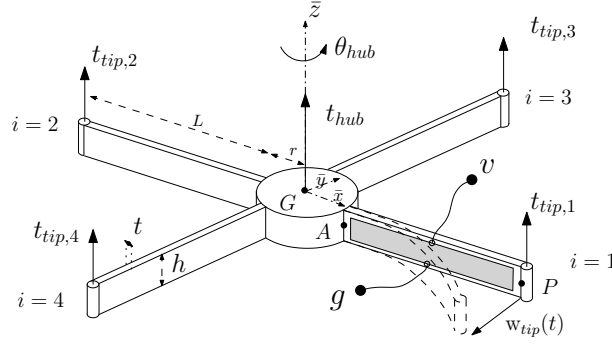


Figure 8.8: Rotatory Flexible Spacecraft with the appendage $i = 1$ actuated with a laminate of piezoelectric material

8.3.1 LFT Model for Co-Design

The derivation of the LFT model of the rotatory spacecraft is done by changing the model of appendage 1 into a piezo-actuated TITOP model, as depicted in Fig. 8.8. The piezoelectric material has the same characteristics as the ones used in Sec. 6.1.2. All appendage TITOP models include their lengths (L_i) as variable parameters, as well for the tip masses M_i located at their ends, all with an allowed variation of 30 % of its nominal value. The LFT TITOP models are assembled to the hub following the same guidelines as in Sec. 6.2. After assembly, the system has a block Δ of 125×125 size, that is, 2 parameter occurrences for each tip mass, 29 parameter occurrences for the non-actuated TITOP models and 30 parameter occurrences for the actuated TITOP of appendage $i = 1$.

The TITOP assembly scheme is changed as shown in Figs. 8.5 and 8.6 in order to have the acceleration disturbance inputs w_{hub} and w_{tip_i} and the performance outputs z_{hub} and z_{tip_i} . The system is thus expressed in a TITOP assembly configuration with the required sets of inputs and outputs to perform ICSD. The system results in a state-space system with a Δ block of size 125×125 , 11 inputs, 11 outputs and 50 states.

It should be highlighted that the ICSD of the rotatory spacecraft strongly demands a modeling technique such as the TITOP modeling technique, since the boundary conditions of the flexible beams are to be changed when varying the mass located at their tips. Thus, by using the TITOP modeling technique, the impact of mass variation in the whole system will be taken into account when ICSD is performed with structured \mathcal{H}_∞ synthesis.

8.3.2 Block Δ Transformation

The final Δ block after LFT TITOP assembly results in a block of size 125×125 containing the parametric variations (uncertainties) of L_i and M_i , being the suffix i the i -th appendage. Since this block contains the data as a LFT object, it needs to be converted into a set of tunable parameters which can be used with the function *systune*.

In the Robust Control Toolbox, the variations of the variable parameters are normalized within the interval $[-1, 1]$, with 0 corresponding to the nominal value. Therefore, the Δ block is initially a diagonal matrix containing sub-matrix blocks with the normalized parametric variations δ_i repeated as much as it is indicated by the number of occurrences. The Δ block of this problem can be written as follows:

$$[\Delta] = \begin{bmatrix} [\delta_{L_1}]_{30 \times 30} & 0 & 0 & 0 & 0 & 0 & 0 & 0 \\ 0 & [\delta_{M_1}]_{2 \times 2} & 0 & 0 & 0 & 0 & 0 & 0 \\ 0 & 0 & [\delta_{L_2}]_{29 \times 29} & 0 & 0 & 0 & 0 & 0 \\ 0 & 0 & 0 & [\delta_{M_2}]_{2 \times 2} & 0 & 0 & 0 & 0 \\ 0 & 0 & 0 & 0 & [\delta_{L_3}]_{29 \times 29} & 0 & 0 & 0 \\ 0 & 0 & 0 & 0 & 0 & [\delta_{M_3}]_{2 \times 2} & 0 & 0 \\ 0 & 0 & 0 & 0 & 0 & 0 & [\delta_{L_4}]_{29 \times 29} & 0 \\ 0 & 0 & 0 & 0 & 0 & 0 & 0 & [\delta_{M_4}]_{2 \times 2} \end{bmatrix} \quad (8.14)$$

Each subblock has to be converted in a subblock of tunable parameters for ICSD with the same number of occurrences as in the lft object. In Sec. D.1 an example of a matlab code to perform this task is described.

8.3.3 Augmented Controller Architecture

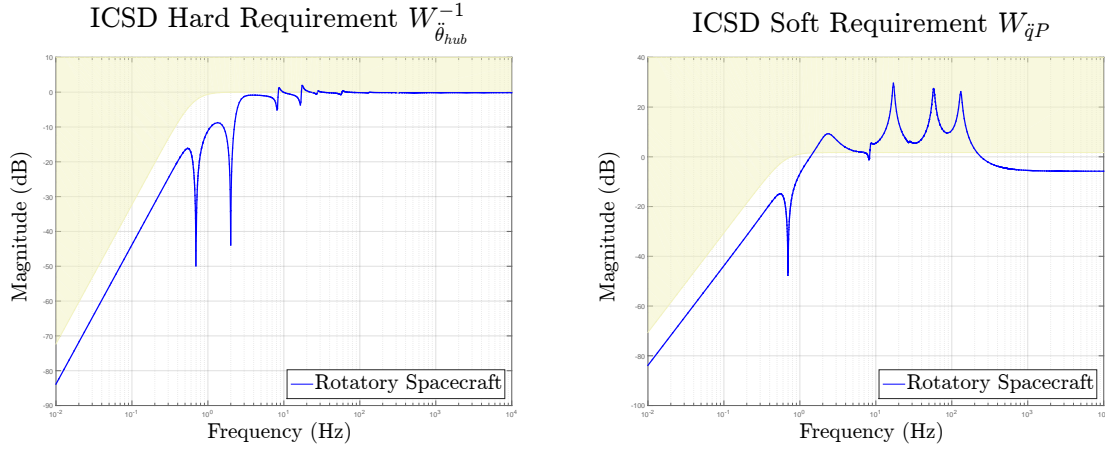
The augmented controller is formed by concatenating the block of tunable parameters Δ with the real controller of the system, $C(s)$. Since the Δ block has been defined in the foregoing section, in this section the structure of $C(s)$ is addressed.

The system needs to reject low frequency disturbances in the rigid body DOF, the system's rotation around the hub, and can be helped by inducing active damping through the piezoelectric laminate installed on appendage 1. Thus, the control system will consist of two decentralized loops: one for the rigid body rotation of the hub, θ_{hub} , and the other to damp the first appendage's tip vibrations, \ddot{y}_{tip1} .

The control of the rigid body motion is achieved with a PD to compute the control torque provided by the reaction wheel located at the hub. The active damping controller will be a simple rate feedback, integrating the first appendage's vertical acceleration (acceleration feedback strategy). Therefore the control law is structured as follows:

$$\{u\} = [C(s)]\{y\} = \begin{Bmatrix} t_{hub} \\ V \end{Bmatrix} = \begin{bmatrix} k_v & 0 & 0 \\ 0 & k_p & 0 \\ 0 & 0 & k_a/s \end{bmatrix} \begin{Bmatrix} \dot{\theta}_{hub} \\ \theta_{hub} \\ \ddot{y}_{tip1} \end{Bmatrix} \quad (8.15)$$

The proportional control gain k_p , the derivative control gain k_v and the damping gain k_a , together with the tunable parameters of the Δ block, are to be optimized with structured



(a) Constraint (yellow) on the hub's dynamics (blue) (b) Constraint (yellow) on the tip's dynamics (blue)

Figure 8.9: Dynamic specifications template and system response before optimization

\mathcal{H}_∞ synthesis. The values of the PD controller are initialized using the standard synthesis of Sec. 7.1.1 giving $k_p = 633.33 \text{ N}\cdot\text{m}$ and $k_v = 231.21 \text{ N}\cdot\text{m}\cdot\text{s}$.

8.3.4 Implementation of Design Specifications

As previously specified, the control of the hub rotation must be able to reject low frequency disturbance torque. The desired closed-loop dynamics for perturbation rejection are $\omega = 1 \text{ rad/s}$ and $\xi = 0.7$, which leads to the following weighting filter:

$$W_{\ddot{\theta}_{hub}} = \frac{s^2 + 1.4s + 1}{s^2} \quad (8.16)$$

The damping of the flexible modes is imposed by weighting the transfer between the hub's acceleration disturbance w_{hub} and the performance output z_{tip1} with $W_{\ddot{q}_P} = L \times W_{\ddot{\theta}_{hub}}^{-1}$. A constant filter as the one in Eq. (8.6) is added in the transfer $F_{tip1} \rightarrow z_{tip1}$ to add additional damping. In Fig. 8.9 the frequency response of the system is compared with the desired frequency response imposed through the templates before ICSD optimization. It is seen that the flexible modes are badly damped and the PD controller gains have a larger value than the needed to respect the template on the ASF of the hub position θ_{hub} .

Once the constraints for rigid and flexible motion have been defined, additional channels can be added to constraint the variation of structural parameters. The constraints for the maximization of the length and tip mass of appendage 1, L_1 and M_1 respectively, are implemented as follows:

$$f_{M_1}(\delta_{M_1}) = \frac{1}{1 + 0.3\delta_{M_1}}; \quad W_{M_1} = 0.75 \quad (8.17)$$

Parameters	COA	ICSD
Controller	PD + AF	PD + AF
Lengths L_1 & L_2	1.22 m	$L_1 = 1.59$ m & $L_2 = 1.36$ m
Masses M_1 & M_2	2.29 kg	$M_1 = 2.98$ kg & $M_2 = 1.60$ kg
Lengths L_3 & L_4	1.22 m	$L_3 = 1.59$ m & $L_4 = 1.54$ m
Masses M_3 & M_4	2.29 kg	$M_3 = 1.75$ kg & $M_4 = 1.60$ kg
Total Appendages Mass	15.51 kg	15.83 kg

Table 8.1: Structural data before optimization (COA) and after performing ICSD to the rotatory flexible spacecraft

$$f_{L_1}(\delta_{L_1}) = \frac{1}{1 + 0.3\delta_{L_1}}; \quad W_{L_1} = 0.75 \quad (8.18)$$

where the β_k values have been fixed to 0.75, a value which can never be reached with the allowed maximal variation, in order to encourage the maximum possible value for δ_{L_1} and δ_{M_1} . The constraint for minimum total mass is:

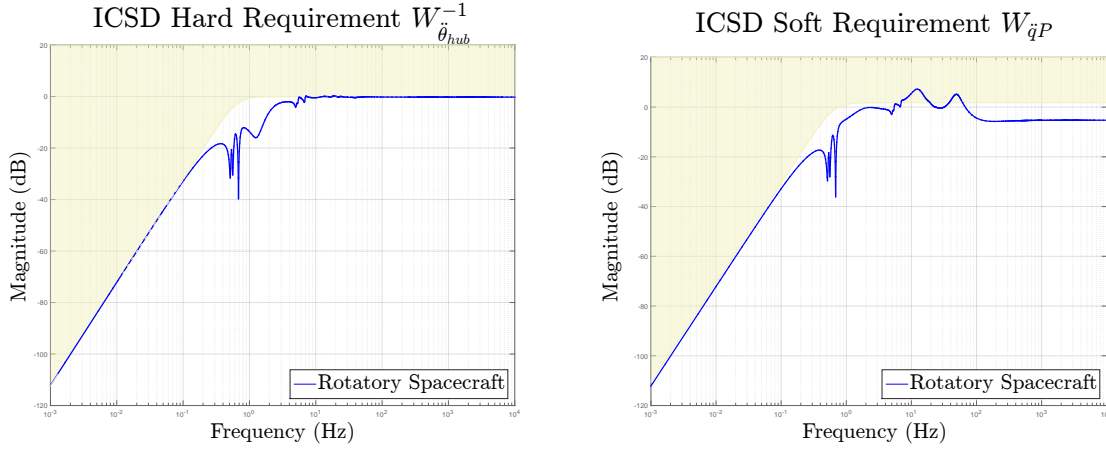
$$f_{M_{total}}(\delta_i) = L_{nom}\rho S(4 + 0.3\sum_{i=1}^4 \delta_{L_i}) + M_{nom}(4 + 0.3\sum_{i=1}^4 \delta_{M_i}); \quad W_{M_{total}} = M_0 \quad (8.19)$$

where $M_0 = 15.51$ kg is the nominal total mass of all the appendages. Equation (8.19) is a combination of all the structural parameters that can be varied, weighted by their impact on the system total mass (total beams mass for the lengths, total tip mass for the tip masses).

8.3.5 Optimization and Results

The optimization of the controller and the structural parameters is performed using the structured \mathcal{H}_∞ synthesis tool *systune*. The results of the ICSD solution are compared with those of a solution with control optimization alone (COA). Table 8.1 shows the optimized and nominal structural parameters. It can be seen that the length and tip mass of appendage 1 have been increased the maximum allowed, 30 %. For appendages 2, 3 and 4 the tip masses have been minimized while the lengths have been increased almost to the maximum, with the exception of appendage 2. Appendage 3 and its opposite appendage 4 are no longer symmetric since they lengths are slightly different and the tip masses difference is around 0.15 kg. The structural optimization meets the specifications: maximization of mass and length of appendage 1 while minimizing the impact on the total system's mass.

Figure 8.10 shows the resulting frequency response for the ASF of θ_{hub} and q_P compared with the desired templates $W_{\ddot{\theta}_{hub}}$ and $W_{\ddot{y}_{tip1}}$ after optimization. The gains of the PD controller have been adjusted to fit the frequency template and flexible modes are shifted and



(a) Constraint (yellow) on the hub's dynamics (blue) (b) Constraint (yellow) on the tip's dynamics (blue)

Figure 8.10: Dynamic specifications template and system response after optimization

more damped when comparing with the response given in Fig. 8.9b. The shift of flexible modes is a consequence of the structural optimization, since tip masses and lengths have been modified. The damping is provided by the active damping provided by the piezoelectric material controlled with an acceleration feedback control law.

The ICSD solution enjoys the same robust performance as the COA solution for the hub position control. The Nichols diagram of the open loop $t_{hub} \rightarrow t_{com}$ response in Fig. 8.11a shows that the ICSD solution has satisfactory phase and gain margins (GM = 20.5 dB, PM = 69.1 deg) which are as good as the COA solution (GM = 13.5 dB, PM = 69.1 deg). However, this is achieved by the ICSD solution with longer appendages which are not symmetric. Indeed, the first flexible mode, located at $\omega = 4.4$ rad/s appears to be uncontrollable in nominal configuration, corresponding to the symmetric bending of the system's appendages. However, the ICSD solution has tuned the system to be completely asymmetric so that the first flexible mode can be governed with the hub torque as well. This is confirmed in Fig. 8.11b, where the bode diagram of the open loop response shows that the first flexible mode appears as a resonance frequency in the ICSD solution and as an anti-resonance frequency for the COA solution.

The uncontrollability of the first symmetric bending mode at $\omega = 4.4$ rad/s is also verified in the time domain response. Figure 8.12 shows the closed-loop response of the hub's acceleration $\ddot{\theta}_{hub}$ and the first appendage tip's acceleration \ddot{y}_{tip_1} to an asymmetric torque disturbance at tips 1 and 3. This input excites the symmetric bending mode of appendages 3 and 4, which cannot be damped by the COA solution. It can be seen as well that the acceleration of the COA solution has a higher overshoot than the ICSD solution, even if the ICSD solution has higher tip mass and length. On the other hand, the ICSD solution needs two times more time for damping the tip vibrations and hub's position oscillations.

The results show that ICSD using structured \mathcal{H}_∞ synthesis can be achieved by implementing the desired specifications in \mathcal{H}_∞ form. The structured \mathcal{H}_∞ synthesis optimizes the

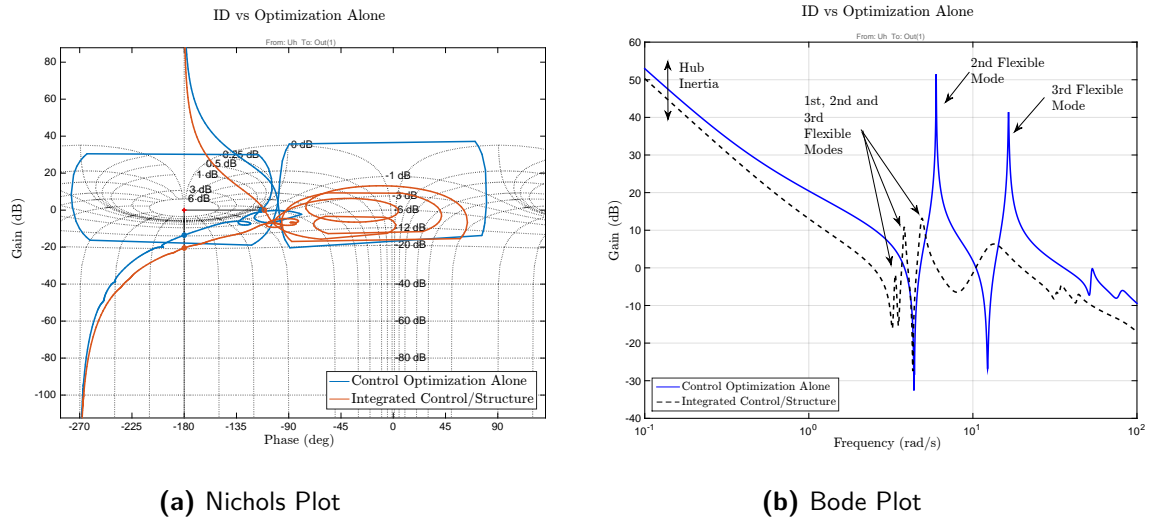


Figure 8.11: Open-loop $t_{hub} \rightarrow t_{com}$ diagrams comparing the frequency domain response of the ICSD and COA solutions

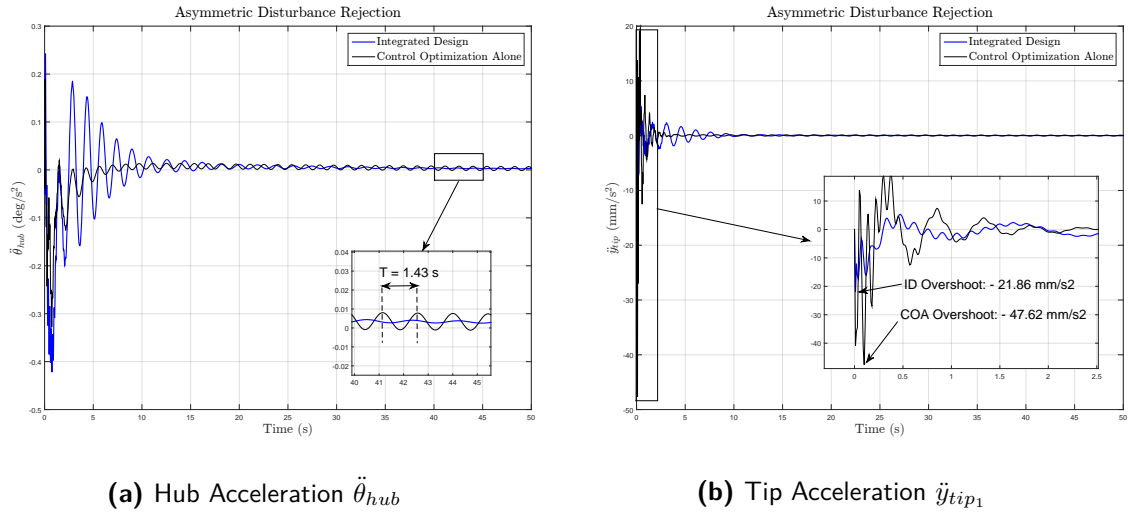


Figure 8.12: Comparison of ICSD and COA solutions in the time-domain, response to an asymmetric torque disturbance at appendages 3 and 4

controller and the structural parameters to better fit the dynamic specifications, while respecting the structural constraints imposed to the varying parameters. The same level of performance can be achieved with a modified structure, discovering new configurations which can improve control performance. The optimization process has provided an intuitive fact: the maximization of the mass of one appendage will decrease the total mass of the others. The optimization has provided a counter-intuitive fact as well: system's asymmetry can help to increase controllability of system's modes and to improve system's performance. Therefore, integrated design is possible and it takes into account the issues and tradeoffs of the physical system.

The implementation of dynamic, structural and controller specifications for the integrated control/structure design have been explained throughout this chapter. The specifications for the rigid body motion are implemented using a SOTAS scheme, while the flexible motion damping is achieved by projecting the rigid body motion template at different points of the FMS. The structural constraints for structured optimization are implemented with additional channels which included the cost functions and weighting filters applied to the varying parameters involved in the constraints. Controller frequency shaping can be stated through a roll-off filter. Finally, the implementation has been exemplified by performing the ICSD of the rotatory flexible spacecraft of Chap. 6. The next chapter uses the same \mathcal{H}_∞ constraints to perform the ICSD of a more complex system, a flexible satellite.

Chapter 9

Integrated Control/Structure Design of a Flexible Satellite

“Example is leadership.”
- Albert Schweitzer

Contents

9.1	System Description	144
9.2	System Modeling	146
9.3	System Specifications	148
9.3.1	Controller Architectures and Controller Specifications	149
9.3.2	Rigid, Flexible and Structural Specifications	149
9.4	Integrated Design Study	151
9.4.1	Robustness Analysis	152
9.4.2	Performance Analysis	154
9.4.3	Computing Cost	157
9.4.4	Analysis of Actuator Placement	158

This chapter applies the concepts developed in the foregoing chapters to a single complex application: the integrated attitude control/structure design of a flexible spacecraft. The flexible spacecraft is in preliminary design phases and, being a FMS with few available data. The modeling and integrated design frameworks developed in this study can be applied to it in order to derive conclusions for its future design.

THE precedent chapters have proposed, developed and applied the models, strategies and specifications needed to perform integrated attitude control/structure design with structured \mathcal{H}_∞ synthesis. In this chapter, all the acquired knowledge is applied to the case of a highly flexible spacecraft, the Extra Long Mast Observatory (ELMO). The proposed system is complex and requires a detailed analysis, what will show the advantages and limitations of the proposed ICSD approach.

The objective is to perform a preliminary study about the different tradeoffs between the control system and the structure of the satellite by obtaining a reliable model with the TITOP modeling technique and by performing ICSD with \mathcal{H}_∞ synthesis. The spacecraft's geometry and specifications are explained in Sec. 9.1. In Sec. 9.2, the flexible satellite is modeled using the TITOP approach. The implementation of system's specifications is explained in Sec. 9.3. Finally, the integrated design study is done in Sec. 9.4.

9.1 System Description

The Extra Long Mast Observatory (ELMO, Fig. 9.1) is the name provided to a virtual interferometry mission. To improve the instrument's performance, the focal length of the X-ray telescope is increased by introducing a long mast which will be deployed in orbit. The mast characteristics are based on a prototype developed by CNES (Centre National d'Etudes Spatiales). The aim is to study and test the feasibility of such a complex technology, that will require improvements on structure conception and attitude control system design. The study can be considered as a preliminary design phase of a large space structure.

The construction of the mast is in its preliminary design phase. Much researches have been done in order to study the feasibility of lighter and more resistant configurations for the onboard deployable mast. Based on previous know-how, the mechanical department has built a 4-meter prototype that is intended to form one of the segments of the deployable mast. The mast takes advantage of the elastic properties of composite materials (such as high-resistance carbon fiber, EC 2216 resin) to build a mast with low weight, thermal resistant and stiff which can be compacted in a few inches and be deployed up to 20 meters [CNES 10b, CNES 10a]. However, up to date the only data available is the one provided by the prototype, other kind of properties of the full deployed mast will have to be predicted with other models.

ELMO is composed of a rigid platform, with center of mass at G , to which a long deployable mast is cantilevered at a point P at which end Q the instrument for the required mission is located (depiction shown in Fig. 9.2). The mast is discretized in three mast segments, each one with the same properties as the prototype. Due to the mast's length, ELMO is predicted to have a highly-directional inertia tensor, with a very high magnitude of the moment-of-inertia in the perpendicular plane to the mast. Thus the main challenge in science-mode control design is to provide just-enough bandwidth to adequately mitigate low-frequency disturbances while minimizing the effects of end displacement and maximizing instrument mass. The integrated attitude control system (ACS)/ Structure design study aims at providing valuable control strategies for the required bandwidth and to maximize the

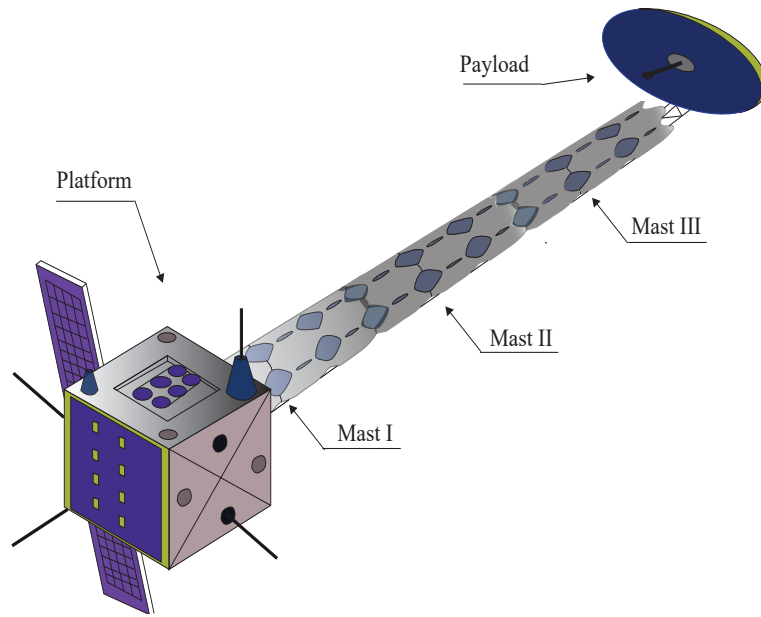


Figure 9.1: Illustration of the Extra Long Mast Observatory (ELMO)

instrument mass located at the end of the mast.

The difficulties of the integrated design study are two-folded: on one hand, there is no available model of the whole assembled system, on the other hand, there is no previous knowledge of what the control system will need in order to achieve the desired specifications. Therefore, the integrated control/structure design of ELMO is exploited to explore the following issues:

1. The computation of a model which takes into account the system's flexibility and which can be used for controller synthesis with structured \mathcal{H}_∞ synthesis.
2. Study of the possibility of increasing the payload mass.
3. The evaluation of the different control architectures that will be needed in order to fulfill mission requirements (pointing specifications)
4. Evaluate the influence of the position of the piezoelectric actuators along the mast

All these problems, addressed either simultaneously or one after each other, should help design engineers to gauge the system's needs and capabilities in the preliminary development phase.

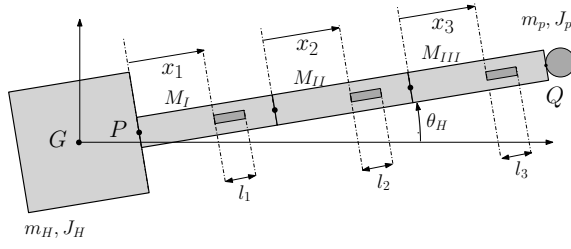


Figure 9.2: Simplified sketch of ELMO

Parameters	Symbol	Value
Hub Inertia	J_H	250 kg/m ²
Hub Mass	m_H	500.0 kg
Hub Dimension	R	1.0 m
Payload Inertia	J_{tip}	0.0 kg/m ²
Payload Mass	m_{tip}	61.0 kg
Length M_I, M_{II}, M_{III}	L	4.06 m
i -th PEA length	l_i	0.2 m

Table 9.1: ELMO configuration parameters

9.2 System Modeling

As stated before, the main difficulty of the ELMO study lies on being a FMS of which a full dynamic model is not available. The model of the full FMS has to be obtained by assembly of the different substructures which form it, that is, the platform, the mast segments and the payload. Only data of a single mast segment is available. To overcome this difficulty, the TITOP modeling technique is used to find a coherent model which can be used to perform integrated design.

The mast prototype has a complex geometry. It can be approximated by a cylindrical shell, of a diameter of 140 mm and variable thickness along the longitudinal axis due to the different layers of materials. The total length of the prototype is 4.06 m. The cylindrical shell consists of meticulously interlaced tiles, in such a manner that, once deployed, only a high compressible effort along the mast longitudinal axis can compress the mast to its initial position. The full FE-model of the mast segment has provided the first bending mode with the mast's tip uncharged at around 5 Hz and a tip displacement does not exceeds 5 mm under a thermal gradient of $[-150^\circ\text{C}, +150^\circ\text{C}]$ (see Fig. 9.3).

A simplified FE-model consisting of beam elements has been computed and some variables have been tuned in order to reproduce the same dynamic behavior for charged and uncharged configuration. In order to consider the improvement of the attitude control system by damping the flexible modes of the mast, piezoelectric laminates of 0.2 m length have been added. In nominal configuration, the piezoelectric actuators are located at $x_1 = 2.8$ m for the first mast segment, mast I, $x_2 = 2.5$ m for mast II and $x_3 = 2.5$ m for mast III. The actuator placement is depicted in a simplified manner in Fig. 9.2. The FE-model of each obtained mast has been computed and set into an actuated TITOP model as explained in Sec. 5.4. Therefore, for each mast the available inputs/outputs are the ones needed for mechanical coupling (acceleration-load transfer between connection points) and the ones needed for vibration damping (voltage v_i as control input, and output f_i as a collocated output, either force or acceleration).

Once all the TITOP models of the mast segments have been derived, the assembly of the whole system is addressed as in Fig. 9.4 in the needed LFT form for integrated design. Mast segments are connected as *actuated TITOP* models, which exchange acceleration-loads through their connection points until the end of the mast, where the payload is placed. The

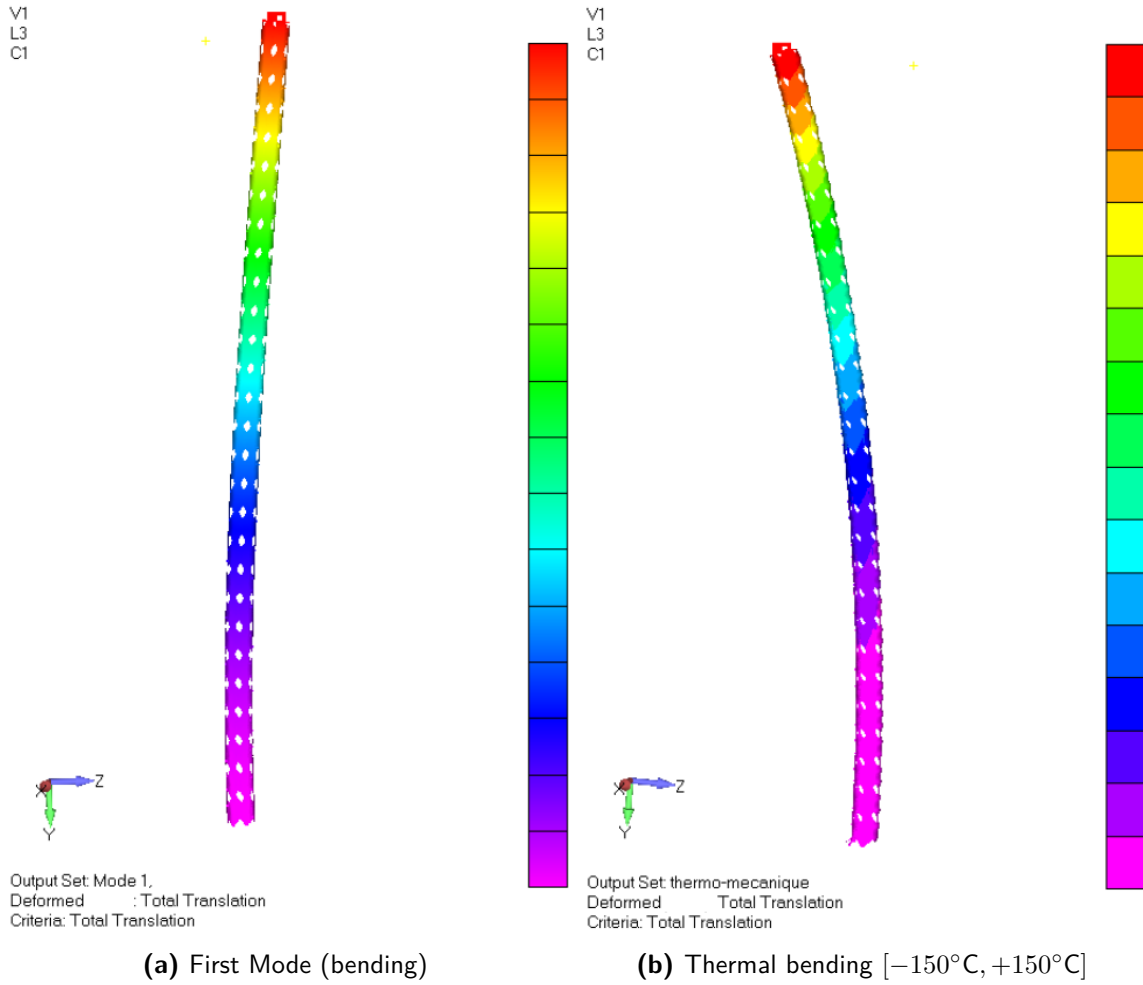


Figure 9.3: Mast prototype FE analysis for the first bending mode and thermal bending (Source: CNES and Latecoere)

masts can be actuated through the input of voltages v_i . The payload has been parametrized so that the mass variation is taken into account through a tunable block Δ_{Mt} for the payload maximization purpose. The whole chain of flexible substructures is connected to the platform as a force feedback, previously transported by the transport dynamics matrix ϕ_{PG}^T which relates the connection point P to the platform center of mass G .

The TITOP modeling technique provides a coherent plant model from which ICSD can be performed. The inputs correspond to forces and torques applied to the platform (F_G, T_G), the forces and torques applied at other points of the structure and the applied voltages in the piezoelectric actuators (v_i). The outputs correspond to the measured accelerations of the platform and payload misalignment. Displacement information is extracted from the electric charge in the piezoelectric components. Final state-space assembly results in a first flexible bending mode at 0.62 Hz, close to the desired bandwidth of 0.182 Hz obtained in Sec. 9.3, a resulting inertia of $11294 \text{ kg}\cdot\text{m}^2$, a system's total mass of 568.15 kg and the center of mass of the whole system located at 1.504 m from the platform's center, G .

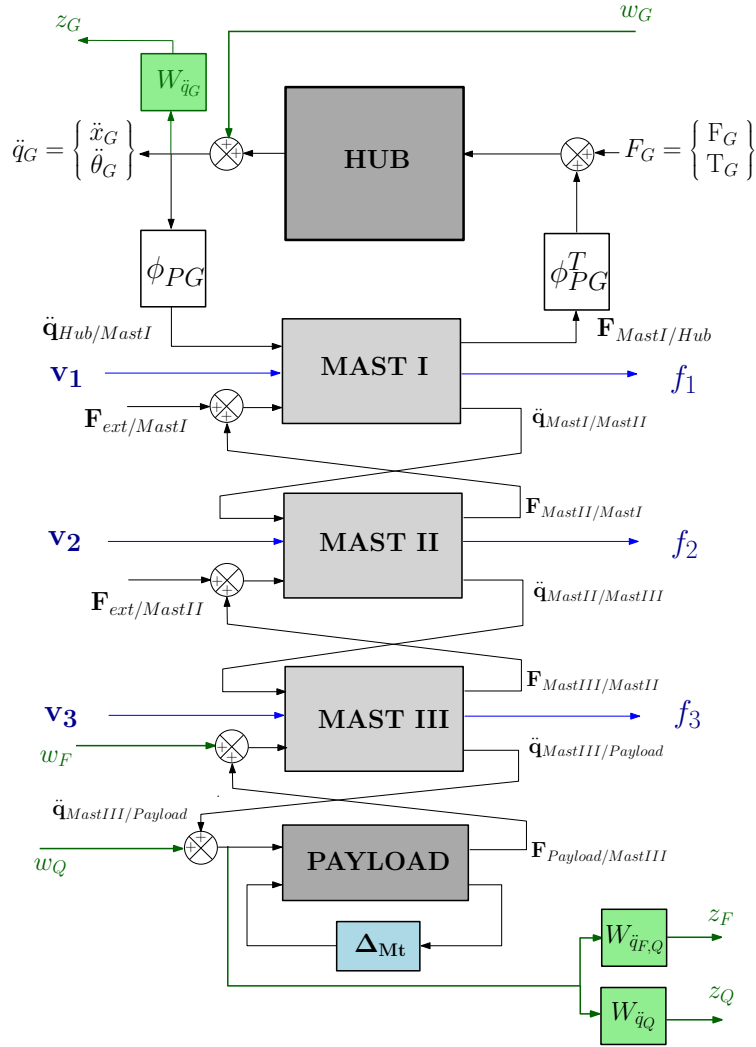


Figure 9.4: TITOP modeling technique applied to ELMO

The obtained LFT results in a large model of 110 states, with 48 outputs, 27 inputs and 2 occurrences of the varying parameter $\delta_{m_{tip}}$. Since the size of the model is too large, the model is reduced using gramian-based input/output balancing for keeping the most significant 35 states. Therefore, the synthesis model is a reduced model of 35 states while the validation model (VM) remains the original one, which will be used to test the control strategies as well.

9.3 System Specifications

This section explains the specifications that the augmented controller (real controller plus structural parameters) has to achieve. First, different control architectures subject to study are explained, specifying which kind of constraints (roll-off) are imposed to each architecture. The estimation and implementation of dynamic specifications is then explained, together with

the specification for payload mass maximization.

9.3.1 Controller Architectures and Controller Specifications

The controller, as stated in Sec. 7.1.4, has a decentralized architecture, with a PD controller governing rigid body motions and an active damping system controlling the flexible motion, either based on an acceleration feedback (AF) or integral force feedback (IFF) approach. The architectures to be tested for ICSD of the system are:

1. PD controller alone for controlling the rigid body motion of the platform, θ_H (PD Alone).
2. PD for rigid body motion, IFF for active damping (PD + IFF).
3. PD for rigid body motion, AF for active damping (PD + AF).
4. PD with roll-off filter for rigid body motion, IFF with a roll-off filter in order to limit the actuation of the active damping system between 1 Hz and 1000 Hz (PDro + IFFro).
5. PD for rigid body motion, IFF with a noncollocated measurement, the tip velocity \dot{y}_{tip} , to see if available measurements at the tip of the mast can be used to improve system's performance (PD + IFFnc).

Moreover, architectures 1,2,3 and 5 have two different versions: one with a single PD controller and another incorporating a roll-off filter to the PD controller. The objective is to evaluate the improvement of the control system performance when a roll-off filter is added to the PD rather than only ensuring minimum control gains.

The weighting filter for the PD roll-off is the same as in Eq. (8.9), with a roll-off frequency one or two decades ahead of the control bandwidth, $\omega_{ro} = 100$ rad/s. The weighting filter for the IFF with roll-off of the fourth control strategy is a pass-band filter 1 Hz and 1000 Hz. The roll-off channels are added as explained in Sec. 8.2.4. When roll-off constraint was not considered for the rigid-body motion, a channel was added in order to impose minimum controller gains.

9.3.2 Rigid, Flexible and Structural Specifications

The mission specifications are stated as low-frequency torque disturbance rejection dynamic requirements for the pointing specifications. The required bandwidth for disturbance rejection of the angle position can be estimated as follows:

$$\omega_{des} = \sqrt{\frac{T_{pert}}{J_t \theta_{spec}}} \quad (9.1)$$

where T_{pert} is the estimated amplitude of the torque perturbation, J_t is the system's inertia around the axis under study and θ_{spec} is the pointing specification. The total inertia around the axis, J_t , can be computed from the system model through the direct gain of transfer load-acceleration channel, and its value has been computed in Sec. 9.2 as $11294 \text{ kg} \cdot \text{m}^2$. The pointing specification θ_{spec} is given by the mission requirements. The torque perturbation, however, can be difficult to estimate because it also depends on spacecraft's properties.

The estimated perturbation torque has to be computed with the maximum expected value. The largest deflections that the mast may undergo will be caused by the bending moment due to the internal thermal couple. The expected internal bending moment due to temperature gradient is computed as in [Johnston 98] (see Appendix C), giving an expected value of $19.03 \text{ N} \cdot \text{m}$ for the estimated cross-section values of the mast. This result has been computed under the hypothesis that there is no thermal control hardware on the mast, which lead to the highest temperature gradients (232° C/m).

The payload misalignment with the line of sight of the platform must not exceed 288 arcsec (0.08 degrees) during observation, which given the total length of the deployable mast can be translated to 17 mm of maximum tip displacement. The mass of the payload is expected to be around 60 kg , but a maximization can be foreseen if this does not affect mission requirements.

These results, together with the system's total inertia computed in Sec. 9.2, leads to a required bandwidth of $\omega_{des} = 1.14 \text{ rad/s}$ or $f_{des} = 0.182 \text{ Hz}$. A classical damping coefficient to avoid overshoot is taken as $\xi = 0.7$ to impose the closed loop dynamics of the attitude control system. It might be possible that the torque value has induced an overestimation of the required control bandwidth. The torque, however, is not instantly applied; it depends on the thermal time constant of the appendage, τ_{app} , as follows:

$$T_{term}(t) = |T_{term}|(1 - e^{-\frac{t}{\tau_{app}}}) \quad (9.2)$$

where τ_{app} is roughly 32 s and $|T_{pert}|$ has the previously mentioned value (the computation of these parameters is shown in Appendix C). The response of the thermal torque results in a signal of a bandwidth of 0.915 rad/s or 0.146 Hz , the same order of magnitude as the previously computed value. The most restrictive value is taken, which is $f_{des} = 0.182 \text{ Hz}$, leading to the following weighting filter for the rigid body DOF of ELMO, θ_H :

$$W_{\ddot{\theta}_H}^{-1} = \frac{s^2}{s^2 + 1.601s + 1.308} \quad (9.3)$$

The damping of the flexible modes is imposed by weighting the transfer between the hub's acceleration disturbance w_G and the performance output z_Q with $W_{\ddot{q}_P} = 3 \cdot L \cdot W_{\ddot{\theta}_H}^{-1}$. A constant filter as the one in Eq. (8.6) is added in the transfer $w_F \rightarrow z_F$ to add additional damping, tuned to have a 5% of damping ratio. In Fig. 9.5 the frequency response of the system is compared with the given templates before ICSD optimization. As in the flexible rotatory spacecraft example, flexible modes are badly damped and the initial PD controller

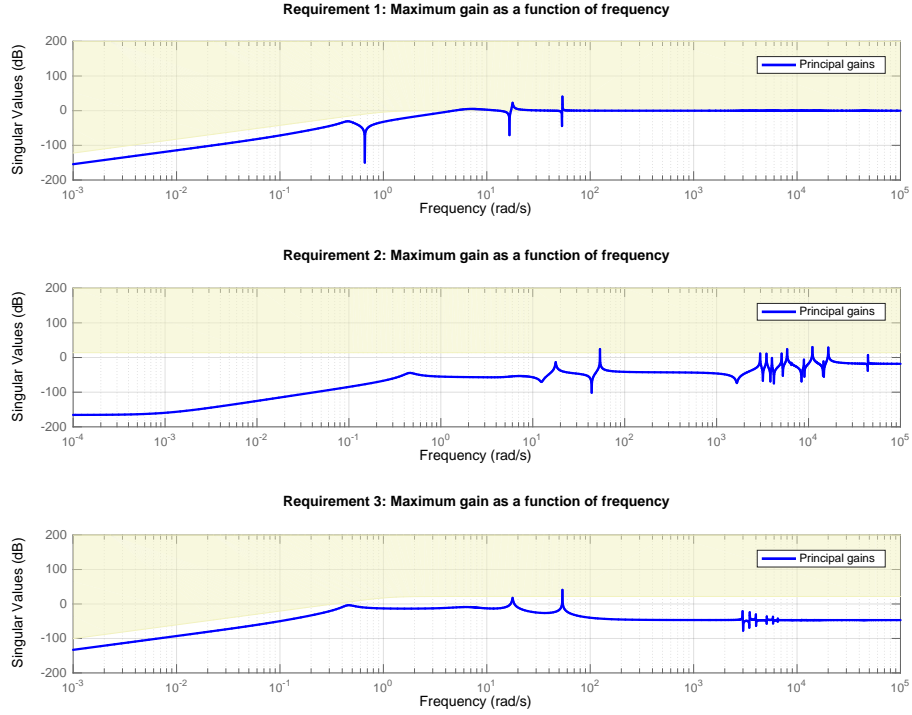


Figure 9.5: Template requirements and ELMO frequency response

gains have a larger value than the needed to respect the template on the ASF of the platform's position θ_H . Figure 9.5 also shows that the most influential flexible modes are the three first bending modes at $\omega_1 = 3.89$ rad/s, $\omega_2 = 17.6$ rad/s and $\omega_3 = 53.8$ rad/s.

With the constraints for rigid and flexible motion already defined, the additional channel for payload mass maximization can be added. The constraint for the maximization of the payload mass is implemented as follows:

$$f_{m_{tip}}(\delta_{m_{tip}}) = 1 - \delta_{m_{tip}}; \quad W_{m_{tip}} = 0.5 \quad (9.4)$$

where the β_k value has been fixed to 0.5 in order to encourage the maximum possible value for m_{tip} .

9.4 Integrated Design Study

The TITOP model of ELMO in LFT form is used in the co-design scheme for structured \mathcal{H}_∞ synthesis. Several attempts were realized for each control strategy, keeping the one which presented the lowest disparity with the rigid body motion template (introduced as

Index	PD Alone	PD + IFF	PD + AF	PDro + IFFro	PD + IFFnc
γ_{perf}	0.9876	1.1190	0.9884	0.9954	1.1377
Opt Mt	69.78 kg	63.56 kg	75 kg	66.55 kg	75 kg
Real RW	✓	✓	✗	✓	✓
Real PEAs	-	✗	✗	✓	✗
Real RW & Real PEAs	✓	✗	✗	✓	✗
Validation Model (VM)	✗	✓	✗	✓	✓
VM & real RW	✗	✓	✗	✓	✓
VM & real RW & PEAs	✗	✗	✗	✓	✗

Table 9.2: Summary of the results of the ICSD of ELMO

hard constraint in the *systune* Matlab function). The obtained controllers are tested in the reduced model and in the validation model computed with the modified payload mass.

Throughout the section the robustness of the synthesized control systems are tested considering real dynamics of reaction wheels (RWs) and piezoelectric actuators (PEAs). The transfer function of the reaction wheel will be considered as a low-pass filter of 10 Hz bandwidth. The transfer function of the piezoelectric actuators are considered as pass-band filters in the range between 0.1 Hz and 1000 Hz.

9.4.1 Robustness Analysis

The optimization driven by the structured \mathcal{H}_∞ synthesis gives controllers which respect the template for the rigid body motion (Fig. 9.6) with a γ_{perf} index close to the unit value. Some strategies have found γ_{perf} below one due to the changes in the nominal structure (payload mass variation). The robustness of the attitude control loop when closing the active damping loop is tested considering real reaction wheel dynamics and real piezoelectric actuators dynamics. A summary of the results is presented in Table 9.2. The acceleration feedback strategy has been removed from the discussion of the results since, being noncollocated, has not given any satisfactory results when compared with the rest of the strategies.

The improvement of the attitude control system robust performance by adding active damping is highlighted in Figs. 9.7a and 9.7b. Considering perfect piezoelectric actuator dynamics, the closed-loop of the active damping control system leads to an increase of the robust performance of the attitude control system. Using a limited bandwidth RW, the PD alone only offers a GM of 3.85 dB and a PM of 10.2 deg, whereas the IFF or IFFro active damping strategies increase the robust performance to GMs larger than 10 dB and PMs larger than 50 deg. In addition, the active damping strategies are stable in the validation model (with perfect actuators dynamics) whereas the PD alone is not.

When comparing the robust performance of the active damping strategies among them

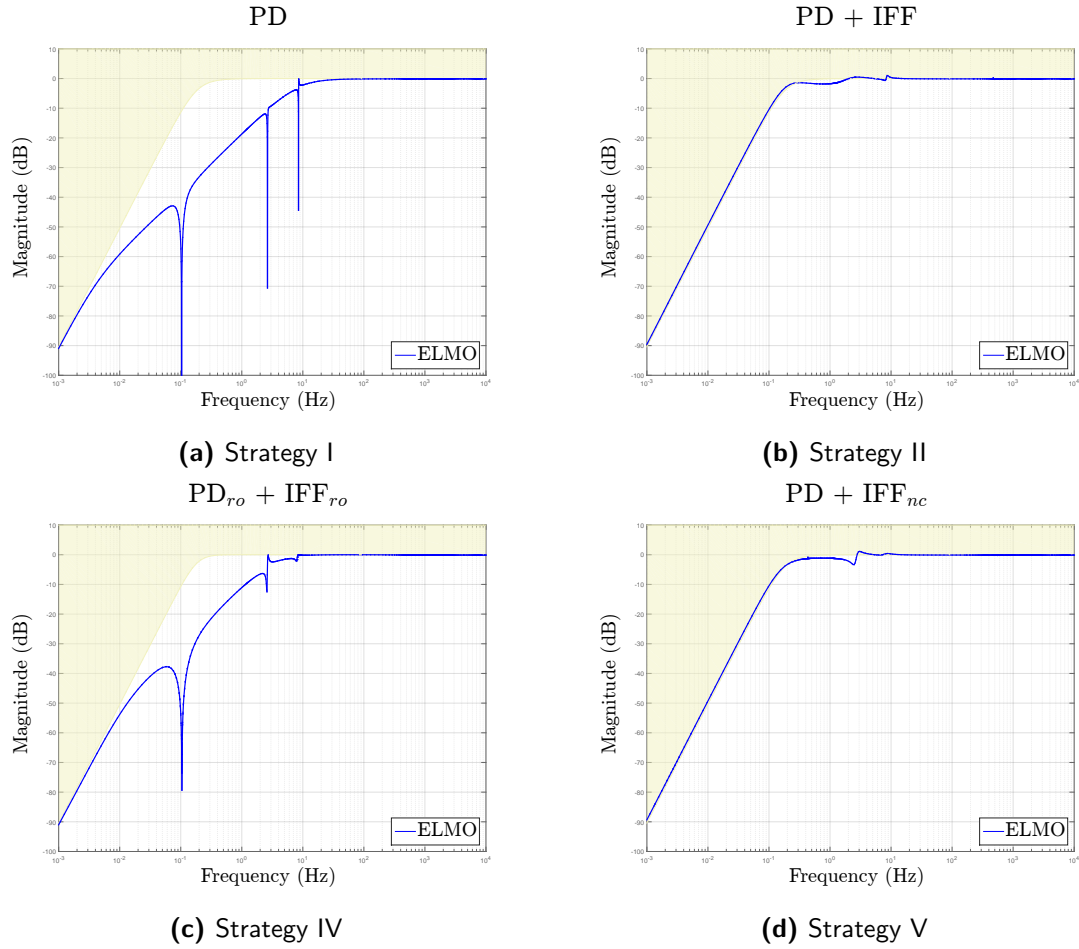


Figure 9.6: Acceleration Sensitivity Function Template (yellow background) and the obtained controlled system transfers

(Fig. 9.8a), values show that the IFF without roll-off gives the highest robustness to the attitude control loop (GM = 48.1 dB, PM = 68.7 deg). IFF with roll-off is even less robust (GM = 11.13 dB, PM = 56 deg) than the noncollocated IFF (GM = 38.1 dB, PM = 73.8 deg). However, this statement is proved wrong when comparing with models with real PEA dynamics (limited bandwidth between 0.1 Hz and 1000 Hz). The active damping loops without roll-off result in unstable attitude control loops, as seen in Fig. 9.8b, whereas the IFF with roll-off remains stable with almost the same performance (GM = 11.3 dB, PM = 56.6 deg). This conclusion could have been predicted from the fact that the optimization algorithm, having no constraints for the active damping control loop gains, has tuned the control gains of IFF and IFF_{nc} to high values which in turn are not achievable. This is also noticed in Figs. 9.7a and 9.7b, where the Nichols diagram of the IFF exhibits unrealistic damping of the flexible modes and the Nichols diagram of the IFF_{ro} still exhibits the loops caused by the flexible modes.

It appears to be that no significant improvements in robust performance or stability are found when adding roll-off filters to the controller of the rigid body motion, either in the re-

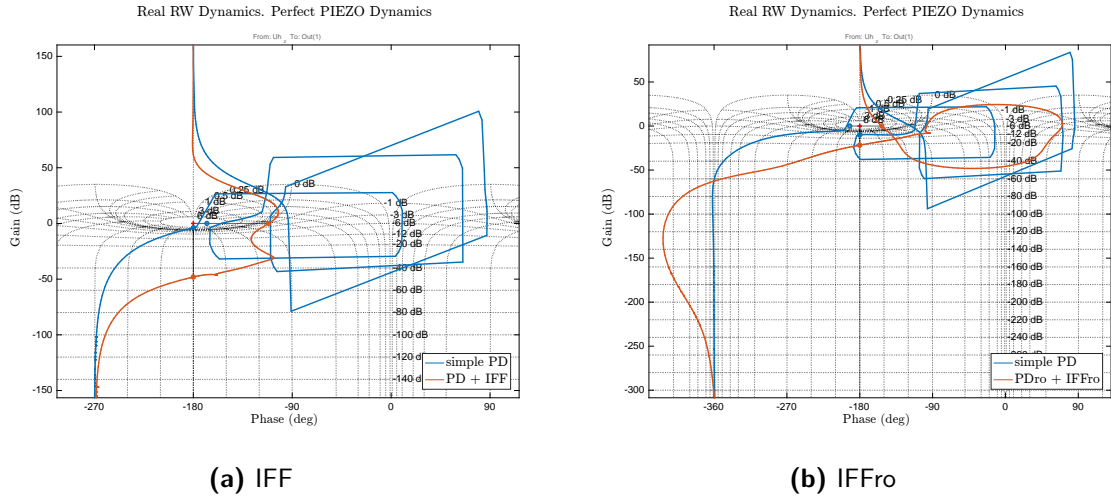


Figure 9.7: Nichols Comparison with/without active damping strategies

duced or the validation model. Constraining the PD controller to have minimum control gains is enough to ensure attitude control system robustness, without the drawback of increasing the order of the controller to be optimized. Figure 9.9 shows that the robust performance of the attitude control system using roll-off filter (GM = 21.7 dB, PM = 27.8 deg) is equivalent to the one which only has minimized attitude controller gains (GM = 11.3 dB, PM = 56 deg), having decreased phase margin to increase the gain margin.

9.4.2 Performance Analysis

The robustness analysis has been performed using the reduced model. Now the \mathcal{H}_∞ -synthesized controllers are tested with the VM in the time domain, either with perfect and real dynamics of actuators.

Considering perfect actuator dynamics, the response to impulse disturbance torques at the platform and at the tip of the mast has been analyzed. Figure 9.10 shows the hub and tip response to an impulse disturbance torque at the hub, and Fig. 9.11 the hub and tip response to an impulse disturbance torque at the tip. It can be noticed that tip displacements with the PD alone strategy are more sensitive to hub or tip disturbance torques than the rest of the strategies. The strategies presenting the highest damping of the flexible modes, IFF and IFFnc, rapidly damp tip vibrations but have a large overshoot of the hub's position. On the contrary, low damping of the flexible modes avoids large overshoot of the hub's position but needs for time for damping the tip's vibrations. Therefore, there is a tradeoff between the flexible modes damping and the control of rigid body modes. The IFFro strategy exhibits a smooth response without large overshoot of the hub's position and with tip's vibrations which are less large than the PD alone case.

When considering real RW dynamics, all systems are stable except for the one with control optimization. Gains have large values and the limitation of the RW bandwidth is translated

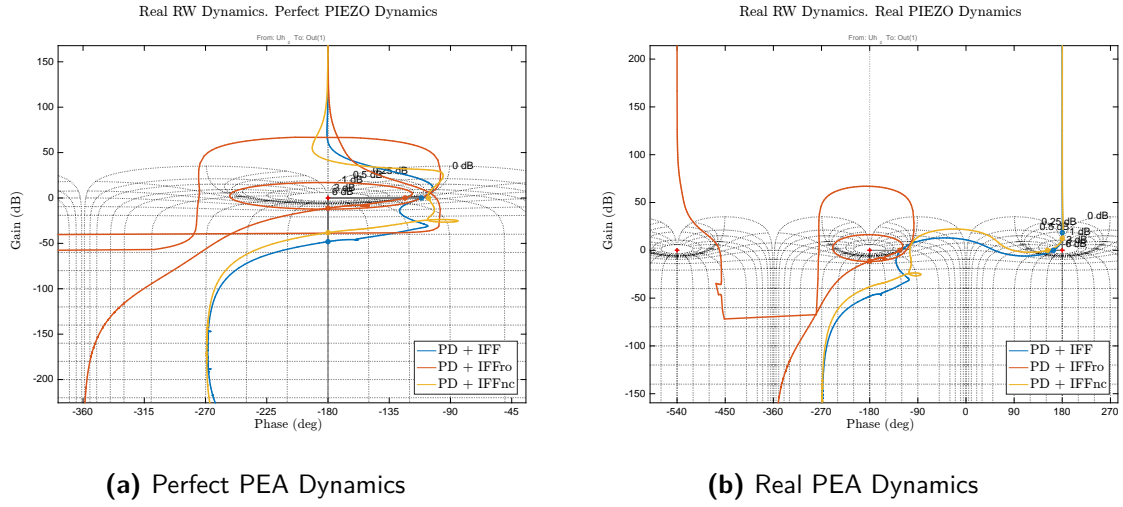


Figure 9.8: Nichols Diagram of the attitude control open loop, closing the active damping loop, comparing active damping strategies

into system's instability, as shown in the impulse responses in Fig. 9.12. If real PEA dynamics are considered for the active damping loop, the only controller capable of stabilizing the system is the IFF with roll-off, the others fail in stabilizing the system as already anticipated with the reduced model.

Finally, the performance of the IFFro strategy is tested with real actuator dynamics in the VM with a more realistic disturbance input, the thermal torque of Eq. (C.6). The application of an internal bending moment is equivalent to applying the same moment at the hub and at the tip but in opposite senses, so two disturbance torques are applied simultaneously at the hub and at the tip, but with opposite signs. The module of the applied torque is $|T_{perf}| = 19.03 \text{ N}\cdot\text{m}$ and the thermal time constant of the mast has been estimated to be $\tau_{mast} = 32 \text{ s}$ [Johnston 98].

In Fig. 9.13a it can be seen that the hub attitude is stabilized using the validation model and real actuator dynamics without exceeding the pointing requirement specification (0.08 deg), with higher overshoot than an ideal situation (standard synthesis of the PD controller with perfect actuator dynamics). Figure 9.15b shows that the tip exhibits the same behavior and it does not exceed the 17 mm of maximum misalignment.

Regarding payload maximization, the results show that no general conclusion can be extracted. It appears clear that for the IFFro strategy the mass can be increased up to 66.5 kg and the system remains stable and with acceptable robust margins in all circumstances. However, the other strategies which have failed at some point of the study have presented a maximization of the payload as well. It is particularly interesting the case of the worst robust performance controllers (AF), which has maximized the payload at the maximum allowed, 75 kg. The PD alone strategy has maximized the payload mass as well, but up to 70 kg. It appears to be that somehow the augmentation of the tip mass, taking into account the drop of the first flexible mode, is more beneficial in terms of reducing the flexible behavior of the

IFFro Active Damping. Real RW Dynamics. Real PIEZO Dynamics

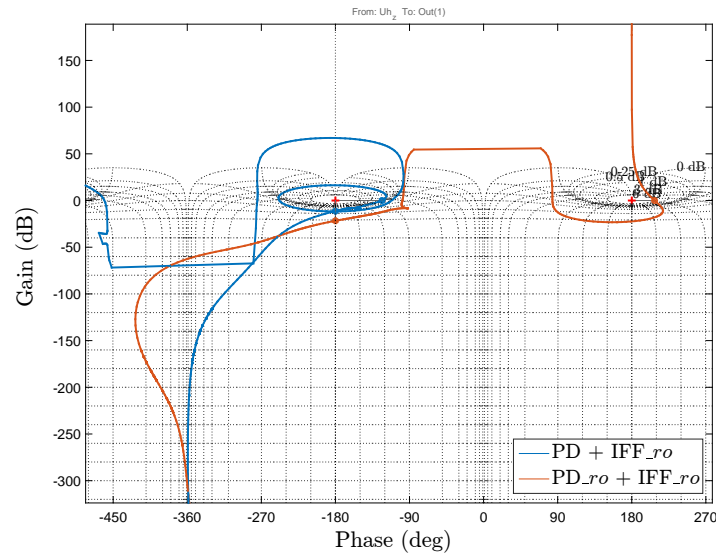
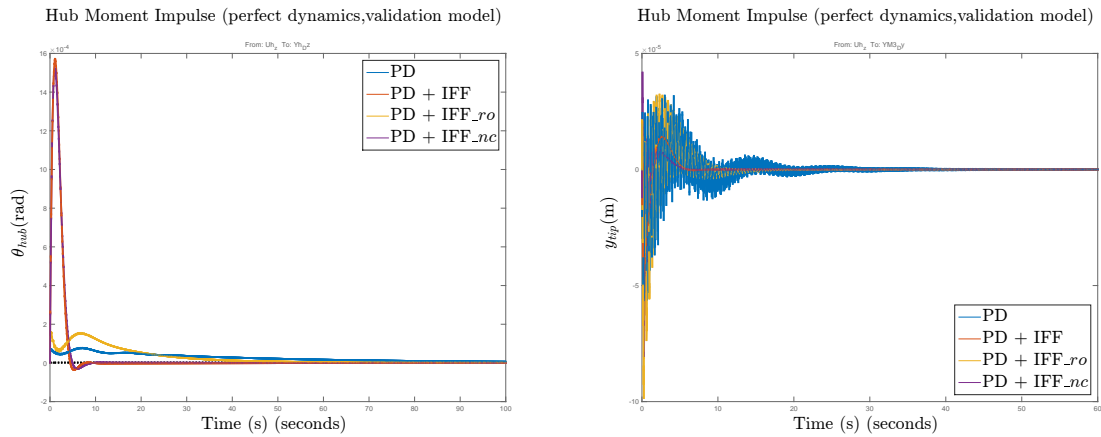


Figure 9.9: Comparison of the IFFro active damping with/without roll-off filter of the attitude control system

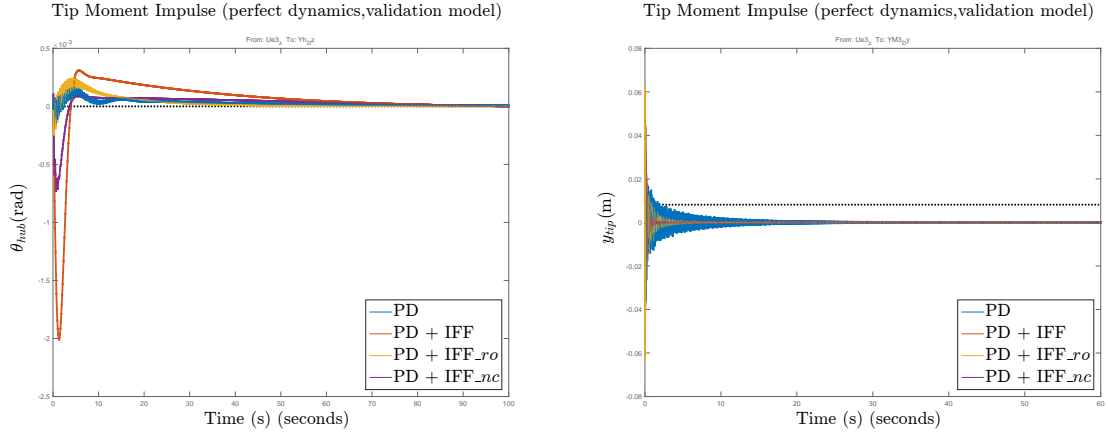


(a) Hub position response to hub impulse

(b) Tip position response to hub impulse

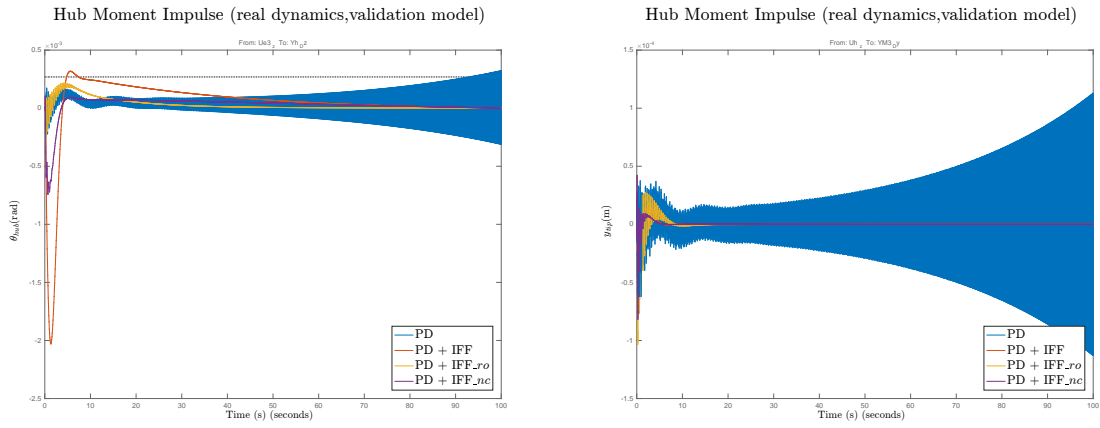
Figure 9.10: Time domain responses of the hub and tip positions for impulse disturbance torque at the hub

system. This fact is confirmed in Sec. 9.4.4 where it is shown that the first flexible mode is smoother for a 75-kg tip mass than for a 61-kg tip mass (Fig. 9.16b). This can be the reason why the optimization tends to increase the tip mass with worse control strategies, in order to have mode shapes which are more favorable (flatter bending) for reducing the impact of the bending modes. However, this maximization penalizes the stability and robustness in the validation model.



(a) Hub position response to tip impulse

(b) Tip position response to tip impulse

Figure 9.11: Time domain responses of the hub and tip positions for impulse disturbance torque at the tip

(a) Hub response to hub impulse

(b) Tip response to hub impulse

Figure 9.12: Unstability of the PD alone strategy in the validation model with real RW dynamics

9.4.3 Computing Cost

The tools for the modeling of ELMO and the structured \mathcal{H}_∞ synthesis were performed in a desktop computer using a dual-core processor Intel Xeon 2.80 GHz with 6 Gb RAM. The modeling and synthesis functions were run in Matlab R2014a with Windows 7 as operating system.

The computing time of LTI TITOP models (those which are not parameterized) can be neglected since the maximum value, corresponding to FE models up to 80 elements, is around 0.20 s. The time employed for TITOP assembly is also negligible. The computation of a LFT TITOP model strongly depends on the number of parameters being varied and if they are included manually or as a part of a full parameterization. For ELMO, the modeling computing

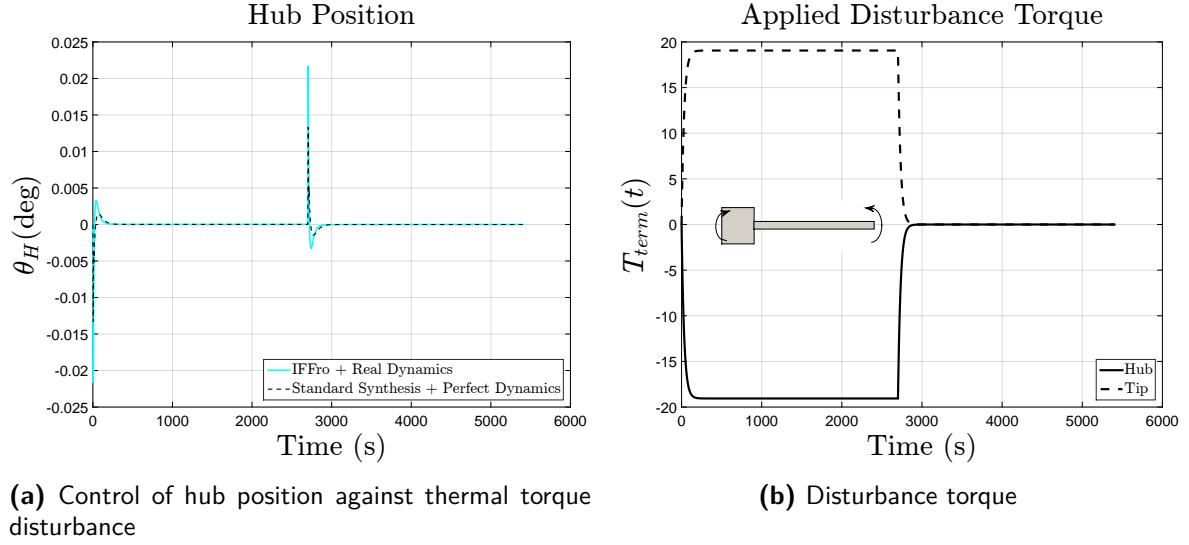


Figure 9.13: Tip damping against thermal torque disturbance

time for describing the piezo position for each mast took around 5 s when three nodes were employed for each sub-segment.

The computing time of the structured \mathcal{H}_∞ synthesis for the system's integrated design varies depending on the number of constraints and the size of the model. For the ELMO case, the optimization of the five strategies takes around 20 minutes, with each strategy being run 8 times to ensure the best result. In average, each optimization took around 1 min since parallel computing was performed using the two processor cores.

9.4.4 Analysis of Actuator Placement

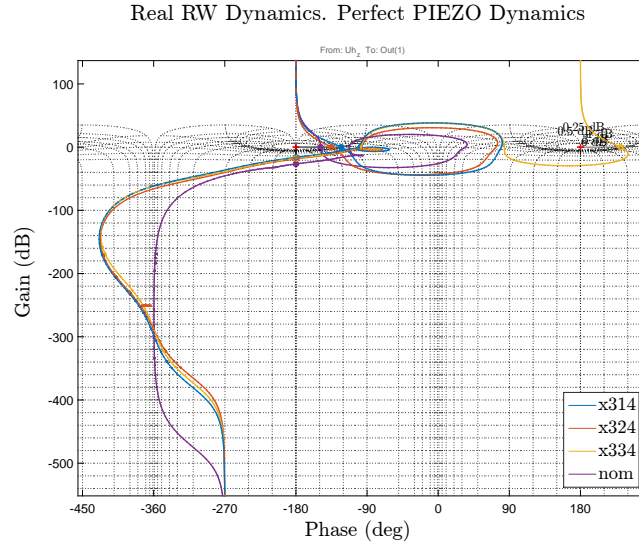
Finally, the influence of PEAs position along the mast is studied. In Sec. 6.1.3 the TITOP model for parameterizing the position of piezoelectric strips along a beam is explained. This model has been used as a substitute of the nominal TITOP models of the mast in order to find the optimal position of the piezoelectric strips. However, after several tests, the structured \mathcal{H}_∞ synthesis reveals that the system could not be stabilized with the proposed controllers. This was due to the fact that the LFT model of the parameterized beam presented unstable real poles at very high frequencies. Unstable high frequency poles do not appear in the real system, and they do not appear with a regular LTI assembly in the desired configuration. The error might be the result either of an incorrect simplification of a varying parameter in the LFT assembly process or of a propagated numeric error. Regardless the source of error, the solution seems to be considering all the parameters without simplification, what makes the model unusable due to its high order.

Therefore, the influence of PEAs position has been analyzed manually. Several models have been created with different piezoelectric configurations. For each i mast, the piezo component has been placed at $x_i = 1, 2, 3, 4$ m (the 4-m position was 3.8 m in reality due to the

$x_1 = 2$	$x_3 = 1$	$x_3 = 2$	$x_3 = 3$	$x_3 = 4$
$x_2 = 1$	✗	✗	✓	✓
$x_2 = 2$	✗	✓	✓	✓
$x_2 = 3$	-	-	-	-
$x_2 = 4$	-	-	-	-

Table 9.3: Fail/success summary of PEAs location

$x_1 = 3$	$x_3 = 1$	$x_3 = 2$	$x_3 = 3$	$x_3 = 4$
$x_2 = 1$	✗	✗	✗	✓
$x_2 = 2$	✓	✓	✓	✓
$x_2 = 3$	✗	✓	✗	✓
$x_2 = 4$	✗	✗	✗	✗

Table 9.4: Fail/success summary of PEAs location**Figure 9.14:** Comparison of the IFFro active damping strategies when varying the second piezo between $x_2 = 1$ m and $x_2 = 3$ m

strip length). Optimization results which gave unstable loops in the VM were automatically rejected. There are configurations which have always failed to find controllers that stabilized the system using the VM, while others always give a solution. Results are summarized in Tables 9.3 and 9.4, where x_1 is fixed to 2 and 3 m since they are the positions which find stabilizing controllers.

The configurations which succeed in finding stable solutions usually involve placements at $x_2 \in [2, 3]$ m and $x_3 = 2$ or 4 m. The IFFro strategy of the obtained configurations varying the position of the second PEA with $x_1 = 3$ m and $x_3 = 4$ m is compared with the one obtained in nominal configuration ($x_1 = 2.8$ m, $x_2 = 2.5$ m, $x_3 = 2.5$ m). Figure 9.14 shows that they all have the same level of robust performance, with GM between 15-25 dB and PM of 35-50 deg. Hence, the piezo component position does not exhibit a significant impact on the robust performance index of the attitude control system.

The performance of each configuration has been tested using the thermal torque disturbance in Sec. 9.4.2. Results are shown in Figs. 9.15a and 9.15b. The x334 configuration ($x_1 = 3$ m, $x_2 = 3$ m, $x_3 = 3.8$ m) exhibits the lowest hub position overshoot and tip misalignment, while the x314 configuration has the largest overshoot and the largest tip misalignment.

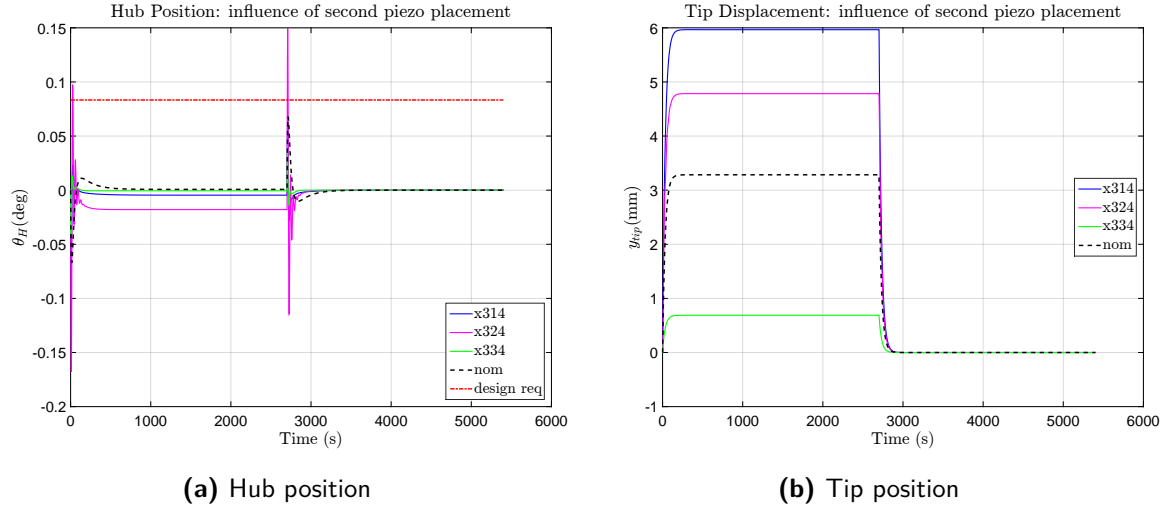


Figure 9.15: Hub and tip position for different placements of the second PEA under thermal torque disturbance

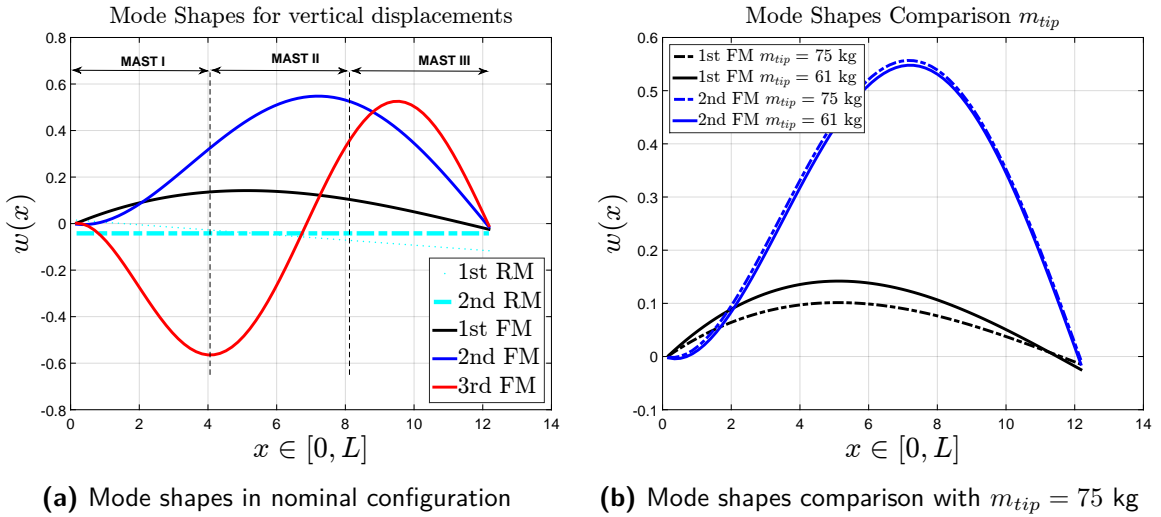


Figure 9.16: Mode Shapes of a flexible beam (rigid mode, RM, flexible mode, FM) with tip masses of 500 kg at $x = 0$ and 61/75 kg at $x = L$

This is directly related to the effectiveness of the PEAs at certain positions.

It appears to be that PEAs are more effective on reducing attitude overshoot and tip displacement when they are placed where the mode shape to be controlled presents the largest values or higher slope. As seen in Sec. 9.3, the three first bending modes are the ones which interfere the most the frequency templates. Figure 9.16a shows the mode shapes of the system (approximated by a beam charged at its ends with masses of 500 kg and 61 kg respectively). It can be evaluated that the second flexible mode (FM) has its maximum at approximately $x_2 = 3$ m, with deflections which are larger than the first FM. The PEA position seems to modify the mode shapes and to be more efficient in order configurations, that is why all the successful optimizations always have PEAs locations for $x_2 = 3$ m and $x_3 = 1$ m to 2 m, since

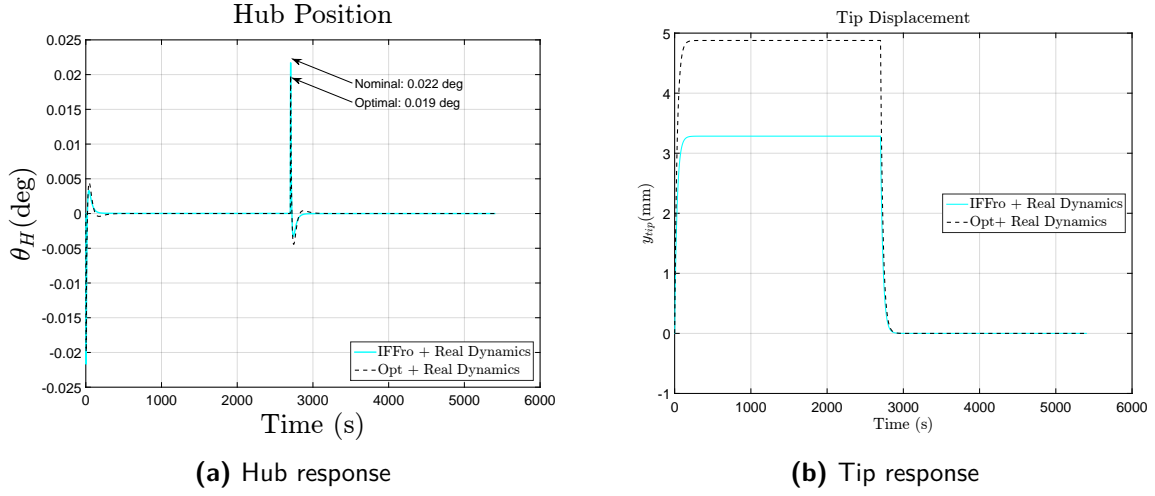


Figure 9.17: Hub and tip position comparison between the nominal PEA configuration and the optimized PEA configuration

they coincide with the maximum of the second and the third mode shapes.

The nominal configuration has exhibited a good performance as well since the piezoelectric component are located at favorable positions. The position of the first piezo is near the first and third FM maximum, the position of the second piezo is at the maximum of the second flexible mode and the position of the third piezo is near the maximum of the third flexible mode. Another optimization is run with a piezo position which might be the optimal one: $x_1 = 3.5$ m, $x_2 = 3.24$ and $x_3 = 1.45$ m. Although the robust performance was found to be similar (GM = 10.2 dB, PM = 53.6 deg for real actuator dynamics), the performance was slightly better than the nominal configuration (lower hub position overshoot in Fig. 9.17a, same order of tip displacement in Fig. 9.17b) but the maximized payload mass was 63 kg, 3 kg less than the nominal configuration. This short gain of performance might be due to fact that the PEA placement modifies the mode shapes shown in Fig. 9.16a due to the added mass and stiffness, which in turn changes the optimal position.

This chapter has performed integrated control/structure design of a flexible satellite by modeling its structure with the TITOP modeling technique and by optimizing the controllers and structure using structured \mathcal{H}_∞ synthesis. The modeling technique has been proved successful for predicting the dynamic behavior of ELMO once its substructures are assembled. The most used parameters of the structure (total mass, center of mass position, total system inertia and flexible mode frequencies) can be derived in order to estimate other specifications such as pointing requirements. Integrated design has been performed using different controller architectures and maximizing the payload mass. The most robust architecture is the PD controller with roll-off filter for controlling the hub's position and an integral force feedback with roll-off, stable either in the reduced model and the validation model, with perfect and real actuator dynamics. Moreover, this architecture offers one of the lowest hub position overshoot and the less tip displacement for the nominal piezoelectric configuration. Manual placement of PEAs at different positions has determined that the piezoactuators should be placed where the mode shapes exhibit maximum displacement or higher slope.

Part III

Conclusions

Chapter 10

Discussion

“The aim of an argument or discussion should not be victory but progress.”

- Joseph Joubert

ALTHOUGH throughout the study the majority of the results have been discussed and assessed, this chapter offers a the general overview of the main contributions of the study, highlighting their advantages and limitations. The main contributions have been classified in two types: findings concerning the linear modeling of flexible multibody systems and findings concerning integrated control/structure design using structured \mathcal{H}_∞ synthesis.

10.1 Results in Flexible Multibody Systems Modeling

One of the main contributions and intermediary result for integrated control/structure design has been the development of a flexible multibody linear modeling technique. The linear and block-diagram-based technique proposed by [Alazard 08] has been expanded in order to link flexible substructures among them and to add piezoelectric actuators and revolute joints. In addition, theoretical foundations have been established and comparisons with other modeling techniques have been performed for the first time.

The FMS linear modeling approach, called the TITOP modeling technique, allows the assembly of star-like and chain-like structures, actuated either with piezoelectric materials or revolute joints at their connection points. This is a step forward in the FMS modeling oriented to linear control, increasing the capabilities of the models proposed in [Alazard 08, Guy 14, Cumer 01]. The models can be derived with FE as input data, and can be assembled using block diagrams of Matlab Simulink, using as overlapping mechanism the DP form, a clear advantage for system assembly when comparing with other substructural assembly techniques such as the ones in [Young 90, Sunar 92]. However, the method is limited to two connection points. More connecting points are possible but it requires a further expansion

of the modeling technique. Another drawback is that the TITOP model uses discretized equations of motion, usually derived with FE analysis, and there is no possibility of including other structural models based on the theory of continuous structures governed by partial differential equations.

The provided models are independent and self-contained, since the substructure's boundary conditions are externalized and the model does not depend on external parameters. This characteristic makes the TITOP models more robust to boundary conditions than other widely accepted modeling techniques such as the Assumed Modes Method, as demonstrated with the flexible rotatory spacecraft example of [Junkins 93]. Nevertheless, the externalization of the boundary conditions is limited by the available two connection points. If a substructure is clamped to more connection points, the current TITOP model will not be able to take it directly into account.

The TITOP models also offer several parameterization degrees for integrated control/structure design. Structural parameters such as the substructure's total mass, center of mass, inertia and flexible modes are accessible in the substructure's state-space representation of the TITOP model. Unlike other integrated design studies where the parameterization was achieved using analytic equations [Messac 92, Onoda 87], the TITOP models offer the possibility of finding several varying parameters in the already assembled model, obtained using FE as input data. However, this is not as powerful as the analytic equations or analytic models, as demonstrated in Sec. 6.1.3, since the variability is only accurate for small ranges of variation.

The TITOP model is an efficient method for the simulation of FMS undergoing small elastic deformations and slow rotational speeds such as satellites and space structures. Furthermore, the modeling technique can also be applied to nonlinear systems, such as in the two-link flexible manipulator of Sec. 6.3 where the expected large nonlinearities did not cause a distinct dynamic behavior from the model of [Luca 91]. However, this characteristic must be claimed with caution since the mechanical characteristics two-link flexible manipulator of [Luca 91] could have shadowed the expected large nonlinearities. For example, using denser, thicker and unequal lengths of the flexible beams might increase the centrifugal stiffness effect and making the TITOP model inaccurate.

The comparisons with the AMM approach and with a nonlinear model have been published in the *ASME Journal of Dynamic Systems, Measurement and Control* [Perez 16b], where a similar description of the TITOP modeling technique is provided as well. The modeling work is complemented in [Perez 16b], where FMS modeling is performed with an approach based on the Craig-Bampton's method.

10.2 Results in Integrated Design

The second part of the study has been devoted to perform integrated control/structure design using structured \mathcal{H}_∞ synthesis. The different possible control architectures have been eval-

uated, showing the advantages and disadvantages of centralized/decentralized control and of active damping control. The framework for performing integrated control/structure design with structured \mathcal{H}_∞ synthesis has been defined and it has been applied to two examples of flexible spacecraft, one academic and the other inspired from real data.

The study has shown that system dynamic specifications and structural constraints can be imposed through \mathcal{H}_∞ constraints. These constraints are in the form of frequency templates that shape the desired response of the rigid body DOF and flexible modes, the frequency response of the controller and the gains of the varying parameters. The constraints are implemented in a more straightforward manner than in other studies such as [Messac 92, Onoda 87, Hiramoto 09] since they arise directly from the system's specifications (desired bandwidth, desired flexible modes damping). However, they are limited by the fact that the \mathcal{H}_∞ framework only allows the norm minimization of the performance channels and other constraints such as parameter equality cannot be implemented. In addition, the addition of too many constraints (more than two per substructure) increases considerably the computing time and compromises the finding of a stabilizing controller.

The integrated control/structure design methodology has been used in two systems: the flexible rotatory spacecraft of [Junkins 93] and the Extra Long Mast Observatory (ELMO). The systems were previously modeled using the TITOP modeling technique to take into account the systems' modularity, giving accurate dynamic systems. The controller and structure optimization performed with structured \mathcal{H}_∞ synthesis showed that the method takes into consideration the system's physical response, increasing or decreasing parameters if the dynamic and structural constraints were compromised. Integrated design with structured \mathcal{H}_∞ synthesis has proven to be more general and practical than the other user-owned algorithms of [Messac 92, Onoda 87, Hiramoto 09]. However, the structural optimization is less impressive than in other studies like [Tsujioka 96, Ou 96] because the possibilities are limited by the model's size.

In addition, thanks to the TITOP modeling technique, an integrated control/structure design method has been applied taking into account the system's modularity, as in [Alazard 13a]. This is the first time that integrated design is applied to a modular structure composed of flexible substructures in chain-like assembly, thanks to the properties of the TITOP modeling technique. For example, the robustness of the TITOP models to changes in boundary conditions has allowed the consideration of payload mass variation without loss of accuracy. The assembly process, as simple as a block diagram scheme, has helped to establish the different dynamic specifications between the channels which link the different substructures among them. Since system's modularity has only been considered in the studies of [Young 90, Sunar 92] for control synthesis, showing that integrated design is possible using this decomposition is a step forward.

The structured \mathcal{H}_∞ optimization has allowed the study of different control strategies for the control of large flexible structures. Decentralized control architectures, with one active damping per substructure, are possible to implement in a centralized synthesis scheme, and they have proven to increase the system's robustness thanks to the active damping of the flexible modes. Feedback control laws for active damping have been studied and implemented

in the available models. The integral force feedback appears to be more robust than the acceleration feedback, even more if it is augmented with a roll-off filter to prevent the limited bandwidth of the PEAs. These conclusions have also been confirmed when applied to the integrated design of ELMO. However, these strategies are usually based on SISO systems. Other MIMO active damping strategies, based on state feedback, have to be explored in order to look for the most suitable strategy.

Other potential uses of the integrated design method combined with the TITOP modeling technique could not be addressed, either limited by the problem's size or limited by the model's nature. Optimal actuator placement could not be accomplished as expected in Sec. 6.1.3 since the model for optimal placement have positive real poles at high frequencies. Other optimizations, such optimizing the mass profile of a flexible appendage [Messac 92] cannot be performed as well due to the large size of the required LFT TITOP with full parameterization.

The results and methods which have allowed the realization of integrated design using \mathcal{H}_∞ synthesis have been published in several international conferences. In [Perez 15b] the general description of the approach was described and parameter variation was performed to the satellite Taranis. In [Perez 16a] and [Perez 16c] the results of the combination of the TITOP modeling and integrated control/structure design were presented for the ELMO spacecraft.

Conclusion

“You only live once, but if you work it right, once is enough.”
- Greg Plitt

THIS study has addressed the integrated attitude control/structure design of a large flexible satellite using structured \mathcal{H}_∞ synthesis, by modeling flexible multibody structures and developing a control strategy for the controller’s synthesis of flexible multibody systems. The study has provided two main contributions for the field of attitude control of large flexible satellites.

The study has allowed the development of models for flexible multibody system modeling oriented to linear control. The models are provided in the form of a state-space representation, are obtainable from FE data and allow star-like or chain-like assembly among them. They are as accurate as other widely used modeling methods and provide the added advantage of being robust to changes in the boundary conditions of the substructures, a crucial feature for integrated control/structure design. In addition, the models have been expanded to substructures actuated through piezoelectric materials or revolute joints, and being applied in a wide variety of examples. The development of these models has allowed the modeling of a flexible spacecraft in preliminary design phase, ELMO, and the utilization of the model to perform integrated control/structure design.

The study has set the framework for integrated control/structure design using \mathcal{H}_∞ synthesis. Dynamic specifications for rigid and flexible modes have been established through \mathcal{H}_∞ constraints. In the same manner, specifications for structural specifications have been also converted to the \mathcal{H}_∞ framework and the synthesis scheme of the structured \mathcal{H}_∞ problem has been modified in order to optimize the required structural parameters. Since structured \mathcal{H}_∞ synthesis allows the definition of the controller’s architecture, several architectures for rigid body control and flexible modes damping have been evaluated in order to use them in the integrated design applications of a flexible rotatory spacecraft and the ELMO flexible satellite. The introduction of the integral force feedback and the addition of roll-off filters

have provided the most reliable controller when facing real actuator dynamics and full-order validation models. In all the applications the integrated design method was proven successful on finding solutions for the proposed controllers and the required payload maximization. The solutions for the controller respect the given specifications and are valid even in large validation models. The solutions for structural parameters respond to the structural needs and the dynamic behavior of the system, maximizing or decreasing parameters to respect the imposed dynamics.

Future work in this field will have to seriously consider the expansion of the modeling method to tree-like assembly of flexible structures, which will result in models which require three or more connection points. The research should focus as well on the extension of the technique to closed-loop mechanisms and on the consideration of distributed loads along the substructure. Further research has to be performed to gauge the limits of the modeling technique when dealing with large nonlinear effects, such as in flexible manipulators or spacecraft with high rotation rates. The integrated design aspect could be improved by analyzing other controller architectures for flexible modes damping, such as centralized ones using state feedback, and other control laws for the large rigid body motion. The approach will also benefit from additional constraints for structural optimization and flexible dynamic motion which can be directly incorporated from the specifications. Further improvements of the parameterization problem are needed in order to perform optimal actuator and sensor placement.

Résumé de Thèse en Français

Chapter 12

Résumé en Français de la Thèse

12.1 Introduction, état de l'art et méthodes

Dans le domaine du contrôle de satellites flexibles de grande dimension, l'un des objectifs principaux est de garantir la stabilité du système face aux perturbations basse fréquence et des vibrations. Néanmoins, la nouvelle génération de satellites devra composer avec des instruments scientifiques de haute précision et réduire les coûts du lancement, ce qui stimule la fabrication de structures de plus en plus larges et de plus en plus légères. Par exemple, la nouvelle génération d'expériences scientifiques spatiales a besoin d'interféromètres à rayons-X et télescopes de grand ligne de vision avec des distances focales très longues, les instruments étant tous deux encastrés à la plateforme du satellite. De plus, les satellites de grande dimension sont souvent modulaires, c'est-à-dire, décomposés en plusieurs sous-structures ou sous-corps pouvant être réutilisés pour d'autres plateformes. D'un côté, sa grande dimension et légèreté impliquent des modes flexibles basse-fréquence qui peuvent interférer avec la bande passante du contrôleur, déstabiliser le système et provoquer éventuellement provoquer la perte du système. Ce problème est appelé Interaction Control-Structure (en anglais : Control-Structure Interaction, CSI). De l'autre côté, la modularité du système implique de pouvoir prédire le comportement dynamique du système une fois assemblé et, en conséquence, empêche de travailler directement sur le dimensionnement des systèmes control/structure.

Dans le secteur spatial, ce problème est résolu en bouclant les informations croisées entre les départements de control et structure, qui établissent des spécifications pour chaque système (ou sous-système) afin d'aboutir à son intégration complète. Les spécifications peuvent être la limitation du premier mode flexible, limitation de la masse maximale ou la largeur maximale d'une sous-structure. Néanmoins, ces contraintes ne permettent pas d'exploiter les capacités optimales de deux systèmes travaillant ensemble.

C'est pour quoi des méthodes de conception nouvelles, qui intègrent simultanément le design de la dynamique de structures flexibles et la conception de lois de contrôle d'attitude, sont nécessaires. L'une des premières approche fut celle de Messac and Malek [Messac 92],

qui développèrent un algorithme pour optimiser simultanément le design de la structure et la loi de commande d'un satellite flexible, en cherchant à contrôler le système face aux perturbations et pour le suivi de consigne, pendant que le profil de l'appendice fut optimisé pour obtenir une minimisation de la masse. Ils utilisèrent un modèle FE du satellite flexible et un contrôleur d'ordre plein pour contrôler la commande en couple. Ils démontrèrent que le co-design mécanique/ contrôle d'attitude était possible et pouvait donner de meilleurs résultats que la seule optimisation du contrôleur. Ensuite les études de Alazard [Alazard 13a] ont montré la possibilité d'utiliser des méthodes de synthèse robuste pour le co-design. Particulièrement, dans [Alazard 13a] la synthèse multi-modèle \mathcal{H}_∞ est utilisée pour co-designer le système de contrôle d'attitude d'un satellite d'observation et les paramètres de son avionique (le retard des actionneurs et capteurs). C'est, à ma connaissance, la première étude à utiliser la commande robuste structurée à une telle fin.

L'objectif principal de cette étude est de réaliser le co-design contrôle d'attitude/mécanique d'un satellite flexible en utilisant la synthèse \mathcal{H}_∞ structurée et en développant une méthode pour la modélisation de systèmes multi-corps flexibles. Cette étude implique une recherche multidisciplinaire à laquelle la modélisation de systèmes mécaniques et la synthèse de lois de contrôle doivent être intégrées. De plus, cette approche doit être capable d'isoler et manipuler les paramètres à optimiser, qu'ils soient mécaniques ou de contrôle. Par conséquent, la thèse commence en adressant la modélisation de systèmes flexibles, la modélisation des actionneurs et capteurs pour le contrôle de structures flexibles et l'implémentation des variations paramétriques dans ces modèles. La thèse continue avec l'évaluation des différentes stratégies de contrôle qui peuvent être utilisées avec les modèles développés lors de cette étude. Pour conclure la mise en oeuvre du co-design avec \mathcal{H}_∞ structuré et son application pour le cas d'un satellite flexible est proposée.

12.2 Cadre pour la Modélisation de Structures Flexibles Multi-Corps

Ce chapitre situe le cadre pour la modélisation de structures flexibles multi-corps (en anglais: Flexible Multibody Systems, FMS) orientée aux applications de contrôle linéaire. Pour cela, nous supposons une sous-structure flexible qui fait partie d'un FMS comme celle de la Fig. 4.1. La sous-structure, appelée \mathcal{A} , est liée à la structure parent, nommée \mathcal{P} , au point de connexion P , et à une sous-structure fils, nommée \mathcal{C} , au point de connexion C . Les efforts extérieurs à \mathcal{A} sont ajoutés aux efforts avec \mathcal{P} au point P et aux efforts avec \mathcal{C} au point C . Les équations du mouvement (en anglais : EOM) de la sous-structure flexible sont obtenues à partir du modèle d'éléments finis (en anglais: FEM) et s'expriment en fonction des coordonnées généralisées avec la équation matricielle Eq. (4.1). Le modèle qui utilise la Eq. (4.1) doit être modifié afin de prendre en compte les interactions avec les structures \mathcal{P} et \mathcal{C} , et être sous une forme de représentation d'états pour que les outils de contrôle linéaire puissent être utilisés. De plus, pour les objectifs du co-design, le modèle doit pouvoir se paramétrer en fonction des variables susceptibles à optimiser telles que les propriétés massiques (masse, densité, inertie,...), propriétés géométriques (longueur, aire des sections. . .) ou les propriétés mécaniques (module

de Young, coefficient de poisson...).

Les prérequis pour la conception d'un tel modèle sont:

- Interconnexion de la sous-structure : l'assemblage entre les différentes sous-structures doit décrire les interactions entre eux. Cette interconnexion s'appelle *overlapping*.
- Indépendance et complétude de la sous-structure : le modèle doit contenir toute l'information nécessaire afin qu'il puisse être utilisé indépendamment des autres sous-structures auxquelles il est connecté. Cela implique que :
- Les conditions de contour doivent être extériorisées, afin de pouvoir utiliser le modèle indépendamment si la sous-structure est encastrée, appuyée ou libre.
- Le modèle de la sous-structure doit être défini par ses propres paramètres dynamiques.
- Paramétrisation de la sous-structure : les variables susceptibles d'être optimisées doivent être localisables dans le modèle.
- Modèle linéaire avec les propriétés requises : les modèles de sous-structures doivent être linéaires afin de pouvoir appliquer les outils de contrôle linéaire (notamment les outils \mathcal{H}_∞ structurée). Par conséquent, les EOM obtenus à partir des modèles de FE doivent être insérés dans un modèle de représentation d'états avec les propriétés mentionnées précédemment.

Dans ce chapitre, un cadre pour la modélisation est proposé afin de satisfaire ces contraintes. Le cadre est basé sur trois piliers : le choix du repère de référence, le choix du mécanisme qui permet d'établir les interactions entre les sous-structures et l'étude des différentes transformations que nous pouvons appliquer aux EOM pour les façonner en modèle d'états. Premièrement, le repère de référence est choisi. Deuxièmement, les interactions entre les sous-structures sont traduites par des échanges accélération-effort entre les sous-structures, ce que nous appellerons l'approche double-port (en anglais : double port approach, DPA). Dernièrement, plusieurs transformations des EOM sont présentées afin de choisir la plus appropriée pour une représentation d'états paramétrée. Ce chapitre a permis la publication de l'approche double-port dans [Alazard 15].

Le repère de référence choisi pour dériver les modèles des sous-structures flexibles, en vue d'une synthèse linéaire, est le repère flottant (en anglais : floating frame). La raison vient du fait que l'étude cherche à reproduire la dynamique du solide rigide en prenant compte les petites perturbations dues à la dynamique flexible du système. Le repère flottant permet de calculer le déplacement total en superposant les petites déformations élastiques à la dynamique rigide. Ce repère est illustré dans la Fig. 4.2, où les repères attachés à chaque sous-structure \mathcal{A} , $\{O_i, x_i, y_i, z_i\}$ sont liés aux repère inertiel fixe $\{O, X, Y, Z\}$ par la matrice de rotation $[R_i]$. Avec cette formulation, en négligeant les termes non linéaires, l'accélération absolue d'un point O_{i+1} peut être exprimée en superposant l'accélération du point O_i et les accélérations dues à la dynamique flexible, comme montré dans l'Eq. (4.4).

De cette façon, le choix du repère flottant permettra de dériver les petits déplacements flexibles à partir des modèles d'éléments finis et les ajouter à la dynamique rigide, sans terme de couplage. De plus, étant donné que chaque sous-structure a son propre repère, elle sera indépendante du reste du FMS et le seul requis pour l'incorporer sera de connaître son orientation, $[R_i]$, par rapport aux autres sous-structures.

Pour établir le mécanisme d'interaction entre les sous-structures, l'approche double-port, DPA, est choisie. Cette approche utilise un double-port pour les entrées/sorties du système. Le mécanisme d'interaction est établi travers un transfert accélération-effort entre les deux points de connexion de la structure. Le premier canal représente le modèle dynamique direct du système (forces comme entrées, accélérations comme sorties) au point de connexion C entre la sous-structure avec la structure fils. Le deuxième canal représente le modèle dynamique inverse (accélérations comme entrées, forces comme sorties) au point de connexion P entre la sous-structure et la structure parent. La forme générique d'un modèle avec DPA est donnée par l'Eq. (4.5).

Dans le DPA, la dynamique rigide est imposée à la sous-structure travers l'entrée en accélération du canal de la dynamique inverse, $\{\ddot{q}_P\}$, qui vient de la structure parent \mathcal{P} . La dynamique rigide plus la dynamique flexible générée par la sous-structure sont transmises à la structure fils avec l'accélération au point C , $\{\ddot{q}_C\}$. Dans la direction opposée, les efforts reçus par la sous-structure au point C dès la structure fils, $\{F_{C/A,C}\}$, sont transmis à la structure parent \mathcal{P} comme l'effort $\{F_{A/\mathcal{P},P}\}$. Le mécanisme est répété travers la chaîne de sous-structures jusqu'à la fin.

La morphologie de l'approche double-port permet d'aborder directement les besoins du modèle pour sous-structures flexibles et l'application du co-design. D'un côté, les conditions limites de la sous-structure sont extériorisées, puisque elles sont imposées par les connexions à travers les canaux de transfert. De l'autre côté, chaque sous-structure continue à être indépendante des autres et le processus d'assemblage est automatisé par l'interconnexion intuitive des transferts accélération-effort entre les sous-structures voisines. Ces propriétés sont illustrées travers l'exemple du système de pointage flexible, où un modèle double-port est créé pour un appendice intermédiaire et les principales caractéristiques sont montrées (mise en forme sous modèle d'états, pulsations encastrées et libres en fonction des conditions limites, inversions des canaux pour obtenir des différents modèles, etc). Par conséquent, l'approche double-port sera utilisée comme mécanisme d'interconnexion entre les différentes sous-structures. La prochaine étape est de transformer les EOM pour qu'elles puissent former un modèle d'états avec les entrées/sorties requises par la DPA.

La manipulation des équations de la dynamique ou EOM est étudiée afin de choisir la meilleure approche pour la DPA. Le but est de transformer l'Eq. (4.1) afin que, une fois mise sous forme de représentation d'états, on reconnaisse un modèle double-port. Pour cela, trois méthodes de transformation basées sur l'analyse modale ont été étudiées: la méthode d'Hurty, la méthode de Craig-Bampton et la méthode d'Imbert.

La méthode d'Hurty utilise trois types de modes pour transformer les EOM: les modes rigides, les modes à contraintes redondantes et les modes à interfaces fixées. Une transforma-

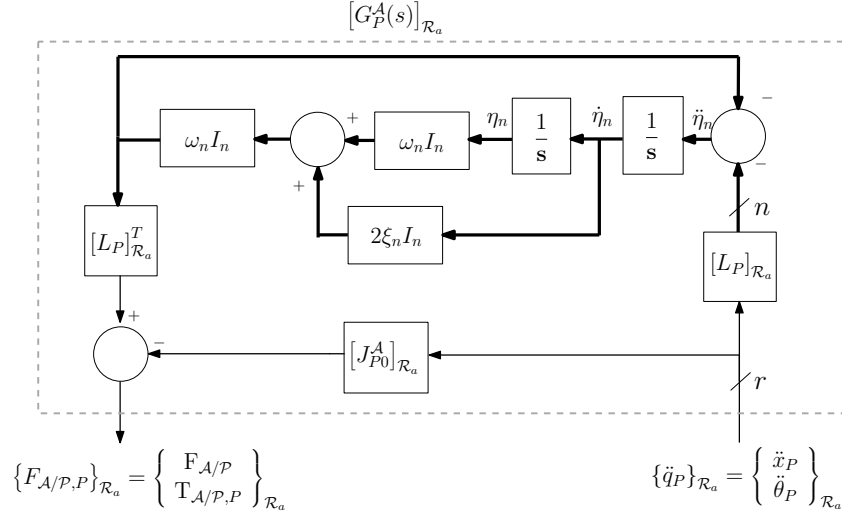


Figure 12.1: Figure 5.2 montrant les connexions pour l'appendice \mathcal{A} , projetées dans le repère \mathcal{R}_a

tion avec tels modes amène à l'Eq. (4.31), dans laquelle on peut distinguer la contribution de la dynamique rigide, la dynamique des contraintes redondantes et la dynamique des modes encastrés. Comme la contribution de la dynamique rigide et la dynamique des modes contraints sont découplées dans la matrice de raideur $[K]$, il est plus facile d'établir une relation entre l'interconnexion des efforts-accélérations, comme requis dans le modèle DP.

Les autres deux méthodes, Craig-Bampton et Imbert, ne permettent pas une claire partition de la dynamique pour imposer facilement une structure double port. La transformation de Craig-Bampton amène à l'Eq. (4.41), mais dans ce cas la dynamique des modes contraints redondants n'est pas découplée et il faut des manipulations additionnelles pour établir la forme DP. Avec la méthode d'Imbert, on retrouve le même désavantage. Par conséquent, ces types des transformations ne seront pas utilisés et dorénavant on ne parlera que de la méthode d'Hurty.

12.3 Modélisation de Systèmes Multi-Corps Flexibles pour le Co-Design

Le Chap. 5 utilise le cadre de modélisation établi dans le Chap. 4 afin de développer des modèles pour l'analyse et contrôle de systèmes multi-corps flexibles, FMS. Pour cela, les EOM transformées avec la méthode de Hurty sont manipulées afin de dériver les modèles à un point de connexion et à deux points de connexion. Ensuite, la méthode est étendue pour les modèles avec un joint pivot au point de connexion P et pour prendre en compte les effets électromécaniques lors de l'insertion des matériaux piézoélectriques dans la structure.

Le modèle à un point de connexion est nommé $[G_P^A(s)]$ vient décrire le modèle linéaire de l'Eq. (5.6):

$$\left\{ \begin{array}{l} \left\{ \begin{array}{l} \dot{\eta}_n \\ \ddot{\eta}_n \end{array} \right\} = \begin{bmatrix} 0_n & I_n \\ -\omega_n^2 I_n & -2\omega_n \xi_n I_n \end{bmatrix} \left\{ \begin{array}{l} \eta_n \\ \dot{\eta}_n \end{array} \right\} + \begin{bmatrix} 0 \\ -L_P \end{bmatrix} \left\{ \ddot{q}_P \right\} \\ \left[F_{\mathcal{A}/\mathcal{P},P} \right] = L_P^T \begin{bmatrix} -\omega_n^2 I_n & -2\omega_n \xi_n I_n \end{bmatrix} \left\{ \begin{array}{l} \eta_n \\ \dot{\eta}_n \end{array} \right\} - \underbrace{\left[J_P^A - L_P^T L_P \right]}_{J_{P_0}^A} \left\{ \ddot{q}_P \right\} \end{array} \right.$$

Dans cette équation, la dynamique du corps rigide est imposée au point de connexion P , ce qui excite les modes flexibles de la structure à travers la matrice de participation modale $[L_P]$. Ces modes flexibles induisent un effort à la structure parent \mathcal{P} qui modifie l'effort que la structure \mathcal{A} aurait induite à \mathcal{P} si elle était rigide ($[J_{P_0}^A]$ fois l'accélération au point P). Ce fait peut être présenté schématiquement comme le déplacement rigide de l'appendice \mathcal{A} perturbé par un feedback de ses propres modes de vibration comme vu dans la Fig. 5.2.

Le modèle à deux points de connexion est nommé $[G_{P,C}^A(s)]$ et est décrit par le modèle linéaire en forme double port de l'Eqs. (5.10 – 5.15) :

$$\left\{ \begin{array}{l} \left\{ \begin{array}{l} \dot{\eta}_n \\ \dot{\eta}_e \\ \ddot{\eta}_n \\ \ddot{\eta}_e \end{array} \right\} = A \left\{ \begin{array}{l} \eta_n \\ \eta_e \\ \dot{\eta}_n \\ \dot{\eta}_e \end{array} \right\} + B \left\{ \begin{array}{l} F_{C/\mathcal{A},C} \\ \ddot{q}_P \end{array} \right\} \\ \left\{ \begin{array}{l} \ddot{q}_C \\ F_{\mathcal{A}/\mathcal{P},P} \end{array} \right\} = C \left\{ \begin{array}{l} \eta_n \\ \eta_e \\ \dot{\eta}_n \\ \dot{\eta}_e \end{array} \right\} + (D + D_\delta) \left\{ \begin{array}{l} F_{C/\mathcal{A},C} \\ \ddot{q}_P \end{array} \right\} \end{array} \right.$$

où A , B , C , D and D_δ sont la notation courte des matrices de représentation d'états suivantes:

$$A = \begin{bmatrix} 0_{n+e} & I_{n+e} \\ -\hat{M}_Q^{-1} \hat{K}_Q & -\hat{M}_Q^{-1} \hat{D}_Q \end{bmatrix}$$

$$B = \begin{bmatrix} 0_{n+e,e+r} \\ \hat{M}_Q^{-1} \begin{bmatrix} 0_{ne} & -\hat{M}_{nr} \\ I_{ee} & -\hat{M}_{er} \end{bmatrix} \end{bmatrix}$$

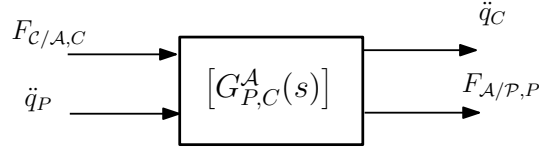


Figure 12.2: Figure 5.4 qui montre le diagram du modèle Two-Input Two-Output Port (TITOP)

$$C = \begin{bmatrix} \begin{bmatrix} 0_{en} & I_{ee} \end{bmatrix} \begin{bmatrix} -\hat{M}_Q^{-1} \hat{K}_Q & -\hat{M}_Q^{-1} \hat{D}_Q \end{bmatrix} \\ \begin{bmatrix} \hat{M}_{rn} & \hat{M}_{re} \end{bmatrix} \begin{bmatrix} \hat{M}_Q^{-1} \hat{K}_Q & \hat{M}_Q^{-1} \hat{D}_Q \end{bmatrix} \end{bmatrix}$$

$$D = \begin{bmatrix} \begin{bmatrix} 0_{en} & I_{ee} \end{bmatrix} \hat{M}_Q^{-1} \begin{bmatrix} 0_{ne} & -\hat{M}_{nr} \\ I_{ee} & -\hat{M}_{er} \end{bmatrix} \\ - \begin{bmatrix} \hat{M}_{rn} & \hat{M}_{re} \end{bmatrix} \hat{M}_Q^{-1} \begin{bmatrix} 0_{ne} & -\hat{M}_{nr} \\ I_{ee} & -\hat{M}_{er} \end{bmatrix} \end{bmatrix}$$

avec

$$\begin{aligned} \hat{M}_Q &= \begin{bmatrix} \hat{M}_{nn} & \hat{M}_{ne} \\ \hat{M}_{en} & \hat{M}_{ee} \end{bmatrix}; \quad \hat{K}_Q = \begin{bmatrix} \hat{K}_{nn} & 0 \\ 0 & \hat{K}_{ee} \end{bmatrix}; \\ \hat{D}_Q &= \begin{bmatrix} \hat{D}_{nn} & \hat{D}_{ne} \\ \hat{D}_{en} & \hat{D}_{ee} \end{bmatrix}; \quad D_\delta = \begin{bmatrix} 0_{er} & \phi_{er} \\ \phi_{er}^T & -\hat{M}_{rr} \end{bmatrix}; \end{aligned}$$

Ces équations décrivent le modèle de la sous-structure \mathcal{A} en assemblage enchaîné, et elles forment ce qu'on appelle le modèle TITOP (en anglais : Two-Input Two-Output Port model). Ce modèle permet d'interconnecter les différentes sous-structures en prenant compte la dynamique flexible. Le diagramme du modèle TITOP est montré dans la Fig. 5.4. Dans ce modèle, les déplacements du corps rigide sont imposés au point P de la sous-structure \mathcal{A} et ils excitent les modes de la structure au travers des matrices de participation modale $[\hat{M}_{rn}]$ et $[\hat{M}_{re}]$ jusqu'à point de connexion C , où l'accélération totale (celle due au mouvement rigide et celle due à la dynamique flexible) est transmise à l'appendice suivant avec $\{\ddot{q}_C\}$. L'effort transmis à la structure parent \mathcal{P} , $\{F_{A/P,P}\}$, dépend de l'effort reçu au point C , $\{F_{C/A,C}\}$, l'accélération reçue au point P , $\{\ddot{q}_P\}$, et les modes flexibles.

Étant donné que le modèle TITOP a une forme DP, nous pouvons considérer plusieurs conditions limites de la sous-structure \mathcal{A} en inversant les canaux supérieurs et inférieurs du modèle. En imposant les entrées à zéro, $[G_{P,C}^A(s)]$ représente le modèle encastré au point P et libre au point C de la sous-structure. De la même manière, $[G_{P,C}^A(s)]^{-1}$ représente le modèle encastré au point C et libre au point P de la sous-structure. Les deux canaux sont inversibles comme montré dans les Eqs. (5.16) et (5.17), ce qui permet de prendre en

compte différentes conditions limites au point P et au point C . L'équation (5.16) représente le modèle encastré-encastré de la sous-structure, tandis que l'équation (5.17) représente le modèle libre-libre.

Le modèle TITOP d'une structure flexible est le modèle le plus général pour modéliser un système flexible multi-corps. En enlevant le deuxième canal, celui du transfert au point C , nous retrouvons le modèle de connexion à un point. Le modèle peut être enrichi pour inclure un joint pivot ou des matériaux piézoélectriques, ce qui étend son domaine d'application.

Pour modéliser un joint pivot au point de connexion P , il suffit de considérer que le degré de liberté associé à la rotation α est imposé, ce qui équivaut à appliquer un couple $t_{rj,P}$. Pour prendre cela en compte, le modèle TITOP est augmenté avec une entrée et une sortie additionnelle, et manipulé comme montré dans l'Eq. (5.18) pour prendre en compte l'imposition de la nouvelle contrainte. Cela donne le modèle dynamique inverse du joint pivot. Si le modèle dynamique direct est souhaité, il suffit d'inverser le canal $\alpha \rightarrow t_{rj,P}$. Cette modélisation permet de prendre en compte aussi n'importe quel mécanisme de contrôle pour agir sur le joint, $K(s)$, comme montré dans la Fig. 5.6.

La prise en compte des effets piézoélectriques a aussi été développée. En manipulant, avec la méthode de Hurty, les équations de la dynamique d'une sous-structure flexible actionnée par des matériaux piézoélectriques, Eqs. (5.25) et (5.26), elles sont transformées en représentation d'états DP pour retrouver un modèle TITOP augmenté, Eqs. (5.37)-(5.42), lequel contient une entrée additionnelle, le voltage appliqué, et une sortie additionnelle, la charge électrique. Ce modèle permettra de prendre en compte les efforts internes induits à une sous-structure lorsqu'on applique un voltage pour contrôler les vibrations.

De plus, le modèle TITOP offre des possibilités de paramétrisation afin d'effectuer un co-design. En effet, la structure de la représentation d'états permet de repérer certaines matrices qui contiennent des variables susceptibles d'être optimisées par le processus de design intégré. Dans la structure du modèle d'états on peut distinguer la matrice du corps rigide, $[M_{rr}]$, où on repère l'inertie, la masse totale et la position du centre de gravité. On peut paramétrer aussi la distance entre les points de connexion en manipulant la matrice $[\tau_{PC}] = [\phi_{er}]$. De plus, les modes flexibles et ses amortissements peuvent être paramétrés en intervenant dans les matrices $[K_{nn}]$ et $[D_{nn}]$.

Finalement, la modélisation de structures flexibles multi-corps est faite avec les modèles TITOP. Les représentations d'états en double-port, qui utilisent des modèles d'éléments finis transformés avec la méthode de Hurty, servent comme briques élémentaires pour construire modèles de systèmes flexibles multi-corps qui suivent des petites déformations. D'une part, le modèle TITOP à un point de connexion peut être utilisé pour modéliser des systèmes flexibles en forme d'étoile ou pour modéliser le système qui termine la chaîne de plusieurs corps flexibles enchaînés. De l'autre part, le modèle TITOP à deux points de connexion peut être utilisé pour connecter tout type de chaîne cinématique ouverte de corps flexibles enchaînés. Le modèle avec joint pivot peut être utilisé pour modéliser des sous-structures tournantes du FMS, comme des panneaux solaires ou antennes. Le modèle avec effet piézoélectrique peut être utilisé pour considérer des structures avec des actionneurs piézoélectriques. Les canaux

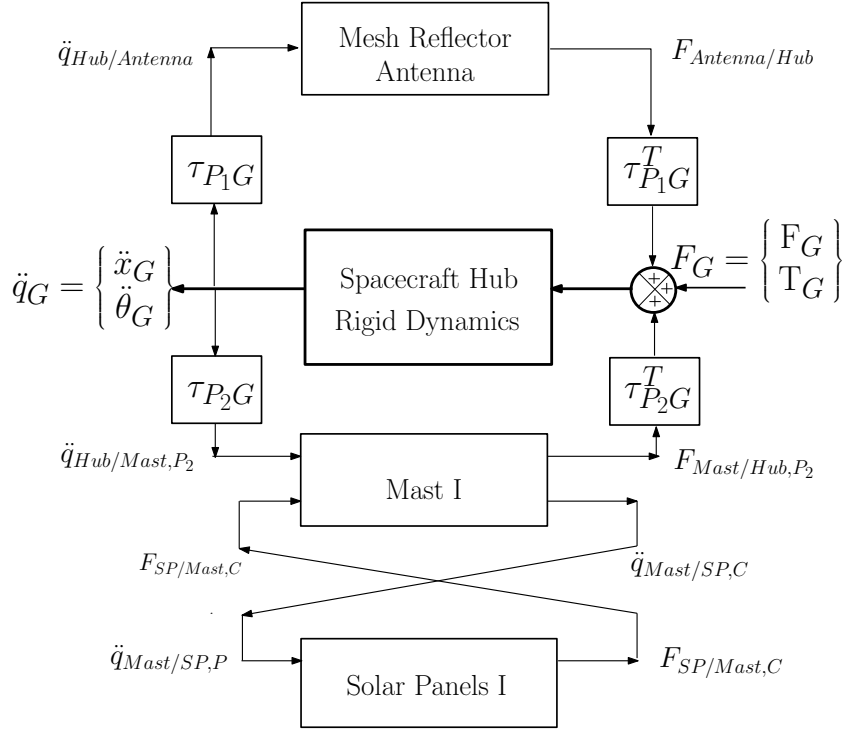


Figure 12.3: Figure 5.11 qui montre l'assemblage entre différents modèles TITOP

qui relient les sous-structures peuvent être modifiés pour ajouter des perturbations ainsi que pour les mesures d'accélération ou des perturbations de forces aux points de connexion.

De cette façon, un satellite flexible de grande dimension, comme celui de la Fig. 5.10, peut être modélisé en enchaînant des blocs élémentaires, comme montré dans la Fig. 5.11. Par conséquent, le modèle TITOP offre trois avantages principaux pour le co-design mécanique/-contrôle :

- **Modélisation.** Les modèles TITOP des sous-structures sont linéaires, indépendants et obtenus à partir des données FE. Il n'y a pas besoin d'informations additionnelles pour le processus de modélisation. Si une sous-structure ne fait plus parti du système, elle peut être enlevée du diagramme et le FMS sera modifié en conséquence sans analyse additionnelle des sous-structures qui restent. De plus, la méthode peut être facilement mise en œuvre dans un environnement de programmation graphique comme Matlab/Simulink.
- **Contrôle.** Le schéma TITOP permet de considérer des architectures de contrôleurs centralisées ou décentralisées. De plus, elle permet la simulation des mesures d'efforts et accélération, l'introduction des perturbations dans les différents points de connexion et la prise en compte des mécanismes de contrôle comme les joints pivot ou les actionneurs piézoélectriques.
- **Co-Design.** Les modèles TITOP peuvent s'utiliser indépendamment des conditions limites du FMS. De plus, les modèles peuvent être paramétrés avec les variables d'intérêt

pour l'optimisation.

12.4 Application et Validation de la Technique TITOP aux FMS

Le Chap. 6 est dédié à l'application et la validation de la technique de modélisation TITOP dans différents exemples de systèmes flexibles multi-corps afin de juger le potentiel de la technique TITOP. Trois types de systèmes sont modélisés: structures en forme de poutre, systèmes composés de parties rigides et flexibles et systèmes avec un joint pivot.

Premièrement, la technique TITOP est appliquée dans des sous-structures de type poutre. Le premier test consiste à enchaîner plusieurs tronçons d'une poutre en 3D et retrouver le même modèle dynamique que la poutre complète. Les Figs. 6.4 et 6.6 montrent l'effort transmis au point P due aux accélérations induites au point P du système de tronçons enchaînés, qui coïncide avec la réponse du modèle de poutre complète.

Ensuite, une couche de matériaux piézoélectrique est ajoutée et le modèle TITOP actionné est dérivé, en analysant les fonctions de transfert entre le voltage appliqué et les efforts internes dans les Figs. 6.8, 6.9 et 6.10. Finalement, afin de montrer les possibilités de paramétrage avec le modèle TITOP, la longueur d'une poutre est paramétrée avec un modèle analytique d'éléments finis et en repérant la longueur manuellement dans la représentation d'états. Les Figs. 6.11, 6.12, 6.13 et 6.14 montrent que les variations sont bien prises en compte pour des petits rangs, tandis que pour des grandes plages de variation la méthode manuelle est moins précise.

Un des objectifs principaux a été également de comparer la technique TITOP avec des autres méthodes utilisées dans le domaine de modélisation de corps flexibles. Pour cela, le modèle d'un satellite tournant de [Junkins 93], obtenu en utilisant la technique des modes assumés (en anglais : assumed modes method, AMM), est comparé avec le modèle du même système obtenu avec la méthode TITOP. La modélisation TITOP est autant précise que l'AMM pour trouver les fréquences propres du système assemblé (voir Table 6.4), et elle présente une meilleure robustesse face aux variations des conditions limites, comme montré dans les Figs. 6.18 et 6.19.

Finalement, la méthode est appliquée à un problème de modélisation classique qui peut présenter des fortes nonlinearités: un bras manipulateur flexible. Pour cela, le modèle non-linéaire de [Luca 91] d'un bras manipulateur flexible à deux segments est utilisé comme modèle de référence. Le bras manipulateur est modélisé avec la méthode TITOP en ajoutant des liaisons pivot et les mêmes modes propres sont retrouvés, comme montré dans la Table 6.6. Une simulation numérique avec des contrôleurs PD montre que les réponses des deux modèles sont identiques. Le modèle TITOP montre ainsi sa capacité pour modéliser aussi des systèmes nonlineaires (Fig. 6.26).

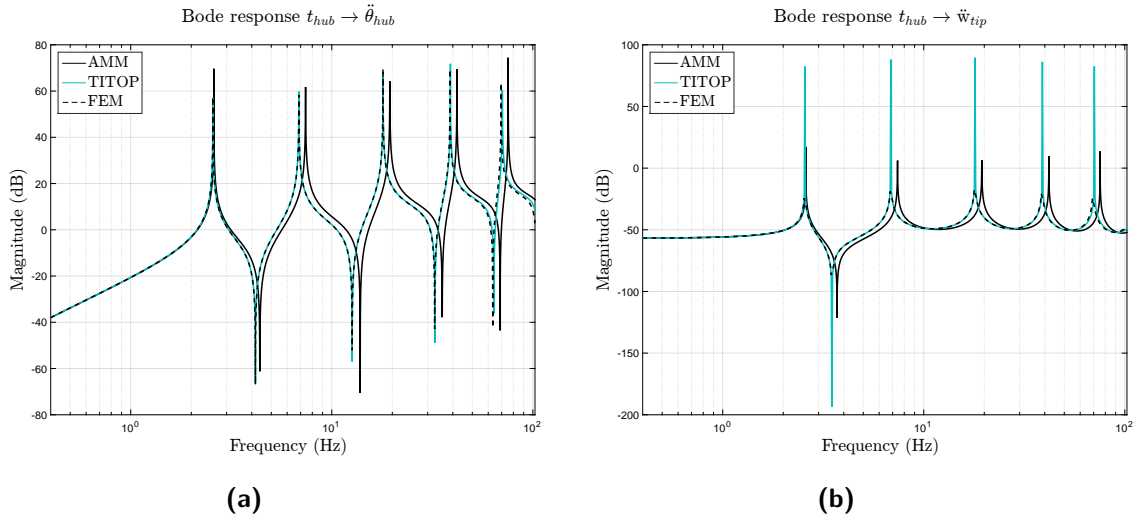


Figure 12.4: Figure 6.19 qui montre la robustesse du modèle TITOP face aux variations des conditions limites ($M_t = 114.5$ kg)

12.5 Evaluation des Stratégies de Contrôle pour les FMS

Le Chap. 7 étudie les possibles architectures de contrôleur pour des satellites flexibles de grande dimension, afin d'évaluer la plus pertinente pour trouver un correcteur stabilisant du système. L'architecture du contrôleur doit adresser le contrôle de la dynamique rigide et la dynamique flexible afin d'assurer la performance et la robustesse du système de contrôle d'attitude. Par conséquent, ce chapitre montre les principales stratégies pour contrôler la dynamique rigide et amortir la dynamique flexible.

Le contrôle de la dynamique rigide est focalisée sur le contrôle de la position des angles de roulis, dérapage et tangage qui déterminent l'attitude du satellite, ce qui est fait en utilisant un contrôleur proportionnel-dérivé (PD) ou proportionnel-intégral-dérivé (PID), combinés avec des filtres pour ajuster son action sur un domaine de fréquences particulier. Les spécifications de pointage sont données par quatre valeurs : deux concernant la dynamique en boucle fermée et deux concernant la robustesse du système face aux perturbations. La dynamique fermée est déterminée par l'amortissement désiré, ξ_{des} , et la bande passante requise, ω_{des} . La marge de gain et de phase (en anglais : GM et PM) de la boucle ouverte sont spécifiées pour assurer un niveau adéquat de robustesse de la réponse en boucle fermée.

L'amortissement des modes flexibles peut améliorer la performance robuste du système de contrôle d'attitude. Pour prouver cela, une loi proportionnelle-dérivée est synthétisée en utilisant des stratégies différentes dans le cas d'un système simplifié de pointage flexible. Premièrement, le système est synthétisé en utilisant une méthode de réglage de gains classique qui fixe la dynamique en boucle fermée souhaitée en considérant le satellite rigide. Ce réglage est effectif lorsque la bande passante est beaucoup plus basse que le premier mode flexible, mais pour des bandes passantes proches au premier mode flexible ce réglage n'est pas robuste. Cela est dû au fait que les gains nécessaires pour ce réglage augmentent avec le carré de la

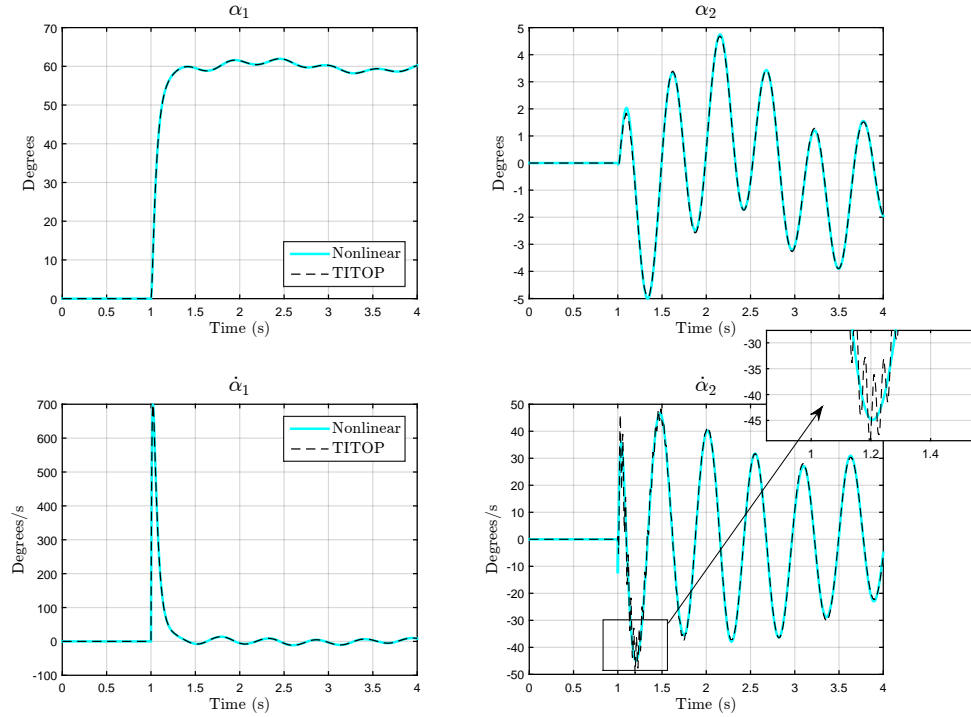


Figure 12.5: Figure 6.26 qui compare l'évolution temporelle du modèle non-linéaire et le modèle TITOP du bras manipulateur flexible

bande passante souhaitée. La synthèse avec des méthodes robustes comme \mathcal{H}_∞ permet de trouver des réglages qui sont plus robustes face aux perturbations de mesures d'accélération. Cependant, l'introduction d'un système d'amortissement actif dans le système de contrôle permet, au premier coup, d'augmenter la robustesse du système. Un retour d'accélération pour amortir le premier mode flexible, réglé soit à la main soit par des synthèses robustes, permet de trouver des réglages plus robustes que ce soit pour des courtes ou larges bandes passantes. Les lieux de Black-Nichols de ces réglages sont montrés dans les Figs. 7.3, 7.5 et 7.6.

Deuxièmement, la comparaison entre architectures centralisées et décentralisées est faite. Dans une architecture centralisée, qui est l'approche conventionnelle, le contrôle est synthétisé en se basant sur un contrôleur du modèle complet du système, réduit. Le contrôleur final est vérifié en utilisant un modèle d'évaluation. Par contre, l'approche décentralisée regarde le système comme un ensemble de sous-systèmes, où la synthèse du contrôleur est réalisée au niveau du sous-système et tous les contrôleurs individuels sont appliqués au système complet. Les FMS sont particulièrement adaptés pour des architectures décentralisées car ils sont déjà discrétisés en plusieurs sous-structures ou sous-systèmes. Cependant, la stabilité du système n'est pas assurée une fois tous les contrôleurs et toutes les sous-structures connectés, ce qui implique une large différence entre les possibilités théoriques et pratiques. Dans cette étude les prérequis théoriques pour une architecture décentralisée stabilisante ne sont pas

étudiés car ils sont hors du sujet. Par contre, l'approche développée ici consiste à utiliser des architectures de contrôle décentralisées et à garantir la stabilité du FMS au travers de l'optimisation de tout le système avec la technique \mathcal{H}_∞ structurée. Par conséquent, notre approche est centralisée concernant le processus d'optimisation, mais décentralisée concernant l'architecture du contrôleur. L'avantage de synthétiser un contrôleur avec cette approche est montré dans la Fig. 7.7, où un contrôleur réglé avec l'optimisation simultanée du PD et le système d'amortissement est comparé avec d'autres méthodes (sans amortissement actif ou avec un amortissement actif réglé séparément), en trouvant un réglage plus robuste.

Dernièrement, plusieurs architectures pour l'amortissement des modes flexibles sont montrées et testées dans le modèle du système de pointage flexible et dans un modèle TITOP. Les stratégies montrées sont implémentées de manière décentralisée, avec un actionneur interagissant avec son propre capteur colocalisé. Des techniques avec retour d'accélération et retour de intégral de force sont revisitées et appliquées aux différents systèmes, en trouvant toujours de retours asymptotiquement stables grâce à la colocation actionneur-capteur. Cependant, une étude plus approfondie du changement de l'alternance pôle-zéro montre que pour systèmes plus flexibles le retour d'accélération n'est plus robuste. En effet, les Figs. 7.12 et 7.13 montrent que les stratégies basées dans le retour d'accélération ne sont plus robustes lorsque les systèmes sont moins raides. Cela vient du fait que en vérité l'approche en retour d'accélération n'est pas vraiment colocalisée en tant que les efforts appliqués (intérieurs) utilisent une mesure inertielle (l'accélération absolue). En revanche, le retour de force intégral est colocalisé, car l'effort intérieur appliqué est colocalisé avec la mesure, qui est la force interne subie par la sous-structure. Finalement, l'effet de la dynamique réelle des actionneurs et capteurs est illustré, en montrant que sa dynamique peut être toujours approximée par un filtre passe-bande qui vient déstabiliser les modes flexibles lorsqu'ils tombent dehors le domaine d'influence (Fig. 7.15).

12.6 Mise en œuvre du Co-Design sous Forme \mathcal{H}_∞ structuré

Le Chap. 8 a pour objectif de montrer l'utilisation de la synthèse \mathcal{H}_∞ structurée comme un outil pour réaliser des études de co-design, en mettant l'accent sur l'application contrôle d'attitude/ mécanique. De cette manière, l'outil pour effectuer \mathcal{H}_∞ structurée est transformé afin de réaliser le co-design. Les spécifications pour le contrôle de la dynamique du système et pour les variables mécaniques sont transformées en contraintes \mathcal{H}_∞ afin de pouvoir appliquer les outils de \mathcal{H}_∞ structurée. Premièrement, le chapitre donne une vue de l'ensemble pour la mise en œuvre du problème du co-design sur un problème \mathcal{H}_∞ structurée multi-modèles. Dans la Sec. 8.2, nous montrons comment transformer les spécifications pour le système dans contraintes \mathcal{H}_∞ . Finalement, un exemple de co-design du satellite flexible tournant du Chap. 6 est montré pour appliquer les concepts développés au long du chapitre.

La méthode pour le co-design de cette étude utilise des outils de commande robuste structurée. Cette méthode comprend cinq étapes:

1. L'obtention d'un modèle LFT du système. La FMS doit être modélisée en utilisant la méthode TITOP ou autre technique de modélisation préférée. Le modèle doit comprendre les paramètres variables qu'il faut optimiser, ce qui résulte dans un modèle LFT avec le bloc Δ incluant les variations paramétriques. Les canaux du schéma du modèle FMS doivent être modifiés afin d'inclure les perturbations en entrée w et les sorties de performance z qui seront utilisées plus tard pour la mise en œuvre des spécifications.
2. Conversion du bloc Δ des paramètres ajustables. Une fois que le modèle LFT de la FMS a été obtenu, il doit être décomposé en un modèle nominal LTI (en anglais, Linear Time Invariant) et un bloc Δ . En fonction du software utilisé, le bloc Δ est souvent présenté comme un objet LFR, comme c'est le cas dans la Matlab Robust Control Toolbox. Comme le bloc Δ doit être présenté comme un ensemble de paramètres ajustables au lieu d'un bloc d'incertitudes, le bloc est converti dans une matrice diagonal Δ_i composée de paramètres ajustables δ_i , qui respectent le nombre d'occurrences pour chaque paramètre.
3. Sélection de l'architecture du contrôleur et création du contrôleur augmenté. En fonction de l'architecture du contrôleur, $C(s)$, le système nominal $G(s)$ devra fournir dans le schéma de synthèse de la Fig. 8.1 les entrées de contrôle nécessaires, y , et les sorties de contrôle nécessaires, u , qui seront utilisées par le contrôleur afin de stabiliser le système avec le feedback $\mathcal{F}_l(G(s), C(s))$. Un contrôleur augmenté, $K(s) = \text{diag}(C(s), \Delta_i)$, est créé en incorporant l'ensemble de paramètres ajustables, Δ_i , qui seront utilisés pour le feedback entre les sorties y^Δ et les entrées u^Δ , et $C(s)$ étant un contrôleur structuré qui liera les sorties et entrées pour le contrôle, y et u respectivement.
4. Sélection des fonction de pondération. Un ensemble de filtres de pondération $[W_z, W_C, W_k]$ doit être obtenu afin d'imposer le comportement dynamique souhaité, donner la forme de la réponse fréquentielle du contrôleur et optimiser les paramètres structuraux.
5. Construction du schéma de synthèse multi-canaux. Avec les éléments obtenus dans les étapes précédentes, le schéma de synthèse est construit en établissant le feedback entre le contrôleur augmenté $K(s)$ avec les entrées/sorties correspondantes avec le système nominal $G(s)$.

La Fig. 8.1 montre le schéma standard \mathcal{H}_∞ multi-canaux pour le co-design du système $G(s)$, où il y a trois types de canaux différents. Le premier canal multidimensionnel lie les perturbations du système, w , aux sorties de performance, z . Le deuxième canal multidimensionnel connecte les entrées du système de contrôle, y_c , aux sorties u_c . Le troisième canal multidimensionnel lie les entrées pour les contraintes des variations paramétriques du bloc $f_k(\delta_i)$, w_k , à ses sorties, z_k . De cette façon, la synthèse \mathcal{H}_∞ structurée appliquée à ce schéma calcule un réglage sub-optimal des paramètres contenus dans $C(s)$ et δ_i intégrés dans $K(s)$ pour imposer la stabilité interne en boucle fermée $\mathcal{F}_l(G(s), K(s))$ tel que:

$$\min_{K(s)} \{ \max \{ \|W_k(s) f_k(\delta_i)\|_\infty, \|W_C(s) C(s)\|_\infty \} \}$$

sous la contrainte

$$\|W_z(s) T_{w \rightarrow z}(s)\|_\infty < \gamma_{perf}$$

C'est-à-dire, elle minimise la norme \mathcal{H}_∞ du transfert entre l'entrée en perturbation w et la performance de la sortie z , $T_{w \rightarrow z}(s)$, tel que $\gamma_{perf} > 0$ pour respecter les spécifications. Essentiellement, le co-design avec \mathcal{H}_∞ structurée ajuste les paramètres contenus dans $K(s)$ pour imposer la stabilité interne de la dynamique en boucle fermée et respecter les contraintes \mathcal{H}_∞ travers les filtres W_z , W_C et W_k . La difficulté principale demeure comment établir des contraintes \mathcal{H}_∞ correctes à partir des spécifications, ce qui est illustré par la suite. Pour cela, les spécifications sont divisées en quatre grands groupes: spécifications sur la dynamique rigide, spécifications sur la dynamique flexible, spécifications sur le contrôleur et spécifications sur la structure à optimiser.

Le contrôle de la dynamique rigide est l'aspect le plus important pour le système de contrôle d'attitude, car elle est la principale responsable de la position de l'angle de pointage face à n'importe quelle type de perturbation. Ces perturbations sont souvent des couples perturbateurs tel que le gradient de gravité, la couple du à la pression solaire ou un couple du à la distorsion thermique. Les spécifications sont souvent données sous la forme d'une bande passante dans laquelle la perturbation doit être rejetée, ω_{des} , ainsi que sous la forme d'un coefficient d'amortissement, ξ_{des} , pour assurer une décroissance de l'erreur et une valeur maximale de celui-ci quand la perturbation a lieu. La dynamique en boucle fermée désirée pour la dynamique rigide du système avec le couple $(\omega_{des}, \xi_{des})$ pour chaque angle d'attitude (roulis, φ , tangage, θ , et dérapage ψ) est imposée à partir de la fonction de sensibilité en accélération (en anglais : acceleration sensitivity function, ASF) comme sortie de performance de chaque DOF de la dynamique rigide. En utilisant le principe du schéma SOTAS (Second Order Template on Acceleration Sensitivity), un filtre de pondération $W_{\tilde{q}}$ sur les ASF des différents DOF afin de pénaliser la plage de basse fréquences de perturbations en accélération. Le filtre est décrit par l'Eq. (8.2), et il s'agit d'un filtre passe-bas qui ne dépend que des spécifications ω_{des} et ξ_{des} . Les modifications pertinentes pour arriver au schéma SOTAS depuis une modélisation TITOP d'un FMS sont montrées dans la Fig. 8.5.

Les contraintes pour l'amortissement des modes flexibles du FMS sont dérivées en utilisant également le schéma SOTAS. Les spécifications concernant le contrôle des modes flexibles sont mises en œuvre comme une extension du champ d'accélération de la dynamique rigide du système. Par conséquent, les contraintes en d'autres points du FMS sont vues comme le comportement désiré du point si la structure était rigide. Donc, pour un point P du FMS localisé avec le vecteur de position $\{GP\}$ dans le repère satellite, l'accélération désirée serait celle qui correspondrait au cas de la dynamique rigide associé au satellite. Le filtre de pondération pour un point P quelconque d'un FMS est écrit comme dans l'Eq. (8.5). Une autre contrainte additionnelle peut être imposée pour empêcher le déplacement maximal, celle de l'Eq. (8.6). Graphiquement, les contraintes sur la dynamique flexible sont montrés dans la Fig. 8.6.

Les spécifications structurelles peuvent être établies en ajoutant des canaux qui apportent contraintes additionnelles pour les variations incluses dans le bloc Δ . Une contrainte structurelle k qui comprend un ensemble de paramètres structuraux δ_i est imposée au travers d'un filtre de pondération W_k et une fonction de coût $f_k(\delta_i)$. La minimisation d'un paramètre peut s'exprimer comme dans l'Eq.(8.7) ou comme dans l'Eq. (8.8), en fonction de la pente

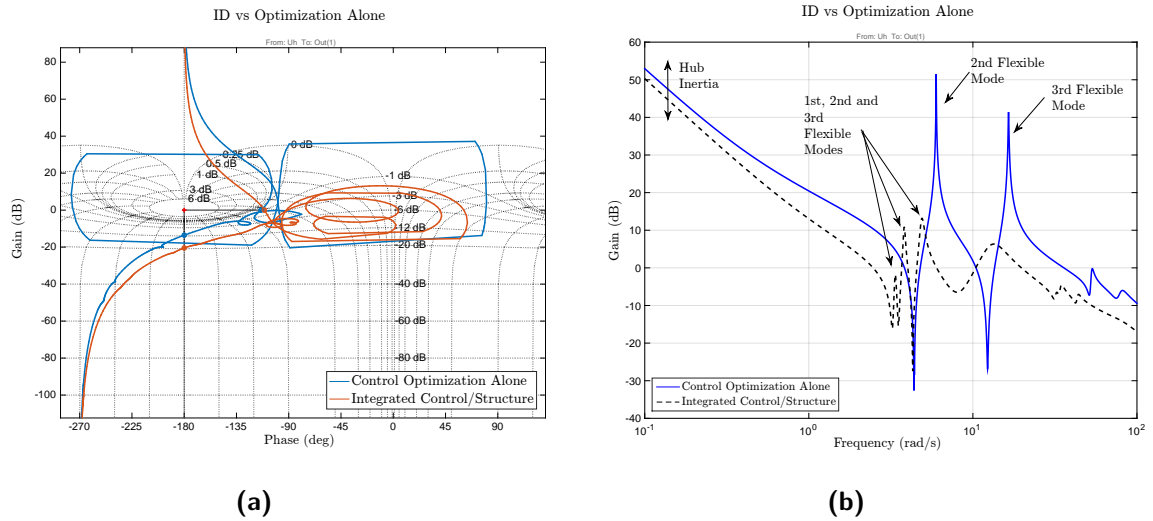


Figure 12.6: Figure 8.11 qui compare la réponse fréquentielle obtenu d'une structure avec optimisation contrôle/structure et une structure avec optimisation du système de contrôle seulement

souhaitée (plus de pente, plus facile pour l'algorithme de chercher l'optimisation).

En plus de contraintes dans la dynamique rigide, la dynamique flexible et les paramètres structuraux, de contraintes sur la réponse fréquentielle du contrôleur peuvent aussi être imposées en ajoutant un canal de roll-off. Cela peut être nécessaire pour éviter l'interaction du système de contrôle avec des fréquences des modes flexibles qui ne sont pas amorties (l'effet spill-over). De cette façon, le contrôleur est maintenant le contrôleur structuré multiplié par la composante de roll-off (par exemple, une fonction de transfert d'ordre deux comme celle de l'Eq. (8.11)), auquel on vient imposer des filtres de roll-off comme montré dans les Eqs. (8.9) et (8.10).

Finalement l'exemple du co-design d'un satellite tournant flexible est abordé. Il s'agit du même exemple que celui du Chap. 6 mais cette fois en ajoutant un actionneur piézoélectrique pour pouvoir contrôler les modes flexibles. Le co-design a pour objectif de synthétiser un contrôleur pour contrôler la dynamique rigide en rotation, amortir les oscillations du premier appendice, prolonger l'appendice 1, maximiser la masse de la charge utile située au bord de l'appendice 1 et minimiser la masse totale du système. L'étude de co-design montre que le processus d'optimisation a bien répondu aux contraintes imposées et qu'elle a été menée à bien en tenant compte des contraintes dynamiques du système.

12.7 Co-Design Contrôle/Structure d'un Satellite Flexible

Les chapitres précédents ont proposé, développé et appliqué les modèles, stratégies et spécifications nécessaires pour réaliser le co-design du système de contrôle d'attitude et une structure flexible avec \mathcal{H}_∞ structuré. Ce chapitre est consacré à l'application des connaissances développés pour le cas d'un satellite très flexible, le ELMO (en anglais : Extra Long

Mast Observatory). L'objectif est de réaliser une étude préliminaire des différents compromis entre le système de contrôle et la structure du satellite, en obtenant son modèle avec la modélisation TITOP et en utilisant la synthèse \mathcal{H}_∞ structurée.

Le satellite ELMO (Fig. 9.1) est une mission fictive pour le développement d'un satellite qui utilisera des technologies d'interférométrie. Pour améliorer les performances de l'instrument, la longueur focale du télescope de rayons X est augmentée avec l'introduction d'un long mât qui sera déployé en orbite. Les caractéristiques du mât sont basées sur un prototype développé par le CNES. L'objectif de l'étude est d'étudier et tester la faisabilité de cette technologie, qui nécessitera des améliorations au niveau conception de structure et système de contrôle d'attitude.

Le satellite est composé d'une plateforme rigide, avec centre de masse G , auquel on vient encastrier au point P un mât déployable dont l'extrémité est nommée comme point Q (Fig. 9.2). Le mât est discrétisé en plusieurs segments, chacun avec les mêmes propriétés que le mât prototype et avec une longueur 4.06 m chacun. Due à la longueur totale du mât (12 mètres approximativement), il est prévu pour ELMO d'avoir un tenseur d'inertie très directionnel, avec une magnitude très élevée du moment d'inertie perpendiculaire au plan du mât. Le défi principal est de apporter une bande passante suffisamment large pour mitiger les perturbations basse fréquence pendant que les déplacements au bout du mât sont minimisés ainsi que la masse de la charge utile située au bout est maximisée. Le co-design AOCS/structure devra donc apporter des stratégies de contrôle pour la bande passante requise et maximiser la masse de la charge utile située au bout du mât.

Pour cela, un modèle TITOP du satellite est obtenu, étant donné qu'il est composé de plusieurs sous-structures rigides (la plateforme et la charge utile) et flexibles (les segments de mât). Un modèle TITOP est dérivé pour chaque tronçon de mât à partir d'un modèle FE modifié pour ajouter des actionneurs piézoélectriques de 0.2 m de longueur qui permettront dans la future étude d'analyser l'influence d'un contrôle actif du mât. Tous les blocs sont assemblés comme montré dans la Fig. 9.4, et le modèle final prévoit une structure avec une inertie en rotation de 11294 kg·m², un premier mode flexible au 0.62 Hz et une masse totale de 568.15 kg. Le centre de masse de tout l'ensemble est situé à 1.504 m à partir du centre de masses G de la plateforme. En tenant compte de la variation paramétrique de la charge utile, les modèle LFT résultant a 110 états, 48 sorties, 27 entrées et 2 occurrences du paramètre ajustable $\delta_{m_{tip}}$. Comme le modèle est très large, le modèle est réduit aux 35 états le plus significatifs selon la méthode du gramian. Par conséquent, le modèle de synthèse est le modèle réduit de 35 états tandis que le modèle de validation (en anglais : validation model, VM) reste l'original, et qui sera utilisé pour tester les stratégies de contrôle.

Les spécifications pour le co-design sont données par les stratégies de contrôle à tester, les exigences pour la dynamique rigide, les exigences pour la dynamique flexible et les contraintes structurales. Les architectures de contrôleurs décentralisées proposées sont composées d'un contrôleur PD pour gouverner la dynamique rigide et un système d'amortissement actif de la dynamique flexible. Les architectures à tester sont un PD seulement, un PD avec un IFF (retour de force intégral, en anglais, integral force feedback), un PD avec un AF (retour en accélération, en anglais, acceleration feedback), un PD avec un filtre de roll-off et un IFF

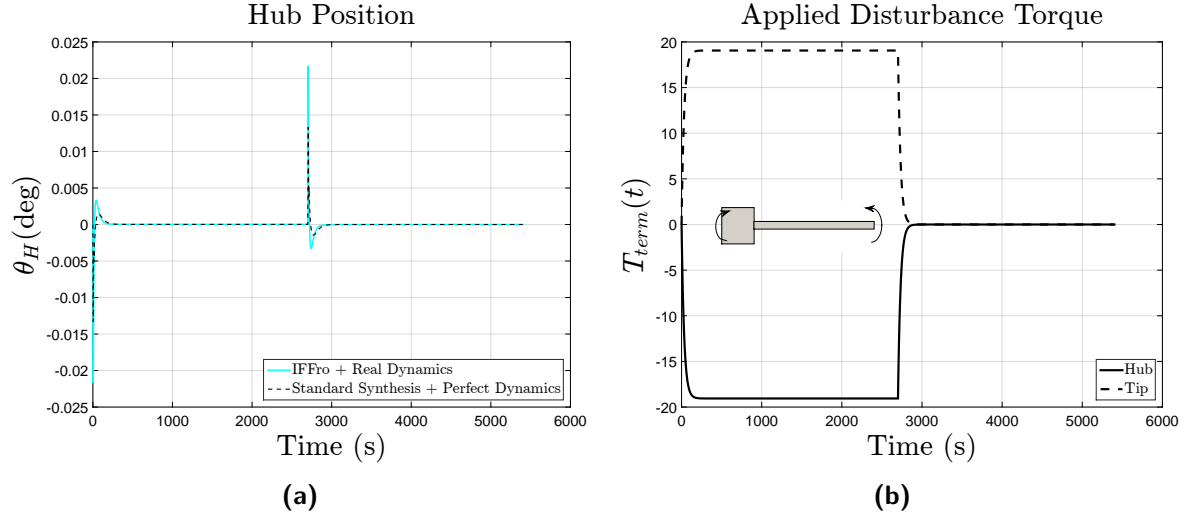


Figure 12.7: Figure 9.17 qui montre la réponse du système contrôlé avec le meilleur contrôleur (IFF avec roll-off) face à un moment perturbateur

avec un filtre de roll-off aussi, et un PD avec un IFF qui utilise des mesures nonlocalisées, notamment la vitesse au bout du mât. Les spécifications pour la dynamique rigide sont une bande passante de 0.182 Hz pour rejeter les perturbations thermiques, un amortissement du 0.7 et un amortissement du mât qui permet d'approximer les déplacements du bout du mât le plus possible au mouvement rigide. La charge utile située au bout du mât doit être maximisée dans une plage du 60 kg au 75 kg.

Toutes les architectures trouvent des solutions au problème du co-design, sauf celle basée sur le retour d'accélération. Les résultats du co-design pour les architectures basées sur l'IFF sont analysés en suivant deux axes différents : robustesse et performance en simulation. La meilleure robustesse, même en tenant compte d'une dynamique réelle pour les roues d'inertie et les actionneurs piézoélectriques, est celle montrée par le PD -IFF avec roll-off (GM = 11.3 dB, PM = 56.6 deg). Les autres stratégies ont des gains très grands car elles n'ont pas eu des contraintes fréquentielles pour limiter leur valeurs, ce qui provoque une perte de robustesse. Pour tester la performance, les lois ont été testées avec le modèle de validation. Un compromis entre les déplacements de la plateforme et les déplacements du bout est trouvé : une action pour empêcher le déplacement d'un côté, l'autre expérimente un déplacement plus important. La seule stratégie à fonctionner même en tenant compte d'une dynamique actionneur sur le modèle de validation est la stratégie PD-IFF avec roll-off, où le déplacement maximal de l'angle de position de la plateforme est respecté ainsi que le déplacement du bout du mât.

Finalement, une étude sur le placement des actionneurs piézoélectriques est faite manuellement. L'objectif est de voir si un placement alternatif des actionneurs piézoélectriques peut améliorer les performances du système, étant donné qu'il ne semble pas affecter la robustesse de la loi de commande. Il se trouve que les optimisations qui réussissent à trouver une solution stabilisante sont celles qui placent les actionneurs au points où les déformées modales ont les plus grands déplacements, notamment la première et la troisième déformée modale. Le

placement nominal des actionneurs étant très proche du placement optimal, aucun placement n'a été trouvé qui réussit à améliorer tous les aspects du meilleur contrôleur nominal (notamment maximisation de la charge utile, déplacement au bout et le dépassement en position de la plateforme). Une étude avec un modèle LFT qui paramétrise la position des actionneurs n'a pas pu être développée du aux contraintes de taille du système et de consistance avec le modèle physique.

12.8 Conclusion

Cette étude a consisté à réaliser le co-design contrôle d'attitude/mécanique d'un satellite flexible en utilisant les outils de la commande robuste structurée et en développant une méthode de modélisation pour des systèmes multi-corps flexibles. Les contributions principales reposent sur deux grands domaines: la modélisation et le co-design.

L'étude a développé une méthode pour la création des modèles de systèmes multi-corps flexibles en vue d'un contrôle linéaire. Les modèles sont présentés sous une forme de représentation d'états, sont obtenus à partir des données FE et peuvent être assemblés en forme de chaîne ou d'étoile. Ils sont aussi précis que d'autres techniques de modélisation utilisées et ils ont l'avantage d'être robustes aux changements des conditions limites. De plus, les modèles ont été étendus pour considérer l'introduction des joints pivot et des matériaux piézoélectriques, et ils ont été appliqués sur une large variété d'exemples : des enchaînement des poutres, satellites flexibles et bras robotique manipulateur.

L'étude a établi le cadre pour réaliser du co-design control/structure avec la synthèse \mathcal{H}_∞ structurée. Les spécifications sur la dynamique rigide et flexible du système ont été établies sur forme de contraintes de norme \mathcal{H}_∞ . De la même manière, les spécifications structurelles ont été aussi converties au cadre \mathcal{H}_∞ et la synthèse du problème \mathcal{H}_∞ structurée a été également modifiée. Comme la synthèse \mathcal{H}_∞ structurée permet le choix de l'architecture du contrôleur, plusieurs architectures pour le contrôle de la dynamique rigide et la dynamique flexible ont été évaluées afin de les utiliser pour les études du co-design. L'introduction du retour de force intégral et l'addition de filtres roll-off a apporté au contrôleur plus de robustesse face aux dynamiques réelles des actionneurs et modèles de validation. Dans toutes les applications la méthode du co-design a prouvé être adéquate pour trouver des solutions qui respectent les spécifications données.

Pour le futur, les travaux devraient étendre la technique de modélisation pour considérer des systèmes flexibles en forme d'arbre, ce qui nécessitera plus de deux points de connexion. La recherche devra se focaliser aussi sur l'expansion de la technique aux chaînes cinématiques fermées et la considération de charges distribuées au long de la sous-structure. Également, des études pour calibrer la limite de la modélisation des effets nonlinéaires doivent être conduites afin de bien comprendre les limitations de la méthode. De l'autre côté, l'étude de co-design contrôle/structure peut se voir enrichi en cherchant d'autres architectures de contrôle, d'autres spécifications pour l'optimisation de la structure et avec des améliorations dans le paramétrage pour le placement optimal des actionneurs.

APPENDIX

Superelements

When a substructure linking two other substructures has a beam-like shape, a model called “superlement” can be used. This model provides a full parametric representation for the length, section surface, section inertia and material properties of the beam-like structure. Main aspects of this model are recalled thereafter. The interested reader can refer to [\[Murali 15\]](#) for a complete description.

The superelement model uses a FE approach that exploits the uniformity of the beam, using a polynomial function of higher order than the conventional finite element for beams. Conventional elements have 3rd order while superelement is 5th order, leading to more accurate mode shapes for a single superlement than for two conventional elements sequence. With this polynomial approximation, the mass and stiffness matrices of the beam superlement in planar deflection read:

$$\widetilde{M} = \frac{\rho s l}{55440} \begin{bmatrix} 55440 & 27720 l & 462 l^2 & 27720 & -5544 l & 462 l^2 \\ 27720 l & 18480 l^2 & 198 l^3 & 19800 l & -3432 l^2 & 264 l^3 \\ 462 l^2 & 198 l^3 & 6 l^4 & 181 l^2 & -52 l^3 & 5 l^4 \\ 27720 & 19800 l & 181 l^2 & 21720 & -3732 l & 281 l^2 \\ -5544 l & -3432 l^2 & -52 l^3 & -3732 l & 832 l^2 & -69 l^3 \\ 462 l^2 & 264 l^3 & 5 l^4 & 281 l^2 & -69 l^3 & 6 l^4 \end{bmatrix} \quad (\text{A.1})$$

$$\widetilde{K} = \frac{EI_z}{70 l^3} \begin{bmatrix} 0 & 0 & 0 & 0 & 0 & 0 \\ 0 & 0 & 0 & 0 & 0 & 0 \\ 0 & 0 & 6 l^4 & -30 l^2 & 8 l^3 & l^4 \\ 0 & 0 & -30 l^2 & 1200 & -600 l & 30 l^2 \\ 0 & 0 & 8 l^3 & -600 l & 384 l^2 & -22 l^3 \\ 0 & 0 & l^4 & 30 l^2 & -22 l^3 & 6 l^4 \end{bmatrix} \quad (\text{A.2})$$

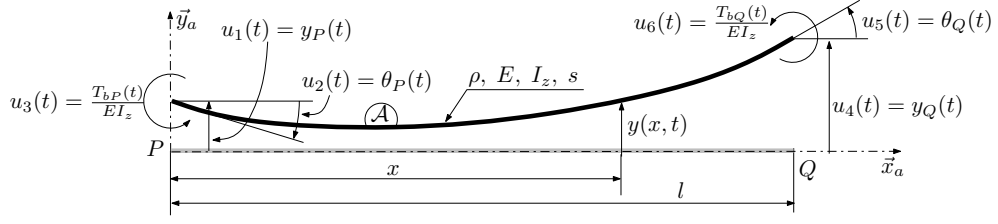


Figure A.1: Parameterization of the superelement's degrees of freedom

being the time-dependent kinematic vector of the superelement (see Fig. A.1):

$$\tilde{u}(t) = \begin{Bmatrix} x_P(t) \\ \theta_P(t) \\ T_{bP}(t)/(EI_z) \\ x_C(t) - x_P(t) - l\theta_P(t) \\ \theta_C(t) - \theta_P(t) \\ T_{bC}(t)/(EI_z) \end{Bmatrix} \quad (\text{A.3})$$

which is the same one as a standard beam element but adding the curvature of the deflected geometry, $T_b(t)/(EI_z)$, and the relative motion between the two beam tips.

It should be noted that vertical displacement, rotation, force and torque at points P and C , respectively y_P/y_C , θ_P/θ_C , f_P/f_C and t_P/t_C are the following projections in the deflection plane $\pi(\vec{x}_a, \vec{y}_a)$:

$$\begin{aligned} y_P &= \vec{y}_a \cdot \{x_P\}; & y_C &= \vec{y}_a \cdot \{q_C\} \\ \theta_P &= \vec{z}_a \cdot \{\theta_P\}; & \theta_C &= \vec{z}_a \cdot \{\theta_C\} \\ f_P &= \vec{y}_a \cdot \{f_{A/P}\}; & f_C &= \vec{y}_a \cdot \{f_{C,A}\} \\ t_P &= \vec{z}_a \cdot \{t_{A/P,P}\}; & t_C &= \vec{z}_a \cdot \{t_{C/C,C}\} \end{aligned} \quad (\text{A.4})$$

Murali [Murali 15] uses Eq.(A.1) and the expressions in Eq.(A.4) and (A.2) to arrange the following state-space representation of the double-port model $T_y R_z(s)$ of the beam restricted to bending in the plane $\pi(\vec{x}_a, \vec{y}_a)$:

$$\begin{Bmatrix} \dot{\tilde{u}}_{(3:6)} \\ \ddot{\tilde{u}}_{(3:6)} \\ \ddot{q}_Q \\ \ddot{\theta}_Q \\ f_P \\ t_P \end{Bmatrix} = \underbrace{\begin{bmatrix} A_{Ty,Rz} & B_{Ty,Rz} \\ C_{Ty,Rz} & D_{Ty,Rz} \end{bmatrix}}_{T_y R_z(s)} \begin{Bmatrix} \tilde{u}_{(3:6)} \\ \dot{\tilde{u}}_{(3:6)} \\ f_Q \\ t_Q \\ \ddot{q}_P \\ \ddot{\theta}_P \end{Bmatrix} \quad (\text{A.5})$$

with:

$$A_{Ty,Rz} = \begin{bmatrix} 0_{4 \times 4} & I_4 \\ -\widetilde{M}_{(3:6,3:6)}^{-1} \widetilde{K}_{(3:6,3:6)} & 0_{4 \times 4} \end{bmatrix} \quad (\text{A.6})$$

$$B_{Ty,Rz} = \begin{bmatrix} 0_{4 \times 2} & 0_{4 \times 2} \\ \widetilde{M}_{(3:6,3:6)}^{-1} \Phi^T & -\widetilde{M}_{(3:6,3:6)}^{-1} \widetilde{M}_{(3:6,1:2)} \end{bmatrix} \quad (\text{A.7})$$

$$C_{Ty,Rz} = \begin{bmatrix} -\Phi \widetilde{M}_{(3:6,3:6)}^{-1} \widetilde{K}_{(3:6,3:6)} & 0_{2 \times 4} \\ \widetilde{M}_{(3:6,1:2)}^T \widetilde{M}_{(3:6,3:6)}^{-1} \widetilde{K}_{(3:6,3:6)} & 0_{2 \times 4} \end{bmatrix} \quad (\text{A.8})$$

$$D_{Ty,Rz} = \begin{bmatrix} D_{Ty,Rz}^{11} & D_{Ty,Rz}^{12} \\ (D_{Ty,Rz}^{12})^T & D_{Ty,Rz}^{22} \end{bmatrix} \quad (\text{A.9})$$

The complete form of Eq. (A.9) can be found in Eq.(A.12). Since the beam can be bended in the planes $\pi(\vec{x}_a, \vec{y}_a)$ and $\lambda(\vec{x}_a, \vec{y}_a)$, the model can be expanded to a full degree of freedom representation, taken into account bending on both planes, $T_y R_z(s)$ and $T_z R_y(s)$, torsion $T_x(s)$, and translation in \vec{x}_a , $R_x(s)$. This leads to the double-port model superelement $[S_{P,Q}^A(s)]$ of the 6 d.o.fs beam is (in projection in the frame $\mathcal{R}_a = (P, \vec{x}_a, \vec{y}_a, \vec{z}_a)$):

$$\left\{ \begin{array}{c} \{ \ddot{u}_Q \}_{\mathcal{R}_a} \\ \{ F_{\mathcal{A}/\mathcal{P},P} \}_{\mathcal{R}_a} \end{array} \right\} = [S_{P,Q}^A(s)]_{\mathcal{R}_a} \left\{ \begin{array}{c} \{ F_{\mathcal{Q}/\mathcal{A},Q} \}_{\mathcal{R}_a} \\ \{ \ddot{u}_P \}_{\mathcal{R}_a} \end{array} \right\} \quad (\text{A.10})$$

where:

$$[S_{P,Q}^A(s)]_{\mathcal{R}_a} = T^T \begin{bmatrix} T_y R_z(s) & & & \\ & T_z R_y(s) & & \\ & & R_x(s) & \\ & & & T_x(s) \end{bmatrix} T \quad (\text{A.11})$$

with T being a permutation matrix of the inputs/outputs computed in Eq. (A.15) described in Appendix B.

As it can be appreciated, the parametrization is more thoroughful since length, section area, cross inertia or density appear at all the levels of the system, having a more accurate influence on the dynamics.

Previously, the following matrices were used:

$$D_{Ty,Rz}^{11} = \Phi \widetilde{M}_{(3:6,3:6)}^{-1} \Phi^T \quad (\text{A.12})$$

$$D_{Ty,Rz}^{12} = \left(\tau - \Phi \widetilde{M}_{(3:6,3:6)}^{-1} \widetilde{M}_{(3:6,1:2)} \right) \quad (\text{A.13})$$

$$D_{Ty,Rz}^{22} = -\widetilde{M}_{(1:2,1:2)} + \widetilde{M}_{(3:6,1:2)}^T \widetilde{M}_{(3:6,3:6)}^{-1} \widetilde{M}_{(3:6,1:2)} \quad (\text{A.14})$$

\mathbf{T} is a permutation matrix defined by:

$$\mathbf{T} = \begin{bmatrix} 0 & 1 & 0 & 0 & 0 & 0 & 0 & 0 & 0 & 0 & 0 & 0 & 0 \\ 0 & 0 & 0 & 0 & 0 & 1 & 0 & 0 & 0 & 0 & 0 & 0 & 0 \\ 0 & 0 & 0 & 0 & 0 & 0 & 0 & 1 & 0 & 0 & 0 & 0 & 0 \\ 0 & 0 & 0 & 0 & 0 & 0 & 0 & 0 & 0 & 0 & 0 & 0 & 1 \\ 0 & 0 & 1 & 0 & 0 & 0 & 0 & 0 & 0 & 0 & 0 & 0 & 0 \\ 0 & 0 & 0 & 0 & 1 & 0 & 0 & 0 & 0 & 0 & 0 & 0 & 0 \\ 0 & 0 & 0 & 0 & 0 & 0 & 0 & 0 & 1 & 0 & 0 & 0 & 0 \\ 0 & 0 & 0 & 0 & 0 & 0 & 0 & 0 & 0 & 0 & 1 & 0 & 0 \\ 0 & 0 & 0 & 1 & 0 & 0 & 0 & 0 & 0 & 0 & 0 & 0 & 0 \\ 0 & 0 & 0 & 0 & 0 & 0 & 0 & 0 & 0 & 1 & 0 & 0 & 0 \\ 1 & 0 & 0 & 0 & 0 & 0 & 0 & 0 & 0 & 0 & 0 & 0 & 0 \\ 0 & 0 & 0 & 0 & 0 & 0 & 1 & 0 & 0 & 0 & 0 & 0 & 0 \end{bmatrix} \quad (\text{A.15})$$

Appendix B

Beam Finite Elements

The mass and stiffness matrices of each piezo element are written as:

$$[\mathcal{M}_{qq}]_{piezo} = \rho_p A_p l \begin{bmatrix} \frac{1}{3} & 0 & 0 & \frac{1}{6} & 0 & 0 \\ 0 & \frac{156}{420} & \frac{22}{420}l & 0 & \frac{54}{420} & -\frac{13}{420}l \\ 0 & \frac{22}{420}l & \frac{4}{420}l^2 & 0 & \frac{13}{420}l & -\frac{3}{420}l^2 \\ \frac{1}{6} & 0 & 0 & \frac{1}{3} & 0 & 0 \\ 0 & \frac{54}{420}l & \frac{13}{420}l & 0 & \frac{156}{420} & -\frac{22}{420}l \\ 0 & -\frac{13}{420}l & -\frac{3}{420}l^2 & 0 & -\frac{22}{420}l & \frac{4}{420}l^2 \end{bmatrix} \quad (\text{B.1})$$

$$[\mathcal{K}_{qq}]_{piezo} = \frac{E_p I_p}{l^3} \begin{bmatrix} \frac{A_p l^2}{I_p} & 0 & 0 & -\frac{A_p l^2}{I_p} & 0 & 0 \\ 0 & 12 & 6l & 0 & -12 & 6l \\ 0 & 6l & 4l^2 & 0 & -6l & 2l^2 \\ -\frac{A_p l^2}{I_p} & 0 & 0 & \frac{A_p l^2}{I_p} & 0 & 0 \\ 0 & -12 & -6l & 0 & 12 & -6l \\ 0 & 6l & 2l^2 & 0 & -6l & 4l^2 \end{bmatrix} \quad (\text{B.2})$$

where $I_p = w_p t_p (t^2 + t_p t + \frac{t_p}{2})$. The mass and stiffness matrices of each beam element are written as:

$$[\mathcal{M}_{qq}]_{beam} = \rho A l \begin{bmatrix} \frac{1}{3} & 0 & 0 & \frac{1}{6} & 0 & 0 \\ 0 & \frac{156}{420} & \frac{22}{420}l & 0 & \frac{54}{420} & -\frac{13}{420}l \\ 0 & \frac{22}{420}l & \frac{4}{420}l^2 & 0 & \frac{13}{420}l & -\frac{3}{420}l^2 \\ \frac{1}{6} & 0 & 0 & \frac{1}{3} & 0 & 0 \\ 0 & \frac{54}{420}l & \frac{13}{420}l & 0 & \frac{156}{420} & -\frac{22}{420}l \\ 0 & -\frac{13}{420}l & -\frac{3}{420}l^2 & 0 & -\frac{22}{420}l & \frac{4}{420}l^2 \end{bmatrix} \quad (\text{B.3})$$

$$[\mathcal{K}_{qq}]_{beam} = \frac{EI}{l^3} \begin{bmatrix} \frac{Al^2}{I} & 0 & 0 & -\frac{Al^2}{I} & 0 & 0 \\ 0 & 12 & 6l & 0 & -12 & 6l \\ 0 & 6l & 4l^2 & 0 & -6l & 2l^2 \\ -\frac{Al^2}{I} & 0 & 0 & \frac{Al^2}{I} & 0 & 0 \\ 0 & -12 & -6l & 0 & 12 & -6l \\ 0 & 6l & 2l^2 & 0 & -6l & 4l^2 \end{bmatrix} \quad (B.4)$$

Note that the mass and stiffness matrices of the beam element are identical as the ones denoted in Eqs. (B.3) and (B.4) but substituting the piezoelectric strip parameters by those of the beam. The 3D beam elements used in Chap. 6 can be extracted from [Imbert 79] and they have been included in the Matlab routines as follows:

```
L = beam.L; % beam length
Iz = beam.Iz; % Z-cross section inertia
Iy = beam.Iy; % Y cross section inertia
Ix = beam.Ix; % torsional inertia
k_S = beam.k_S; % for factor of the section
S = beam.S ; % section surface
E = beam.E; % Young Modulus
G = beam.G ; % total elastic modulus
nu = beam.nu ; % poisson coefficient
rho = beam.rho; % beam volumetric density
xi = beam.xi; % damping ratio

EIz = E*Iz;
EIy = E*Iy;

% Beam discretization:

n = nodes-1; % number of elements

dof = 6; % each node can translate in x,y,z and rotate around x,y, z

% node= [u v w thetaX thetaY thetaZ]

% 3D beam element

l = L/n; % element length
m_e = rho*S*l; % mass of the element

phi_Y = 12*EIz/(k_S*G*S*l^2); % Y shear effort
phi_Z = 12*EIy/(k_S*G*S*l^2); % Y shhear effort

% Stiffness matrix K

K_e = zeros(dof*2,dof*2);

K_e(1,1) = E*S/l;
K_e(1,7) = -E*S/l;

K_e(2,2) = 12*EIz/(l^3*(1+phi_Y));
```

```

K_e(2,6) = 6*EIz/(l^2*(1+phi_Y));
K_e(2,8) = -12*EIz/(l^3*(1+phi_Y));
K_e(2,12) = 6*EIz/(l^2*(1+phi_Y));

K_e(3,3) = 12*EIy/(l^3*(1+phi_Z));
K_e(3,5) = -6*EIy/(l^2*(1+phi_Z));
K_e(3,9) = -12*EIy/(l^3*(1+phi_Z));
K_e(3,11) = -6*EIy/(l^2*(1+phi_Z));

K_e(4,4) = G*Ix/l;
K_e(4,10) = -G*Ix/l;

K_e(5,3) = -6*EIy/(l^2*(1+phi_Z));
K_e(5,5) = (4+phi_Z)*EIy/(l*(1+phi_Z));
K_e(5,9) = 6*EIy/(l^2*(1+phi_Z));
K_e(5,11) = (2-phi_Z)*EIy/(l*(1+phi_Z));

K_e(6,2) = 6*EIz/(l^2*(1+phi_Y));
K_e(6,6) = (4+phi_Y)*EIz/(l*(1+phi_Y));
K_e(6,8) = -6*EIz/(l^2*(1+phi_Y));
K_e(6,12) = (2-phi_Y)*EIz/(l*(1+phi_Y));

K_e(7,1) = -E*S/l;
K_e(7,7) = E*S/l;

K_e(8,2) = -12*EIz/(l^3*(1+phi_Y));
K_e(8,6) = -6*EIz/(l^2*(1+phi_Y));
K_e(8,8) = 12*EIz/(l^3*(1+phi_Y));
K_e(8,12) = -6*EIz/(l^2*(1+phi_Y));

K_e(9,3) = -12*EIy/(l^3*(1+phi_Z));
K_e(9,5) = 6*EIy/(l^2*(1+phi_Z));
K_e(9,9) = 12*EIy/(l^3*(1+phi_Z));
K_e(9,11) = 6*EIy/(l^2*(1+phi_Z));

K_e(10,4) = -G*Ix/l;
K_e(10,10) = G*Ix/l;

K_e(11,3) = -6*EIy/(l^2*(1+phi_Z));
K_e(11,5) = (2-phi_Z)*EIy/(l*(1+phi_Z));
K_e(11,9) = 6*EIy/(l^2*(1+phi_Z));
K_e(11,11) = (4+phi_Z)*EIy/(l*(1+phi_Z));

K_e(12,2) = 6*EIz/(l^2*(1+phi_Y));
K_e(12,6) = (2-phi_Y)*EIz/(l*(1+phi_Y));
K_e(12,8) = -6*EIz/(l^2*(1+phi_Y));
K_e(12,12) = (4+phi_Y)*EIz/(l*(1+phi_Y));

% Mas matrix M

M11 = zeros(6,6);
M11(1,1) = 1/3;
M11(2,2) = 13/35 + 6*Iz/(5*S*l^2);
M11(3,3) = 13/35 + 6*Iy/(5*S*l^2);
M11(4,4) = Ix/(3*S);

```

```

M11(5,5) = l^2/105 + 2*Iy/(15*S);
M11(6,6) = l^2/105 + 2*Iz/(15*S);
M11(6,2) = 11*l/210 + Iz/(10*S*l);
M11(2,6) = M11(6,2) ;
M11(5,3) = -11*l/210 - Iy/(10*S*l);
M11(3,5) = M11(5,3) ;

M22 = -M11 + 2*diag(diag(M11));

M21 = zeros(6,6);
M21(1,1) = 1/6;
M21(2,2) = 9/70 - 6*Iz/(5*S*l^2);
M21(3,3) = 9/70 - 6*Iy/(5*S*l^2);
M21(4,4) = Ix/(6*S);
M21(5,5) = -l^2/140 - Iy/(30*S);
M21(6,6) = -l^2/140 - Iz/(30*S);
M21(6,2) = -13*l/420 + Iz/(10*S*l);
M21(2,6) = -M21(6,2);
M21(5,3) = 13*l/420 - Iy/(10*S*l);
M21(3,5) = -M21(5,3);

M_e = m_e*[M11, M21'; M21, M22];

```

Thermal Induced Vibrations

Throughout the study the performance of the control system facing thermal disturbances has been tested. In Sec. 9.3 the bending moment of the deployable mast due to thermal gradient is computed in order to estimate the required system's bandwidth for perturbation rejection. This estimation is based on [Johnston 98], and it is recalled here for better understanding.

Thermal disturbances are the result of temperature differences through the cross section of appendages lead to differential thermal expansion, i.e., the hot side of the appendage expands more than the cold side, which results in structural deformations. Slowly developing temperature differences lead to quasistatic deformations, whereas rapidly changing temperature differences may lead to dynamic structural motions. Depending on the structural dynamics of the appendage, the deformations induced by thermal disturbances may lead to the excitation of the system's natural frequencies, inducing slightly damped frequencies. Motions of flexible appendages result in rigid-body rotations of the entire spacecraft, because the total angular momentum of the system is conserved (see Fig. C.1a). These potentially large attitude disturbances can violate mission pointing accuracy requirements. This phenomena can be experienced by booms and solar arrays.

The thermally induced dynamic response can be foreseen by a key parameter called the *Boley* parameter, given by Boley and Weiner [Boley 60]. The Boley parameter is defined as the square root of the ratio of the characteristic thermal and structural response times of the system:

$$B = \sqrt{\frac{t_T}{t_S}} \quad (\text{C.1})$$

where the characteristic thermal response time t_T is given Eq. (2), described later in this section, and the characteristic structural response time t_S is the period of the fundamental mode of vibration for the appendage. A dynamic amplification factor is built in order to relate the maximum dynamic displacement to the maximum quasistatic displacement:

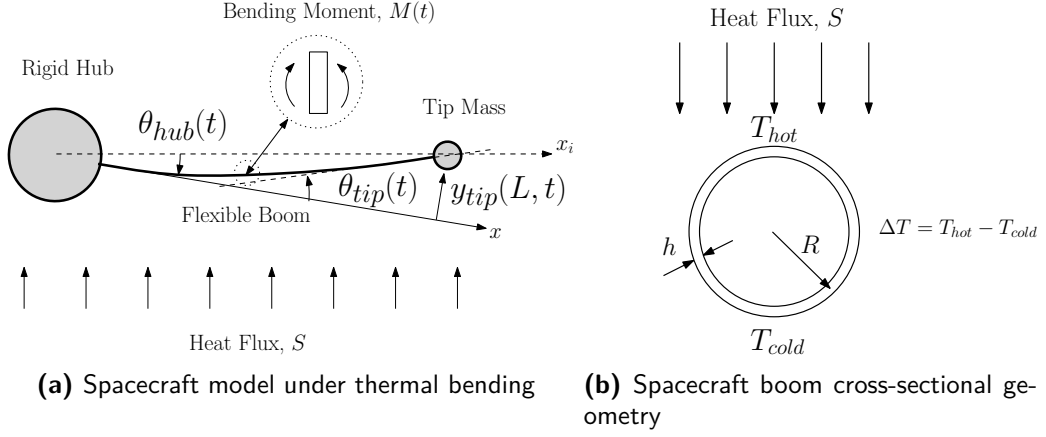


Figure C.1: Thermally induced vibrations of a flexible spacecraft

$$\frac{\nu_{dyn}}{\nu_{sta}} = 1 + \frac{1}{\sqrt{1 + B^2}} \quad (C.2)$$

In structures with large values of B , $B \gg 1$, the quasistatic thermal-structural analysis is justified. For structures with small values of B , the inertial terms should be included in the thermal-structural analysis since the amplification factor is greater than one. For values of B in the order of one, structures may experience thermal induced vibrations when subjected to rapid heating.

The system under study in Chap. 9, the ELMO spacecraft, is suspected to experience thermal induced vibrations since its Boley parameter value is around $B = 7$, which gives an amplification factor greater than one, that is $\nu_{dyn}/\nu_{sta} = 1.14$. The boley parameter has been computed according to the thermal time constant of an appendage with cylindrical cross-section (see Fig. C.1b), which according to [Johnston 98] is written as follows:

$$t_T = \tau_{app} = \left[\frac{k}{\rho c R^2} + \frac{4\sigma_o \epsilon}{\rho c h} \cdot \left(\frac{\alpha S_o}{\pi \sigma_o \epsilon} \right)^{\frac{3}{4}} \right]^{-1} \quad (C.3)$$

where $k = 2.165 \cdot 10^{-4} \text{ m}^2/\text{s}$ is the thermal diffusivity, ρ the volumetric density of the appendage, c the appendage's specific heat, R is the radius of the appendage, $\sigma_o = 5.670373 \cdot 10^{-8} \text{ W/m}^2 \cdot \text{K}^{-4}$ is the Stefan-Boltzman constant, ϵ the appendage's emissivity, α the appendage's absorptivity, h the cross-section thickness and $S_o = 1366 \text{ W/m}^2$ is the solar heat flux. When using the CNES mast values, the thermal time constant is around $\tau_{app} = 32 \text{ s}$. The first term in Eq. (C.3) is associated with conduction heat transfer and the second term corresponds to radiation heat transfer. For typical metallic spacecraft booms the first term dominates the thermal time constant, but in a composite spacecraft boom the second term is the more dominant. This parameter dominates the transient response of the system

The order of the thermal bending moment experienced by the appendage due to the heat flux depends on the temperature's distribution along the cross-section of the appendage.

Assuming one-dimensional conduction around the circumference of the appendage and heat loss from emitted radiation on its external surface, an approximate analytical solution for the temperature distribution is given by:

$$\Delta T(t) = \underbrace{\frac{\alpha S_o \tau_{app}}{\rho c h}}_{\Delta T_{SS}} (1 - e^{-\frac{t}{\tau_{app}}}) \quad (\text{C.4})$$

The temperature distribution $\Delta T(t)$ determines the thermal bending moment, which can be computed across the cross-sectional area as follows:

$$M(t) = \int_A E \alpha_{cte} \Delta T(t) y dA \quad (\text{C.5})$$

where E is the Young's modulus of the cross-sectional area and α_{cte} is the coefficient of thermal expansion. Integrating Eq. (C.5) over the cross-section of the appendage results in the following general expression for the thermal moment:

$$M(t) = \frac{1}{2} \pi E \alpha_{cte} h R^2 \Delta T_{SS} (1 - e^{-\frac{t}{\tau_{app}}}) \quad (\text{C.6})$$

Because the temperature does not vary along the length of the appendage, the thermal moment is a function only of time. The mast model used in the numerical study of Chap. 9 gives a thermal moment of an amplitude of 19.03 N·m. This corresponds to an internal coupling moment that will perturb the satellites position due to the mast's deformation, as depicted in Fig. C.1a.

Appendix D

Code Matlab Functions

Contents

D.1	Conversion of Δ block	207
D.2	Derivation of the TITOP Model	208

THIS appendix shows the corresponding matlab code of the most used and most important matlab functions of the study.

D.1 Conversion of Δ block

This function converts the uncertain block Δ in a diagonal matrix with tunable parameters, with the same parameters and the same occurrences as the uncertain block.

```
% Extract of uncertain parameters information:
[satelliteLFT_nom, delta, BLKSTRUCT, NORMUNC] = lftdata(satelliteLFT); % delta
    is normalized between -1 and +1
[n_delta_notact, m_delta] = size(delta);

% False Controller augmentation or variable to be optimized
nDelta = length(BLKSTRUCT);

uncertNames = struct_upField(BLKSTRUCT, 'Name');
uncertOccurrences = struct_upField(BLKSTRUCT, 'Occurrences');

% Create the deltaControl matrix of tunable parameters from uncertain
    information:
% Initialize deltaControl with the first uncertainty Name and size
% "Occurrences"
iDelta = 1;
tuningParameter(iDelta) = ltiblock.gain(strcat('d', uncertNames(iDelta, :)), 0);
```



```

tuningParameter(iDelta).Blocks.(strcat('d',uncertNames(iDelta,:))).Gain.Minimum
    = -1;
tuningParameter(iDelta).Blocks.(strcat('d',uncertNames(iDelta,:))).Gain.Maximum
    = +1;
deltaControl = eye(uncertOccurrences(iDelta))*tuningParameter(iDelta);
% Aggregate other uncertainties:
for iDelta = 2:nDelta

    tuningParameter(iDelta)= ltiblock.gain(strcat('d',uncertNames(iDelta,:)),0)
    ;
    tuningParameter(iDelta).Blocks.(strcat('d',uncertNames(iDelta,:))).Gain.
        Minimum = -1;
    tuningParameter(iDelta).Blocks.(strcat('d',uncertNames(iDelta,:))).Gain.
        Maximum = +1;
    deltaControl = blkdiag(deltaControl,eye(uncertOccurrences(iDelta))*
        tuningParameter(iDelta));

end
% deltaControl is the matrix with the tunable parameters

```

D.2 Derivation of the TITOP Model

The most used function of the study, *getTITOP* obtains a TITOP model from raw FE data, by specifying which nodes correspond to the rigid body motion and which nodes correspond to the redundant boundary nodes. The FE model in *MDKF* form is then converted into a double-port state-space representation.

```

function TITOP = getTITOP(appendageData,rr,ee,ii)
%-----TITOP = getTITOP(appendageData,rr,ee,ii)
%
%
% Function for building a proper Two-Input Two-Output Port (TITOP) model of a
% finite element model of a substructure
%
% INPUTS:
%
%   - appendageData: Structure containing all necessary data for
%       appendage modelization:
%
%       * appendageData.name : substructure name (string)
%       * appendageData.M:    Mass Matrix of the substructure
%       * appendageData.K:    Stiffness Matrix of the substructure
%       * appendageData.C:    Damping Matrix of the substructure
%       * appendageData.nodes: Number of nodes of the substructure
%   - rr: location of rigid body coordinates dof
%   - ee: location of redundant boundary coordinates dof. ee = [] declares
%       there are
%       not redundant boundary coordinates (terminal appendage: rightmost
%       or leftmost appendage)
%   - ii: location of internal degrees of freedom
%

```

```

% OUTPUTS:
%
%      - TITOP: state space model for the substructure. [AccR,Fe]->[Fr,AccE]
%
%
% NOTES: nodes are supposed ordered as follows: q = {ux,uy,uz,thetax,thetay,
%          thetaz}
%
% Last revision:
% J. Alvaro Perez 18th February 2016
%
% % Verification examples: files TEST_FESS_ULTIMATE.m, TEST_FESS.m (TITOP is
%   the new version of FESS with arranged i/o)
%-----

%% Perform Checks
% Check for Mass Matrix
if isfield(appendageData,'M')
    M = appendageData.M;
else
    error('A Mass Matrix has to be provided to build the state-space model')
end
% Check for Stiffness Matrix
if isfield(appendageData,'K')
    K = appendageData.K;
else
    K = zeros(size(M));
    disp('Warning: No Stiffness Matrix Found. Computing as rigid model')
end
% Check for Damp Matrix
if isfield(appendageData,'C')
    C = appendageData.C;
else
    C = zeros(size(M));
end

nodes = appendageData.nodes;
%% Build TITOP model

if isempty(ee) == 0 % Chain-like appendage

    Nr = length(rr);
    Ne = length(ee);
    n = length(ii);
    dof = (n+Ne+Nr)/nodes;

    % Writting outputs/inputs :
    if dof == 6
        name = strcat(appendageData.name,'_');
        inputs = [ strcat(name,'{Fe_x}'); strcat(name,'{Fe_y}'); strcat(name,'{
            Fe_z}'); strcat(name,'{Me_x}'); strcat(name,'{Me_y}'); strcat(name,'
            {Me_z}');
            strcat(name,'{Ar_x}'); strcat(name,'{Ar_y}'); strcat(name,'{Ar_z}')
            ; strcat(name,'{Gr_x}'); strcat(name,'{Gr_y}'); strcat(name,'{
            Gr_z}')];
    end
end

```

```

        outputs = [ strcat(name, '{Ae_x}'); strcat(name, '{Ae_y}'); strcat(name, '{Ae_z}');
                    strcat(name, '{Ge_x}'); strcat(name, '{Ge_y}'); strcat(name, '{Ge_z}');
                    strcat(name, '{Fr_x}'); strcat(name, '{Fr_y}'); strcat(name, '{Fr_z}');
                    ; strcat(name, '{Mr_x}'); strcat(name, '{Mr_y}'); strcat(name, '{Mr_z}')]];

elseif dof == 3
    if Ne == dof && Nr == dof
        name = strcat(appendageData.name, '_');
        inputs = [ strcat(name, '{Fe_x}'); strcat(name, '{Fe_y}'); strcat(name, '{Me_z}');
                    strcat(name, '{Ar_x}'); strcat(name, '{Ar_y}'); strcat(name, '{Gr_z}')
                    ];
        outputs = [ strcat(name, '{Ae_x}'); strcat(name, '{Ae_y}'); strcat(name, '{Ge_z}');
                    strcat(name, '{Fr_x}'); strcat(name, '{Fr_y}'); strcat(name, '{Mr_z}')
                    ];
    else
        name = strcat(appendageData.name, '_');
        inputs_r = strcat(name, '{Arx}', num2str(1));
        outputs_r = strcat(name, '{Arx}', num2str(1));
        for il = 0:dof:Nr-dof
            coord = ceil(il/dof+0.1);
            inputs_r(il+1,:) = strcat(name, '{Arx}', num2str(coord));
            inputs_r(il+2,:) = strcat(name, '{Ary}', num2str(coord));
            inputs_r(il+3,:) = strcat(name, '{Arz}', num2str(coord));
            outputs_r(il+1,:) = strcat(name, '{Fr_x}', num2str(coord));
            outputs_r(il+2,:) = strcat(name, '{Fr_y}', num2str(coord));
            outputs_r(il+3,:) = strcat(name, '{Fr_z}', num2str(il));
        end

        inputs_e = strcat(name, '{Arx}', num2str(1));
        outputs_e = strcat(name, '{Arx}', num2str(1));
        for il = 0:dof:Ne-dof
            coord = ceil(il/dof+0.1);
            inputs_e(il+1,:) = strcat(name, '{Fex}', num2str(coord));
            inputs_e(il+2,:) = strcat(name, '{Fey}', num2str(coord));
            inputs_e(il+3,:) = strcat(name, '{Fez}', num2str(coord));
            outputs_e(il+1,:) = strcat(name, '{Aex}', num2str(coord));
            outputs_e(il+2,:) = strcat(name, '{Aey}', num2str(coord));
            outputs_e(il+3,:) = strcat(name, '{Aez}', num2str(coord));
        end
        inputs = [ inputs_e; inputs_r];
        outputs = [ outputs_e; outputs_r];
    end
elseif dof == 2

    if Ne == dof && Nr == dof

        name = strcat(appendageData.name, '_');
        inputs = [ strcat(name, '{Fe_y}'); strcat(name, '{Me_z}');
                    strcat(name, '{Ar_y}'); strcat(name, '{Gr_z}')
                    ];
        outputs = [ strcat(name, '{Ae_y}'); strcat(name, '{Ge_z}');
                    strcat(name, '{Fr_y}'); strcat(name, '{Mr_z}')
                    ];
    end
end

```

```

else
    name = strcat(appendageData.name, '_');
    % Initialize inputs/outputs
    inputs_r = strcat(name, '{Arx}', num2str(1));
    outputs_r = strcat(name, '{Arx}', num2str(1));
    for il = 0:dof:Nr-dof
        coord = ceil(il/dof+0.1);
        inputs_r(il+1,:) = strcat(name, '{Arx}', num2str(coord));
        inputs_r(il+2,:) = strcat(name, '{Ary}', num2str(coord));
        outputs_r(il+1,:) = strcat(name, '{FrX}', num2str(coord));
        outputs_r(il+2,:) = strcat(name, '{Fry}', num2str(coord));
    end
    % Initialize inputs/outputs
    inputs_e = strcat(name, '{Arx}', num2str(1));
    outputs_e = strcat(name, '{Arx}', num2str(1));
    for il = 0:dof:Ne-dof
        coord = ceil(il/dof+0.1);
        inputs_e(il+1,:) = strcat(name, '{Fex}', num2str(coord));
        inputs_e(il+2,:) = strcat(name, '{Fey}', num2str(coord));
        outputs_e(il+1,:) = strcat(name, '{Aex}', num2str(coord));
        outputs_e(il+2,:) = strcat(name, '{Aey}', num2str(coord));
    end
    inputs = [ inputs_e; inputs_r];
    outputs = [ outputs_e; outputs_r];
end

else
    error('Please, insert a model with 2-3 d.o.f per node (2D case) or 6 d.
        o.f per node (3D case)')
end

%% Load Matrix : this is the necessary shape for the TITOP model (load
% matrix which acts in the redundant nodes and and the rigid nodes
Q = [eye(dof); zeros(nodes*dof-2*dof, dof); eye(dof)];

Mii = M(ii, ii); Mie = M(ii, ee); Mir = M(ii, rr);
Mei = M(ee, ii); Mee = M(ee, ee); Mer = M(ee, rr);
Mri = M(rr, ii); Mre = M(rr, ee); Mrr = M(rr, rr);

Kii = K(ii, ii); Kie = K(ii, ee); Kir = K(ii, rr);
Kei = K(ee, ii); Kee = K(ee, ee); Ker = K(ee, rr);
Kri = K(rr, ii); Kre = K(rr, ee); Krr = K(rr, rr);

Cii = C(ii, ii); Cie = C(ii, ee); Cir = C(ii, rr);
Cei = C(ee, ii); Cee = C(ee, ee); Cer = C(ee, rr);
Cri = C(rr, ii); Cre = C(rr, ee); Crr = C(rr, rr);

% New Indexes (Normalized)
rr = [n+Ne+1 : n + Ne + Nr];
ee = [n + 1 : n+Ne];
ii = [1:n];

% Fixed-interface normal modes:
[phi_in, D] = eig(Kii, Mii);
PHI_n = [phi_in; zeros(Ne, n); zeros(Nr, n)];

```

```

% Redundant-interface constraint modes:
phi_ie = -inv(Kii)*Kie;
PHI_e = [phi_ie; eye(Ne); zeros(Nr,Ne)];

% Rigid body modes:
PHI_r = [-inv([Kii Kie; Kei Kee])*[Kir; Ker]; eye(Nr)];
phi_er = PHI_r(ee,:);

% Component Modes Matrix
PHI = [PHI_n PHI_e PHI_r];

% Reshaping Matrices:

K = [Kii Kie Kir; Kei Kee Ker; Kri Kre Krr]; M = [Mii Mie Mir; Mei Mee Mer;
    Mri Mre Mrr];
C = [Cii Cie Cir; Cei Cee Cer; Cri Cre Crr];

Knorm = PHI'*K*PHI;
Mnorm = PHI'*M*PHI;
Cnorm = PHI'*C*PHI;
Qnorm = PHI'*Q;

%% Normalized Matrices

Miinorm = Mnorm(ii,ii); Mienorm = Mnorm(ii,ee); Mirnorm = Mnorm(ii,rr);
Meinorm = Mnorm(ee,ii); Meenorm = Mnorm(ee,ee); Mernorm = Mnorm(ee,rr);
Mrinorm = Mnorm(rr,ii); Mrenorm = Mnorm(rr,ee); Mrnorm = Mnorm(rr,rr);

Kiinorm = Knorm(ii,ii); Kienorm = Knorm(ii,ee); Kirnorm = Knorm(ii,rr);
Keinorm = Knorm(ee,ii); Keenorm = Knorm(ee,ee); Kernorm = Knorm(ee,rr);
Krinorm = Knorm(rr,ii); Krenorm = Knorm(rr,ee); Krrnorm = Knorm(rr,rr);

Ciinorm = Cnorm(ii,ii); Cienorm = Cnorm(ii,ee); Cirnorm = Cnorm(ii,rr);
Ceinorm = Cnorm(ee,ii); Ceenorm = Cnorm(ee,ee); Cernorm = Cnorm(ee,rr);
Crinorm = Cnorm(rr,ii); Crenorm = Cnorm(rr,ee); Crrnorm = Cnorm(rr,rr);

% Build Matrix Blocks
MIE = [Miinorm Mienorm; Meinorm Meenorm];
KIE = [Kiinorm Kienorm; Keinorm Keenorm];
CIE = [Ciinorm Cienorm; Ceinorm Ceenorm];
QIE = [zeros(n,Ne) -Mirnorm; eye(Ne) -Mernorm];

%% Build State Space Representation:
AA = [zeros(n+Ne) eye(n+Ne);
    -inv(MIE)*KIE -inv(MIE)*CIE];
BB = [zeros(n,Ne) zeros(n,Nr);
    zeros(Ne,Ne) zeros(Ne,Nr);
    inv(MIE)*QIE];

CC_nue = [zeros(Ne,n) eye(Ne,Ne)]*[-inv(MIE)*KIE -inv(MIE)*CIE];
DD_nue = [zeros(Ne,n) eye(Ne,Ne)]*[inv(MIE)*QIE];

CC_ue = CC_nue;

```

```

DD_ue = DD_nue + [zeros(Ne,Nr) phi_er];

CC_fr = -1*[Mrinorm Mrenorm]* [-inv(MIE)*KIE -inv(MIE)*CIE];
DD_fr = -1*[-phi_er' Mrnorm] - [Mrinorm Mrenorm]*[inv(MIE)*QIE];

CC = [CC_ue; CC_fr];
DD = [DD_ue; DD_fr];

TITOP = ss(AA,BB,CC,DD, 'inputname',inputs, 'outputname',outputs);

% Re-arrange i/o: [AccR,Fe]->[Fr,AccE] (with this form LFT concatenation is
      straightforward)
TITOP = TITOP([Ne+1 : Nr+Ne, 1:Ne ],[Ne+1 : Ne+Nr, 1:Ne ]);

elseif isempty(ee)==1 % Appendage at the end of the chain

Nr = length(rr);
n = length(ii);
dof = (n+Nr)/nodes;

% Extract Matrices:
Q = [eye(dof); zeros(nodes*dof-2*dof,dof); eye(dof)]; % Load Matrix

Mii = M(ii,ii); Mir = M(ii,rr);
Mri = M(rr,ii); Mrr = M(rr,rr);

Kii = K(ii,ii); Kir = K(ii,rr);
Kri = K(rr,ii); Krr = K(rr,rr);

Cii = C(ii,ii); Cir = C(ii,rr);
Cri = C(rr,ii); Crr = C(rr,rr);

% New Indexes (Normalized)
rr = [n+1 : n + Nr];
ii = [1:n];

% Fixed-interface normal modes:
[phi_in,D] = eig(Kii,Mii);
PHI_n = [phi_in; zeros(Nr,n)];

% Rigid body modes:
PHI_r = [-inv(Kii)*Kir; eye(Nr)];

% Component Modes Matrix
PHI = [PHI_n PHI_r];

% Reshaping Matrices:

K = [Kii Kir; Kri Krr]; M = [Mii Mir; Mri Mrr]; C = [Cii Cir; Cri Crr];

Knorm = PHI'*K*PHI;
Mnorm = PHI'*M*PHI;
Cnorm = PHI'*C*PHI;
Qnorm = PHI'*Q;

```

```

%% Normalized Matrices

Miinorm = Mnorm(ii,ii); Mirnorm = Mnorm(ii,rr);
Mrinorm = Mnorm(rr,ii); Mrrnorm = Mnorm(rr,rr);

Kiinorm = Knorm(ii,ii); Kirnorm = Knorm(ii,rr);
Krinorm = Knorm(rr,ii); Krrnorm = Knorm(rr,rr);

Ciinorm = Cnorm(ii,ii); Cirnorm = Cnorm(ii,rr);
Crinorm = Cnorm(rr,ii); Crrnorm = Cnorm(rr,rr);

% Build Matrix Blocks
MIE = Miinorm;
KIE = Kiinorm;
CIE = Ciinorm;
QIE = -Mirnorm;

%% Build State Space Representation:
AA = [zeros(n) eye(n);
      -inv(MIE)*KIE -inv(MIE)*CIE];
BB = [zeros(n,Nr);
      inv(MIE)*QIE];

CC_fr = -1*[Mrinorm] * [-inv(MIE)*KIE -inv(MIE)*CIE];
DD_fr = -1*[Mrrnorm] - [Mrinorm] * [inv(MIE)*QIE];

CC = CC_fr;
DD = DD_fr;

% Writting outputs/inputs :
if dof == 6
    name = strcat(appendageData.name, '_');
    inputs = [strcat(name, '{Ar_x}'); strcat(name, '{Ar_y}'); strcat(name, '{
        Ar_z}')]; strcat(name, '{Gr_x}'); strcat(name, '{Gr_y}'); strcat(name, '{
        Gr_z}')];
    outputs = [strcat(name, '{Fr_x}'); strcat(name, '{Fr_y}'); strcat(name, '{
        Fr_z}')]; strcat(name, '{Mr_x}'); strcat(name, '{Mr_y}'); strcat(name, '{
        Mr_z}')];

elseif dof == 3

    name = strcat(appendageData.name, '_');
    inputs = [strcat(name, '{Ar_x}'); strcat(name, '{Ar_y}'); strcat(name, '{
        Gr_z}')];
    outputs = [strcat(name, '{Fr_x}'); strcat(name, '{Fr_y}'); strcat(name, '{
        Mr_z}')];

elseif dof == 2

    name = strcat(appendageData.name, '_');
    inputs = [strcat(name, '{Ar_y}'); strcat(name, '{Gr_z}')];

```

```
        outputs = [strcat(name, '{Fr_y}'); strcat(name, '{Mr_z}')];

    else
        error('Please, insert a model with 2-3 d.o.f per node (2D case) or 6 d.o.f per node (3D case)')
    end

    if Nr == dof;
        TITOP = ss(AA,BB,CC,DD, 'inputname', inputs, 'outputname', outputs);
    else
        disp('Warning: The number of rigid dof does not correspond to the node dof')
        TITOP = ss(AA,BB,CC,DD);
    end

else
    error('No mathing cases have been found: enchainned appendage or final appendage')
end
```


Other Figures

Contents

E.1	Complementary Figures from Chapter 6	217
E.2	Complementary Figures from Chapter 7	220

E.1 Complementary Figures from Chapter 6

The following figures correspond to results shown in Chap. 6, mainly to the parameter varying section.

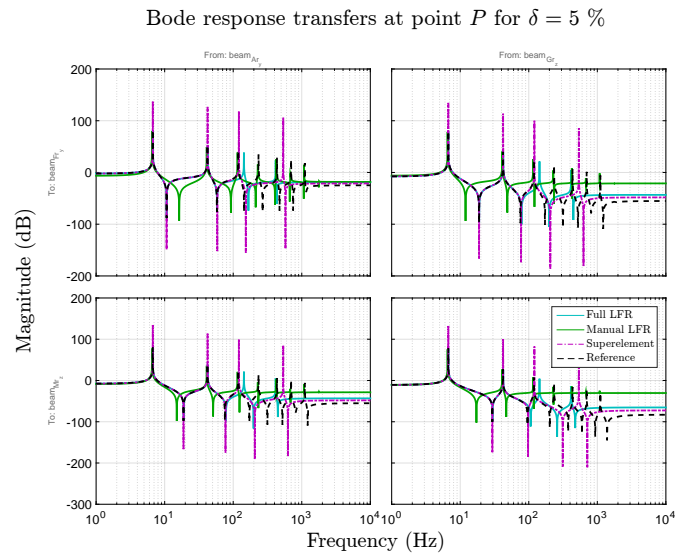


Figure E.1: Transfer Functions at point P for small variations on the beam's length

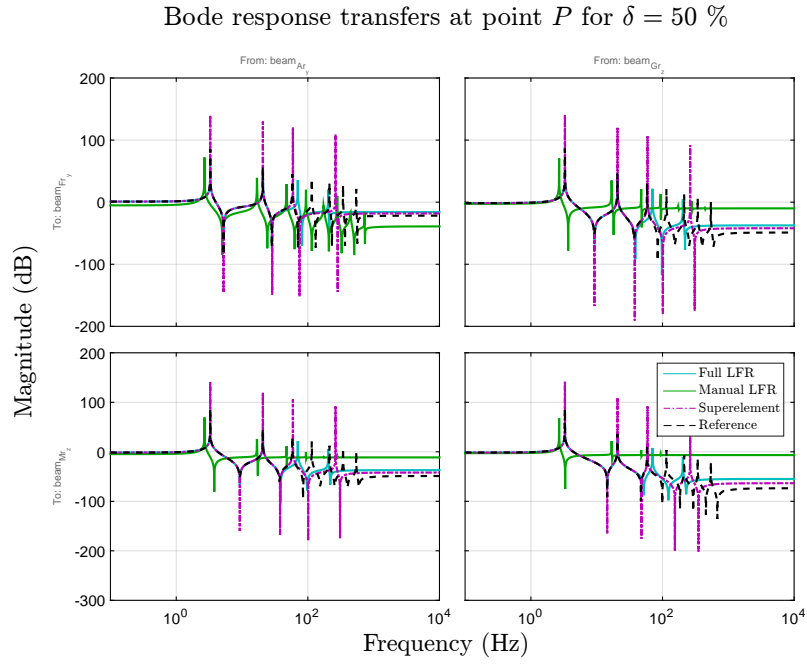


Figure E.2: Transfer Functions at point P for large variations on the beam's length

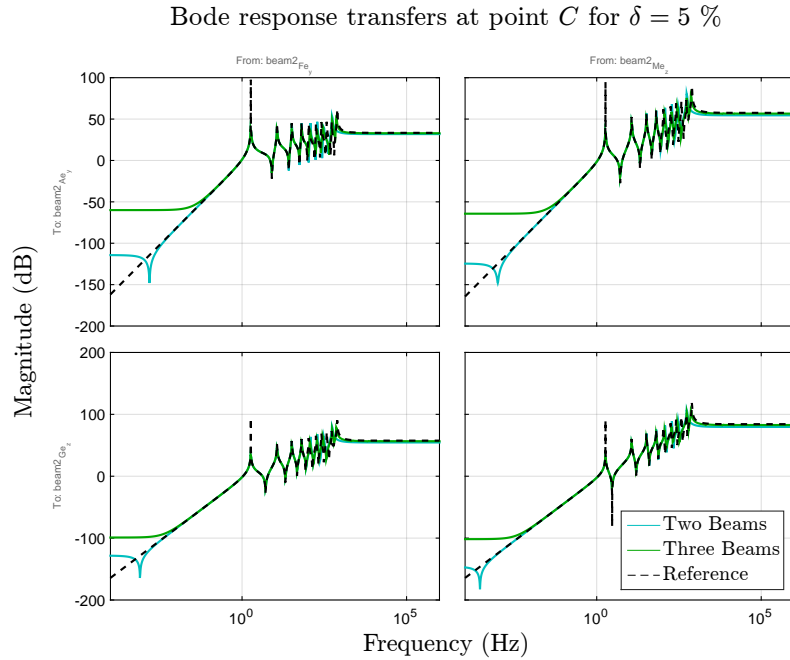


Figure E.3: Transfer Functions at point C for small variations on the beam's length inside the chain of beams

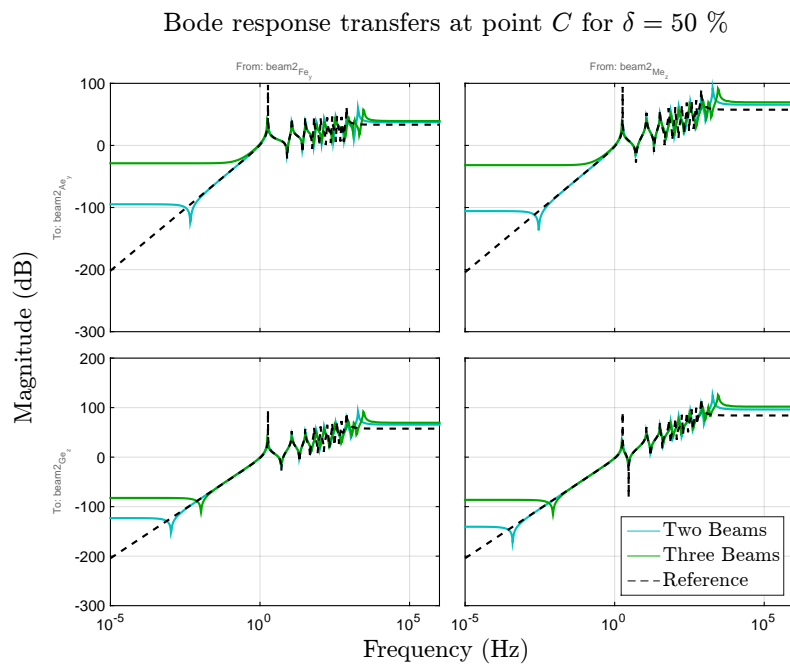


Figure E.4: Transfer Functions at point C for large variations on the beam's length inside the chain of beams

E.2 Complementary Figures from Chapter 7

When testing the collocated/noncollocated systems in Chap. 7, the following figures were not included due to their redundancy:

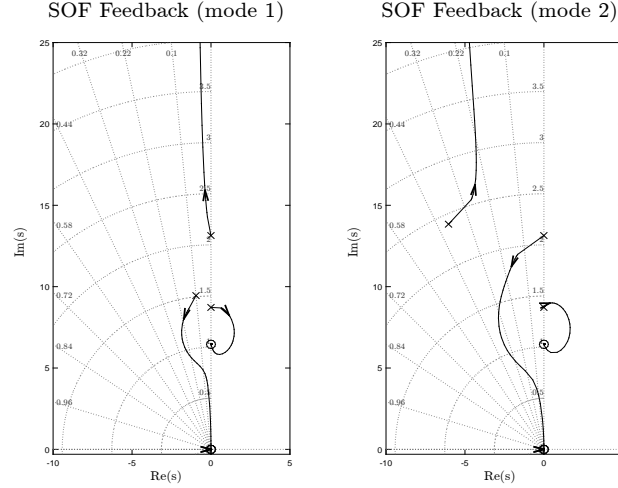


Figure E.5: SOF controller applied to the flexible pointing system with heavy flexible appendage ($m_2 = 1.2$ kg)

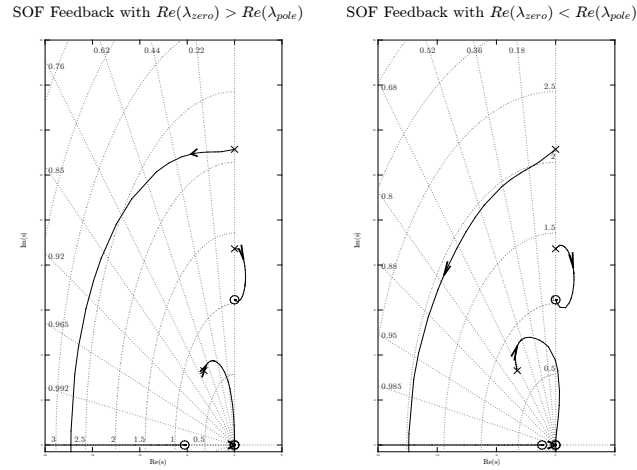


Figure E.6: SOF controller with complex zero applied to the flexible pointing system with heavy flexible appendage ($m_2 = 1.2$ kg)

Bibliography

- [Adriaens 00] Han Adriaens, Willem L De Koning & Reinder Banning. *Modeling Piezo-electric Actuators*. IEEE/ASME Transactions on Mechatronics, vol. 5, no. 4, pages 331–341, 2000. [17](#)
- [Alazard 08] Daniel Alazard, Christelle Cumer & K. Tantawi. *Linear Dynamic Modeling of Spacecraft with Various Flexible Appendages and On-Board Angular Momentums*. In 7th ESA Guidance, Navigation and Control Conference, Tralee (Ireland), June 2008. [15](#), [16](#), [23](#), [26](#), [27](#), [48](#), [54](#), [55](#), [60](#), [75](#), [165](#)
- [Alazard 13a] Daniel Alazard, Thomas Loquen, Henry De Plinval & Christelle Cumer. *Avionics/Control Co-Design for Large Flexible Space Structures*. In AIAA Guidance, Navigation, and Control (GNC) Conference, Boston, Massachusetts, USA, August 2013. [8](#), [22](#), [23](#), [125](#), [167](#), [174](#)
- [Alazard 13b] Daniel Alazard, Thomas Loquen, Henry De Plinval, Christelle Cumer, C. Toglia & P. Pavia. *Optimal Co-Design for Earth Observation Satellites with Flexible Appendages*. In AIAA Guidance, Navigation, and Control (GNC) Conference, 2013. [8](#), [9](#), [22](#)
- [Alazard 15] Daniel Alazard, Jose Alvaro Perez, Thomas Loquen & Christelle Cumer. *Two-Input Two-Output Port Model for Mechanical Systems*. In AIAA Science and Technology Forum and Exposition, Kissimmee, Florida, January 2015. [9](#), [39](#), [59](#), [63](#), [175](#)
- [Balas 05] Gary Balas, Richard Chiang, Andy Packard & Michael Safonov. *Robust Control Toolbox*. For Use with Matlab. User’s Guide, vol. 3, 2005. [74](#)
- [Banerjee 97] A.K. Banerjee & S. Nagarajan. *Efficient Simulation of Large Overall Motion of Beams undergoing Large Deflection*. Multibody System Dynamics, vol. 1, no. 1, pages 113–126, 1997. [17](#)
- [Belcastro 99] Christine M. Belcastro, Kyong B. Lim & Eugene A. Morelli. *Computer-Aided Uncertainty Modeling of Nonlinear Parameter-Dependent Systems. II. F-I6*

- example*. In Computer Aided Control System Design, 1999. Proceedings of the 1999 IEEE International Symposium on, pages 16–23. IEEE, 1999. [74](#)
- [Benhabib 81] R.J. Benhabib, R.P. Iwens & R.L. Jackson. *Stability of Large Space Structure Control Systems Using Positivity Concepts*. J. of Guidance and Control, vol. 4, no. 5, sept-oct 1981. [20](#), [118](#)
- [Bennani 11] Samir Bennani, Finn Ankersen, Marco Arcioni, Massimo Casasco, Luca Massotti & Pierluigi Silvestrin. *Robust Attitude Control Design for the BIOMASS satellite (Earth explorer core mission candidate)*. In 18th IFAC World Congress, 2011. [19](#)
- [Bokhari 08] Syed Fawad Raza Ali Bokhari, Saulat Shuja Chughtai & Herbert Werner. *A Tool for Converting FEM Models into Representations Suitable for Control Synthesis*. In 17th IFAC World Congress, volume 17, pages 6066–6071, 2008. [14](#)
- [Boley 60] Bruno A Boley & Jerome H Weiner. Theory of thermal stresses. Wiley, 1960. [203](#)
- [Boscariol 10] Paolo Boscariol, Alessandro Gasparetto & Vanni Zanotto. *Active Position and Vibration Control of a Flexible Links Mechanism using Model-Based Predictive Control*. ASME Journal of Dynamic Systems, Measurement, and Control, vol. 132, no. 1, page 014506, 2010. [12](#), [14](#)
- [Boyd 94] Stephen P. Boyd, Laurent El Ghaoui, Eric Feron & Venkataramanan Balakrishnan. Linear Matrix Inequalities in System and Control Theory, volume 15. SIAM, 1994. [22](#)
- [Burke 06] J.V. Burke, D. Henrion, A.S. Lewis & M.L. Overton. *HIFOO A Matlab Package for Fixed-Order Controller Design and \mathcal{H}_∞ Optimization*. In 5th IFAC Symposium on Robust Control Design, 2006. [19](#), [22](#), [33](#), [124](#)
- [Butler 03] S.L. Butler & A.K. Dhingra. *Integrated Structure and Control Design of Actively Controlled Structures using Substructure Decomposition*. Journal of Engineering Optimization, vol. 35, no. 4, pages 325–340, 2003. [20](#)
- [Chatlat. 09] Withit Chatlat. & Peter H. Meckl. *Model-Independent Control of a Flexible-Joint Robot Manipulator*. ASME Journal of Dynamic Systems, Measurement, and Control, vol. 131, no. 4, page 041003, 2009. [12](#), [14](#)
- [Choura 91] Slim Choura, Suhada Jayasuriya & Matthew A Medick. *On the Modeling, and Open-Loop Control of a Rotating Thin Flexible Beam*. ASME Journal of Dynamic Systems, Measurement, and Control, vol. 113, no. 1, pages 26–33, 1991. [14](#)
- [CNES 10a] CNES. *Patent B0808-FR: Mât déployable à ossature repliée déployable se verrouillant par construction à l'état déployé. Mât déployable gonflable.*, 2010. [144](#)

- [CNES 10b] CNES. *Patent B0825-FR: Mât déployable à ossature repliée spontanément déployable et rigide a l'état déployé. Mât déployable précontraint*, 2010. [144](#)
- [Craig Jr 00] Roy R. Craig Jr. *A Brief Tutorial on Substructure Analysis and Testing*. In Proceedings of the International Modal Analysis Conference-IMAC, volume 1, pages 899–908, 2000. [15](#), [51](#), [56](#)
- [Craig 68] R. Craig & M. Bampton. *Coupling of Substructures for Dynamic Analysis*. AIAA Journal, vol. 6, no. 7, 1968. [15](#), [48](#), [52](#)
- [Cumer 01] Christelle Cumer & J.P. Chretien. *Minimal LFT Form of a Spacecraft Built Up from Two Bodies*. In AIAA Guidance, Navigation and Control Conference., Montreal, Canada, 2001. [16](#), [23](#), [165](#)
- [Damaren 00] C.J. Damaren. *Passivity and Noncollocation in the Control of Flexible Multi-body Systems*. J. of Dynamic Systems, Measurement and Control, vol. 122, pages 11–17, March 2000. [20](#)
- [Dang 05] X. Dang & Y. Tan. *An Inner Product Based Dynamic Neural Network Hysteresis Model for Piezoceramic Actuators*. Sensors and Actuators A: Physical, vol. 121, no. 2, pages 535–542, 2005. [18](#)
- [Dhingra 94] A.K. Dhingra & B.H. Lee. *Optimal Placement of Actuators in Actively Controlled Structures*. J. of Engineering Optimization, vol. 23, pages 99–118, 1994. [15](#)
- [Dignath 00] F. Dignath & W. Schiehlen. *Control of the Vibrations of a Tethered Satellite System*. Journal of Applied Mathematics and Mechanics, vol. 64, no. 5, pages 715–722, 2000. [17](#)
- [Dokainish 72] M.A. Dokainish. *A New Approach for Plate Vibrations: Combination of Transfer Matrix and Finite Element Technique*. Transactions of the American Society of Mechanical Engineers, Journal of Engineering for Industry, vol. 94, pages 526–530, 1972. [16](#)
- [Doyle 81] John C Doyle & Gunter Stein. *Multivariable feedback design: Concepts for a classical/modern synthesis*. In IEEE Trans. on Auto. Control. Citeseer, 1981. [31](#)
- [Doyle 89] John C Doyle, Keith Glover, Pramod P Khargonekar & Bruce A Francis. *State-space solutions to standard \mathcal{H}_2 and \mathcal{H}_∞ control problems*. IEEE Transactions on Automatic control, vol. 34, no. 8, pages 831–847, 1989. [31](#)
- [Elgohary 15] Tarek A. Elgohary, James D. Turner & John L. Junkins. *Analytic Transfer Functions for the Dynamics & Control of Flexible Rotating Spacecraft Performing Large Angle Maneuvers*. The Journal of the Astronautical Sciences, vol. 62, no. 2, pages 168–195, 2015. [94](#), [95](#)

- [Ersal 08] T. Ersal, H.K. Fathy, D.G. Rideout, L.S. Louca & J.L. Stein. *A Review of Proper Modeling Techniques*. ASME Journal of Dynamic Systems, Measurement, and Control, vol. 130, no. 6, page 061008, 2008. [15](#)
- [Falcoz 15] Alexandre Falcoz, Christelle Pittet, Samir Bennani, Anne Guignard, Cedric Bayart & Benoit Frapard. *Systematic Design Methods of Robust and Structured Controllers for Satellites*. CEAS Space Journal, vol. 7, no. 3, pages 319–334, 2015. [19](#)
- [Fanson 90] J.L. Fanson & T.K. Caughey. *Positive Position Feedback Control for Large Space Structures*. AIAA Journal, vol. 28, no. 4, pages 717–724, 1990. [20](#)
- [Ferrerres 99] Gilles Ferreres. A practical approach to robustness analysis with aeronautical applications. Springer Science & Business Media, 1999. [74](#)
- [Fezans 08] Nicolas Fezans, Daniel Alazard, N. Imbert & B. Carpentier. \mathcal{H}_∞ Control Design for Generalized Second Order Systems based on Acceleration Sensivity Function. In 16th IEEE Mediterranean Conference on Control and Automation, 2008. [127](#)
- [Gahinet 11] P. Gahinet & Pierre Apkarian. *Structured \mathcal{H}_∞ Synthesis using MATLAB*. In 18th IFAC World Congress, Milano, Italy, August 2011. [19](#), [22](#), [33](#), [74](#), [124](#)
- [Goldfarb 97] Michael Goldfarb & Nikola Celanovic. *Modeling Piezoelectric Stack Actuators for Control of Micromanipulation*. Control Systems, IEEE, vol. 17, no. 3, pages 69–79, 1997. [17](#)
- [Guy 12] Nicolas Guy, Daniel Alazard, Christelle Cumer & C. Carbonnel. *Reduced Order \mathcal{H}_∞ Controller Synthesis for Flexible Structures Control*. In 7th IFAC Symposium on Robust Control Design, Aalborg, Denmark, June 2012. [19](#), [129](#)
- [Guy 14] Nicolas Guy, Daniel Alazard, Christelle Cumer & C. Charbonnel. *Dynamic Modeling and Analysis of Spacecraft With Variable Tilt of Flexible Appendages*. J. of Dynamic Systems, Measurement and Control, vol. 136, 2014. [12](#), [16](#), [23](#), [55](#), [71](#), [165](#)
- [Hale 85] A.L. Hale, R. J. Lisowski & W.E. Dahl. *Optimal Simultaneous Structural and Control Design of Maneuvering Flexible Spacecraft*. J. of Guidance, vol. 8, no. 1, 1985. [21](#)
- [Hamelin 01] Jennifer L. Hamelin, Mark C. Jackson, Christopher B. Kirchwey & Roberto A. Pileggi. *STS-99 Shuttle Radar Topography Mission Stability and Control*. Quebec City; Canada, 30 Jul. - 2 Aug. 2001 2001. AAS/AIAA Conference. [19](#)
- [Hintz 75] Robert Morris Hintz. *Analytical Methods in Component Modal Synthesis*. AIAA Journal, vol. 13, no. 8, pages 1007–1016, 1975. [15](#)

- [Hiramoto 06] K. Hiramoto & K.M. Grigoriadis. *Integrated Design of Structural and Control Systems with a Homotopy Like Iterative Method*. International Journal of Control, vol. 79, no. 9, page 1062–1073, September 2006. [22](#)
- [Hiramoto 09] K. Hiramoto, J. Mohammadpour & K.M. Grigoriadis. *Integrated Design of System Parameters, Control and Sensor Actuator Placement for Symmetric Mechanical Systems*. In 48th IEEE Conference on Decision and Control, Shanghai, China, December 2009. [22](#), [167](#)
- [Housner 84] Jerrold M. Housner. *Convected Transient Analysis for Large Space Structures Maneuver and Deployment*. In Proceedings of 25th Structures, Structural Dynamics and Materials Conference, numéro No 84-1023, pages 616–629, 1984. AIAA Paper. [17](#)
- [Housner 88] Jerrold M. Housner, S.C. Wu & C.W. Chang. *A Finite Element Method for Time Varying Geometry in Multibody Structures*. In Proceedings of 29th Structures, Structural Dynamics and Materials Conference, numéro 88-2234, 1988. AIAA Paper. [17](#)
- [Hughes 74] Peter C. Hughes. *Dynamics of Flexible Space Vehicles with Active Attitude Control*. Celestial Mechanics, vol. 9, no. 1, pages 21–39, March 1974. [14](#)
- [Hurty 65] Walter C. Hurty. *Dynamic Analysis of Structural Systems Using Component Modes*. AIAA Journal, vol. 3, no. 4, pages 678–685, 1965. [15](#), [30](#), [48](#), [49](#), [51](#), [52](#)
- [IEEE 88] Institute of Electrical IEEE & Electronics Engineers. *IEEE Standard on Piezoelectricity*. ANSI/IEEE Std 176-1987, 1988. [66](#)
- [Imbert 79] J.F. Imbert. *Analyse des Structures par Elements Finis*. ENSTA. CEPAD, cepaudes edition, 1979. [15](#), [48](#), [54](#), [72](#), [200](#)
- [Johnston 98] John D Johnston & Earl A Thornton. *Thermally Induced Attitude Dynamics of a Spacecraft with a Flexible Appendage*. Journal of Guidance, Control, and Dynamics, vol. 21, no. 4, pages 581–587, 1998. [150](#), [155](#), [203](#), [204](#)
- [Junkins 93] J. L. Junkins & Y. Kim. *Introduction to Dynamics and Control of Flexible Structures*. AIAA, 1993. [90](#), [94](#), [98](#), [166](#), [167](#), [182](#)
- [Kajiwarara 99] Itsuro Kajiwarara & Akio Nagamatsu. *Integrated Design of Structure and Control System considering Performance and Stability*. In Proceedings of the 1999 International Conference on Control Applications, Hawaii, USA, August 1999. [22](#)
- [Kane 80] Thomas R. Kane & David A. Levinson. *Formulation of Equations of Motion for Complex Spacecraft*. Journal of Guidance, Control, and Dynamics, vol. 3, no. 2, pages 99–112, 1980. [13](#)

- [Kane 81] Thomas R. Kane & David A. Levinson. *Simulation of Large Motions of Nonuniform Beams in Orbit. Part I - The Cantilever Beam, Part II: The Unrestrained Beam*. J. Astronaut. Sci., vol. 29, no. 3, pages 213–276, 1981. [13](#)
- [Khot 88] N.S. Khot. *Structure/Control Optimization to Improve the Dynamic Response of Space Structures*. Computational Mechanics, vol. 3, pages 179–186, 1988. [21](#)
- [Kraker 93] B. Kraker. *Generalization of the Craig-Bampton CMS Procedure for General Damping*. Technical report, Technische Universiteit Eindhoven, Eindhoven, 1993. [30](#)
- [Krauss 10] R.W. Krauss & W. J. Book. *Transfer Matrix Modelling of Systems with Noncollocated Feedback*. J. of Dynamic Systems, Measurement and Control, vol. 132, 2010. [16](#), [20](#)
- [Leamy 01] Michael J. Leamy, Ahmed K. Noor & Tamer M. Wasfy. *Dynamic Simulation of a Tethered Satellite System using Finite Elements and Fuzzy Sets*. Computer Methods in Applied Mechanics and Engineering, vol. 190, no. 37, pages 4847–4870, 2001. [17](#)
- [Leckie 60] F. Leckie & E. Pestel. *Transfer Matrix Fundamentals*. International Journal of Mechanical Sciences, vol. 2, pages 137–167, 1960. [16](#), [41](#)
- [Likins 67] Peter W. Likins. *Modal Method for Analysis of Free Rotations of Spacecraft*. AIAA Journal, vol. 5, no. 7, pages 1304–1308, 1967. [14](#)
- [Likins 69] Peter W. Likins. *Dynamics and Control of Flexible Space Vehicles*. Technical Report 32-1329, California Institute of Technology, Pasadena, California, 1969. [13](#)
- [Likins 73] Peter W. Likins, J. Barbera & Victor Baddeley. *Mathematical Modeling of Spinning Elastic Bodies for Modal Analysis*. AIAA journal, vol. 11, no. 9, pages 1251–1258, 1973. [14](#)
- [Loquen 12] Thomas Loquen, Henry De Plinval, Christelle Cumer & Daniel Alazard. *Attitude Control of Satellite with Flexible Appendages: Structured \mathcal{H}_∞ Approach*. In AIAA Guidance, Navigation, and Control (GNC) Conference, Mineapolis (Minesota), August 2012. [19](#), [125](#)
- [Luca 91] Alessandro De Luca & Bruno Siciliano. *Closed-Form Dynamic Model of Planar Multilink Lightweight Robots*. IEEE Transactions on Systems, Man and Cybernetics, vol. 21, no. 4, pages 826–839, 1991. [99](#), [101](#), [166](#), [182](#)
- [MacNeal 71] Richard H. MacNeal. *A Hybrid Method of Component Mode Synthesis*. Computers & Structures, vol. 1, no. 4, pages 581–601, 1971. [15](#)

- [Maghami 96] Peiman G. Maghami, Sandeep Gupta, Kenny B. Elliot & Suresh M. Joshi. *Integrated Controls-Structures Design Methodology: Redesign of an Evolutionary Structure*. Journal of Guidance, Control and Dynamics, vol. 19, no. 2, March-April 1996. [21](#)
- [Masoudi 11] Ramin Masoudi & Mojtaba Mahzoon. *Maneuvering and Vibrations Control of a Free-Floating Space Robot with Flexible Arms*. ASME Journal of Dynamic Systems, Measurement, and Control, vol. 133, no. 5, page 051001, 2011. [12](#), [14](#)
- [McDaniel 77] T. J. McDaniel & K.B. Eversole. *A combined Finite Element - Transfer Matrix Structural Analysis Method*. Journal of Sound and Vibration, vol. 51, no. 2, pages 157–169, 1977. [16](#)
- [McLaren 87] M.D. McLaren & G.L. Slater. *Robust Multivariable Control of Large Space Structures Using Positivity*. J. of Guidance, vol. 10, no. 4, July-August 1987. [20](#)
- [Meiyu 10] Cui Meiyu & Xu Shijie. *Optimal Attitude Control of Flexible Spacecraft with Minimum Vibration*. In AIAA Guidance, Navigation and Control Conference, AIAA-2010-8201. AIAA Toronto, 2010. [19](#)
- [Messac 92] Achille Messac & Kamal Malek. *Control Structure Integrated Design*. AIAA Journal, vol. 30, no. 8, pages 2124–2131, August 1992. [8](#), [21](#), [166](#), [167](#), [168](#), [173](#)
- [Mucino 81] V. H. Mucino & V. Pavelic. *An Exact Condensation Procedure for Chain-Like Structures Using a Finite Element - Transfer Matrix Approach*. Journal of Mechanical Design, vol. 103, pages 295–303, 1981. [41](#)
- [Murali 15] H. Murali, D. Alazard, L. Massotti, F. Ankersen & C. Togli. *Mechanical-Attitude Controller Co-design of Large Flexible Space Structures*. In EURO Guidance, Navigation and Control Conference, Toulouse, France, 2015. [71](#), [73](#), [96](#), [195](#), [196](#)
- [Ohga 83] M. Ohga, T. Shigematsu & T. Hara. *Structural Analysis by a combined Finite Element - Transfer Matrix Method*. Computers & Structures, vol. 17, no. 3, pages 321–326, 1983. [16](#)
- [Oliver 97] R.I. Oliver & S.F. Asokanthan. *Control/Structure Integrated Design for Flexible Spacecraft Undergoing On-Orbit Maneuvers*. J. of Guidance, Control and Dynamics, vol. 20, no. 2, 1997. [21](#)
- [Onoda 87] J. Onoda & Raphael T. Haftka. *An Approach to Structure/Control Simultaneous Optimization for Large Flexible Spacecraft*. AIAA, vol. 25, pages 1133–1138, 1987. [21](#), [166](#), [167](#)
- [Ou 96] J.-S. Ou & N. Kikuchi. *Integrated Optimal Structural and Vibration Control Design*. Structural Optimization, vol. 12, pages 209–216, 1996. [21](#), [167](#)

- [Park 02] Sang-Young Park. *Thermally Induced Attitude Disturbance Control for Spacecraft with a Flexible Boom*. Journal of Spacecraft and Rockets, vol. 39, no. 2, pages 325–328, 2002. [19](#)
- [Pascal 88] Madeleine Pascal. *Dynamics analysis of a system of hinge-connected flexible bodies*. Celestial mechanics, vol. 41, no. 1-4, pages 253–274, 1987/1988. [14](#)
- [Perez 15a] Jose Alvaro Perez, Daniel Alazard, Thomas Loquen, Christelle Cumer & Christelle Pittet. *Linear Dynamic Modeling of Spacecraft with Open-Chain Assembly of Flexible Bodies for ACS/Structure Co-Design*. In Advances in Aerospace Guidance, Navigation and Control, pages 639–658. Springer, 2015. [9](#), [10](#), [56](#)
- [Perez 15b] Jose Alvaro Perez, Christelle Pittet, Daniel Alazard, Thomas Loquen & Christelle Cumer. *A Flexible Appendage Model for Use in Integrated Control/Structure Spacecraft Design*. In IFAC Workshop on Advanced Control and Navigation for Autonomous Aerospace Vehicles, Seville, Spain, 2015. [9](#), [10](#), [168](#)
- [Perez 16a] Jose Alvaro Perez, Daniel Alazard, Thomas Loquen & Christelle Pittet. *Linear Modeling of a Flexible Substructure Actuated through Piezoelectric Components for Use in Integrated Control/Structure Design*. In 20th IFAC Symposium on Automatic Control in Aerospace, 2016. [9](#), [10](#), [168](#)
- [Perez 16b] Jose Alvaro Perez, Daniel Alazard, Thomas Loquen, Christelle Pittet & Christelle Cumer. *Flexible Multibody System Linear Modeling for Control using Component Modes Synthesis and Double-Port Approach*. ASME Journal of Dynamic Systems, Measurement and Control, vol. 138, no. 12, December 2016. [9](#), [10](#), [166](#)
- [Perez 16c] Jose Alvaro Perez, Christelle Pittet, Daniel Alazard & Thomas Loquen. *Integrated Control/ Structure Design of a Large Space Structure using Structured \mathcal{H}_∞ Control*. In 20th IFAC Symposium on Automatic Control in Aerospace, 2016. [10](#), [168](#)
- [Piefort 01] V. Piefort & André Preumont. *Modeling of Smart Piezoelectric Shell Structures with Finite Elements*. In Proceedings of the International Seminar on Modal Analysis, volume 2, pages 869–876. KU Leuven; 1998, 2001. [17](#), [66](#)
- [Preumont 02] André Preumont, Arnaud François, Frédéric Bossens & A. Abu-Hanieh. *Force Feedback versus Acceleration Feedback in Active Vibration Isolation*. Journal of Sound and Vibration, vol. 257, no. 4, pages 605–613, 2002. [20](#)
- [Preumont 11] André Preumont. *Vibration Control of Active Structures: An Introduction*, volume 179. Springer Science & Business Media, 2011. [20](#), [46](#), [113](#), [119](#)
- [Rong 11] B. Rong, X. Rui & G. Wang. *Modified Finite Element - Transfer Matrix Method for Eigenvalue Problem of Flexible Structures*. Journal of Applied Mechanics, vol. 78, 2011. [14](#), [16](#)

- [Rui 08] X. Rui, G. Wang, Y. Lu & L. Yun. *Transfer Matrix Method for Linear Multibody System*. Multibody System Dynamics, vol. 19, pages 179–207, 2008. [16](#)
- [Ruth 10] Mike Ruth, Ken Lebsack & Cornelius Dennehy. *What's New is What's Old: Use of Bode's Integral Theorem (circa 1945) to Provide Insight for 21st Century Spacecraft Attitude Control System Design Tuning*. In AIAA Guidance, Navigation, and Control Conference, August 2010. [6](#)
- [Safonov 91] M.G. Safonov, R.Y. Chiang & H. Flashner. \mathcal{H}_∞ Robust Control Synthesis for a Large Space Structure. J. of Guidance, vol. 14, no. 3, May-June 1991. [20](#)
- [Sankar 80] S. Sankar & S. V. Hoa. *An extended Transfer Matrix - Finite Element Method for Free Vibration of Plates*. Journal of Sound and Vibration, vol. 70, no. 2, pages 205–211, 1980. [16](#)
- [Savant 99] S.V. Savant & H.H. Asada. *Integrated Structure/Control Design Based on Model Validity and Robustness Margin*. In Proceedings of the American Control Conference, San Diego, California, June 1999. [22](#)
- [Schaft 06] Arjan Schaft. *Port-Hamiltonian systems: an introductory survey*. In Proceedings of the International Congress of Mathematicians, pages 1339–1365, 2006. [41](#)
- [Scherer 97] Carsten Scherer, Pascal Gahinet & Mahmoud Chilali. *Multiobjective Output-Feedback Control via LMI Optimization*. Automatic Control, IEEE Transactions on, vol. 42, no. 7, pages 896–911, 1997. [22](#)
- [Schoen 09] Marco P. Schoen, Randy C. Hoover, Sinchai Chinvorarat & Gerhard M. Schoen. *System Identification and Robust Controller Design using Genetic Algorithms for Flexible Space Structures*. ASME Journal of Dynamic Systems, Measurement, and Control, vol. 131, no. 3, page 031003, 2009. [12](#)
- [Shabana 97] Ahmed A. Shabana. *Flexible Multibody Dynamics: Review of Past and Recent Developments*. Multibody System Dynamics, vol. 1, pages 189–222, March 1997. [13](#), [39](#), [41](#)
- [Siljak 11] Dragoslav D Siljak. Decentralized control of complex systems, volume 138 of *Mathematics in Science and Engineering*. Georgia Institute of Technology, 2011. [111](#)
- [Smith 94] R.S. Smith, C. Chu & J. L. Fanson. *The Design of \mathcal{H}_∞ Controllers for an Experimental Non-Collocated Flexible Structure Problem*. IEEE Transactions on control systems technology, vol. 2, no. 2, June 1994. [20](#)
- [Smits 91] Jab G. Smits, Susan I. Dalke & Thomas K. Cooney. *The Constituent Equations of Piezoelectric Bimorphs*. Sensors and Actuators, vol. 28, pages 41–61, 1991. [18](#)

- [Su 95] T. Su, V. Babuska & R.R. Craig. *Substructure-Based Controller Design Method for Flexible Structures*. J. of Guidance, Control and Dynamics, vol. 18, no. 5, September-October 1995. [15](#), [20](#)
- [Sunar 92] M. Sunar & S.S. Rao. *A Substructure-Decomposition Method for the Control Design of Large Flexible Structures*. AIAA Journal, vol. 30, no. 10, pages 2573–2575, 1992. [15](#), [41](#), [165](#), [167](#)
- [Tan 90] T.M. Tan, A. Yousuff, L.Y. Bahar & M. Konstantinidis. *A modified Finite Element - Transfer Matrix for control design of space structures*. Computers & Structures, vol. 36, no. 1, pages 47–55, 1990. [16](#)
- [Tsujioka 96] K. Tsujioka, I. Kajiwaru & A. Nagamatsu. *Integrated Optimum Design of Structure and H-infinity Control System*. AIAA Journal, vol. 34, no. 1, pages 159–165, January 1996. [22](#), [167](#)
- [Turner 80] James D. Turner & John L. Junkins. *Optimal Large-Angle Single-Axis Rotational Maneuvers of Flexible Spacecraft*. Journal of Guidance, Control, and Dynamics, vol. 3, no. 6, pages 578–585, 1980. [14](#)
- [Tutt 69] G.E. Tutt & W.S. Widnall. *Effects of Structural Flexibility on Spacecraft Control Systems*. Technical Report N69-37030, National Aeronautics and Space Administration, NASA, April 1969. [5](#)
- [Usoro 86] P.B. Usoro, R. Nadira & S.S. Mahil. *A Finite Element/Lagrange Approach to Modeling Lightweight Flexible Manipulators*. ASME Journal of Dynamic Systems, Measurement, and Control, vol. 108, no. 3, pages 198–205, 1986. [14](#)
- [Vu-Quoc 87] L. Vu-Quoc & Juan C. Simo. *Dynamics of Earth-Orbiting Flexible Satellites with Multibody Components*. Journal of Guidance, Control, and Dynamics, vol. 10, no. 6, pages 549–558, 1987. [17](#)
- [Wasfy 00] Tamer M. Wasfy & Ahmed K. Noor. *Multibody Dynamic Simulation of the Next Generation Space Telescope using Finite Elements and Fuzzy Sets*. Computer Methods in Applied Mechanics and Engineering, vol. 190, no. 5, pages 803–824, 2000. [17](#)
- [Wasfy 03] Tamer M. Wasfy & Ahmed K. Noor. *Computational Strategies for Flexible Multibody Systems*. ASME Journal of Applied Mechanics, vol. 56, no. 6, November 2003. [12](#), [13](#), [41](#)
- [Woerkhom 93] P. Th. L. Woerkhom. *Synthesis and Survey of Control Laws for Large Flexible Spacecraft*. Control-Theory and Advanced Technology, vol. 9, no. 3, pages 639 – 669, 1993. [20](#)
- [Worak. 11] C. Worak. & A. Oonsivilai. *Transfer Function of Piezoelectric Material*. World Academy of Science, Engineering and Technology, vol. 5, 2011. [17](#), [18](#)

- [Wu 92] Shih-Chin Wu, Che-Wei Chang & Jerrold M. Housner. *Finite Element Approach for Transient Analysis of Multibody Systems*. Journal of Guidance, Control, and Dynamics, vol. 15, no. 4, pages 847–854, 1992. [17](#)
- [Young 90] K. D. Young. *Distribute Finite - Element Modeling and Control Approach for Large Flexible Structures*. J. of Guidance, vol. 13, no. 4, pages 703–713, July-August 1990. [15](#), [16](#), [20](#), [41](#), [165](#), [167](#)
- [Young 00] J.T. Young. *Primer on Craig-Bampton CMS Procedure Method : An Introduction to Boundary Node Functions, Base Shake Analyses, Load Transformation Matrices, Modal Synthesis and Much More*. Technical report, NASA, October 2000. [53](#)
- [Yousuff 86] A. Yousuff. *Controller Design via Structural Modeling by FETM*. Technical report, Drexel University, Dep. of Mechanics, Philadelphia, Pennsylvania 19104, 1986. [16](#)
- [Zheng 05] Jianhua Zheng, Stephen P. Banks & Hugo Alleyne. *Optimal Attitude Control for Three-Axis Stabilized Flexible Spacecraft*. Acta astronautica, vol. 56, no. 5, pages 519–528, 2005. [19](#)
- [Zhu 97] W.D. Zhu & C.D. Mote. *Dynamic Modeling and Optimal Control of Rotating Euler-Bernoulli Beams*. ASME Journal of Dynamic Systems, Measurement, and Control, vol. 119, no. 4, pages 802–808, 1997. [14](#)

Résumé — Dans cette étude de thèse, le problème du co-design mécanique/contrôle d’attitude avec méthodes de la commande robuste structurée est considéré. Le problème est abordé en développant une technique pour la modélisation de systèmes flexibles multi-corps, appelé modèle Two-Input Two-Output Port (TITOP). En utilisant des modèles d’éléments finis comme données d’entrée, ce cadre général permet de déterminer, sous certaines hypothèses, un modèle linéaire d’un système de corps flexibles enchaînés. De plus, cette modélisation TITOP permet de considérer des variations paramétriques dans le système, une caractéristique nécessaire pour réaliser des études de co-design contrôle/structure. La technique de modélisation TITOP est aussi étendue pour la prise en compte des actionneurs piézoélectriques et des joints pivots qui peuvent apparaître dans les sous-structures.

Différentes stratégies de contrôle des modes rigides et flexibles sont étudiées avec les modèles obtenus afin de trouver la meilleure architecture de contrôle pour la réjection des perturbations basse fréquence et l’amortissement des vibrations. En exploitant les propriétés d’outils de synthèse \mathcal{H}_∞ structurée, la mise en œuvre d’un schéma de co-design est expliquée, en considérant les spécifications du système (bande passante du système et amortissement des modes) sous forme de contraintes \mathcal{H}_∞ . L’étude d’un tel co-design contrôle d’attitude/mécanique d’un satellite flexible est illustré en utilisant toutes les techniques développées, optimisant simultanément une loi de contrôle optimisée et certains paramètres structuraux.

Mots clés : \mathcal{H}_∞ structuré, systèmes flexibles multi-corps, co-design, contrôle d’attitude, contrôle de vibrations, modélisation TITOP.

Abstract — In this PhD thesis, the integrated control/structure design of a large flexible spacecraft is addressed using structured \mathcal{H}_∞ synthesis. The problem is endeavored by developing a modeling technique for flexible multibody systems, called the Two Input Two Output Port (TITOP) model. This general framework allows the assembly of a flexible multibody system in chain-like or star-like structure, using finite element models as input data. Additionally, the TITOP modeling technique allows the consideration of parametric variations inside the system, a necessary characteristic in order to perform integrated control/structure design. In contrast to another widely used method, the assumed modes method, the TITOP modelling technique is robust against changes in the boundary conditions which link the flexible bodies. Furthermore, the TITOP modeling technique can be used as an accurate approximation even when kinematic nonlinearities can be large. The TITOP modeling technique is extended to the modeling of piezoelectric actuators and sensors for the control of flexible structures and revolute joints.

Different control strategies, either for controlling rigid body and flexible body motion, are tested with the developed models for obtaining the best controller’s architecture in terms of perturbation rejection and vibration damping. The implementation of the integrated control/structure design in the structured \mathcal{H}_∞ scheme is developed considering the different system’s specifications, such as system’s bandwidth or modes damping, in the form of \mathcal{H}_∞ weighting functions. The integrated attitude control/structure design of a flexible satellite is performed using all the developed techniques and the optimization of the control law and several structural parameters is achieved.

Keywords: structured \mathcal{H}_∞ , flexible multibody systems, integrated design, attitude control, vibration control, TITOP modeling.
